VIPER: PATHFINDING IN-SITU RESOURCE UTILIZATION.

Daniel Andrews[1], [1]NASA Ames Research Center, M/S 200-1, Moffett Field, CA 94035

Introduction: With the Artemis Program, NASA plans to return humans to the Moon to stay. To help support extended stays on the moon, use of local materials - so-called in-situ resources could be invaluable. Since the moon's polar regions have confirmed the presence of volatiles, as revealed by LCROSS, LRO and other lunar missions, the next step is to understand the nature and distribution of those candidate resources and how they might be extracted. Recent studies have even indicated that if those volatiles are practically available for harvesting, they could be processed into propellants and human life-support resources, significantly aiding in sustaining humans on the Moon, and eventually and later to support missions to Mars.

The Volatiles Inspecting Polar Exploration Resource (VIPER) is an in-situ resource utilization (ISRU) mission within NASA's Science Mission Directorate (SMD), based on the pathfinding development of the Resource Prospector (RP) mission concept. This clever mission is currently planned to launch in 2022/23 and spend 100 days mapping and surveying four different Ice Stability Regions to understand the nature and distribution of water and volatiles already confirmed to be there, including measuring mineralogical content such as silicon and light metals from lunar regolith.

The knowledge attained by a mission like VIPER could have many-fold benefits for space exploration, but also commercial applications. VIPER is an essential, early mission supporting the "moon rush" which has developed over the past few years, with both governments and commercial entities making their cases for lunar exploration. VIPER aims to understand just how the water-ice and other volatiles are distributed, both horizontally and vertically, enabling creation of volatiles resource maps, which will guide what might be required to harvest those resources on a large scale.

With sufficient infrastructural investment, led by governments and then optimized by the commercial marketplace, VIPER will be a pathfinder mission addressing early strategic knowledge gaps and enabling commercial markets – a stepping-stone to a great future economy on the moon.

Crystallization of a Model Silicate Moon.

E. Baker[1] (edward.baker@seh.ox.ac.uk), Dr. J Wade[1] and Prof. B Wood[1].
1 (Department of Earth Sciences, University of Oxford)

The Moon is almost indistinguishable from the Earth across a range of refractory isotope systems (e.g. W, O, Cr etc), which suggests a close genetic link with the Earth [1], [2]. Although broadly similar to the terrestrial mantle, the silicate Moon's major element chemistry appears to differ in one key respect - the reported silicate Moon's iron content (up to 17wt% FeO) may be notably higher that the Earth (8wt%FeO). These elevated lunar FeO contents are, however, primarily based upon interpretations of the lunar surface rocks, and in particular the melting and crystallisation history of the silicate Moon.

Given the established genetic link between silicate Earth and Moon, do lunar surface rocks really require a mantle source that is significantly richer in iron? Or is the silicate Moon merely a snapshot of the terrestrial mantle?

My experiments investigate a fractionally crystallizing lunar magma ocean of fertile pyrolytic composition. Starting with McDonough and Sun (1995)[3] primitive mantle, with volatile elements (e.g. K and Na) reduced by 2/3rds. Experiments started at 85% liquid with 15% Olivine removed from primitive composition. At each step the melt from the previous experiment is the bulk composition for the next step. For long duration experiments, graphite lined Pt capsules were used to prevent CaF_2 ingress. Experiments lie between fO_2 of C-CO and IW+1.5 and follow the lunar pressure gradient, from 2.5GPa, 1675°C for the primitive melts to 0.5GPa, 850°C for evolved melts.

*Figure 1: Fractional and Batch models used phMELTS. Mineral stability fields are taken from MELTS too. My experimental line of descent differs from that modelled and enables the mixing of late and early fractions to produce the bulk rock compositions of Mare basalts. *Ferroan Anorthosite Suite*

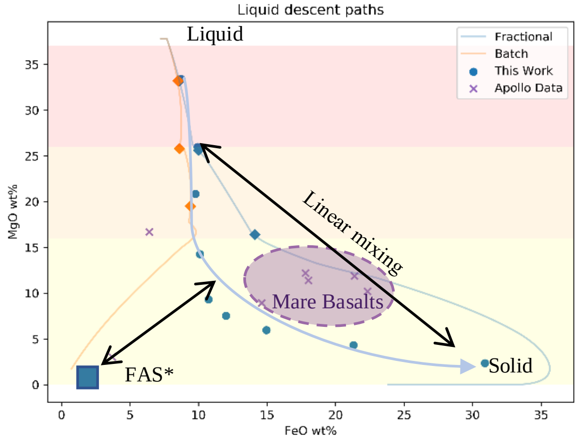

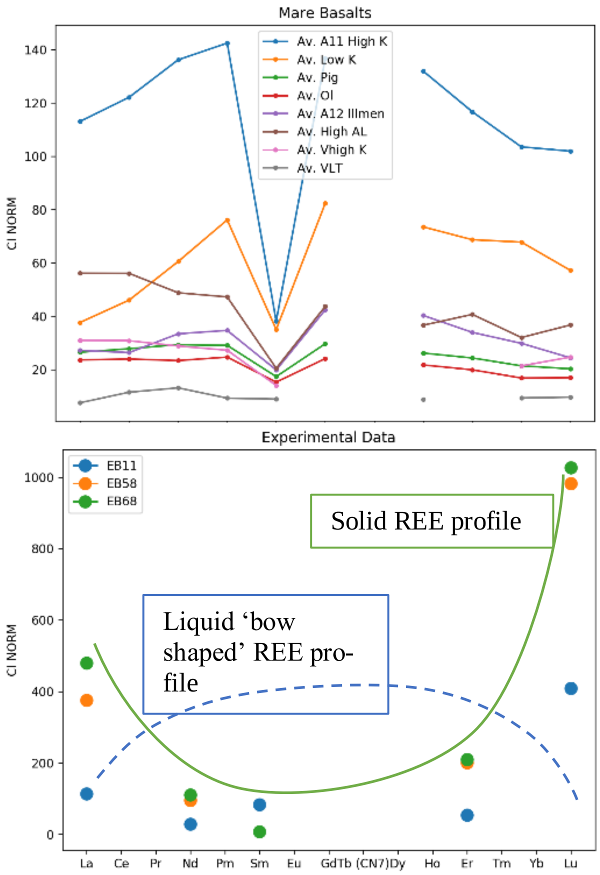

Figure 2a: Rare Earth Element plots for Mare basalts.
Figure 2b: My experiments show an enrichment of the solid phases in Heavy REEs. Data from LA-ICPMS.

Data from [4]

In major element space my experimental crystallization has shown that linear mixing of early and late stages can reproduce much of the bulk rock geochemistry of the Mare basalts.

Mare basalts have a characteristic 'Bow' Shaped rare earth element trend, depletion in both heavy and light rare earth elements. KREEP, rich in LREEs can be the sink for the light REEs. On the Moon, the lower pressure precludes the formation of Garnet; another sink is therefore needed to explain the depletion of the HREEs.

A high temperature pyroxenoid phase in the early stages of the crystallization is able to accept large amounts of the HREEs. I propose this as the sink for the HREEs.

The complete fractionation curve, when re-mixed, is able to explain the bulk of the major and rare earth element observations of the surface of the Moon. It is possible to have vigorous mixing between the Earth and Impactor, explaining the Major element, and Isotopic composition of the Apollo Basalts.

[1] E. D. Young, I. E. Kohl, P. H. Warren, D. C. Rubie, S. A. Jacobson, and A. Morbidelli, "Oxygen isotopic evidence for vigorous mixing during the Moon-forming giant impact," *Science (80-.).*, vol. 351, no. 6272, pp. 493–496, Jan. 2016, doi: 10.1126/science.aad0525.

[2] H. S. C. O'Neill, "The origin of the moon and the early history of the earth-A chemical model. Part 1: The moon," *Geochim. Cosmochim. Acta*, vol. 55, no. 4, pp. 1135–1157, 1991, doi: 10.1016/0016-7037(91)90168-5.

[3] W. F. Mcdonough and S. -s. Sun, "The composition of the Earth," *Chem. Geol.*, vol. 120, pp. 223–253, 1995.

[4] G. H. HEIKEN, D. T. VANIMAN, and B. M. FRENCH, "Lunar Sourcebook," *Cambridge Univ. Press*, p. 778, 1991, doi: 10.1017/CBO9781107415324.004.

i-DRILL: SURFACE AND SUB-SURFACE PROFILING OF LUNAR VOLATILES AND RESOURCES BY AN INSTRUMENTED DRILL.

S. J. Barber[1], S. Sheridan[1], A. D. Morse[1], M. Anand[1], P. Harkness[2], R. Timoney[2], K. Worrall[2], N. J. Murray[3], R. Trautner[4] and C. J. Howe[5]. [1]School of Physical Sciences, The Open University, Milton Keynes, MK7 6AA, UK simeon.barber@open.ac.uk [2]School of Engineering, University of Glasgow, Glasgow, G12 8QQ, UK. [3]Dynamic Imaging Analytics, Milton Keynes, MK14 6GD, UK. [4] ESA ESTEC, Keplerlaan-1, Noordwijk, The Netherlands. [5]STFC RAL Space, Harwell Campus, Didcot, OX11 0QX, UK.

Introduction: The nature and occurrence of water and other volatiles on and below the surface of the Moon is an important topic at the convergence of lunar science and exploration. Volatiles are key factors in our understanding of the history and evolution of the Earth and its satellite and the wider consequences throughout the Solar System. Their ramifications for lunar exploration are manifested through the concept of in-situ resource utilization (ISRU), in which for example water could be harvested at the Moon for life support or rocket propulsion purposes.

Yet our knowledge of lunar water and related resources is far from complete. We do have an increasingly detailed understanding of the lunar samples, including more recent discoveries of elevated concentrations of OH in certain minerals [1, 2]. But these samples are from geographically limited lunar regions notably distant from the poles, and were collected under conditions not conducive to the preservation of the most volatile components. Meanwhile we also have an increasing body of evidence supporting the presence of elevated levels of water ice in colder, high-latitude regions of the Moon [3, 4]. But the remote nature of these measurements and the associated complications in data retrievals/processing, mean that these data are insufficient either to fully test scientific hypotheses or as a firm basis for planning ISRU.

It is therefore increasingly clear that new landed missions are necessary, to provide ground truth data to fill in the knowledge gaps. Data are required *across the surface*, adding detail to the broad-brush picture obtained from orbit. And crucially, data are required from the *sub-surface*, particularly within the upper ~1 m i.e. those depths probed by remote sensing techniques such as neutron spectroscopy [5]. Finally, the measurements should be *specific* i.e. providing unequivocal identification of individual volatiles, and *quantitative*.

i-Drill Overview: i-Drill is an integrated suite of drill and scientific instruments, and provides a tool for answering current scientific and exploration knowledge gaps outlined above. It is readily accommodated on a mobile platform to enable rapid acquisition of volatiles identity, concentration and distribution to a depth of ~1 m below the lunar surface. The drill is optimized for rapid penetration into the regolith surface. The mechanical perturbation and heat generated by the drilling is utilized to release volatiles from the regolith and to convey them upwards within the drill string to a mass spectrometer for real-time identification and quantification as a function of drilling depth. A borehole camera (BoreCam) captures a depth-correlated, (radial) 360-degree movie of the borehole as viewed from within the string as it is advanced, providing geologic context. A permittivity sensor (PerSen) surveys any ice content in the surrounding regolith. The surface camera (SurfCam) records a multispectral 3D movie of the evolving cuttings pile enabling insight into regolith geochemistry, geotechnical properties and hydration state with depth.

i-Drill would optimally be deployed upon a small or medium class lunar rover where it could quickly survey volatiles (as outlined above) at waypoints during the rover's traverse across the lunar surface. During the traverse itself, SurfCam would be operated to record a multispectral 3D movie of the lunar surface, with the rover wheel tracks within field of view to study surface geotechnical properties. i-Drill could also be deployed on a static lander, enabling proof of concept and the coordinated measurement of volatiles content versus depth together with geologic context. Added value would be achieved through incorporation of a simple lateral translation mechanism to enable i-Drill to obtain a number of discrete borehole surveys.

i-Drill Status, Heritage and Instruments: i-Drill is a powerful tool for lunar volatiles science and prospecting, at a resource requirement (mass, power, volume, data, development cost and interface simplicity) compatible with multiple rover and static platforms.

The Drill seeks to reach its full depth in approximately one hour, using a relatively high power setting for this short period of time. The drill cycle will proceed under autonomous control, managing auger torque and weight-on-bit according to the desired power setting, rate-of-progress, and local geotechnical considerations. A rotary-percussive system largely decouples the augering and rock-fracturing efforts, which provides the flexibility required to deal with different target materials, and the bottom of the drill-string provides an aperture (with dust filter) so that volatiles may be drawn up into the instrument casing for mass spectrometry. The architecture overall will be arranged so that there is a clear line-of-sight (e.g.

through an in-bit optical element) through the drill string, rotation, and percussion mechanisms, allowing the BoreCam to remain above ground while still imaging the very bottom of the hole.

Mass Spectrometer: the Ion Trap Mass Spectrometer (ITMS) is a very compact and lightweight device, capable of detecting volatiles up to m/z ~150 (so including e.g. water, xenon and light organics). It is derived from ongoing developments with ESA's PROSPECT program [6] including the development of the Exospheric Mass Spectrometer (EMS) within the PITMS instrument for NASA Artemis/CLPS [7]. The EMS program will develop an ITMS mass spectrometer with associated power, control and data electronics by 2020 that serve as a basis for re-use in i-Drill with addition of further electronics and code as required.

BoreCam and SurfCam: These imagers utilize plenoptic (light-field) optics which capture both the intensity and direction of photons emanating from a scene. Each output frame therefore provides the conventional 2D (*x*,*y*) view of the scene, with the added advantage that the depth (in *z*) of any feature in the scene can be calculated accurately. Thus 3D images can be achieved from a single exposure. Optionally one or both cameras may operate in multiple spectral bands to achieve a snapshot 3D multispectral camera configured to observe for example characteristic absorption of O-H bonds. BoreCam is configured to record a 3D movie of the borehole as it is cut by the drill; SurfCam records in 3D the evolution of the related cuttings pile. Each has heritage from the Sample Camera (SamCam) [8] being developed within ESA PROSPECT [6]; SurfCam development is presently under EU Horizon 2020 funding.

Permittivity sensor (PerSen): a small electrode integrated in the drill rod surface emits an AC signal. This enables the dielectric constant of the surrounding regolith to be measured accurately. The dielectric constant of lunar regolith varies with depth, and can be expected to lie in the range of about 1.6 (low density regolith) to 10 (dense rocks or pebbles). It would also be strongly influenced by the presence of water ice in the surrounding regolith. Thus PerSen enables compilation of an electrical subsurface image and contextual information on the presence of permittivity trends, density changes and water ice presence to be interpreted in conjunction with the other i-Drill sensors. PerSen benefits from heritage within ESA's PROSPECT [6].

Conclusion: i-Drill would address key scientific and exploration knowledge gaps through identification, quantification, and mapping of volatiles in the upper 1 m of lunar regolith. Compatible with various platforms, it leverages on ongoing development programs and targets flight opportunities from 2021/22.

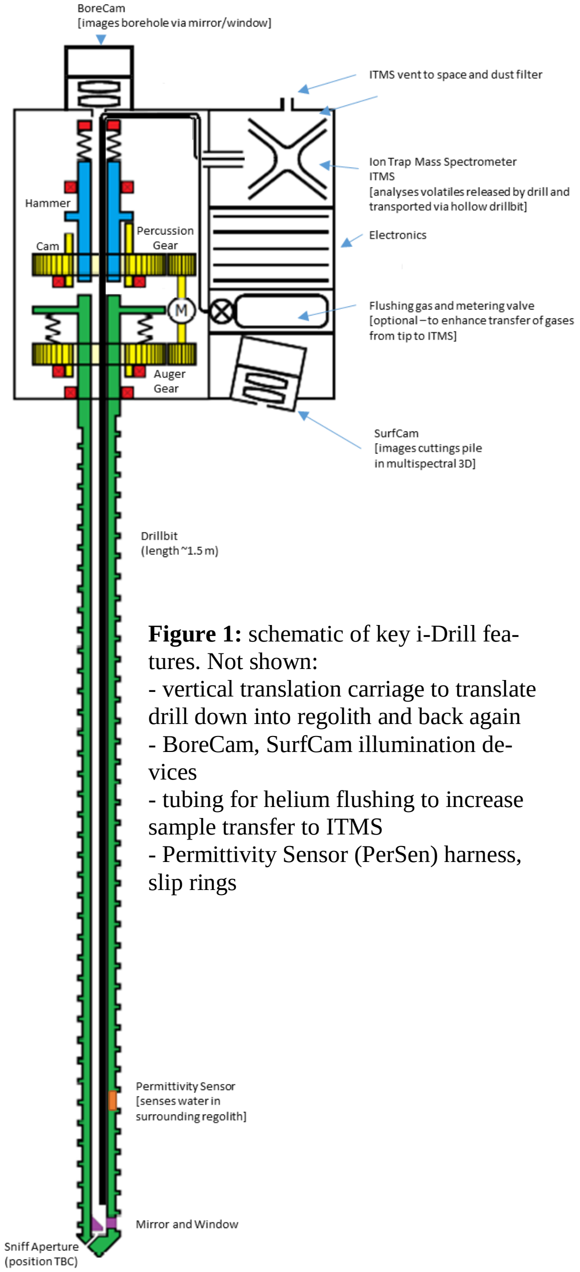

Figure 1: schematic of key i-Drill features. Not shown:
- vertical translation carriage to translate drill down into regolith and back again
- BoreCam, SurfCam illumination devices
- tubing for helium flushing to increase sample transfer to ITMS
- Permittivity Sensor (PerSen) harness, slip rings

Acknowledgments: EMS and PROSPECT are projects of and funded by the European Space Agency. SurfCam is funded by the European Union's Horizon 2020 program under grant agreement No. 822018.

References: [1] A. Saal et al. (2008) *Nature* 454(7201):192-5. [2] M. Anand et al. (2014) Phil. Trans. A, 372, 20130254 [3] E. A. Fisher et al. (2017) *Icarus*, 292, 74-18. [4] S. Li et al. (2018) *PNAS*, 115, 8907–8912. [5] I. G. Mitrofanov et al. (2010) *Science* 330, 483 [6] R. Trautner et al. (2018) IAC-18,A3,2B,2,x42773 [7] B. A. Cohen et al. LPSC 51 [8] N. J. Murray et al. LPSC 51.

PITMS: AN ION TRAP MASS SPECTROMETER FOR IN-SITU STUDIES OF THE LUNAR WATER CYCLE ON THE NASA ARTEMIS CLPS PEREGRINE LANDER.

S. J. Barber[1], B. A. Cohen[2], W. M. Farrell[2], P. Landsberg[1], A. D. Morse[1], S. Sheridan[1], N. M. Curran[2], M. Leese[1], C. Howe[3], T. Morse[3], P. Driggers[2] & R. Trautner[4]. [1]The Open University, Milton Keynes, UK (simeon.barber@open.ac.uk), [2]NASA Goddard Space Flight Center, Greenbelt MD, [3]STFC RAL Space, Harwell Campus, Didcot, UK, [4]ESA/ESTEC, Noordwijk, The Netherlands.

Introduction: PITMS leverages the ESA PROSPECT development for the Russian Luna-27 mission and develops a standalone mass spectrometer suitable for small lunar landers. It is a partnership between NASA Goddard, The Open University (OU) and ESA. The Peregrine Ion Trap Mass Spectrometer (PITMS) was selected for development and flight in the NASA Commercial Lunar Payload Services (CLPS) program, and is manifested aboard the first flight of Astrobotic's Peregrine lunar lander. PITMS will consist of the European-provided ITMS sensor and front-end electronics, newly developed controller and power supply boards, and a GSFC wrapper including thermal control and dust protection hardware. It will monitor the tenuous near-surface lunar exosphere in response to natural and artificial stimuli (e.g., diurnal temperature cycle, lander activities). Exospheric measurements by PITMS will significantly improve our knowledge of the abundance and behavior of volatiles on the Moon, linking the lunar surface to LADEE measurements, and informing future robotic and human mission design.

Lunar near-surface water: The Moon has a tenuous atmosphere (exosphere) primarily made of neon, helium and argon [1], molecular hydrogen [2], with smaller abundances of methane [3], sodium and potassium [4]. Because of the rate at which atoms escape from the lunar atmosphere, there must be a continuous source of particles to maintain even a tenuous atmosphere. Characterizing lunar volatile reservoirs and evaluating their interrelations is a high priority for both lunar science and for exploration purposes, as water could represent a key resource for human utilization.

Multiple spacecraft have observed water and hydroxyl in the lunar mid-latitudes as detected in the 2.8-micron absorption feature in the IR reflectance spectrum [5-9]. This surface reflectance feature may exhibit seasonal and possibly even diurnal variability. The LADEE Neutral Mass Spectrometer (NMS) and Ultraviolet Spectrometer (UVS) identified the primary atmospheric constituents at this altitude, their density, and variability [1, 4]. To date, water and OH have only been reported in the exosphere during meteor stream events by the LADEE NMS and UVS [10]. A definitive observation of exospheric water and OH released from the surface during nominal times remains elusive.

Landed mass spectrometers are uniquely positioned to assess the volatile components of the lunar regolith and exosphere and observe their behavior from dawn to dusk, addressing international science and exploration goals. The only corresponding surface measurement was made by the Lunar Atmospheric Composition Experiment (LACE) on Apollo 17. LACE was a miniature magnetic deflection mass spectrometer deployed on the surface and oriented to intercept and measure the downward flux of gases. This instrument had a mass range of 1-110 amu and a sensitivity of 1 cps (~200 $\mathrm{cm^{-3}}$), and operated for 9 months. LACE was routinely swamped by artifacts emanating from the nearby lunar module descent stage and other abandoned equipment during the

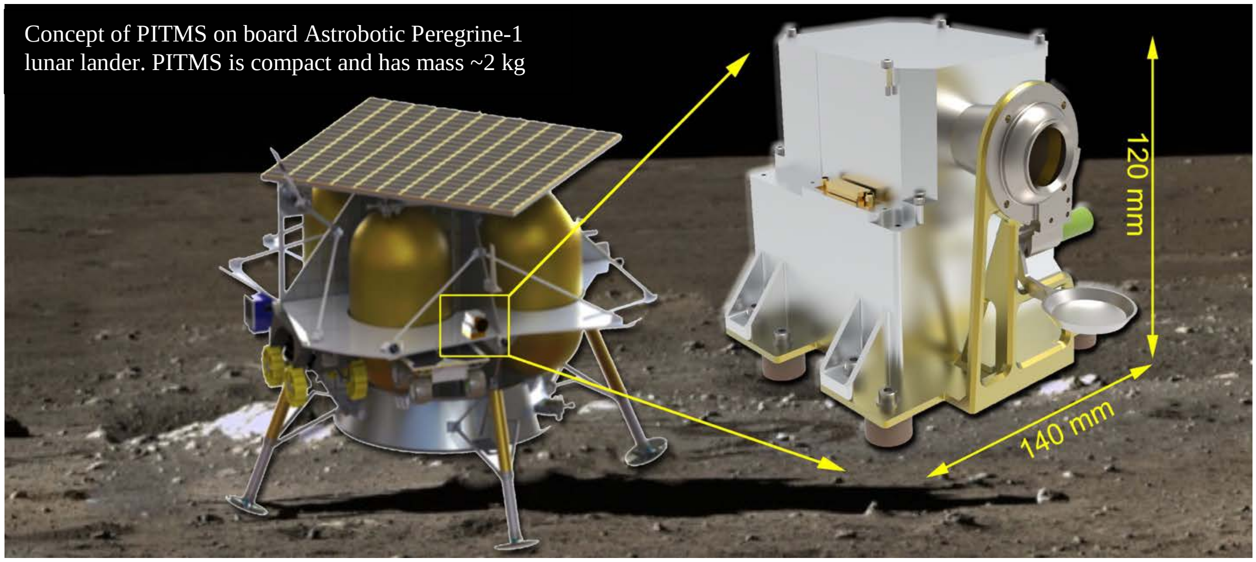

Concept of PITMS on board Astrobotic Peregrine-1 lunar lander. PITMS is compact and has mass ~2 kg lunar daytime, but obtained firm detections of two species, argon and helium. Possible pre-sunrise detections of other species were obtained (see review in [11]), but only upper limits were determined for most of the volatile species of interest, including N_2, CO, CO_2, and CH_4; moreover OH/H_2O was not determined due to the high backgrounds both inside and outside the instrument.

Lander Effects: Volatile compounds (including water) will be deposited onto the lunar surface by the lander itself. Observing the release of these vapor species over the lunar day will provide information on the properties of the regolith and the nature of the landing plume interaction with it, both important to future human activities. The exposed regolith is constantly being activated through bombardment by the solar wind and impactors, creating sites that bind volatile species such as water. Laboratory observations of water bound to lunar regolith shows a distribution of activation energies peaking near 0.7 eV, but with a high energy tail beyond 1 eV [12-14]. If *in situ* lunar regolith has the same properties, the water molecules will outgas from the surface over time as the surface is progressively warmed. If PITMS still senses considerable water surface outgassing near local noon (~400K), it implies that the surfaces contain sites with very high activation energy for water trapping, with values above 1.0 eV, as one might expect for mature highland samples. In this case, the surface is a potent sorption substrate. If, however, the local regolith has little outgassing at local noon, then this implies that *in-situ* exposed surfaces have outgassed at lower activation energies/lower temperatures. In this case, the surface may be a far less potent sorption substrates than environmentally dormant samples used in the lab, affecting our models of plume-originating water retention in the actual space environment.

Development & operation: PITMS consists of an ITMS built by OU in collaboration with STFC RAL Space under contract from ESA, and a wrapper built by NASA GSFC that will integrate the ITMS with the Astrobotic lander. The ITMS has direct heritage from the Ptolemy mass spectrometer that made the first *in situ* measurements of volatiles and organics on comet 67P with the Rosetta lander, Philae [6]. It has a unit mass resolution up to an upper mass-to-charge (m/z) limit of 150 Da. Operating in a passive sampling mode, ambient gases enter PITMS through an aperture and diffuse around the mass analyzer cavity. They will be ionized through interaction with electrons emitted by one of a pair of redundant heated wire filaments, and the resulting positively charged ions will be trapped in a radiofrequency field formed by application of suitable potentials to a set of three hyperbolic electrodes. Manipulation of the field facilitates the ejection of the ions into the electron multiplier detector in order of increasing m/z with amplitudes related to abundance. This passive technique was used during Rosetta's flyby of asteroid Lutetia [7] and at 67P during Philae's "bounce" after landing [6], achieving detection limits of around 1E-10 mbar, some five orders of magnitude better than that achieved by the LACE experiment.

GSFC will build the wrapper, consisting of a thermal base plate, a radiator, and a deployable dust cover, and will integrate and test the ITMS with the wrapper. The integrated PITMS payload and science investigation will be operated from GSFC. PITMS is manifested on the first flight of Astrobotic's Peregrine lander, which will fly as a co-manifested payload aboard the maiden flight of ULA's Vulcan Centaur vehicle in 2021. The lander targets the Lacus Mortis basaltic lava plain in the northeastern part of the Moon, near an apparent skylight [15]. PITMS operations will commence soon after touchdown with the release of the dust cover. PITMS will continually scan at up to 10 Hz and integrate the mass spectra onboard if needed to build signal to noise. It will monitor the decay in the lunar exosphere from its post-landing peak, punctuated by any stimuli that create transient increase. PITMS observations will complement the descent plume characterization by SEAL [16].

Summary: PITMS will provide a modern measurement of OH/H_2O on the lunar surface, improving quantification of exospheric species of interest to both science and human exploration. Such an investigation is recommended for all future landed missions, to characterize the interaction of the lander with the lunar environment and to perform fundamental science and understand potential resources. Reflight of PITMS on equatorial landers would enable comparisons with LADEE, whilst polar siting would monitor migration of water molecules toward PSRs.

References: [1] Benna, M., et al. (2015) *Geophys. Res. Lett.* **42**, 3723-3729. [2] Hurley, D.M., et al. (2017) *Icarus* **283**, 31-37. [3] Hodges Jr., R.R. (2016) *Geophys. Res. Lett.* **43**, 6742-6748. [4] Colaprete, A., et al. (2016) *Science* **351**, 249. [5] Clark, R.N. (2009) *Science* **326**, 562-4. [6] Hendrix, A.R., et al. (2019) *Geophys. Res. Lett.* **46**, 2417-2424. [7] Li, S., et al. (2018) *Proc. Nat. Academy of Sciences* **115**, 8907. [8] Pieters, C.M., et al. (2009) *Science* **326**, 568-72. [9] Sunshine, J.M., et al. (2009) *Science* **326**, 565-8. [10] Colaprete, A. (2015) *AGU Fall Meeting Abstracts* **53**. [11] Stern, S.A. (1999) *Reviews of Geophysics* **37**, 453-491. [12] Farrell, W.M., et al. (2015) *Icarus* **255**, 116-126. [13] Poston, M.J., et al. (2015) *Icarus* **255**, 24-29. [14] Hibbitts, C.A., et al. (2011) *Icarus* **213**, 64-72. [15] Hong, I.-S., et al. (2015) *J. of Astronomy and Space Sciences* **32**, 113-120. [16] Benna at al. (2019) LPSC 50, #2132

NWA 11962: A NEW LUNAR METEORITE AND ITS PRESUMED SOURCE REGION/CRATER IN THE PROCELLARUM KREEP TERRANE.

A. Bechtold[1], C. Koeberl[1,2], F. Brandstätter[2], R. Greenwood[3]
[1]Department of Lithospheric Research, University of Vienna, Austria (andreas.bechtold@univie.ac.at), [2]Natural History Museum, Vienna, Austria, [3]The Open University, Milton Keynes, UK.

Introduction: Lunar meteorites are an important addition to Apollo and Luna samples for deciphering the geological evolution of the Moon. However, the main disadvantage is that their places of origin on the lunar surface are unknown. Here we report on the mineralogy and petrology of the new lunar meteorite Northwest Africa (NWA) 11962 and briefly discuss possible pairing relationships to other lunar meteorites. Furthermore, we correlate its bulk chemistry to element concentrations on the lunar surface as measured by the Lunar Prospector gamma-ray spectrometer, in order to locate possible source regions. Ultimately, we compare these possible source regions with coordinates of recently formed lunar impact craters to find possible source craters.

Sample and Methods: NWA 11962 was found as a single stone (~85 gram total mass) whose oxygen isotopic composition, petrological characteristics, and bulk chemistry is consistent with a lunar origin. The specimen is a flat and rounded individual with regmaglypts exhibiting a black shiny surface with in places dull brownish areas. A cut and polished face (3 cm^2) reveals two different lithologies comprising a fine-grained, dark-gray matrix with mainly submillimeter-sized light clasts and a black compact area (1 × 0.5 cm) of impact melt (see Fig. 1).

Figure 1. *Macroscopic view of NWA 11962. The cut and polished face shows the texture of the meteorite's interior.*

Two polished thin sections were carbon-coated and examined using a Jeol JSM 6610-LV scanning electron microscope and a Jeol JXA 8530-F field emission electron microprobe. Additionally, a homogenized bulk powder from a 1.5 gram piece of the meteorite was prepared. Two subsamples of this powder were used for instrumental neutron activation analysis (INAA).

Lunar Origin: The lunar origin has been confirmed by the oxygen isotopic composition ($\delta^{17}O$ = 3.14 per mil, $\delta^{18}O$ = 6.03 per mil, $\Delta^{17}O$ = 0.01 per mil) of the meteorite. Atomic Fe/Mn ratios of pyroxenes and olivines in NWA 11962 plot on lunar trend lines. Lithic and mineral clasts are typical for the lunar near side. This also holds for the trace element concentrations. The rare earth elements for example show a typical KREEP pattern.

Petrology and Mineralogy: Abundant glass spherules in one of the two thin sections led to the the classification of NWA 11962 as a regolith breccia [1]. The matrix of the breccia is formed by a highly vesicular, brown glass which in places forms veins with schlieren structures. A fusion crust is absent and no agglutinates have been observed. The breccia contains a variety of different lithic and monomineralic clasts, but is dominated by only two types of clasts. On the one hand these are gabbroic clasts and on the other hand felsites and quartz monzogabbros (QMGs) of the alkali-suite (Fig. 2).

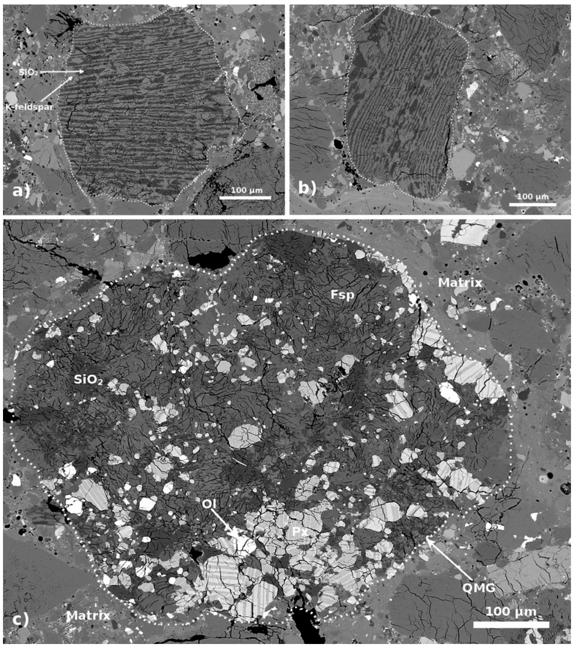

Figure 2. *Back scattered electron (BSE) images of alkali-suite clasts, typical constituents of NWA 11962, bedded in the matrix. a) and b) granophyric intergrowths of silica and K-feldspar (lunar felsites). c) Quartz monzogabbro clast.*

Felsites and QMGs are rare rock types of the lunar alkali-suite [2], making NWA 11962 a valuable object for petrogenetic studies. Additionally, the regolith breccia contains lithic clasts such as basalts, impact melt breccias and symplectites as well as different glasses such as spherules and vitrophyrs.

Pyroxenes (En_{34-62} $Fs_{20-46}Wo_{9-35}$) in the gabbroic clasts are complexly zoned. Exsolved pyroxenes in the quartz monzogabbro clasts consist of pigeonite lamella ($Fs_{56.4-69.9}$ $Wo_{2.3-4.7}$) in a augite ($Fs_{29.3-39.4}$ $Wo_{35.3-44.2}$) host. The mineral chemistry of pyroxenes in

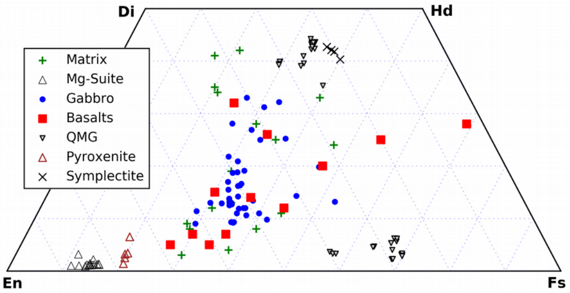

Figure 3. *Quadrilateral plot of pyroxene compositions in NWA 11962.*

other clasts of NWA 11962 can be seen from Figure 3. Silica and K-feldspar ($An_{3.0-6.5}$ $Or_{63.2-82.6}$ $Cn_{2.8-6.5}$) are abundant phases in the alkali suite clasts and fragments. Plagioclases range from anorthitic to labradoritic ($An_{53.4-97.7}$ $Ab_{2.3-44.1}$ $Or_{0.0-2.5}$) and olivine compositions range from Fa_{12} to Fa_{61}. Accessory phases in the breccia include ilmenite, spinel, zircon, zirconolite, troilite, barringerite, Fe-Ni metal and nickel-free native iron.

Discussion: The INAA revealed an iron content of 9.28 wt% and a thorium content of 6.6 ppm. Together with high incompatible trace element concentrations (e.g., Sm: 16.5 ppm) this points toward an origin of the meteorite from within the Procellarum KREEP Terrane [e.g., 3]. According to [4], there are at least six lunar meteorites that have a similar bulk iron and thorium content to NWA 11962. Specifically, these are the paired stones NWA 4472/4485, Miller Range 13317, Calcalong Creek, SAU 169, Dhofar 1442, and NWA 6687. Of these NWA 4472/4485 [5] is the closest match when comparing bulk iron and thorium concentrations and petrology with NWA 11962. Nonetheless, no CRE ages of both meteorites are available, which makes paring considerations quite uncertain.

To constrain the lunar source region we compared the bulk iron, thorium, and titanium concentrations of NWA 11962 with the Lunar Prospector gamma-ray spectrometer abundance data (2 degree/pixel) of these elements [6]. This method previously used by e.g., [7] resulted in possible source regions of NWA 11962 as shown in Figure 4. In addition to the bulk meteorite element concentration, we furthermore considered the iron and titanium contents of glassy impact melt spherules that occur in the breccia. The bulk element concentrations of the meteorite represent the regolith chemistry at the location of the source crater, or at least the spallation zone from which the meteorite was launched. As the impact melt spherules we considered are deformed it can be assumed that they did not fly over large distances. Therefore they might represent samples of the regolith in the vicinity of the NWA 11962 source crater. This approach therefore enlarges the sampled area which results in a better ratio of sampled area to the size of the remote sensing pixel area. Figure 4 further shows recently formed lunar impact craters with diameters larger than 300 meters as reported by [8]. One of these craters lies within a possible source region of NWA 11962, making it a possible source crater for this lunar meteorite. The crater with a diameter of 320 meters and the coordinates 3.009 lon -0.387 lat lies next to Sinus Medii at the eastern limb of the Procellarum KREEP terrane. It has to be mentioned that information on recently formed impact craters is limited to latitudes +/-50° [8]. As can be seen from Figure 4 large possible source areas lie outside this limit (dashed white line).

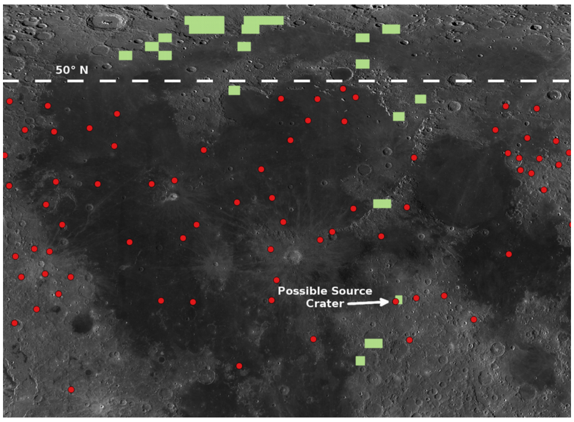

Figure 4. *Detail of a lunar map (LROC WAC Global 100m/pixel) with all regions that have similar iron, thorium, and titanium surface concentrations as NWA 11962 shown in green. Red dots are recently formed impact craters with diameters larger than 300 meters [8]. The white arrow points toward a possible source crater.*

Future Work: We plan to apply the above method to search for possible source craters of other lunar meteorites. This future work may also include additional information like basalt ages, mineralogy, etc., to improve the likelihood of a reliable result.

References:

[1] Meteoritical Bulletin, no. 107 (in preparation). [2] Jolliff, B.L. et al. (2011) Nature Geoscience 4(8), 566–571. [3] Haskin, L.A. et al. (2000) J. Geophys. Res. 105(E8), 20403-20415.
[4] http://meteorites.wustl.edu/lunar/moon_meteorites_list_alumina.htm (Retrieved January 12, 2020).
[5] Joy, K.H. et al. (2011) GCA 75(9): 2420–2452. [6] Prettyman, T. et al. (2006) J. Geophys. Res. 111(E12): E12007. [7] Calzada-Diaz, A. et al. (2015) MAPS 50(2): 214-228. [8] Williams, J.P. et al. (2018) J. Geophys. Res. 123(9): 2380-2392.

LUNAR PYROCLASTIC DEPOSITS AS POTENTIAL RESOURCES. K. A. Bennett[1], L. M. Pigue[2], L. Gaddis[1], C. C. Allen[3], B. T. Greenhagen[4], D. A. Paige[5], L. Keszthelyi[1], B. Horgan[6] [1]USGS Astrogeology Science Center (2255 N Gemini Dr., Flagstaff AZ); [2]Northern Arizona University, Flagstaff, AZ; [3]NASA Johnson Space Center (retired), Houston, TX; [4]Johns Hopkins University Applied Physics Laboratory; [5]University of California Los Angeles, Los Angeles CA; [6]Purdue University, West Lafayette, IN.

Introduction: Explosive volcanic deposits on the Moon are compelling targets, both scientifically and as potential future resources. Lunar pyroclastic deposits represent material sourced from the lunar mantle, and therefore provide a window into the composition of the lunar interior. Pyroclastic material, particularly the iron, titanium, and volatile-rich volcanic glass and crystallized beads [1] formed during fountaining or explosive volcanic events, has also been hypothesized to be an important potential resource due to its relatively consistent spherical shape and size, which would make processing the particles easier. Additionally, many pyroclastic deposits are glass-rich, which is easier to break down than a fully crystalline rock [2]. Iron-rich pyroclastic material has been shown to release the most oxygen of any lunar sample during high-temperature hydrogen reduction experiments [3]. Oxygen is a critical resource that is necessary for creating water and fuel. To target the material with the maximum resource potential, it is important to know the iron and glass content of each deposit.

Here we obtain the Christiansen Feature (CF) value and an estimate of the FeO wt. % for lunar pyroclastic deposits to identify the most iron-rich deposits that may have the highest resource potential. We also compare the strength and distribution of visible/near-infrared glass spectral signatures across several iron-rich pyroclastic deposits.

Methods: We use Lunar Reconnaissance Orbiter Diviner Lunar Radiometer Experiment thermal data to obtain the CF value and an estimated iron abundance. The CF value is the wavelength position of the emission maximum near 8 μm, and this compositional indicator can be estimated using Diviner's three channels located near 8 μm [4]. The CF value is dependent on the degree of polymerization of silica. For crystalline materials shorter CF values indicate tectosilicates like feldspar and higher values indicate inosilicates of nesosillicates like pyroxene and olivine. A strength of the CF parameter is that it is equally effective on amorphous silicates; this is important for pyroclastic deposits because they range from crystalline to glassy. Here we use the global (0-360° lon, ± 60° lat) standard CF map that is publicly available from the PDS (***Figure 1***).

Because the CF wavelength position has been correlated to silicate mineralogy, it can be used to roughly estimate the amount of iron present [5]. Using laboratory spectra of returned Apollo samples, Allen et al. [5] empirically found that the relationship between Diviner CF values and FeO wt. % is: $FeO = 74.24 \times CF - 599.9$. [Eq 1]

Using the global list of 151 identified pyroclastic deposits (***Figure 1***) compiled by Glaspie et al. [6], in ArcMap we create regions of interest (ROI) corresponding to each deposit. We then calculate the average CF value of each ROI and convert this value into FeO wt. %.

To constrain whether a deposit contains glass we use Moon Mineralogy Mapper [M^3; 7] near infrared data to map the presence and distribution of volcanic glasses. Data processing (including continuum removal, spectral smoothing, and band parameter derivation) is completed using the methods of Horgan et al. [8]. The glass band parameter used here

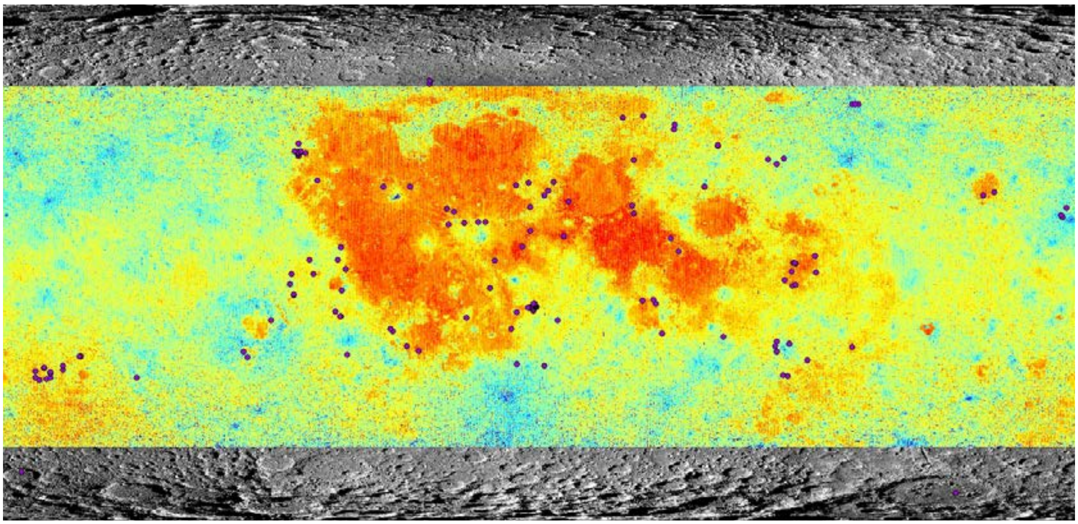

Figure 1: Diviner CF map (red indicates long CF values and blue indicates short CF values) with the locations of all known lunar pyroclastic deposits.

was created by taking the average of the depth below the continuum at three wavelengths: 1.15, 1.18, and 1.20 µm [8]. This parameter also detects olivine if it is present, so analysis of individual spectra is necessary to confirm the presence of glass.

Preliminary Results: Thus far we have measured the CF value of 34 pyroclastic deposits that are located in and near the mare basins. This includes pyroclastic deposits of a variety of sizes, from large regional deposits (~49000 km^2) to small localized deposits (~100s of km^2) [9]. Our preliminary results from this subset of pyroclastic deposits show a range of average CF values from 8.20 to 8.43 µm.

The pyroclastic deposits in our preliminary study that exhibit the highest CF values are: Sulpicius Gallus, Mare Vaporum, Taurus-Littrow Valley, Sinus Aestuum, and Rima Bode. These range from 8.43 µm (Sulpicius Gallus) to 8.38 µm (Rima Bode). The highest estimated iron content (Sulpicius Gallus) is 26.0 wt. % FeO. Many of these deposits were designated "black spots" in early telescopic studies because of their very low albedos, later associated with high iron and titanium contents and abundant crystalline beads [10].

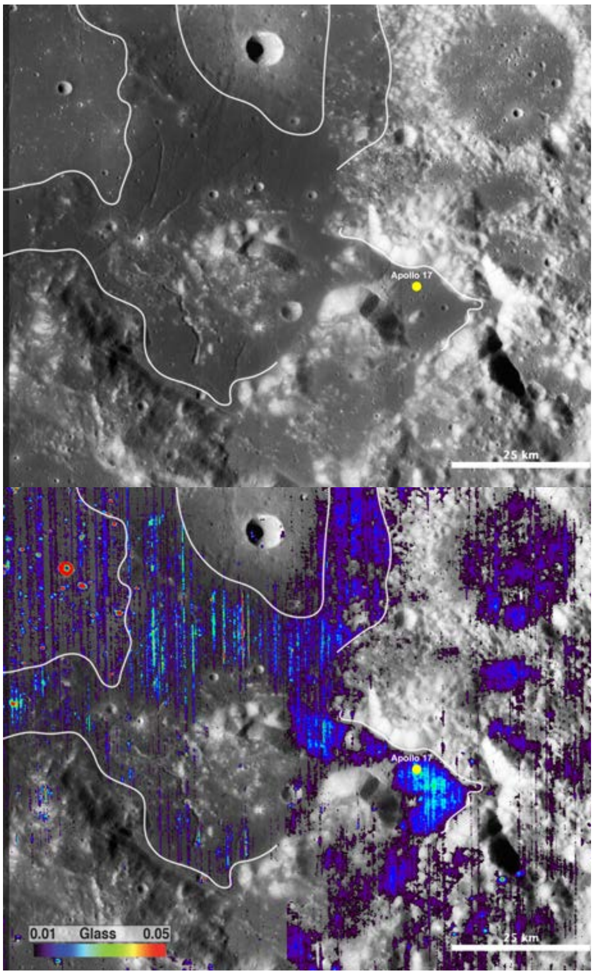

Figure 2: (top) LROC WAC mosaic showing the Taurus Littrow pyroclastic deposit (outlined in white). (bottom) M^3 glass parameter map of Taurus-Littrow.

We found that the Taurus-Littrow pyroclastic deposit (Figure 2) has a relatively high CF value of 8.39 µm and 23.3 wt % FeO. Apollo samples from this deposit show similar values and contained both crystalline and glass beads. The M^3 glass parameter map suggests the presence of glass in this deposit, although analysis of individual spectra is necessary to confirm this possibility. Additional work is necessary to cross-reference the Diviner data with the M^3 data to investigate whether the iron-rich and glass-rich areas within the deposit are co-located. The combination of glass-rich, iron-rich material could have a high resource potential for future lunar exploration.

Discussion: The range in iron content of pyroclastic beads from the Apollo samples is 16.5 – 24.7 wt. % [11]. Our preliminary study shows a range in FeO of pyroclastic deposits studied here of ~8.8 – 26.0 wt. %. These preliminary results show that the deposits with the highest CF values are large regional deposits. This is consistent with previous results that have shown that energetic lava fountaining is driven by magmas ascending directly from mantle without stalling and evolving in the crust [i.e., 12]. Iron-rich, glass-rich deposits that are also large in size have higher resource potential than smaller deposits because they contain more potentially useful material.

Future Work: We will extract and compare CF and iron content estimates for all identified pyroclastic deposits. The publicly available global CF map only spans ± 60° latitude, so we will calculate the CF values directly from Diviner data for the few deposits that are not covered. We will also analyze M^3 data in further detail to validate the presence of glass at the most iron-rich pyroclastic deposits. The results of these analyses could be crucial for more sophisticated USGS assessments of lunar resources that expand upon the ongoing assessment of bulk regolith [13].

References: [1] McCubbin, F. M. et al. (2015) *American Mineralogist*, *100*(8–9), 1668–1707. [2] Taylor & Carrier (1992) *AIAA Journal*, Vol 30 No. 12. [3] Allen et al. (1996) *JGR – Planets* 101, pp. 26,085-26,095. [4] Greenhagen, B. et al. (2010) *Science* 17, Vol. 329, Issue 5998, pp. 1507-1509. [5] Allen, C.C. et al. (2012) *JGR, 117*, E00H28. [6] Glaspie et al., (2018) *GSA Annual Meeting*, 67-8. [7] Pieters et al. (2009) *Curr. Sci 96* (4), 500–505. [8] Horgan et al. (2014) *Icarus*, 234, 132-154. [9] Gaddis L. et al. (2003) *Icarus* 161.2:262–280. [10] Pieters, C. et al. (1973) *JGR 78*, 5867-5875. [11] Delano, J. (1986) *Proc. Lunar Planet. Sci. Conf., 16th,* 201–213. [12] Shearer C & Papike J (1993) *Geochimica Et Cosmochimica Acta,* 57(19), 4785–4812. [13] Keszthelyi, L. et al. (2020) *LPSC 51*(submitted).

GEOLOGICAL INVESTIGATION OF THE LUNAR SOUTH POLE: POTENTIAL EVA TARGETS AND IMPLICATIONS FOR ARTEMIS 2024.

S. J. Boazman[1,2], S. H. Halim[3], N. Barrett[4], A. J. Gawronska[5], C. M. Gilmour[6], Harish[7], K. McCanaan[8], A. V. Satyakumar[9], J. Shah[10] and D. A. Kring[11,12]. [1]Natural History Museum, London, UK (s.boazman@nhm.ac.uk). [2]University College London, UK, [3]Birkbeck, University of London, UK. [4]University of Alberta, Edmonton, Canada. [5]Miami University, Oxford, OH, USA. [6]York University, Toronto, Canada. [7]Physical Research Laboratory, India. [8]University of Manchester, UK. [9]CSIR – National Geophysical Research Institute (CSIR-NGRI), India. [10]The University of Western Ontario, London, Canada. [11]Lunar and Planetary Institute, Universities Space Research Association, Houston, TX, USA. [12]NASA Solar System Exploration Research Virtual Institute.

Introduction: The lunar south pole lies on the rim of the Imbrian (3.5 Ga) aged, ~21 km diameter, ~4 km deep Shackleton crater [1, 2], which, in turn, lies on the margin of the South Pole-Aitken (SPA) basin [1, 2]. The lunar south polar region is of interest because it has been chosen as a landing site for a NASA Artemis mission. The region contains both permanently shadowed regions (PSRs), that may hold caches of volatiles, and also a few topographic high points with >50% illumination [3], that may assist with solar power generation. A landing on the rim of Shackleton may provide access to Shackleton impact ejecta, potentially with impact melts from Shackleton, SPA, and other pre-Nectarian and Nectarian age impacts. It may also provide fragments of the original highland crust and potentially cryptomare from SPA [4]. In this study, we take a closer look at the formation of Shackleton and its current geological state to better assess potential targets for crew sampling, including those that will support science objectives outlined by the NRC [5].

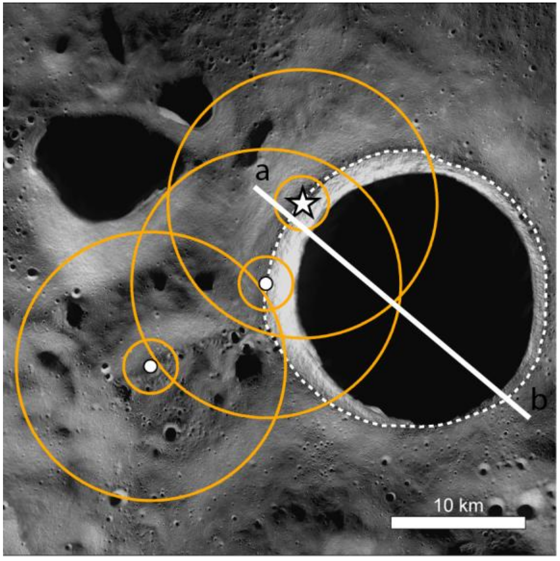

Fig. 1: *Averaged NAC mosaic showing 2 and 10 km exploration zones, as defined by the Apollo missions, around the south pole (white star). Two additional points of highest illumination (filled white circles) [3] are shown: (89.78°S, 155.73°W), (89.45°S, 137.31°W). Profile from south pole to opposite side of the crater is the topographic profile of Shackleton used in Fig. 4.*

Data and Methods: The iSALE shock physics hydrocode [6-8] was used to simulate the formation of Shackleton with a chondrite-like projectile [9, 10] vertically impacting a gabbroic anorthosite target [11]. A volatile-rich subsurface layer, using wet-tuff [12, 13] as a proxy, was also inserted to investigate changes in crater morphology. Using a 2D half-space with cylindrical geometry, the computational cell size was set to 50 m and simulations ran for 500 s post-impact. A photogeological analysis using NAC images (0.5-1.2 m/pixel, incidence angle ~87-91°) identified geological features of interest. Lunar Orbiter Laser Altimeter (LOLA) derived topography and slope maps (5 m/pixel) were used to evaluate accessibility of those features.

Results: The morphology of Shackleton crater can be produced by a 1.5 km asteroid striking the pole at 15 km/s (Fig. 2a). The addition of a 100 m thick, mixed volatile-regolith layer at a depth of 500 m better represents the relatively flat topography seen on the rim opposite to the south pole (Fig. 2b). About 150 m of ejecta covers the rim.

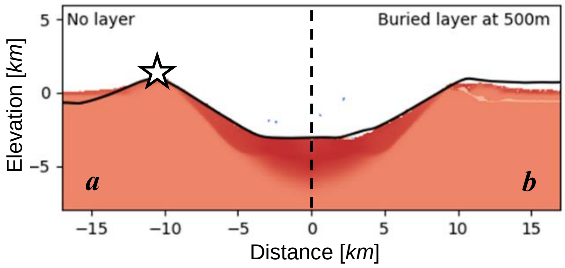

Fig. 2: *Final crater morphologies for a surface with: (a) homogenous target and (b) target with a 100 m thick volatile layer buried at 500 m. Black line = LOLA profile of Shackleton from the south pole (star) rim to the opposite rim.*

Shackleton was excavated from two types of terrains: (i) a crystalline highland terrain composed, in part, of pure anorthosite (PAN) (Fig 3) and (ii) a layered terrain that may be composed of ejecta blankets from nearby craters. Large blocks of rock, hundreds of meters in size and corresponding to PAN spectra [14], are visible in the crater walls near the south pole (Fig 3). The layered terrain is on the opposite side of the crater and is composed of strata ~10-20 m thick producing a unit with a total thickness of ~100-200 m. Ejecta from Amundsen, de Gerlache, Nobile, Slater, Sverdrup, and Cabeus are among the candidate sources for the layers. Both terrains are sources of debris in Shackleton ejecta.

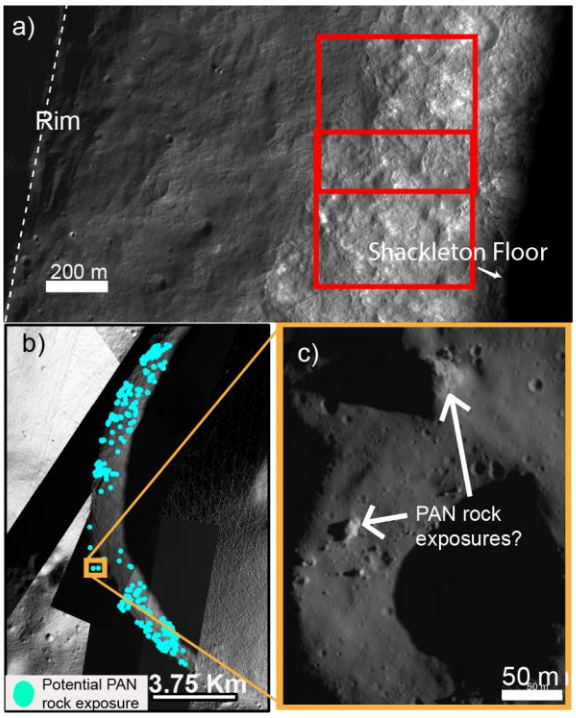

Fig. 3: *a) PAN outcrops (100s m) (red boxes) in the crater wall, initially identified by Yamamoto et al. [14]. b) Distribution of possible PAN rock exposures along the crater rim, orange box shows location of c.*

Our photogeologic analysis of that ejecta surface around the south pole revealed 13 potential EVA targets, 11 of which are within a 2 km south pole radial boundary and 2 are within the 10 km radial boundary of the highest illumination point on the rim. The identified targets include rock exposures, boulders, and craters of varying levels of accessibility (Fig. 4). One of the rock exposures identified may potentially host a PSR (Fig. 4e), suitable for volatile investigations. These targets would add to and enhance collections of regolith and clast components along the rim of Shackleton.

Conclusions: The south polar region is a topographically challenging area. A set of samples can be collected along the rim on relatively flat terrain, but large blocks of debris that may provide a more detailed geologic context, are on the outer rim of the crater with slopes >15° (Fig. 3). The sizes of the rock exposures (100s of m) could provide important clues about the crystallization of the lunar crust if composed of PAN and/or other magmatic lithologies. Material in Shackleton ejecta provides access to a ~4 km deep cross-section of the south polar crust of the Moon.

Acknowledgements: We thank USRA-LPI, CLSE, and NASA SSERVI for support. We also thank the developers of iSALE.

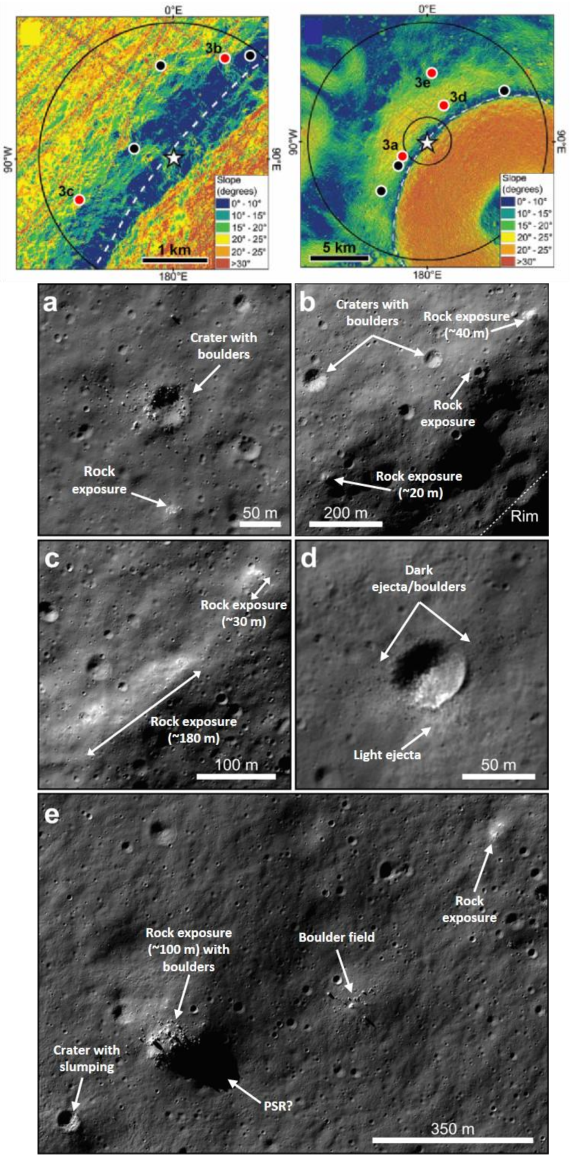

Fig. 4: *Slope maps of the south pole region with the locations of the potential EVA targets (red and black dots), a-e, within the 2 and 10km exploration zones.*

References: [1] Spudis P.D. et al. (2008) *GRL*, 35, L14201. [2] Tye A.R. et al. (2015) *Icarus*, 255, 70–77. [3] Mazarico E. et al. (2011) *Icarus*, 211, 114-120. [4] Kring. D. (2019) ESF. [5] NRC (2007) *The Scientific Context for Exploration of the Moon* [6] Collins G. S. et al. (2004) *MAPS*, *39*, 217–231. [7] Wünnemann K. et al. (2006) *Icarus*, *180*, 514–527. [8] Amsden A. A. et al. (1980) *US Department of Commerce, National Technical Information Service* [9] Benz W. et al. (1989) *Icarus*, *81*, 113–131. [10] Pierazzo E. et al. (1997) *Icarus*, *127*, 408-423. [11] Ahrens T. J. & O'Keefe J. D. (1977) in *Impact and Explosion Cratering*, 639–656. [12] Allen R. T. (1967) *DASA, General Dynamics Report GA MD-7834*. [13] Wünnemann K. et al. (2005) *GSA Special Paper*, *384*. [14] Yamamoto Y. et al. (2012) *GRL*, 39, L1320.

EXPLORING THE LOW RADIO FREQUENCY UNIVERSE FROM THE FARSIDE OF THE MOON.

Jack O. Burns[1], [1]Center for Astrophysics and Space Astronomy, University of Colorado Boulder, Boulder, CO, 80309, USA, jack.burns@colorado.edu.

Introduction: The farside of the Moon is a pristine, quiet platform to conduct low radio frequency observations of the early Universe's Dark Ages, as well as space weather and magnetospheres associated with habitable exoplanets. I will describe NASA-funded concept studies of a lunar-orbiting spacecraft, DAPPER (*Dark Ages Polarimeter PathfindER*), that will measure the 21-cm global spectrum at redshifts 40-100, and an array of low frequency dipoles on the lunar farside surface, FARSIDE (*Farside Array for Radio Science Investigations of the Dark ages and Exoplanets*).

DAPPER: The early Universe's Dark Ages, probed by the highly redshifted 21-cm neutral hydrogen signal, is the ideal epoch for a new rigorous test of the standard cosmological model. The Dark Ages Polarimeter PathfindER (DAPPER), operating in a low lunar orbit above the radio-quiet farside, shall search for divergences from the standard model that will indicate new physics such as heating or cooling produced by dark matter [1]. DAPPER will observe this pristine epoch (17-38 MHz; $z\sim83$-36), and will measure the amplitude of the 21-cm spectrum to the level required to distinguish (at $>5\sigma$) the standard cosmological model from that of additional cooling derived from current, published results. The main challenge of this measurement is the removal of bright foregrounds. DAPPER is designed to overcome this by utilizing two techniques: (1) a polarimeter to measure both intrinsically polarized emission and polarization induced by the anisotropic foregrounds and large antenna beam to aid in the separation of the foregrounds from the isotropic, unpolarized global signal; and (2) a pattern recognition pipeline based on well-characterized training sets of foregrounds from sky observations, instrument systematics from simulations and laboratory measurements, and signals from theoretical predictions.

Rigorous end-to-end simulations of the DAPPER instrument including thermal noise, systematics from the spectrometer/ polarimeter and the beam-averaged foreground, along with 21-cm models, which include added cooling meet our sensitivity requirements to separate the standard cosmological models from ones that point toward new physics. DAPPER's science instrument consists of dual orthogonal dipole antennas and a tone-injection spectrometer/polarimeter based on high heritage components from the Parker Solar Probe/FIELDS, THEMIS, and the Van Allen Probes.

FARSIDE: FARSIDE is a Probe-class concept to place a low radio frequency interferometric array on the farside of the Moon. A NASA-funded design study, performed in collaboration with JPL, focused on the instrument, a deployment rover, the lander and base station, delivered an architecture broadly consistent with the requirements for a Probe mission [2]. This notional architecture consists of 128 dipole antennas deployed across a 10 km area by a rover, and tethered to a base station for central processing, power and data transmission to the Lunar Gateway, or an alternative relay satellite (Fig. 2). FARSIDE would provide the capability to image the entire sky each minute in 1400 channels spanning frequencies from 100 kHz to 40 MHz, extending down two orders of magnitude below bands accessible to ground-based radio astronomy. The lunar farside can simultaneously provide isolation from terrestrial radio frequency interference, auroral kilometric radiation, and plasma noise from the solar wind. It is thus the only location within the inner solar system from which sky noise limited observations can be carried out at sub-MHz frequencies. This would enable near-continuous monitoring of the closest stellar systems in the search for the radio signatures of coronal mass ejections and energetic particle events, and would also detect the magnetospheres for the nearest candidate habitable exoplanets (Fig. 1). Simultaneously, FARSIDE would be used to characterize similar activity in our own solar system, from the Sun to the outer planets, including the hypothetical Planet Nine. Through precision calibration via an orbiting beacon, and exquisite foreground characterization, FARSIDE would also measure the cosmic Dark Ages global 21-cm signal at redshifts z ~50–100. It would be a pathfinder for a larger 21-cm power spectrum instrument by carefully measuring the foreground with high dynamic range. The unique observational window offered by FARSIDE would enable an abundance of additional science ranging from sounding of the lunar

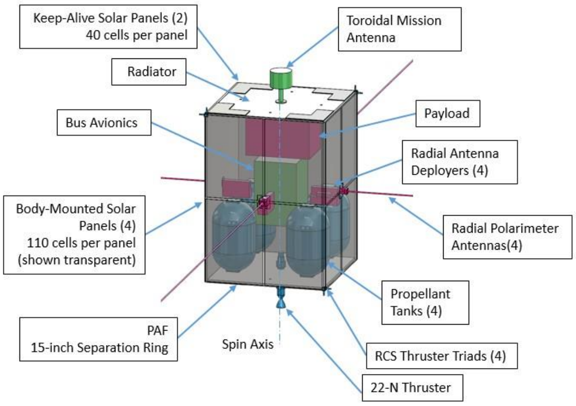

Figure 1. DAPPER spacecraft with features highlighted.

subsurface to characterization of the interstellar medium in the solar system neighborhood.

Acknowledgments: This work was directly supported by the NASA Solar System Exploration Virtual Institute cooperative agreement 80ARC017M0006. We thank the DAPPER and FARSIDE teams for their excellent work on design studies for these mission concepts.

References: [1] Burns, Jack et al. 2019, “Dark Cosmology: Investigating Dark Matter & Exotic Physics in the Dark Ages using the Redshifted 21-cm Global Spectrum”, 2019, Astro2020: Decadal Survey on Astronomy and Astrophysics, science white papers, no. 6; Bulletin of the American Astronomical Society, Vol. 51, Issue 3, id. 6; [2] Burns, Jack O, G Hallinan, L Teitelbaum, T-C Chang, J Kocz, J Bowman, R MacDowall, J Kasper, R Bradley, M Anderson, D Rapetti, Z Zhen, W. Wu, J Pober, S Furlanetto, J. Mirocha, A Austin, 2019, “Probe Study Report: FARSIDE (Farside Array for Radio Science Investigations of the Dark ages and Exoplanets)”, NASA, https://smd-prod.s3.amazonaws.com/science-red/s3fs-public/atoms/files/FARSIDE_FinalRpt-2019-Nov8.pdf

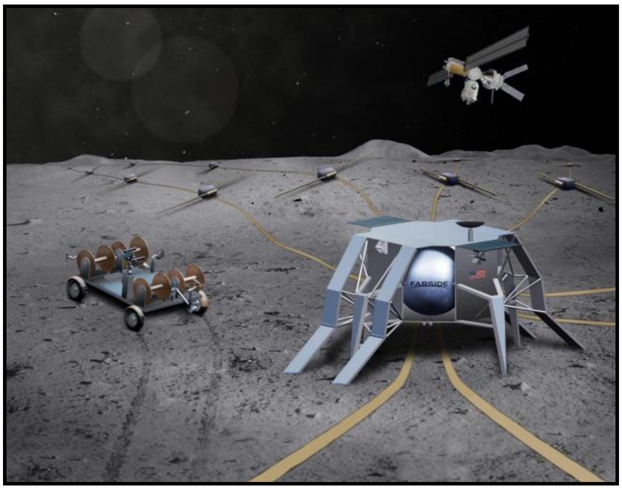

Figure 2. Overview of the FARSIDE observatory after deployment of tethers and antennas. Credit: Robin Clarke, JPL.

PROCLUS CRATER: A WINDOW INTO LUNAR HIGHLANDS.

C. Carli[1] , L. Giacomini[1], R. Pozzobon[2], M. Massironi[2], G. Serventi[3] and M. Sgavetti[3], [1]IAPS-INAF (Via Fosso del Cavaliere 100, 00133, Roma), [2]Geoscience Department, University of Padova; [3] SCVSA Department, University of Parma.

Introduction: Mafic regions embedded in the Lunar highlands have been recently observed [1] and, moreover, the presence of an absorption band at ca. 1250nm, assigned to Fe^{2+} transition in plagioclase (PL), has been detected in central peaks of some impact craters (e.g. [2]). The provence of these mafic enrichment zones is still an open point, if they are coming from other crater ejecta, are upwelling of mantel portion or subcrustal magmantic chambers.

Data & Methods: We used some M3 (Chandrayaan mission) spectral cubes in particular the image (m3g20090202t024131) where a small interesting crater (Proclus) is completely present in the image. We classified the crater by using the Spectral Angle Mapper (SAM) method [3], building our spectral library directly from the images by means of Purity Pixel Index (PPI, [4]). We iteratively chose SAM acceptance angle to highlight outcrops of well defined spectral properties.

Preliminary Results: Here, we analyze the M3 (Chandrayaan mission) reflectance spectra of Proclus crater (16.1° N, 47.0° E), a 28 km crater located in a highland portion on the west of Mare Crisium, were high amount of PL have been previously detected (e.g. [5]). First, we classified the crater in different spectral regions, using the SAM method (Figure 1), with a spectral library build by means of PPI, on the basis of the different spectral properties in the reflectance data (Figure 2). Then, we related the spectral parameters of each region to the mineralogical composition. To this purpose, the M3 data have been compared with laboratory spectra acquired on well characterized mixtures of PL and mafic minerals, such as pyroxene (PX) and olivine (OL) (e.g. [6] and references therein). We recognized regions with different spectral behaviors: 1) PL regions located mainly in the crater walls; 2) PX regions in both the walls and the floor of the crater; 3) OL regions in the southeast portion of the crater walls; and 4) PL (90%)+PX regions in the crater wall. Here we have highlighted how a comparison with laboratory spectra can strongly help to obtain information about the mineral content and composition of a planetary surface (Figure 3).

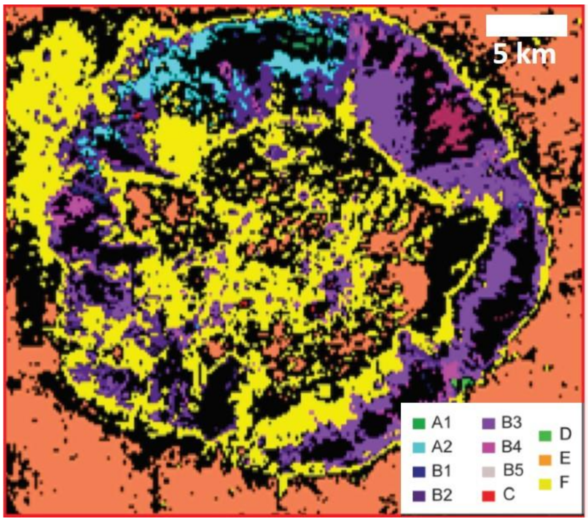

Figure 1 – SAM classification with 0.1 rad of sensitivity. Orange and yellow represent regolith spectral properties.

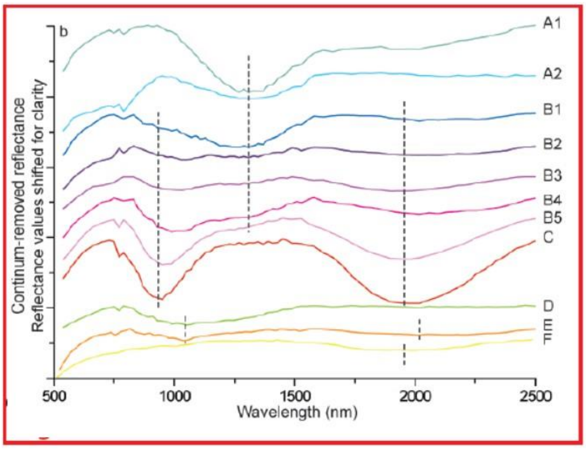

Figure 2 – M3 averaged spectra representative of the different units extrapolated by means of PPI. Color correspond with figure 1 units.

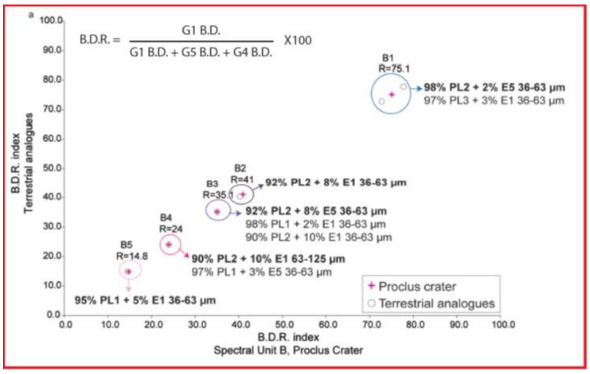

Figure 3 – Comparison between spectral units from M3 data and analogue mixture spectra using a band depths ratio parameter.

Future works: A comparison with morphology and a 3D reconstruction is ongoing to assess a geological setting of this fresh crater and to identify the origin of the mafic outcrops.

Acknowledgements: This work was partially supported by European Union's Horizon 2020 research grant agreement No 776276- PLANMAP.

References:

[1] Yamamoto et al. (2015) J.G.R. Planets, 120, 831-848. [2] Cheek L.C. et al. (2012) 2nd conference on the lunar highland crust. Abstract# 9022. [3] Kruse F. A. et al. 1993. Remot.Sens.Environ 44, 145-163. [4] Boardman J.W. 1993. In Memories of the 4th JPL A.Geos.W, 11-14. [5] Donaldson Hanna et al. (2014) J.G.R. Planets, 119. [6] Serventi et al. (2016) Icarus, 272, 1-15.

PB-PB AND U-PB GEOCHRONOLOGY OF SHOCKED APOLLO 17 MG-SUITE PHOSPHATES.

A. Černok[1,2,3], L. White[1,2], M. Anand[3,4], K. Tait[1,2], M. Whitehouse[5], S. Kamo[2], T. Casagrande[6], and J. Darling[7]. [1]Centre for Applied Planetary Mineralogy, Department of Natural History, Royal Ontario Museum, Toronto, M5S 2C6, Canada, (acernok@rom.on.ca). [2]Department of Earth Sciences, University of Toronto, Toronto, M5S 3B1, Canada. [3]School of Physical Sciences, The Open University, Milton Keynes, MK7 6AA, UK. [4]Department of Earth Sciences, Natural History Museum, London, SW7 5BD, UK. [5]Department of Geosciences, Swedish Museum of Natural History, Stockholm SE-104 05, Sweden. [6]Canadian Centre for Electron Microscopy (CCEM), McMaster University, Hamilton, L8S 4M1, Canada. [7]University of Portsmouth, School of the Environment, Geography and Geosciences, Portsmouth, PO1 3QL, UK.

Introduction: The first lunar crust formed by solidification of anorthosites on the top of the Lunar Magma Ocean (LMO) [1]. The crustal solidification was followed by secondary magmatic processes in the lunar interior, which produced magmas that intruded into the early anorthositic crust [1]. The timing and duration of lunar crust formation is still poorly constrained, with one of the outstanding questions being the source and the timing of the so called *Mg-suite* intrusive rocks [2]. The origin of these cumulate rocks that have high abundance of incompatible elements is often debated, either to have its source in the lunar interior [3], or alternatively, to be impact-related [4]. Nevertheless, numerous geochronological investigations of Mg-suite samples have been carried out [summarized in 2]. However, *in situ* age determination in Mg-suite phosphate minerals apatite and merrillite that are particularly sensitive to impacts, remain scarce [5]. Here we focus on exploring the U-Pb and Pb-Pb ages of apatite and merrillite in a set of variably shocked rocks sampled by the Apollo 17 mission in the Taurus-Lithrow Valley. The selection of the samples builds on previous micro- and nanostructural analyses of the phosphates [6].

Samples: In this study, six different samples of Mg-suite norite, troctolite and gabbro were selected from the Apollo 17 collection, based on increasing levels of shock deformation [6]: unshocked S1 troctolite 76535, brecciated S2 anorthositic troctolite 76335, breccia 76255 with troctolite, norite and gabbro clasts (S2, S3-4 and recrystallized grains) within impact melt, 73235 S3 shocked troctolite, 72255 (Civet Cat norite fragment, S3-4), and 78235 & 78236 S5-S6 shocked norites.

Methods: In the first part of the study, we carried out U-Pb and Pb-Pb analyses of ~50 phosphate grains from across the six samples using the CAMECA 1280 ion microprobe at the NordSIMS facility (Stockholm), following established protocols [5]. Further on, we identified three individual phosphates found in contact with the impact melt of 76255 breccias for high-precision U-Pb and Pb-Pb analyses by ID-TIMS (Jack Satterly Lab, University of Toronto). For this purpose we applied a recently developed FIB-TIMS approach [7], extracting phosphate grains directly from thin sections using a Xe^+ plasma FIB (FPIB) at CCEM. After the final pFIB cutting and polishing, the grains were left in contact with the surrounding material via a thin bridge (Fig. 1). The entire thin-section was then placed in a large petri dish before being entirely submerged in ethanol. Fine tipped tweezers and custom pipettes (made within the Jack Satterly Lab) were used to physically knock the PFIB-isolated grain loose under an optical microscope, where the individual ~70 x 95 x 20 µm or smaller cuboids of phosphates (0.13-0.4 µg) were liberated. Details on ID-TIMS procedure of this approach are provided elsewhere [7].

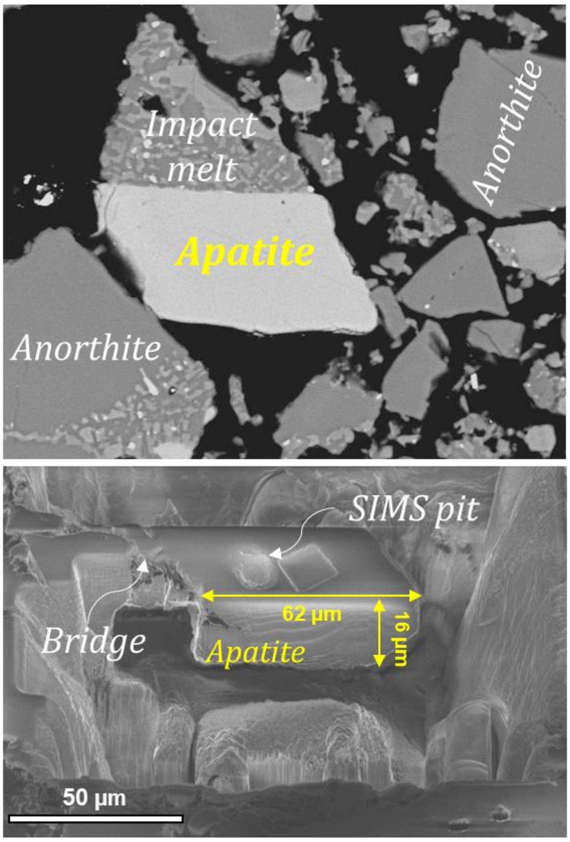

Figure 1. *BSE image of apatite in 76255,71 surrounded by impact melt and anorthite (top panel); SE image of the apatite grain after* Xe^+ *plasma FIB cutting and final polishing (bottom panel). The thin bridge holding the sample is annotated. Apatite mass is 0.13 µg.*

Results: As determined by SIMS, $^{207}Pb/^{206}Pb$ systematics of the unshocked or weakly shocked apatite in 76535 and 76335 are undisturbed, implying cooling of the rock below the closure temperature of Pb diffusion in apatite (~450 ºC) at ~4.2 Ga [for more details see 8]. This age is ~100 Ma younger than what is interpreted as the rock's crystallization age [9], but is in good agreement with Ar-Ar dating [e.g. 10]. Phosphates that experienced similar levels of deformation but were in proximity or in direct contact with the impact melt in samples 76255 and 72255 show almost complete age resetting (~3.92 Ga, see [8]). In particular, a weighted average SIMS age of 15 phosphate analyses in sample 76255 is 3921.9 ± 6.8 Ma (2σ) (Fig. 3). This agrees with the previously published $^{207}Pb/^{206}Pb$ phosphate ages of impact melt breccias collected from the same boulder and interpreted to reflect the timing of the Imbrium impact [5]. SIMS U-Pb analysis of highly shocked phosphates (78235 and 78236) reveal a discordia line with an upper intercept of ~4.2 Ga and a lower intercept of ~0.5 Ga [11]. We interpret this new, younger age as a minor thermal event that reactivated existing shock-induced nm-scale grain boundaries within the apatite population to allow for Pb-loss at ~0.5 Ga. We propose a small crater located near the Apollo 17 landing as a possible source of this sample.

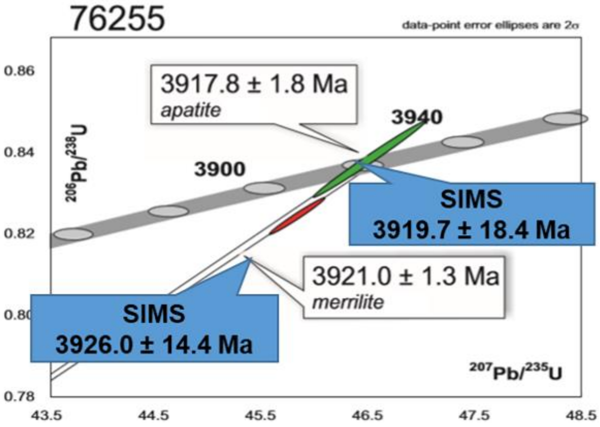

Figure 2. *ID-TIMS obtained U-Pb concordia diagram of pFIB-extracted phosphates, with individual $^{207}Pb/^{206}Pb$ ages (TIMS – white, SIMS – blue) annotated. All quoted uncertainties are 2σ.*

The results of one apatite (76255,71) and one merrillite (76255,75) ID-TIMS analyses, presented in Figure 2. yield Pb-Pb ages with significantly lower internal uncertainties than that of the individual SIMS measurements, 3917.8 ± 1.8 Ma and 3921.0 ± 1.3 Ma (2σ), respectively. While the apatite is concordant, the merrillite shows minor discordance (1.5 %), plotting along a line with an upper intercept slightly older than that of the concordant apatite. The third phosphate (apatite 78255,68) is significantly more discordant (32 %), with an upper intercept of 3930 ± 25 Ma. As presented in Figure 3, the two TIMS ages are within the range of the weighted average of the 76255 SIMS ages (3921.9 ± 6.8 Ma, 2σ, n=15). These two values may represent differing degrees of resetting of the phosphates incorporated within the impact melt, or perhaps even record multiple impact events close in time to what is interpreted as the Imbrium event.

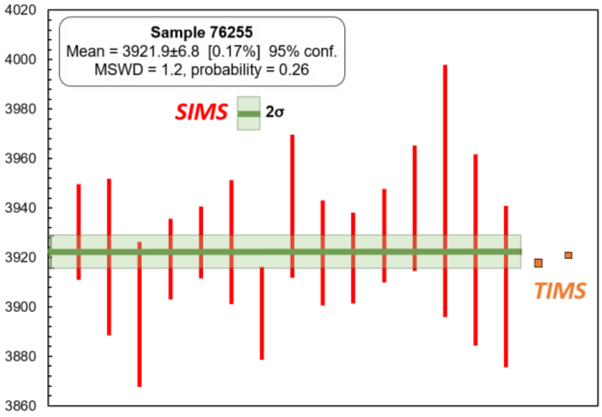

Figure 3. *$^{207}Pb/^{206}Pb$ ages of the 76255 phosphates. Red bars are SIMS ages with the green area indicating the weighted average over 15 individual measurements. TIMS ages are presented in orange. All bars include 2σ uncertainties.*

Conclusion: Apollo 17 Mg-suite rocks show a great variability in Pb-Pb and U-Pb systematics, that can be related to their complex bombardment history. By correlating micro- to nanostructural characterization with *in situ* U-Pb and Pb-Pb systematics we show that apatite and merrillite hold great potential to be utilized as sensitive thermochronometers of impact events. We establish FIB-TIMS as a powerful tool for high-precision age determination of single phosphate grains that can discriminate between temporally similar events. This can greatly aid in unravelling the bombardment record of the early lunar and solar system history, and be helpful when dealing with samples of restricted availability, for example material obtained by space return missions.

Acknowledgement: We thank NASA CAPTEM for allocation of Apollo samples. AC and MA acknowledge the funding through MSCA fellowship to AC from the EU's Horizon 2020 research and innovation program (grant agreement No 704696). AC, LW, and KT acknowledge the Hatch Ltd. Funding. KT acknowledges the ROM Peer Review grant for funding and a NSERC Discovery Grant.

References: [1] Shearer, C. K. et al (2015) *Am. Mineral.* 100, 294–325. [2] Carlson et al. (2014). *Phil.Trans.R.Soc*. A372, 20130246. [3] Shearer, C.K. et al (2005) *GCA* 69, 3445–3461 [4] Hess P. C. (1994) *JGR* 99, 19083–19093 [5] Thiessen et al. (2017). *MaPS* 52, Nr 4, 584–611. [6] Cernok et al. (2019) *MaPS* 54, 1262-1282. [7] White, L. F. et al. (2019) *Geochron.*, https://doi.org/10.5194/gchron-2019-17. [8] Cernok et al. (2019), *LPSC L*, Abstract ##2232. [9] Borg et al. 2017. *GCA 201*, 377-391. [10] Gerrick-Bethell, I. et al. (2017) *JGR* 122, 76-93. [11] Cernok et al. (2019), *LPSC L*, Abstract ##2228.

SAMPLE CONTAINMENT FOR IN SITU ANALYSIS ON THE MOON: TESTING SEALING MATERIALS IN THE PRESENCE OF DUST.

H. E. Chinnery[1], F. A. J. Abernethy[1] and S. J. Barber[1]. [1]School of Physical Sciences, The Open University, Walton Hall, MK7 6AA (hannah.chinnery@open.ac.uk)

Introduction: The lunar regolith is formed by high velocity micrometeorite impacts, which have pulverised the lunar surface into highly angular lithic fragments and impact melt. The impact melt solidifies to form silica-rich glass rinds around grains, which become brittle and shatter, resulting in sharp, angular particles that are highly abrasive and can interfere with the operation of equipment on the surface [e.g. 1]. Lunar regolith is also easily disturbed and electrostatically charged [2], which is particularly problematic when it is necessary to form gas tight seals in-situ, as it is highly likely that the sealing surfaces would become contaminated with dust.

ESA's PROSPECT (Package for Resource Observation and in-Situ Prospecting for Exploration, Commercial exploitation, and Transportation) is due to fly on the Russian Luna 27 mission to the lunar south pole with the goal of identifying the presence and distribution of water in the subsurface. The ProSPA (PROSPECT Sample Processing and Analysis) package [3] is a miniaturized chemical analysis laboratory consisting of a gas processing system and two mass spectrometers, designed to provide information on the abundance, nature, and distribution of lunar volatiles, as well as to demonstrate In Situ Resource Utilization (ISRU). Samples of icy regolith will be sealed within miniature ovens, heated and then analysed. A wide range of temperatures will be experienced, from the approx. -100°C of the lunar surface, through to the maximum operating temperature of the ovens at ~1000°C. However, the oven design will allow for the seal to only have to withstand up to ~300°C. An effective seal will need to be maintained across the temperature range, most likely with dust particles embedded on the surface of the sealing material. Whilst dust mitigation strategies for gas-tight seals do exist (such as those used on NASA's MSL rover [4, 5] and the upcoming ExoMars rover [6]) these involve relatively complex, large-scale, heavy sample handling hardware and are therefore prohibited by the mass limitations of ProSPA (10 kg). Given these limitations, the sealing mechanisms are modelled on the Rosetta Philae SD2 sampling system [7], designed to be small and lightweight, but meaning only low sealing forces (<400 N) are able to be exerted.

Methods: Experimental work has been undertaken to assess the leak rate of seals using different materials and a range of sealing forces. This work builds on the results from Abernethy et al. [8], which assessed the efficacy of Kalrez®7075 and indium as a single-use sealing material. Both materials are highly deformable, enabling seals to be made at relatively low forces (<400 N), and were tested clean and contaminated with the lunar simulant JSC-1A.

To extend the scope of this work, new measurements of the leak rate of seals have been made. These were conducted using two metal alloys manufactured by Indium Corporation (Indalloy 164, chemical composition 5% indium, 92.5% lead and 2.5% silver; and Indalloy 171, composed of 95% lead and 5% tin), and the fluoropolymer resin Polytetrafluoroethylene (PTFE). The sealing potential of these materials has been tested using two different circular knife edges, with cross-sectional profile angles of 45° and 90° at the tip of the knife edge (see Fig. 1) in order to also assess the effect of seal geometry on seal quality.

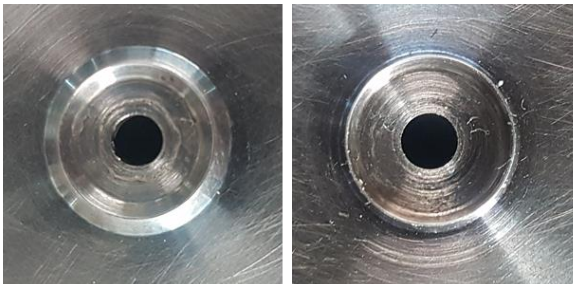

Figure 1. Circular knife edges used to perform sealing tests. *Left* 90°, *right* 45°. Both 10 mm diameter at the peak of the knife edge, and 1 mm in height.

A custom rig was used to test the leak rates of sealing materials. A force, measured by a load cell, was applied to the sealing material against the knife edge. The applied force was then gradually increased and the sealed volume within the knife edge evacuated, and the leak rate tested incrementally until a good quality seal was achieved, as per the methods detailed in Abernethy et al. [8]. A leak rate of 10^{-6} mbar.l.s^{-1} is the requirement for the ProSPA ovens, and so seals with a leak rate equal to or less than this threshold is deemed to be a "good quality" seal. Fig. 2 depicts the equipment set-up used to pump down the sealed volume and then measure the rise in pressure due to leaks in the seal. Valve 1 (V1) leads to a vacuum pump; valve 2 (V2) to a 1 Torr Baratron™ capacitance manometer; valve 3 (V3) to the seal testing apparatus; and the final valve (V4) is kept closed. Once the volume was evacuated, the valve to the pump was closed off, leaving the Baratron and seal test apparatus valves open. The pressure on the Baratron was sampled over a 45s period, or until the Baratron reached the maximum pressure reading. The leak rate was then calculated from the rise in pressure over time within the sealed volume through the ideal gas equation.

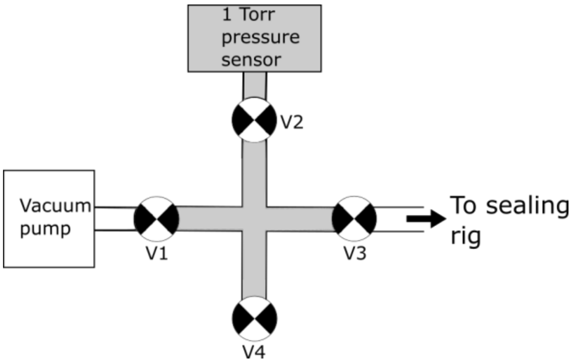

Figure 2. Schematic of equipment used to measure pressure rise in sealing tests [4].

Results: Leak rate measurements have been undertaken on three candidate seal materials: Indalloy 164, Indalloy 171 and PTFE. These were performed using a circular knife edge of 45° and 90° in profile. Measurements were then repeated with the seals contaminated by JSC-1A lunar regolith simulant, in order to get an initial assessment of how these seals could perform in a dusty environment, such as the lunar surface (see Fig. 3 for examples of sample materials after sealing achieved). For these tests the extent of dust coverage was not quantified, just visually assessed to be evenly coated in a thin layer of dust.

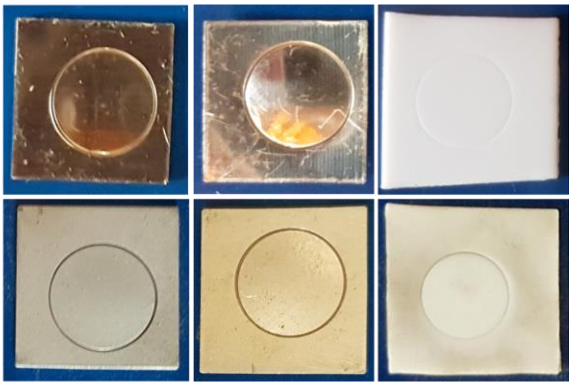

Figure 3. Samples of tested seal materials. *Top row:* clean seals; *Bottom row:* seals loaded with JSC-1A dust. *Left to right:* Indalloy 164, Indalloy 171, PTFE.

Analysis of the data so far has shown that the broader 90° angled knife edge achieves the required leak rate of 10^{-6} mbar.l.s^{-1} more consistently and at lower sealing forces than when using the 45° knife edge. Additionally, the 90° knife edge forms a seal with a lower leak rate than the 45° knife edge when the seals are contaminated with simulant dust. It is likely that this is due to the larger surface area over which a seal is made with the broader knife edge, which causes the simulant grain to be encapsulated in the seal completely. Room temperature tests so far show that PTFE is the most promising candidate seal material, forming a good seal at low sealing forces (<300 N) when clean, and requiring ~400 N sealing force to achieve the required leak rate when dusty. The softer Indalloy 171 performed within the requirements when clean, achieving the leak rate of 10^{-6} mbar.l.s^{-1}at a sealing force of ~400 N, but required >500 N sealing forces when dusty, whilst the harder and least deformable Indalloy 164 performed the least consistently across all scenarios.

Further Work: This investigation is ongoing. A new sealing rig is being assembled to enable testing of seal materials under vacuum conditions and over the temperature range from that experienced at the lunar pole, to oven operating temperatures. The system will be automated for greater reproducibility of the results. Different materials may perform better at higher or lower temperatures, and so further sealing materials will be tested, in addition to the two alloys and PTFE tested so far. A range of knife edge sealing geometries will be used, and tested on both sides of the seal (the knife edge, as tested here, and the oven side of the seal). Additionally, a dust distribution system has been developed to more evenly distribute lunar simulant dust onto the samples, and assess the quantity and distribution of the dust coating prior to experiment commencement.

References: [1] Colwell, J. E., Batiste, S., Horányi, M,. Robertson, S., Sture, S. (2007) Lunar surface: dust dynamics and regolith mechanics. *Rev. Geophys. 45* (2), RG2006. [2] Grün, E., Horányi, M,.Sternovsky, Z. (2011) The Lunar dust environment. *Planet. Space Sci.* 59, 1672-1680. [3] Barber, S. J. et al. (2018) ProSPA: Analysis of lunar polar volatiles and ISRU demonstration on the Moon, *49th Lunar and Planetary Science Conference*, Abstract #2083. [4] Kennedy, T., Mumm, E., Myrick, T., Frader-Thompson, S. (2006) Optimisation of a Mars sample manipulation system through concentrated functionality, *Space 2006. AIAA SPACE forum*, San Jose, USA #7402. [5] Mumm, E., Roberts, D., Kennedy, T., Carlson, L., Rutberg, M., Ji, J. (2008) Sample manipulation system for sample analysis at Mars. *AIAA SPACE forum*, San Diego, USA #7736. [6] Richter, L., Carianni, P., Durrant, S., Hofmann, P., Muhlbauer, Q., Musso, F., Paul, R., Redlich, D. (2015) Progress report on development of the Exomars 2018 sample processing and distribution subsystem (SPDS) and related OHB sample handling studies. *Proceedings of ASTRA 2015*, The Netherlands. [7] Finzi, E. A., Zazzera, F. B., Dainese, C., Malnati, F., Magnani, P. G., Re, E., Bologna, P., Espinasse, S., Olivieri, A. (2007) *Space Sci. Rev. 128*. [8] Abernethy, F. A. J., Sheridan, S., Barber, S. J. (2020) Gas containment for in situ sample analysis on the Moon: Utility of sealing materials in the presence of dust *Planet. Space Sci., 180*

UNRAVELING THE MYSTERY OF VALLIS SCHRÖTERI J. D. Clark[1] and M. S. Robinson[1], [1] School of Earth and Space Exploration, Arizona State University, Tempe, AZ, USA (jclark@ser.asu.edu)

Introduction: Vallis Schröteri is located on the Aristarchus Plateau, a block of ancient crust surrounded by basaltic maria [1]. Sinuous rilles are typically 20 to 40 km in length and less than a kilometer wide, however, the primary rille of Vallis Schröteri is 155 km long, up to 6 km in width and on average 500 m in depth [2]. The formation of Vallis Schröteri is likely the result of both lava thermal and mechanical erosion, where the primary rille was created during a large discharge event and the secondary rille formed from a smaller discharge event [3-5]. The highly sinuous secondary rille meanders across the floor of the primary rille, eroding into its steep walls [6]. After traversing ~200 km away from the lava source [7], the secondary rille terminates in one of the youngest maria units on the Moon [8].

The formation time for Vallis Schröteri has been of interest due its position on Aristarchus plateau, its proximity to Aristarchus Crater and the youngest maria unit [8]. Although an age has not yet been determined for the pyroclastic deposits on the plateau, model ages derived from crater size-frequency distribution (CSFD) measurements indicate that Aristarchus crater is less than 200 Ma [9-12] and the youngest maria unit P60 is ~ 1.2 Ga. With the secondary rille terminating in P60, it seemed plausible that the rille is the source of the P60 maria unit. A first attempt at dating the rille was completed by [2] using CSFD techniques on Kaguya images. To better understand the geologic history for the area, we obtained CSFD measurements for the rille from Lunar Reconnaissance Orbiter Camera (LROC) Narrow Angle Camera (NAC) images and investigate where the lava that carved the rille deposited outside of the plateau.

Data and Methods: NAC images were processed using the Integrated Software for Imagers and Spectrometers (ISIS) [13,14], only images with incidence angles between 65°-75° were considered [15]. ArcGIS, count areas and CSFD measurements were defined and generated using CraterTools [15]. The CSFDs were plotted and fit in Craterstats [17], using the techniques described in [15]. The derived absolute model ages (AMAs) are based on the production and chronology functions [18], valid for lunar craters >10 m and <100 km in diameter.

CSFD measurements (Fig. 1) were conducted on three sections of the floor of the primary sinuous rille: (A) near the opening of the rille, (B) in the center, and (C) adjacent to the source vent (Cobra Head). These areas were later combined to estimate the formation age of the primary rille. Due to Vallis Schröteri's proximity to Aristarchus crater, we were meticulous to omit ejecta rays from the digitized count areas (especially for Area C). The Buffered Crater Counting technique for the primary and secondary rilles was considered, however, (1) the primary rille is too broad to use the technique, (2) the secondary rille has likely undergone a faster rate of resurfacing due to slumping from the walls of the primary rille, and (3) the secondary rille contains a large amount of blocks making it difficult to conduct CSFD measurements.

Results: Our CSFD derived model age for Vallis Schröteri is 2.5 ± 0.5 Ga (Fig. 2). This AMA was determined by combining the CSFD measurements of areas A-C (80 km²). Individually, the AMAs for areas A-C ranged from 2 to 2.7 Ga, all overlapping within their uncertainty estimates.

A similar age for the rille of 2.5 ± 0.5 Ga was determined by [2], however, the count area was not documented in that work and therefore, it is unclear what sections of the rille, primary or secondary, was used for age determination. The resurfacing tool was applied to CSFDs to account for minor resurfacing due to the Aristarchus cratering event. [2] conducted CSFD measurements on the Cobra Head, attempting to correlate its age to the rille. Although an age of 3.1 (+0.3, -0.7) Ga was determined, it is likely not a representative age due to its proximity to Aristarchus

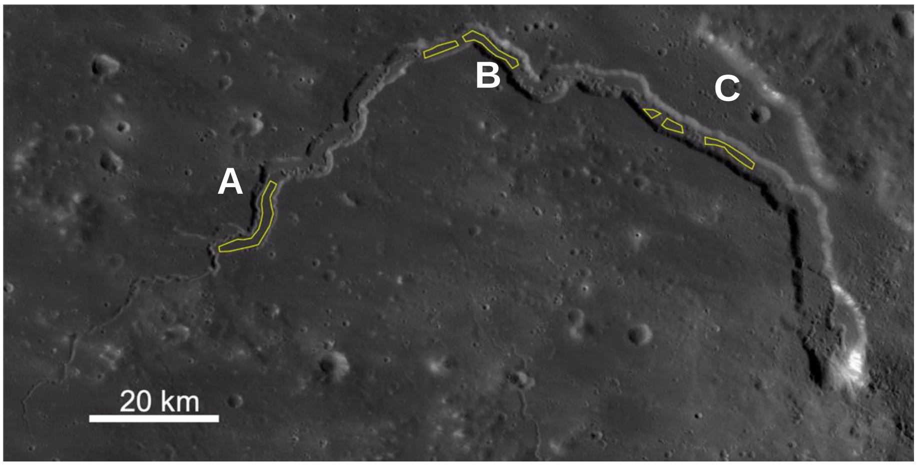

Figure 1: Vallis Schröteri (centered: 26°N, -50.9°W) shown in LROC Wide Angle Camera Global Morphologic basemap (100 m/pix)[9]. Count areas for CSFD measurements are marked in yellow boxes (A-C).

Crater and therefore, being affected by ejecta material and secondaries.

Discussion: With the primary rille being Erastothenian in age (~2.5 Ga), it is unlikely to be the source for the youngest mare basalts on the Moon (unit P60 at ~1.2 Ga). The primary rille abruptly stops 25 km before the edge of the P60 mare unit and is facing west (Fig. 3), suggesting that the rille terminus was covered by the mare unit or the Aristarchus pyroclastic deposits (whose age remains unknown). If the primary rille had earlier terminated into the maria, continuing in a western direction, it is possible that the nearby P32 basalts might have been sourced by the rille as their age ranges (2.76 +0.3/-0.2 [8]) overlap with our estimates for the primary rille.

At the primary rille terminus (Fig. 3), the secondary rille takes a sharp 90º turn to the south, cross-cutting the wall of the primary rille, and eventually fades away near the contact or within the P60 mare basalts [8]. This course change suggests that the rilles formed at two distinct times.

The area of the terminus of the secondary rille, based on Clementine data, is chemically distinct relative to the surrounding units and may be a complex mixture of P60, ash, and Aristarchus ejecta. Therefore, an additional CSFD measurement on area could determine if it has similar age to P60.

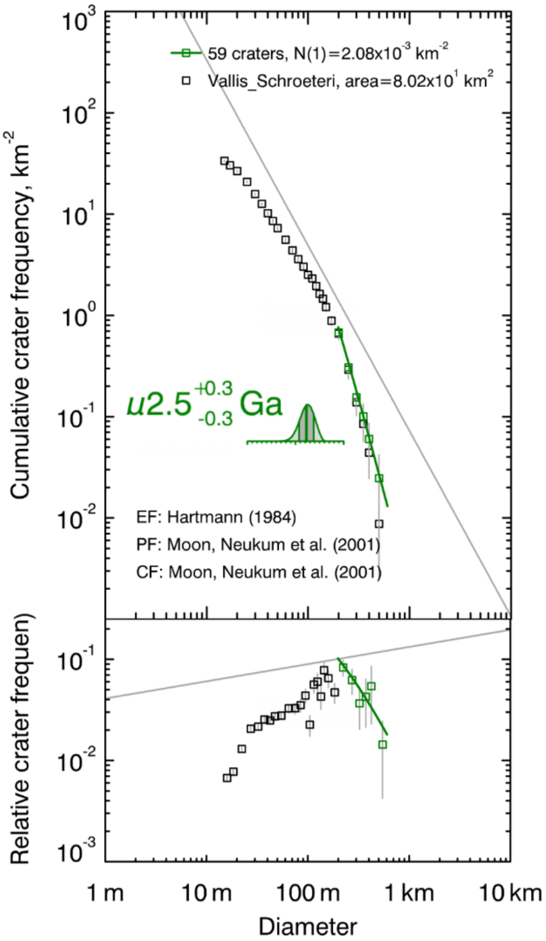

Figure 2: Absolute model age determined from the combined CSFD measurement areas on the floor of Vallis Schröteri. A Poisson timing analysis was used to fit the CSFDs. Fit shown in cumulative and r-plot.

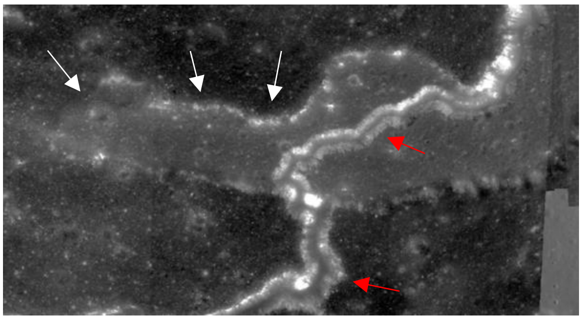

Figure 3: Low-incidence angle NAC image showing theend of the primary rille (white arrows). The secondary rille (red arrow) continues south for another ~50 km.

From a morphological standpoint, we find no indication that the primary and secondary rilles are superposed by ash deposits, however, a thin ash veneer might not have a strong morphological expression in orbital images. Generally, the floor of the primary rille has the same Clementine color signature as the plateau (suggesting ash on the rille floor). Based on our observations, we offer a potential sequence of events: (1) the vent opened and a voluminous flow event created the primary rille, (2) the primary rille was then blanketed in a veneer of ash, 3) the primary rille terminus was blocked (ash or other?) (4) the vent was reactivated and the secondary rille formed, and (5) the Aristarchus impact event redistributed surface materials and nearby subsurface materials. Key questions include a) how was the primary rille terminus blocked b) was there a significant time hiatus between primary rille formation, the blocking event, and secondary rille formation?

Rover-based high-resolution imaging, as well as mineralogical and chemical measurements [19] of the primary and secondary rille materials as well as of the P60 mare unit would clarify the sequence of magmatic events. Additionally, magnetic field strengths and polarity between the rilles and nearby mare could clarify relative age differences.

References: [1] Zisk, S.H. et al. (1977) Moon, 17, 59-99. [2] Honda, C. et al. (2009) LPSC XL, #1524. [3] Hulme, G. (1973) Mod. Geol., 4, 107-117. [4] Carr, M.H. (1974) Icarus, 22, 1-23. [5]Greeley, R. et al. (1971) Science, 172, 722-725. [6] Garry, W.B. et al. (2008) LPSC XXXIX, #2261. [7] Cataldo et al. (2019) LPSC 2019, #2297. [8] Hiesinger et al. (2003) JGR, 108, E7, 5065. [9] König et al. (1976) LPSC VIII, 555-559. [10] Young (1975) LPSC VII, 3457-3473. [11] Zanetti et al (2013) LPSC XLIV, 1842. [12] Zanetti et al. (2017) Icarus 298, 64-77. [13] Robinson et al. (2010) Space Sci. Rev. 150, 55. [14] Anderson et al. (2004) LPSC XXXV, #2039. [15] Ostrach et al (2011) LPSC XLII, #1202. [15] Kneissl et al. (2011) PSS 59, 1243-1254. [16] Michael and Neukum (2010) EPSL 294, 223. [17] Neukum (1983) Meteoritenbombardement und Datierung planetarer Oberflächen, Habil. Thesis, Univ. Munich. [18] Neukum et al. (2001) Space Sci. Rev. 96, 55. [19] Robinson et al. (2019) LEAG, #5049.

NASA'S LUNAR DISCOVERY AND EXPLORATION PROGRAM. S.W. Clarke[1], B.E. Bailey[1], D.B.J. Bussey[1], J.E. Jenkins[1], A.M. Melito[1], S.K. Noble[1], and J.B. Wolfe[1], , [1]NASA Science Mission Directorate, NASA HQ, 300 E St SW Washington D.C. 20546 (steven.w.clarke@nasa.gov)

Introduction: The Lunar Discovery and Exploration Program (LDEP), within NASA's Science Mission Directorate, is responsible for several lunar-related activities. These include

- Commercial Lunar Payload Services (CLPS)
- Instruments to fly on CLPS missions
- Instrument Development
- Lunar Reconnaissance Orbiter
- Lunar SmallSats
- Future medium-class landers and rovers

Commercial Lunar Payload Services (CLPS): NASA is looking to jumpstart the U.S. commercial lunar lander services industry. In November 2018, NASA selected nine providers for the CLPS catalogue, with an additional five companies added late 2019. These companies all have plans to launch landers to the lunar surface, selling available payload space. NASA will be one of the early customers for these companies. The fourteen CLPS providers are:

- Astrobotic Technology Inc.
- Blue Origin
- Ceres Robotics
- Deep Space Systems
- Draper
- Firefly Aeronautics Inc.
- Intuitive Machines, LLC
- Lockheed Martin Space
- Masten Space Systems Inc.
- Moon Express
- Orbit Beyond
- Sierra Nevada Corporation
- Space X
- Tyvak Nanosatellite Systems

NASA released the first delivery Task Orders in 2019, with Astrobotic and Intuitive Machines selected to deliver payloads to the lunar surface in 2021. LDEP's goal is to enable at least two CLPS deliveries to the lunar surface every year.

Instruments to fly on CLPS Landers: NASA recently put out two calls for ready (or near-ready) to fly instruments to fly on early CLPS missions.

NASA Provided Lunar Payloads (NPLP). The NASA Provided Lunar Payload call supports ready-to-fly and the completion of near ready-to-fly science and technology payloads. In February 2019 NASA announced the first 12 NPLP selections. The selected payloads include a wide selection of scientific instruments. These instruments provide the majority of the manifests for the first two CLPS deliveries.

Lunar Surface Instrument and Technology Payloads (LSITP): LSITP was a call to the external (non-NASA) science, technology and exploration communities for potential payloads to fly on early CLPS missions. 12 instruments were selected July 2019. These instruments provide the bulk of the manifests for the third and fourth CLPS lunar surface deliveries

Payloads & Research Investigations on the Surface of the Moon (PRISM): PRISM is an instrument solicitation for new PI-led investigations through individual or suites of instruments that are either destination agnostic or uniquely adapted to study specific. PRISM will generate a catalogof instruments/technology demonstratoons that are available from the science community. PRISM will be the primary method by which US payloads are selected for future CLPS deliveries.

Instrument Development. It is the goal of LDEP to have a healthy supply of instruments ready to fly with the CLPS providers. The Development and Advancement of Lunar Instrumentation (DALI) call is a lunar instrument development program with the purpose of maturing the instrument development to TRL-6.

Lunar Reconnaissance Orbiter (LRO): LRO has been in orbit around the Moon for a decade and continues to acquire key new data sets. In addition to conducting scientific discovery, LRO will be used, where possible, to help the CLPS providers with landing site reconnaissance.

Small Satellites: The Small Innovative Missions for Planetary Exploration (SIMPLEX) is a call for small innovative planetary exploration missions. Any lunar missions that are selected will be managed under LDEP.

Medium Class Landers and Rovers: It is also in the LDEP portfolio to study the options for flying medium class (~500 Kg payload) landers and potential accompanying rovers. An example for such a mission could be a polar prospecting mission.

SPACESHIP EAC ACTIVITIES FOR NOVEL OXYGEN PRODUCTION ISRU AND PURIFICATION.

A. Cowley[1], L. Schlüther[1], T. Schild[1], L. Turk[1], [1]European Astronaut Centre EAC, European Space Agency, 51170 Köln, Germany.

Introduction: Spaceship EAC is a multidisciplinary innovation-driven team based within the European Astronaut Centre which aims to develop and validate operational concepts and low-TRL-level technologies in support of lunar human exploration scenarios, as part of the ESA E3P/EXPERT (European Exploration Envelope Programme/Exploration Preparation, Research and Technology). In the past the team has focused on planetary fabrication approaches with ISRU, focusing on utilizing both direct microwave heating and indirect susceptor driven heating of regolith simulant in order to enable an additive manufacturing methodology using this material (following from the ESA General Studies Programme project concept proposed in 2013 [1]).

In the past year, the initiative has begun to investigate novel O_2 production, extraction and capture methodologies. Herein we present our progress and results on a range of these ongoing activities:

Novel Oxygen Production Techniques – we are investigating distinct novel approaches to Oxygen production via processing of regolith simulant. It is known that Fluorine is a powerful extracting agent, whereby aqueous HF and F_2 can readily reduce many of the compounds present in regolith. Heretofore uninvestigated, we report on initial work on developing a PFC/SF_6 low-pressure plasma activated process for extracting O_2 from regolith. In addition, two electrolysis processes are being compared and evaluated for ISRU: one is performed in molten Calcium Chloride and the other is done in an aequeous NaOH solution. Both processes used industrially for the production of titanium and pure iron respectively.

Flexible Toolkit for Lunar Regolith Processing & Offgasing (FLOP) - All ISRU oxygen extraction processes have one thing in common: They produce a gas that contains O_2, H_2O, CO_2 or other oxygen-bearing compounds. But the purification and the gas treatment to yield in pure oxygen or water requires further steps [2]. Therefore, a modular gas treatment toolkit is developed by matching gas separation and purification technologies with the output compositions from oxygen extraction processes and the input requirements of user technologies such as life support systems and liquid fuel engines.

In all our activities, concept/technology development and demonstration projects are coordinated with ESA centres and exploit synergies with EAC facilities as well as with the surrounding DLR campus, commercial partners and European research groups [3].

References:

[1] ESA GSP study on Lunar Base 3D printing: http://www.esa.int/Our_Activities/Space_Engineering_Te chnology/Buildingalunarbasewith3Dprinting

[2] Schlüter, L. and Cowley, A. (2019) Planetary and Space Science, 104753.

[3] Spaceship EAC: https://www.esa.int/About_Us/EAC/Spaceship_EAC

MOTOR CONTRO SYSTEM OF LASER RETROREFLECTORS FOR THE RETURN TO THE MOON AND BEYOND.

M. Di Paolo Emilio[1], U.Denni[1], L. Rubino[1,2], L. Salvatori[1], M. Tibuzzi[1], L. Porcelli[1] and S. Dell'Agnello[1].
[1]INFN Laboratori Nazionali di Frascati, 00044 Frascati, Italy,
[2]Dipartimento di Matematica e Fisica, Università degli Studi "Roma Tre", Roma, Italy.

Diverse and specific payload design, prototyping and space testing activities were completed in the last five years by INFN-LNF, in particular for Moon-LIGHT-100/NGLR = Moon Laser In-strumentation for General relativity High accuracy test. This 100 mm single, large reflector is intended for direct lunar laser ranging from stations in USA, Italy (ASI-CGS) and France (Grasse). Its main applications are the Lunar Geophysical Network (LGN) and precision tests of General Relativity (GR) and new theories of fundamental relativistic gravity.

Since this time and for the very first returning mission to the Moon, the deployment of CCRs will not be assisted by astronauts, INFN-LNF has been designing, prototyping, manufacturing and space-qualifying a MoonLIGHT Pointing Actuator (MPAc). For the correct deployment of ML100 during the lunar day, the MPAc must be able to perform two continuous rotations. "Azi-muth": around the normal to the (horizontal) lander deck surface on which it is installed. "Eleva-tion": around an axis parallel to the lander deck. The MPAc axes will also be locked during launch, during the trans-lunar flight and lunar landing. The locked state is the default condition when the gimbals are not powered. The MPAc must work in UH-vacuum space conditions and in an wide operating temperature range during the lunar day.

MAPPING THE COMPOSITION OF THE MOON USING THERMAL INFRARED SPECTROSCOPY: CURRENT AND FUTURE OBSERVATIONS.

K. L. Donaldson Hanna[1,2], N. E. Bowles[2], B. L. Ehlmann[3], B. T. Greenhagen[4], P. O. Hayne[5], R. L. Klima[4], P. G. Lucey[6], D. P. Osterman[7], D. A. Paige[8], and C. M. Pieters[9], [1]University of Central Florida, Orlando, FL, USA (Kerri.DonaldsonHanna@ucf.edu), [2]University of Oxford, Oxford, UK, [3]California Institute of Technology, Pasadena, CA, USA, [4]Johns Hopkins Applied Physics Laboratory, Laurel, MD, USA, [5]University of Colorado, Boulder, CO, USA, [6]University of Hawaii, Honolulu, HI, USA, [7]Ball Aerospace, Boulder, CO, USA, [8]University of California Los Angeles, Los Angeles, CA, USA, [9]Brown University, Providence, RI, USA.

Introduction: Much of what we know today about the Moon's composition comes from orbital spacecraft mapping its upmost surface. Instruments used to probe the composition of the crust have included multispectral imaging systems (NASA's Clementine Ultraviolet/Visible Camera and the Lunar Reconnaissance Orbiter Wide Angle Camera), spectrometers (NASA's Lunar Prospector Gamma Ray and Neutron Spectrometers, ISRO's Chandrayaan-1 Moon Mineralogy Mapper, and JAXA's Kaguya Multiband Imager and Spectral Profiler), and radiometers (NASA's Lunar Reconnaissance Orbiter Diviner Lunar Radiometer). Particularly, the visible to near infrared (VNIR) and thermal infrared (TIR) remote sensing measurements have been used to identify and characterize the mineralogical diversity of the lunar crust by comparing observations with analog materials measured in the laboratory. Highlights from these observations include the identifications of: (1) regions of the primary anorthositic crust [e.g., 1-4], (2) a limited number of olivine-rich regions (possibly indicative of the mantle) [e.g., 5-6], (3) regions of silicic volcanism [e.g., 7-8], (4) a new lunar-rock type dominated by Mg-rich spinel [e.g., 9-10], and (5) the effects of space weathering on TIR measurements [e.g., 11].

With NASA's Moon to Mars exploration program, new observations of the lunar surface are expected, which should further enable our understanding of the composition. In this presentation we will discuss the current understanding of the Moon's composition based on thermal infrared observations from Diviner [e.g, 12-13], how Diviner TIR observations combined with VNIR spectral measurements place important constraints on the composition of the crust [e.g., 4,6], and what we will learn from thermal infrared observations of the Moon at the surface (Lunar Compact Infrared Imaging System) and from orbit at higher spatial resolutions (Lunar Trailblazer).

Current TIR Spacecraft Observations of the Moon: The Moon is one of the most well-studied Solar System airless bodies at thermal infrared wavelengths in large part due to a decade of observations from the Diviner Lunar Radiometer [e.g., 12-13]. Diviner is a nine band TIR radiometer launched onboard NASA's Lunar Reconnaissance Orbiter (LRO) in June 2009. Three narrow bands near 8 μm were specifically chosen to map the Christiansen feature (CF), an emissivity maximum in TIR spectra indicative of bulk mineralogy, to provide global (see **Figure 1**), and local maps of composition.

Upcoming TIR Spacecraft Observations of the Moon: The Lunar Compact Infrared Imaging System (L-CIRiS) is a multi-spectral imaging radiometer based on Ball Aerospace's Compact Infrared Radiometer in Space (CIRiS) cubesat [14]. In July 2019, L-CIRiS was selected by NASA to go to the lunar surface on board a Commercial Lunar Payload Services (CLPS) mission where it will map the compositional and thermophysical properties of the surface in a polar environment. Radiometric imaging will be accomplished in four infrared bands between

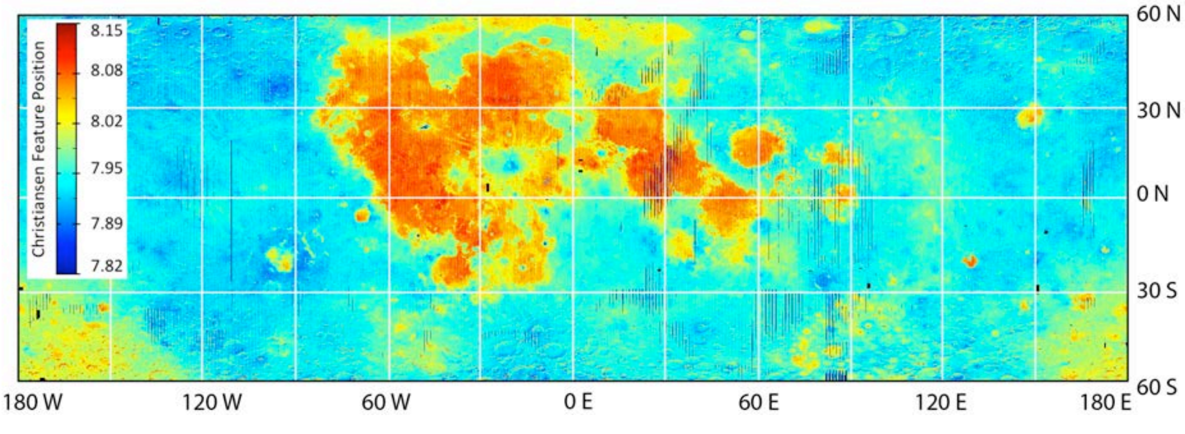

Figure 1. Diviner Christiansen feature (CF) map that has been corrected for soil maturity [11].

7 and 14 μm at a spatial resolution of < 1cm near the lander and ~40 cm at 100 m from the lander. L-CIRiS's main science objectives are to (1) determine the Moon's surface composition at small scales, (2) determine small-scale thermophysical properties of the Moon as well as indicators of rover trafficability, and (3) determine the Moon's volatile cold-trapping potential at small scales. New observations from L-CIRiS will also be critical for ground-truthing orbital observations as its in situ measurements will be compared to Diviner measurements of the landing site.

In June 2019, NASA selected the SIMPLEx mission Lunar Trailblazer for Phase A/B development, with a Preliminary Design Review in September 2020 on the path to flight [15]. Lunar Trailblazer's objectives are to (1) detect and map water on the lunar surface at key targets to determine its form (OH, H_2O, or ice), abundance, and distribution as a function of latitude, soil maturity, and lithology; (2) assess possible time-variation in lunar water on sun-lit surfaces; and (3) map the form, abundance, and distribution of water ice in the PSRs, finding any operationally useful deposits of lunar water and locations where it is exposed at the surface for sampling. In all cases, Lunar Trailblazer simultaneously (4) measures surface temperature to quantify the local gradients and search for small cold traps. Lunar Trailblazer includes the High-resolution Volatiles and Minerals Moon Mapper (HVM^3), an imaging VNIR spectrometer, and Lunar Thermal Mapper (LTM), a TIR imaging radiometer. LTM will radiometrically image the lunar surface using eleven infrared bands between 7 and 10 μm at a spatial resolution of < 35 m [16]. New observations from LTM would also be critical for linking higher spatial resolution orbital observations with L-CIRiS in situ observations of the surface and with orbital observations from Diviner.

References: [1] Pieters C. M et al. (2009), *LPS XL*, Abstract #2052. [2] Ohtake M. et al. (2009), *Nature, 461*, doi:10.1038/nature08317. [3] Yamamoto S. et al. (2012), *GRL, 39*, doi:10.1029/2012GL052098. [4] Donaldson Hanna K. L. et al. (2014), *JGR, 119*, doi:10.1002/2013JE004476. [5] Yamamoto S. et al. (2010), *Nat. Geosci., 3*(8), doi:10.1038/ngeo897. [6] Arnold J. A. et al. (2016), *JGR Planets, 121*, doi:10.1002/2015JE004874. [7] Glotch T. D. et al. (2010), *Science, 329*, doi:10.1126/science.1192148. [8] Glotch T. D. et al. (2011), *GRL, 38*, doi:10.1029/2011GL049548. [9] Pieters C. M. et al. (2011), *JGR, 116*, doi:10.1029/2010JE003727. [10] Pieters C. M. et al. (2014), *Am. Min., 99*, 1893-1910. [11] Lucey P. G. et al. (2017), Icarus, 283, doi:10.1016/j.icarus.2016.05.010. [12] Paige D. A. et al. (2010), *Space Sci. Rev., 150*, doi:10.1007/s11214-009-9529-2. [13] Greenhagen B. T. et al. (2010), *Science, 329*, doi:10.1126/science.1192196. [14] Osterman D. P. et al. (2019), *Proc. SPIE 11131*, doi:10.1117/12.2531404. [15] Ehlmann B. L. et al. (2020) *LPS L*, Abstract #1956. [16] Bowles et al. (2020) *LPS L*, Abstract #1380.

Improving In-situ Recognition of Planetary Minerals through Custom Database and Classification Software.

I. Drozdovskiy[1], F. Sauro[2], S.J. Payler[1, 3], P. Jahoda[4], M. Franke[4], P. Lennert[4], P. Vodnik[4], G. Ligeza[4], L. Turchi[1], L. Bessone[1] [1]Directorate of Human and Robotics Exploration, European Astronaut Centre (EAC) - European Space Agency (Linder Höhe, D-51147 Cologne, Germany; igor.drozdovskiy@esa.int), [2]Geological and Environmental Sciences, Italian Institute of Speleology - Bologna University, [3]Agenzia Spaziale Italiana, Rome, Italy, [4]ESA-EAC, CAVES & PANGAEA intern

Introduction: The ESA-PANGAEA Mineralogical Toolkit aims to enhance the recognition of planetary minerals through creating a custom structured database containing information on all known minerals present on the Moon, Mars and other planetary bodies, and to use novel Machine Learning methods of data analysis to enable in-situ spectroscopic identification of these minerals. Developed and tested together, this mineral library & the minerals recognition software is conceived as a real-time decision support tool for future human and robotic planetary surface exploration missions. The Mineralogical Toolkit is composed of the PANGAEA Mineralogical Database, and Machine Learning (ML) software for recognition of minerals from multispectral data.

PANGAEA Mineralogical Database: The Mineralogical database [1] can be viewed as two distinct products: a catalogue of petrographic information and an analytical library. The catalogue consists of petrographic information on all currently known minerals identified on Moon, Mars, and found primarily, or exclusively, within meteorites. The catalogue is envisioned to provide essential analytical in-field information for each mineral to assist in rapid identification and understanding of significance in real time geological exploration. Each mineral entry includes: IMA recognized Name, Chemical Formula, Mineral Group, surface abundance on planetary bodies, geological significance in context of planetary exploration (occurrence, environmental conditions, marker for important processes, etc.), number of collected VNIR and Raman spectra and their spectral discoverability and the possible spectral features. In addition, supplementary characteristics for each mineral that may help with its identification are included, such as chemical abundances calculated from the known empirical chemical formula, as well as basic physical properties (hardness, specific gravity, crystal system, etc.). The database was compiled through systematic literature research, followed by the careful cross-validation ("out-of-sample" testing) of all mineral characteristic information (including flagging of doubtful or erroneous data).

The second major contribution provided by the PANGAEA Mineralogical Database is a customized library of analytical data from all known planetary terrestrial analogue minerals. This covers four analytical methods: reflective Visual-to-Near- & Shortwave-Infrared (VNIR), Raman vibrational (molecular) spectroscopy, Laser-Induced-Breakdown (LIBS), and X-Rays Fluorescence (XRF) atomic spectroscopy. This library also includes a set of standard spectra, which is used for evaluating the detectability of minerals with different analytical methods.

Part of the archive consists of spectra collected from available open access on-line catalogues, such as experimental Raman (RRUFF) and VNIR (USGS, Relab, ECOSTRESS), as well as from our own and our collaborators bespoke spectroscopic measurements (VNIR, Raman, LIBS & XRF) of planetary analogue minerals taken from different collections, and synthetic spectral libraries, such as LIBS NIST; see [2] and references therein. Only the high-quality spectra of confirmed mineral samples are included as determined by the quality flag in the original database, or by our statistical evaluation of the within-class spectra. We removed outliers from all available single-method spectra of each mineral by finding the average spectrum for each class and subsequently removing spectra that have cosine distance from the average spectrum higher than 0.5 [2]. Outlier removal is performed to ensure that the set is not skewed by extremely divergent spectra due to the random instrumental artefacts or misclassification of the sample. The current census of the minerals with available molecular spectra is shown on Fig. 1 (below). This multispectral library is designed to be used for the recognition of planetary materials, and acts as a training dataset for our mineral recognition software.

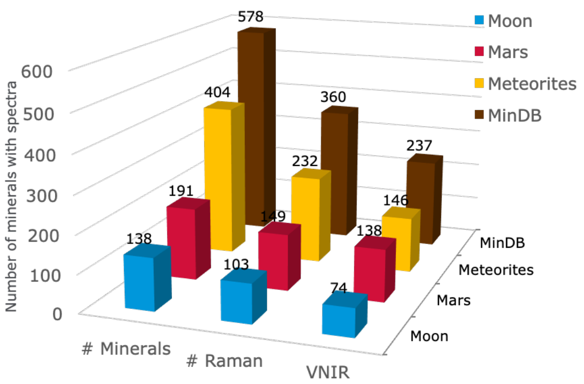

Figure 1: The current census of the minerals with available Raman or VNIR spectra is shown below.

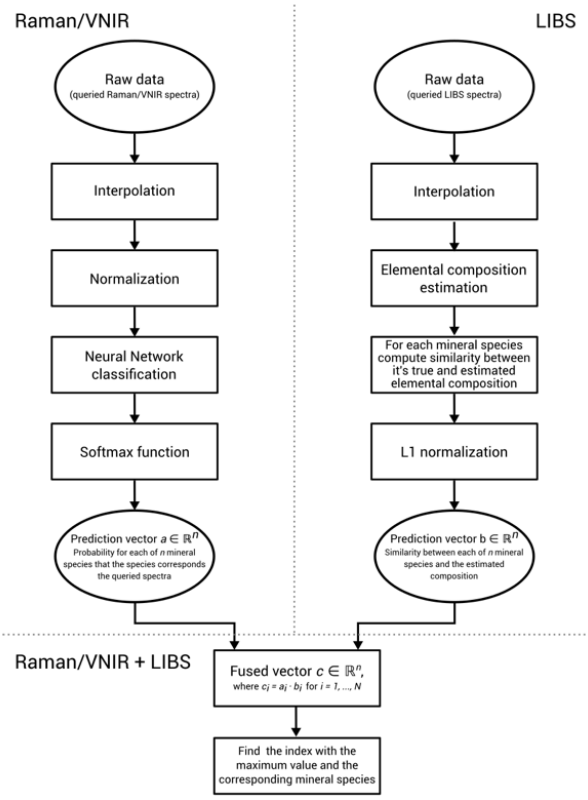

Figure 2: A simplified flow diagram, depicting our method for recognizing minerals from combined Raman/VNIR and LIBS spectra.

Machine Learning (ML) software for recognition of minerals from multispectral data: To utilize the PANGAEA Mineralogical Database for identifying minerals in the field from the output of analytical tools, we also developed identification methods that combine types of material characteristics, mineral structure (obtained with VNIR and Raman spectra) and its chemical composition (derived from XRF and LIBS spectra). To achieve this, we chose to use a ML-based approach. This was for several reasons: ML is fast and accurate when developed properly, can handle multimethod datasets, and the accuracy can be progressively improved by adding new training data to the classification models without losing the recognition speed.

After evaluating various Machine Learning approaches used to identify mineral species from single analytical methods (Raman, VNIR or LIBS), we have developed a flexible and modular algorithm that can classify minerals either from standalone spectroscopic methods, or using a combination thereof. The flow diagram detailing this methodology is shown in Figure 2.

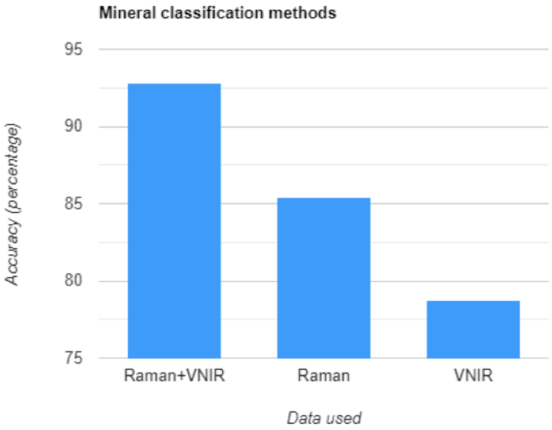

Figure 3: Better mineral predictions rates from combined Raman and VNIR spectra than from single-method spectroscopy.

Our new approach was then evaluated using our own internal archive of analytical data, as well as in some cases, on publically available spectroscopic datasets. Our cross-validation tests show that multi-method spectroscopy paired with ML paves the way towards rapid and accurate characterization of rocks and minerals [2] (see Figure 3).

PANGAEA Mineralogical Tookit as an Analytical Toolset for Moon Surface Exploration: The PANGAEA Mineralogical Toolkit is envisioned as a part of the PANGAEA Electronic Fieldbook Tool Suite (EFB) [3]. The EFB is a deployable system that enhanced scientific outcome of field mission operations, enabling scientific documentation of field traverses and geological sampling. The EFB enables situational interaction with science and mission support teams through exchange of contextual data. The EFB can interface with handheld instrumentation intended for planetary exploration, feeding the Mineralogical Toolkit with mineral signatures and therefore allowing an efficient categorization of samples. Combining within the EFB Tool Suite a set of handheld analytical tools and the instrument agnostic nature of the PANGAEA Mineralogical Toolkit will enable fast and reliable in-situ recognition of rocks and minerals, thus becoming a crucial decision support tool for future human and robotic planetary surface exploration missions.

References: [1] Drozdovskiy I. et al. (2020, in prep); [2] Jahoda P. and Drozdovskiy I. (2020, in prep) [3] Turchi L. *ELS VIII,* Abstract #.

The FLY-Spec instrument working on the Lunar surface.

S. Ferrari[1], P. Zuppella[2], V. Da Deppo[2], M. Massironi[1,3], P. Nicolosi[4], S. Sadaf Zehra[4], C. Carli[5], F. Nestola[3], C. Meyzen[3], J. Nava[3], P. Chioetto[2], A. Slemer[2], [1] University of Padova - Centro di Ateneo di Studi e Attività Spaziali “G. Colombo” (CISAS), Via Venezia 15, 35131 Padova, Italy (sabrina.ferrari@unipd.it), [2] National Research Council (CNR) - Institute for photonics and nanotechnologies (IFN), Via Trasea 7, 35131 Padova, Italy, [3] University of Padova - Department of Geosciences, Via Gradenigo 6, 35131 Padova, Italy, [4] University of Padova - Department of Information Engineering (DEI), Via Gradenigo 6, 35131 Padova, Italy, [5] National Institute for Astrophysics (INAF) - Institute for space planetology and astrophysics (IAPS), Vi Fosso del Cavaliere 100, 00133 Roma, Italy.

Introduction: Near-term objectives of the space exploration envision the robotic and human survey of the inner Solar System, in preparation of long-term explorations of worlds that in the future could support a continuous human presence such as Mars. The Moon and the cislunar space, in particular, are currently designated as training sites to accomplish a range of science and exploration objectives with human crews. Within this framework, one of the main capabilities needed for surface robotic and human missions is the sampling technique in harsh environments.

Lunar sampling shall satisfy both scientific targets such as improving the understanding of origin, evolution and composition of Moon, as well as operational needs, which inter alia indicate how to sustain human and robotic space explorations using local resources. Lunar priority samples are then ancient crustal rocks, young effusive materials and water-bearing clastic to metamorphic materials and meteoritic remnants. In particular, pyroclastic glassy spherules trapping gas phases, hydrated silicates, and steady low-temperature regoliths are considered the main potential lunar volatile reservoirs [1]. Still, priority samples include lithologies that have been identified by orbital missions but remain unsampled, like mantle rocks of the Moon’s far side [2].

Sampling accomplished by human-robotic synergies in harsh environments aims at a rapid but unambiguous identification of minerals, rocks and soils, as well as of a suitable storage of in situ chemical and mineralogical data. Those requirements can be fully satisfied with a very compact instrument that combines and contextualizes chemical and mineralogical analyses.

FLY-Spec concept: The UV-VIS-NIR reFLectometrY and laser-induced breakdown Spectroscopy (FLY-Spec) instrument consists of a camera, a laser induced breakdown spectroscopy (LIBS) unit and a NIR imaging reflectometer. This payload aims to guarantee a multi-scale analysis of the sampling area, which has not been envisaged yet by combined instruments with similar tasks. Each routine implies: (i) a panchromatic acquisition of the local context, which assists the measurement site selection and specific targets identification, (ii) a first hyperspectral image of the targeted sample that provides textural and mineralogical information, (iii) a grid of LIBS shootings co-registered to the hyperspectral image that provides a chemical analysis pattern and (iv) a second hyperspectral acquisition over the grid. In this way a good quite comprehensive sampling of the surface will be accomplished.

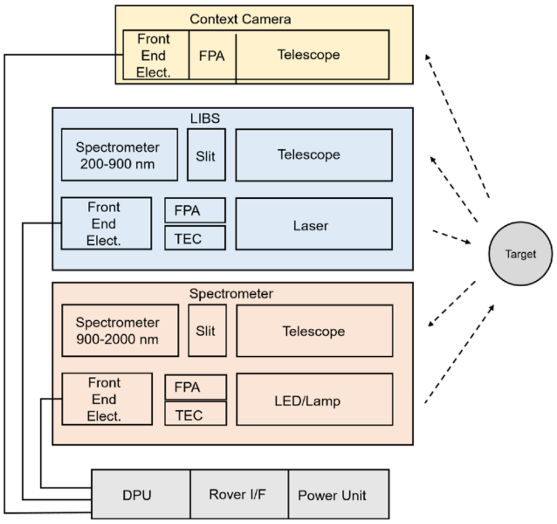

Figure 1: The functional block diagram of FLY-Spec instrument.

The CPU operates the two main systems, LIBS and reflectometer, both independently and synergistically in real time.

LIBS spectroscopy uses relatively powerful laser pulses focused on a target to generate plasma (laser produced plasma LPP) that emits radiation in the form of discrete lines. The radiation is collected by a VIS-NIR spectrometer. Resulting lines are characteristic of the ions and molecular species, whereas the continuous spectrum corresponds to recombination and bremsstrahlung emission. The analysis of the LPP spectra allows the compositional classification of the target materials. LIBS is based on the interaction of relatively powerful laser pulses (typically 10-100 mJ in a few ns) focused on target materials. The laser power density achieved on the target can be in the range of GW/cm^2, enough to generate a plasma (laser produced plasma-LPP). The LPP physical parameters, high temperature (up to several 100’s of eV) and density (up to the critical value for laser light), are such that the plasma is highly ionized and expands rapidly because of the high pressure. The LPP emits radiation in the form of discrete lines, characteristic of the ion and molecular species, and with continuous spectra corresponding to recombination and bremsstrahlung emission. This technique has been quite recently applied in minerals and rocks identification in space exploration [3].

NIR Reflectometry is based on the spectral analysis of the light specularly reflected and diffused by materials in order to identify the specific spectral features due to the elements and chemical components of materials [4]. Hyperspectral imaging consists in the spectral observation of a sample area [5]. This can be achieved by projecting the entrance slit of a spectrometer on a surface so that each point of the slit corresponds to different points on a linear surface section, then the area can be scanned by continuously shifting the slit projection. In this way for each point of the surface the reflectance spectrum is recorded, producing a 3D dataset with local spectral characteristics of the surface.

NIR imaging dataset will be combined with punctual, high-scale LIBS information to obtain a comprehensive mineralogical and elemental understanding. The FLY-Spec control and processing unit, indeed, is thought to be implemented with a spectral signature archive and matching processing system. The FLY-Spec suite will therefore be able to recognize and classify minerals giving the correspondent reliability degree and producing a prioritization tree in function of the scientific objectives of the mission.

FLY-Spec in the lunar surface: FLY-Spec is thought to achieve on the Lunar surface the following results: (i) quickly distinguish olivines from pyroxenes, which display the same primary elements (Si, O, Mg, Fe etc.) but different absorptions in the NIR; (ii) detect sialic solid solutions such as plagioclases, which are almost featureless in NIR range, but whose solid solution constituents (Ca and Na) can be easily detected in LIBS spectra; (iii) distinguish mafic solid solutions combining elemental detection with the exact position of the transition-element absorption bands; (iv) distinguish and classify different chondrites, iron and stony-iron meteorites; (v) distinguish CAI and hydrated carbonaceous material on meteorites; (vi) distinguish the presence of volatile either on regolith or trapped in pyroclastic glasses; (vii) evaluate relative phase abundances of the outcrop/soil.

References: [1] McCubbin M. et al. (2015) *Am. Mineral., 100/8–9*, 1668–1707. [2] Pieters C. M. et al. (2001) *J. Geophys. Res. Planets, 106/E11*, 28001–28022. [3] Blake D. F. et al. (2013) *Science, 341/6153*, 1239505. [4] Siesler H. W. (2002) Near-infrared spectroscopy: principles, instruments, applications. Wiley-VCH. [5] Kruse F. A. (1996) *Int. J. Remote Sens., 17/9*, 1623–1632.

KAGUYA TERRAIN CAMERA: UPDATED SPICE KERNELS AND NEW PROCESSING CAPABILITIES.

L. Gaddis[1], L. Weller[1], L. Adoram-Kerchner[1], T.M. Hare[1], B. Archinal[1], S. Goossens[2,3], E. Mazarico[3], E. Speyerer[4], J. Haruyama[5], T. Iwata[5], and N. Namiki[6]. [1]USGS Astrogeology Science Center, Flagstaff, AZ 86001, USA; [2]Univ. Maryland, Baltimore County, Baltimore, MD, USA; [3]NASA Goddard Space Flight Center, Greenbelt, MD, USA; [4]Arizona State University, Tempe, AZ, USA; [5]JAXA, Sagamihara, Japan; [6]National Astronomical Observatory of Japan, Tokyo, Japan (lgaddis@usgs.gov).

Introduction: The SELenological and ENgineering Explorer (SELENE) "Kaguya" spacecraft mission to the Moon from the Japan Aerospace Exploration Agency (JAXA) returned several types of data, including high-resolution monochrome and color images and laser altimeter data. Launched in September 2007, the Kaguya primary mission (PM) was completed at the end of October 2008 and the extended mission (XM) phase started at the beginning of November 2008. During XM and until the end of the mission in June 2009, Kaguya was in a lower orbit at 50 km average altitude compared to 100 km altitude during PM. Although data collected during Kaguya XM have an increased spatial resolution, the orbit errors during this phase are much larger, up to several km [1] due to larger gravitational perturbations on the spacecraft, a reduction in the amount of tracking after the end of the nominal mission, and spacecraft attitude control problems associated with loss of the reaction wheels. The resulting degraded orbit quality during XM severely limits the usability and scientific value of these high-quality data (***Figure 1***). Here we report on our work to improve the orbital data for the Kaguya mission, update SPICE kernels, develop tools for processing and working with the Terrain Camera (TC) data in the USGS Integrated Software for Imagers and Spectrometers (ISIS3) for building improved mosaics, and archive the resulting products and tools.

Improved XM Orbits: We recently published results showing a significant improvement for the Kaguya XM orbits [2]. These orbits have been redetermined for the main satellite using 1) improved gravity field models of the Moon derived from Gravity Recovery and Interior Laboratory (GRAIL) mission data [3] and 2) adjustments of the spacecraft orbit such that the LALT altimetry tracks fit a precise topographic basemap based on the Lunar Reconnaissance Orbiter's (LRO) Lunar Orbiter Laser Altimeter (LOLA) data [4]. Through analysis of orbit overlaps, we developed geodetically accurate orbits tied to the precise LOLA/LRO frame; the inclusion of altimetry improves the orbit precision from several kilometers to several tens of meters. When altimetry data are not available, the combination of GRAIL gravity and radio tracking results in an orbit precision of several hundred meters for the low-altitude phase of the extended mission. Our greatly improved orbits result in better geolocation of the Kaguya extended mission data set. These orbit data, as updated trajectory data (SPICE SPK kernels), along with adjusted LALT altimetric and Kaguya LMAG magnetic data are served at NASA GSFC (https://pgda.gsfc.nasa.gov/); the updated SPKs are also available at the JAXA DARTS archive (https://darts.isas.jaxa.jp/planet/pdap/selene/).

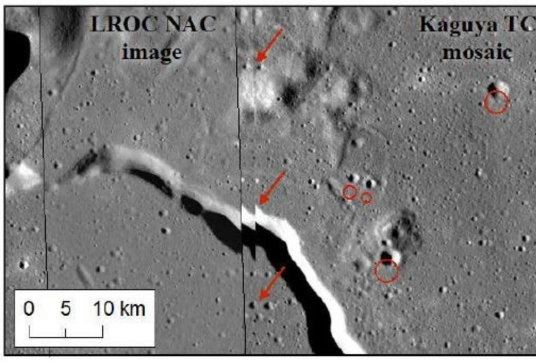

Figure 1. A LROC NAC image (M1127106676R, 1.3 m/pixel) of the Apollo 15 landing site area overlain on a TC mosaic with original degraded quality. We have significantly improved co-registration of TC images, and their registration to other lunar datasets such as LRO/LROC WAC and NAC. Red arrows and circles show duplication of features.

ISIS3 Software for TC: To support the validation of these improved orbits, we used ISIS3 to develop a test mosaic from Kaguya Terrain Camera (TC) data of the Apollo 15 landing site area near Hadley Rille. Two ISIS3 programs were developed: 1) an ingestion program (*kaguyatc2isis*) that reads a TC file header and imports data into a single-band ISIS3 cube file and label, and 2) a linescan camera model for the two TC instruments (used in *spiceinit*). Geometric camera models describe the mathematical relationship between the coordinates of a 3D scene and its projection onto the image plane of a camera; for orbital imaging systems such models must also account for spacecraft coordinates and movements. The goal is to be able to treat data from the two TC cameras as ISIS3 cube files so that they can be geometrically rectified and map-projected accurately onto the lunar surface. Both "singlescopic" (L2B0, s) and stereo (L2B0, w) TC data are supported. The camera model includes camera parameters such as focal length, pixel pitch, boresight coordinate, affine coefficients for focal plane mapping, and optical distortion coefficients. These programs are publicly released with ISIS3.

Test Mosaic: We focus in this project on the Apollo 15-Hadley Rille area for several reasons: 1) The region has been a "standard" test site for many lunar mapping products, with several other publicly available mosaics and digital terrain models (DTMs) for comparison of our products (see https://astrogeology.usgs.gov/maps/moon-lro-dtms-and-mosaics); 2) The availability of high-resolution mapping of the central portion of this area done under the Lunar Mapping and Modeling Project [e.g., 5, 6; these data are currently available at the MoonTrek Web site (https://trek.nasa.gov/moon/), and will be archived with the PDS], including a ~20 x 20 km, 0.50 m/pixel image mosaic, and a 1.5 m/pixel DTM [7]. 3) Most types of lunar terrain are covered in this area, including flat plains to high mountains; 4) Surface photographs from the Apollo 15 mission are available for comparison with any surface image or 3D products; and 5) This site contains the largest (105 x 65 cm) of the five Lunar Laser Ranging RetroReflector (LRRR) arrays. This array serves as the primary target for laser ranging to the Moon, with a 3D position measurable (relative to the Earth and the other arrays) at the cm level and known absolutely to the meter level so that it can be used for absolute coordinate system comparisons.

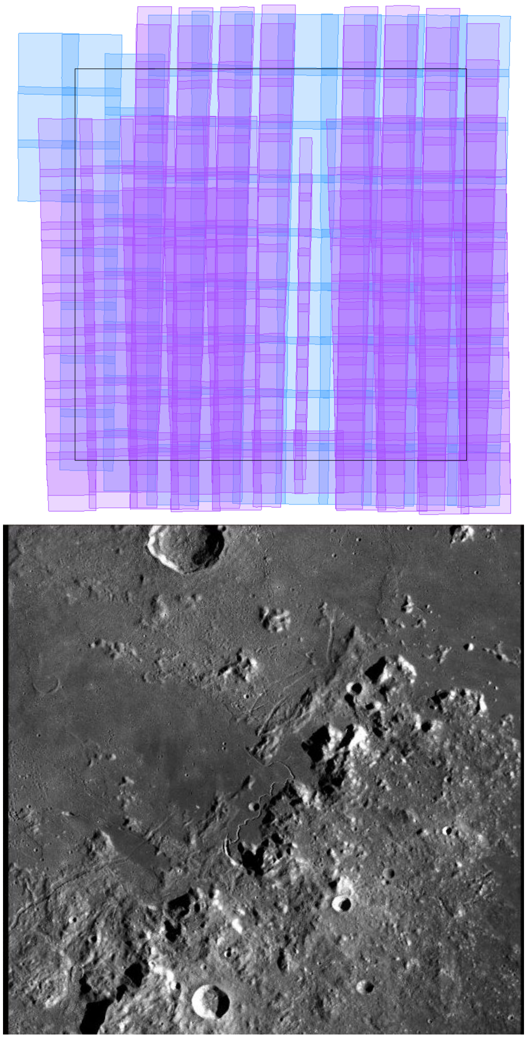

Figure 2. (top) TC morning frame coverage, 10°x10° centered on the Apollo 15 site (~300 km across). Purple boxes are XM stereo frames, blue boxes are PM monoscopic frames. (bottom) Draft uncontrolled TC mosaic using morning, monoscopic data from the PM. This will serve as a base mapping layer as we add XM data.

To develop a 10°x10° TC mosaic for the Apollo 15 site, we first assessed the coverage of the PM and XM data from the L2B0 collection, both for morning and evening (left- and right-look) illuminations and stereo and monoscopic viewing (***Figure 2, top***). We determined that good coverage of the Ap15 site is afforded from the morning illumination stereo XM data, but completion of a full mosaic requires use of both XM and PM stereo and monoscopic coverage (***Figure 2, bottom***). Spatial resolution of the input TC images vary from 4.5 to ~11.2 m/pixel.

We are currently completing three regional TC mosaics: 1) an uncontrolled mosaic, using the *a priori* SPICE data (***Figure 3a)***; 2) an uncontrolled mosaic, using our updated SPK (orbit) data in ISIS3 (***Figure 3b***); and 3) a controlled mosaic, where we derive corrections to the SPK and CK (pointing) data and equalize the frame brightness in ISIS3. Our capability to construct the controlled mosaic is greatly improved by using the updated Kaguya orbits. In total, we expect to control about 381 images (268 stereo XM, 91 mono PM, and about 16 mono XM), with ~300 of those visible on top in the controlled mosaic. The third, controlled mosaic will be archived with the PDS as a final product.

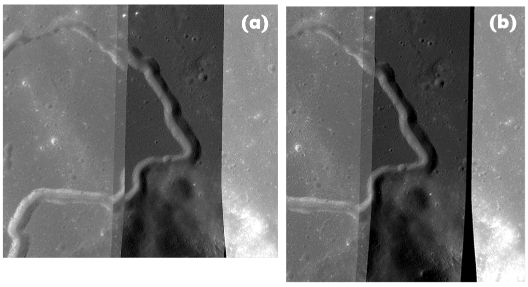

Figure 3. Kaguya TC views of the Apollo 15 landing site near Hadley Rille (1.5 km across, 400 m deep), using extended mission data (~5 m/pixel). (a) Uncontrolled, unequalized mosaic before updating the orbits. (b) Uncontrolled, unequalized mosaic after updating the orbits.

References: [1] Goossens et al. (2009) *Proceedings of the 19th Workshop on JAXA Astrodynamics and Flight Mechanics*, 247–256, Inst. Space Astronautical Sci., JAXA. [2] Goossens et al., *Icarus*, 226, 113454, doi:10.1016/j.icarus.2019.113454. [3] Zuber et al. (2012) *Science*, doi:10.1126/science.1231507. [4] Smith et al. (2017) *Icarus*, doi:10.1016/j.icarus.2016.06.006 [5] Noble et al. (2009) *LEAG Annual Meeting*, abs. #2014. [6] Rosiek et al. (2012) *LPS XLIII*, abs. #2343. [7] Archinal et al. (2011) *LPS XLII*, abs. #2316.

CRATER SIZE-FREQUENCY DISTRIBUTIONS OF NORTH RAY AND SOUTH RAY CRATERS NEAR THE APOLLO 16 LANDING SITE.

T. Gebbing[1], H. Hiesinger[1], W. Iqbal[1], and C. H. van der Bogert[1], [1]Institut für Planetologie, Westfälische Wilhelms-Universität, Wilhelm-Klemm-Str. 10, 48149, Münster, Germany, (thorsten.gebbing@uni-muenster.de).

Introduction: Exposure ages of samples collected at the North Ray crater by the Apollo 16 astronauts provide one of the calibration points for the lunar cratering chronology [e.g. 1-3]. The data from the Lunar Reconnaissance Orbiter Camera (LROC) is being used to revise and improve such calibration points for the Apollo landing sites, because the lunar chronology is used to date unsampled surface across the Moon and is modified for use on other terrestrial bodes [e.g. 4-6]. Here, we report new crater size-frequency distributions (CSFDs), $N(1)$ values, and absolute model ages (AMAs) for the two young craters, North Ray and South Ray, and compare the results with previous work.

North Ray and South Ray Craters: North Ray crater (~950 m in diameter) is located 4.2 km north of the Apollo 16 landing site. Samples 67015 and 67016 from near the crater have exposure ages of ~50 to 51.1 Ma [7,8], which were used to calibrate the lunar cratering chronology [1,9].

South Ray crater (~700m in diameter) is located 6 km southwest of the landing site. With sample ages of ~ 2 Ma [10], it is one of the youngest sampled craters on the Moon. A calibration point has not been made for South Ray crater.

Methods: LRO Narrow Angle Camera (NAC) images were processed using the Integrated Software for Imagers and Spectrometers (ISIS) [11] and imported into ArcGIS. The count areas and measurements were done with CraterTools [12] in ArcMap. We defined the count areas around the craters using albedo and morphological contrast, Clementine spectral data, and a NAC digital terrain model (DTM). We measured the crater size-frequency distributions (CSFDs) around the two craters (*Fig. 1*, red and green areas*)*. Noticeable secondary craters were excluded, and randomness analysis [13] was used to identify and exclude additional crater clustering. The CSFDs were imported into Craterstats 2.0 and plotted in cumulative and relative forms [14,15] using the production function and chronology of [9] to derive absolute model ages (AMAs) (*Fig. 2*).

Results: The merged areas around North Ray crater (*Fig. 1a*, red areas 1-4) give an average $N(1)$ value of 4.26×10^{-5} km^{-2}, and the area for South Ray (*Fig. 1b*, green area) yields an $N(1) = 8.95\times10^{-7}$ km^{-2}. Applying the production function and chronology function of [9], our newly determined ages are 50.8 ± 2.5 Ma and 1.07 ± 0.26 Ma, respectively.

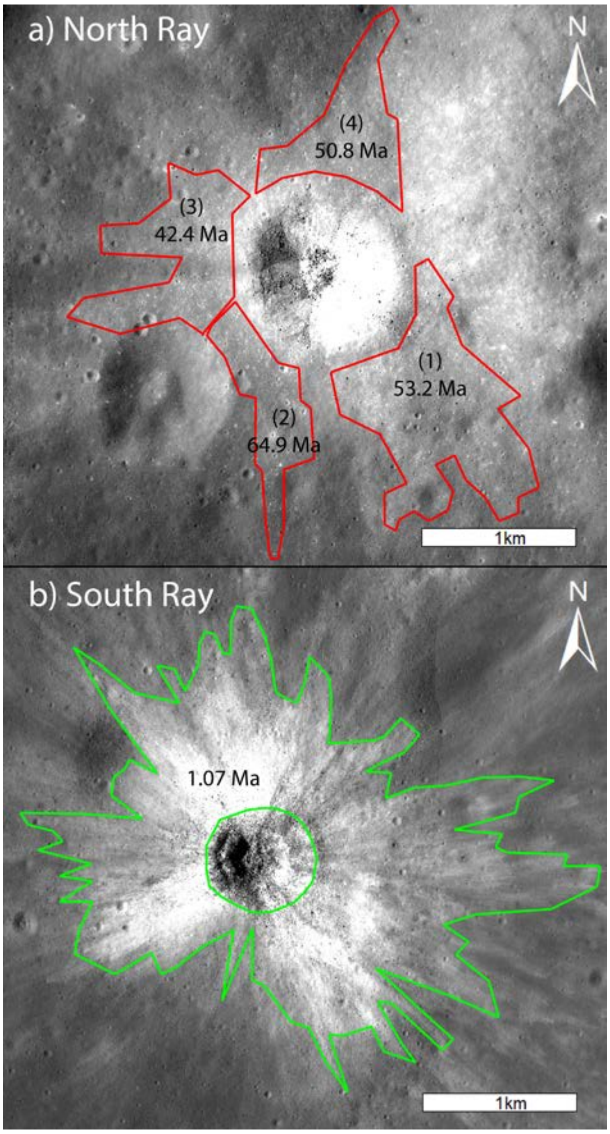

Figure 1*. Count areas around the North Ray (a) and South Ray (b) craters near the Apollo 16 landing site. (a) The red boundaries mark the four new count areas for North Ray crater and show the newly determined AMAs (black numbers). (b) The green boundary marks the new counting area on the rays of South Ray crater. The results of the North Ray crater counts on NAC images are similar and are consistent with previous results from [1,3,4]. The AMA of South Ray is younger than previous results [16,17].*

Table 1. *N(1)s and AMAs of North Ray and South Ray craters near the Apollo 16 landing site. The seventh line represents the combined four areas around North Ray crater.*

Unit	***N(1) (km^{-2})***	***AMA (Ma)***
North Ray		
1	4.46×10^{-5}	53.2±4.2
2	5.44×10^{-5}	64.9±7.2
3	3.55×10^{-5}	42.4±4.6
4	4.04×10^{-5}	48.2±5.2
1-4 merged	4.26×10^{-5}	*50.8±2.5*
South Ray	8.95×10^{-7}	*1.07±0.26*

Discussion: Previously determined $N(1)$ values for North Ray crater include: $N(1) = 6.01\times10^{-5}$ km^{-2} [4], 4.4×10^{-5} km^{-2} [1], as well as 3.90×10^{-5} km^{-2} and 3.84×10^{-5} km^{-2} [3]. These values correspond to ages of 50.0 ± 1.4 Ma [1], 50.3 ± 0.8 Ma [16], and 45.8 ± 3.7 and 46.5 ± 3.7 Ma [3], respectively. Previous work also yielded ages for South Ray crater of 2.04 ± 0.08 Ma [16] or 2.00 ± 0.2 Ma [16]. The results (*Table 1*) for the $N(1)$ and AMA values are within the error of [1,3,16] for North Ray crater.

Thus, our values for South Ray crater give younger AMAs compared to [16,17]. This could be due to a slightly different count area, differences in the illumination angles of the images used, or because of slight differences in the measurement of the diameters of the few craters available around South Ray.

Outlook: We are in the process of correlating the collected CSFD data with Apollo 16 sample ages related to the craters. This work is part of our ongoing reinvestigation of the Apollo 16 landing site [18].

References: [1] Neukum (1983) *Habil. thesis, U. of Munich*. [2] Stöffler et al. (2006) *Reviews in Mineral. & Geochem. 60*, 519-596. [3] Hiesinger et al. (2012) *JGR 11*, E00H10. [4] Robbins (2014) *Earth and Planet. Sci. Lett. 403*, 188-198. [5] Iqbal et al. (2019) *Icarus 333*, 528-547. [6] Hiesinger et al. (2020) *LPSC 51*, #2045. [7] Marvin et al. (1973) *LPSC 4*, 2037-2048. [8] Turner and Cadogene (1975) *LPSC 6*, 1509-1538. [9] Neukum et al. (2001) *Space Sci. Reviews 96*, 55-86. [10] Eugster (1999) *Meteoritics & Planetary Science 34*, 385-391. [11] Anderson et al. (2004) *LPSC 35*, #2039. [12] Kneissl et al. (2011). *PSS 59*, 1243-1254. [13] Michael et al. (2012) *Icarus 218*, 169-177. [14] Michael et al. (2016) *Icarus 277*, 279-285. [15] Michael et al. (2010) *EPSL 294*, 223-229. [16] Moore et al. (1980) *Moon and the Planets 23*, 231-252. [17] Stöffler and Ryder (2001) *Space Science Reviews 96*, 9-54. [18] Gebbing et al. (2019) *LPSC 50*, #2337.

Figure 2. *CSFD measurements of our count area(s) representative of North Ray (red) and South Ray (green) craters, counted on LROC NAC data shown in a cumulative plot and fit with absolute model ages. Shown above are the randomness analyses of the NAC count areas and, below, the relative crater frequency plot.*

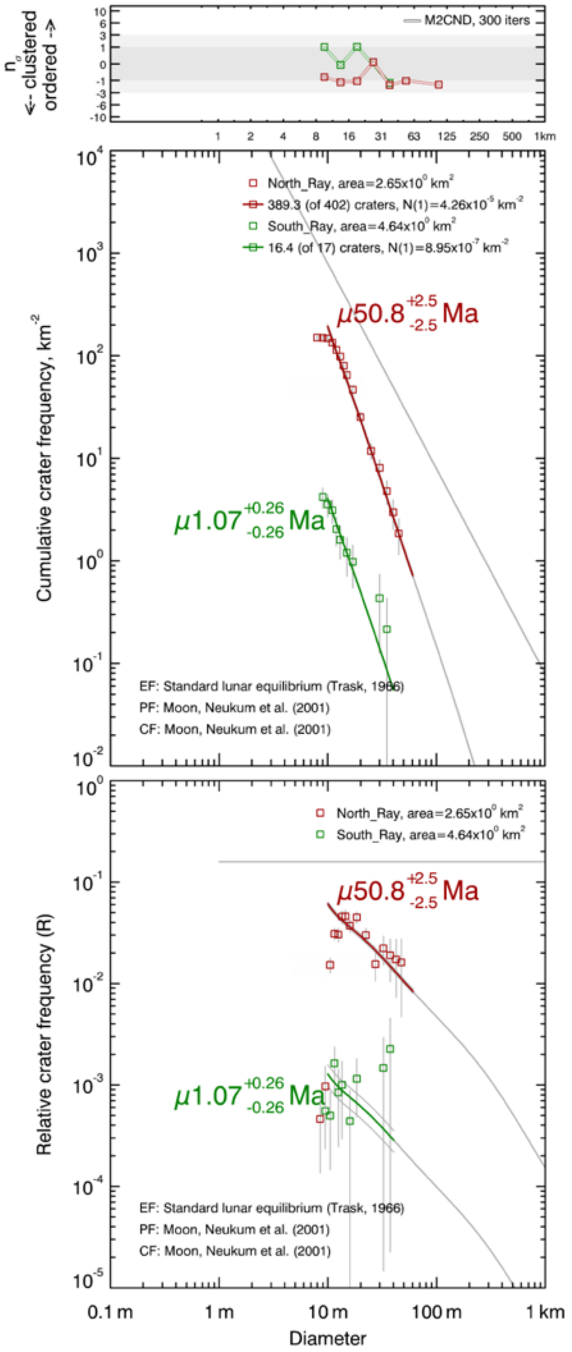

LUNAR EXOSPHERIC HELIUM THERMAL ACCOMMODATION AND OUTGASSING RATE CONSTRAINED FROM LRO-LAMP OBSERVATIONS OF THE HEI 58.4 NM EMISSION LINE.

C. Grava[1*], D. M. Hurley[2], P. D. Feldman[3], K. D. Retherford[1], W. R. Pryor[4], T. K. Greathouse[1], G. R. Gladstone[1], K. E. Mandt[2]. [1]Southwest Research Institute, San Antonio, TX, USA, [2]John Hopkins University, Applied Physics Laboratory, Laurel, MD, USA, [3]John Hopkins University, Department of Physics and Astronomy, Baltimore, MD, USA, [4]Central Arizona College, Coolidge, AZ, USA. [*]email: cesare.grava@swri.org

Introduction: Helium was one of the first species discovered in the lunar exosphere, detected by the LACE surface mass spectrometer deployed during the Apollo 17 mission [1]. With a density of the order of 10^5 atoms cm^{-3}, this noble gas was found to be among the most abundant species of the lunar surface-bound exosphere. Since then, helium has been observed remotely [2-6] by the EUV imaging spectrograph LAMP [7] on board the Lunar Reconnaissance Orbiter (LRO) and in situ [8] by the Neutral Mass Spectrometer on board LADEE. Soon after its discovery, it was found that its density correlates with the geomagnetic index Kp, a proxy for solar wind flux. This correlation suggested that neutralization of solar wind alpha particles (He^{++}) impacting the lunar surface are the main source for lunar exospheric helium [9]. However, there is a non-negligible amount due to outgassing from the interior of the Moon, as ^4He is the product of radioactive decay of of ^{232}Th and ^{238}U within the lunar crust. Estimates of the fraction of this outgassing component compared to the solar wind influx vary from 15% [8] to ~40% [5-6].

Another source of debate concerns the thermalization of helium with the lunar surface. We express this with the accommodation coefficient $\alpha = (E_o-E_i)/(k_BT-E_i)$, where E_i is the energy of the impacting helium atom, E_o is the energy of the atom leaving the surface, and T is the surface temperature. A value of α of 1.00 implies that the atoms are fully thermalized with the lunar surface temperature. Therefore, hop length and ejection velocity will be maximal, and exospheric density minimal, at the subsolar point. The debate concerns whether the helium is fully accommodated to the lunar surface ($\alpha = 1.00$), due to the high porosity of the regolith [10], or not ($\alpha < 1.00$). In the latter case helium atoms would have a "memory" of their energy prior to collision with the surface [11]. An intermediate hypothesis is that the accommodation coefficient varies with local time, e.g., with α=1.00 on the dayside and α=0.75 on the nightside [12].

Observations: To address these outstanding questions and to have a better understanding of the temporal and spatial evolution of the lunar exosphere, LAMP was used to perform a series of observations of the HeI emission line of helium at 58.4 nm from 2013 to 2016, taking advantage of dedicated off-nadir maneuvers by LRO. LAMP observed the HeI line (due to resonant scattering) when He atoms were illuminated by sunlight and the instrument's field of view pointed at the nightside lunar surface, to minimize the background (Figure 1).

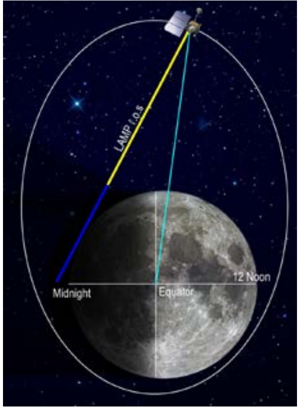

Figure 1 Geometry of observations. LRO was pitched off nadir while LAMP line of sight (l.o.s.) was pointing at the lunar dark surface. Yellow indicates the illuminated portion of the l.o.s., where helium atoms resonantly scatter sunlight.

Method: LAMP brightness is converted into column density using g-factors from the Solar Dynamics Observatory's EVE (EUV Variability Experiment) solar irradiance at 58.4 nm [13]. LAMP column densities are then compared to those predicted by models of exospheric helium with different values of α [6].

Results: We find that the model with an accommodation coefficient of 1.00 best reproduces LAMP column densities (Figure 2), implying that helium atoms are fully thermalized with the lunar surface.

Using the model with α=1.00, we derive a helium source rate from the LAMP data and compare it with the solar wind alpha particles flux measured in situ by the electrostatic analyzer on board the ARTEMIS twin spacecraft [14]. The scatter plot (Figure 3) shows a linear relationship, but not 1:1. A linear least-square fit provides a slope of (0.64±0.02) % and an intercept of $(1.44\pm0.13)\cdot10^6$ cm^{-2} s^{-1}. The value (1.0-slope) is the fraction of helium that is not detected by LAMP, either because the solar wind alpha particles are backscattered as ions, implanted deep into the regolith, or released as energetic neutral atoms. The intercept is the amount of helium that is outgassing from the interior of the Moon. This rate amounts to ~100 ton/year, or 18% of the solar wind alpha flux.

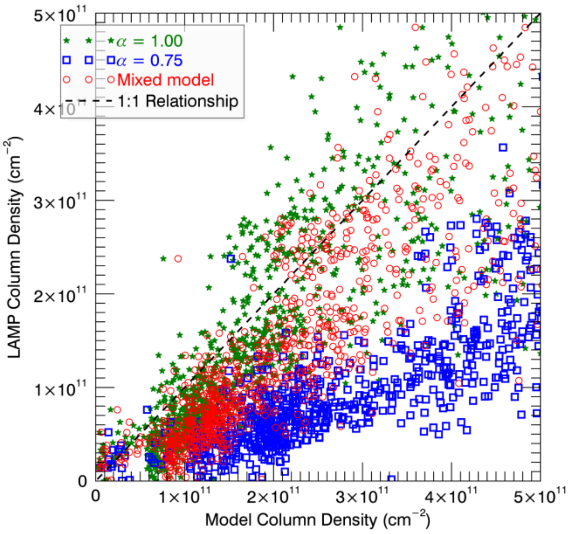

Figure 2 The model with α=1.00 better reproduces LAMP column densities.

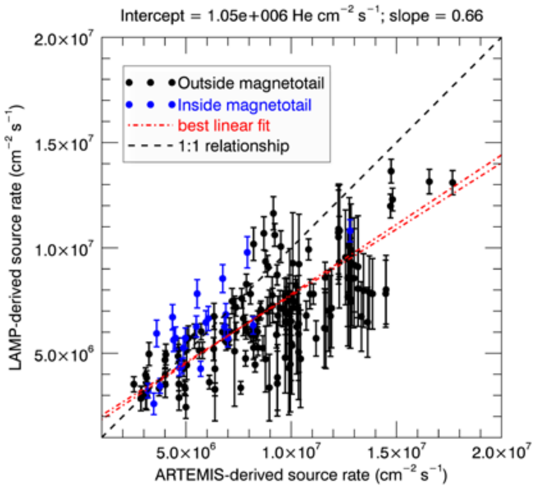

Figure 3 Scatter plot of helium source rates. Red lines indicate the best linear fit including all the points (inside and outside the magnetotail).

This value further constrains previous in-situ measurements by mass spectrometry [8] and is consistent with theoretical grounds [10] which were based on the assumption that the pathway for outgassing of ^{4}He from the interior of the Moon into the exosphere is the same as that of ^{40}Ar (a byproduct of radioactive decay of ^{40}K in the crust), which has a source rate of $6.3 \cdot 10^{4}$ cm^{-2} s^{-1} [15].

Finally, we bin our observations by selenographic coordinates (latitude and longitude) regardless of local time, to search for regions of active outgassing. Figure 4 shows the ratio of LAMP/model column densities. We find no evidence for such regions. A simulation of propagation of helium from a plume shows that helium atoms are quickly dispersed. In order to be detected by LAMP, a plume would require an unrealistic amount of helium.

References: [1] Hoffman, J. H. et al. (1973) *LPSC IV*, 2865. [2] Stern S. A. et al. (2012) *GRL*, *39*(12). [3] Feldman P. D. et al. (2013), *Icarus*, *221*(2), 854-858. [4] Cook J. C. & Stern S. A. (2014) *Icarus*, *236*, 48-55. [5] Grava et al. (2016) *Icarus*, *273*, 36-44. [6] Hurley D. M. et al. (2016) *Icarus*, *273*, 45-52. [7] Gladstone G. R. et al. (2010) *Sp. Sci. Rev.*, *150(1-4)*, 161-181. [8] Benna M. et al. (2015) *GRL*, *42*, *10*, 3723 – 3729. [9] Hodges R. R. and Hoffman J. H. (1974) *GRL*, *1(2)*, 69-71. [10] Hodges R. R. (1980) JGR, *85*(A1), 164-170. [11] Shemansky D. E. & Broadfoot A. L. (1977) *Rev. of Geophys.*, *15*(4), 491-499.. [12], Leblanc F. & Chaufray J.-Y. (2011) *Icarus*, *216*(2), 551-559. [13] Woods T. N. et al. (2012), *Sol. Phys.*, *275*, 115. [14] Angelopoulos, V. (2011), *Sp. Sci. Rev.*, *165*, 3–25. [15] Hodges R. R. (1975) *The Moon*, *14*(1), 139-157.

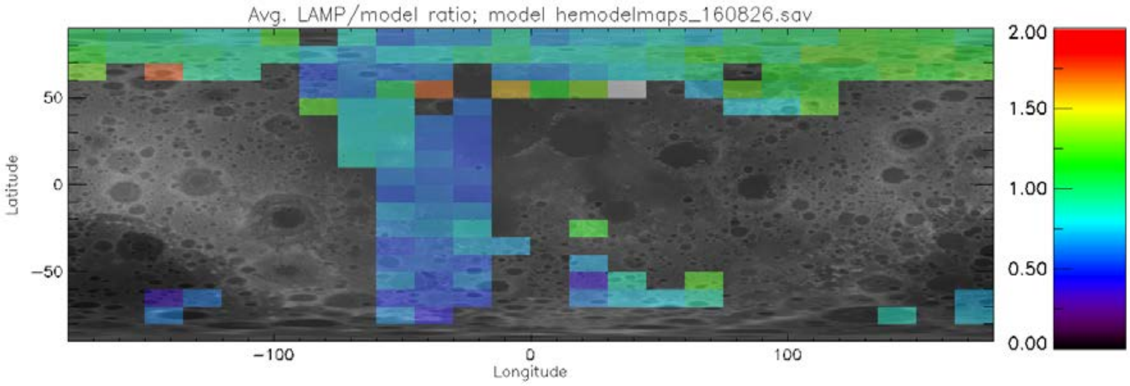

Figure 4 Map of ratio LAMP/model column densities for all observations. No regions of active outgassing could be identified.

SIMULATED LUNAR ENVIRONMENT EXPERIMENTS: KEY TO INTERPRETATION OF LRO DIVINER AND FUTURE THERMAL INFRARED DATASETS

B.T. Greenhagen[1], C.M. Wagoner[1], C.N. Yasanayake[1], K.L. Donaldson Hanna[2], N.E. Bowles[3], and P.G. Lucey[4]; [1]Johns Hopkins Applied Physics Laboratory, [2]University of Central Florida, [3]University of Oxford, [4]University of Hawaii. Email:benjamin.greenhagen@jhuapl.edu

Introduction: On airless bodies, the uppermost portion of regolith, the “epiregolith”, represents the boundary layer between the surface and space that dominates spectral observations from far-ultraviolet reflectance to far-infrared emission. On the Moon, this layer is typically less than 2 mm in thickness and is estimated to be characterized by significant thermal gradients (~60K / 100 μm) [1]. These thermal gradients make spectral emission from the Moon wholly different from Earth and Mars (where the epiregolith is essentially isothermal) and complicate the interpretation of spectral emission remote sensing data. Therefore, thermal infrared (TIR) spectroscopy experiments and spectral libraries measured in ambient laboratory conditions are not comparable to remote sensing datasets of airless bodies that contain significant emission components.

We work to overcome this challenge by measuring TIR emission spectra in a chamber that illuminates and heats particulate samples under vacuum to generate a thermal gradient akin to that found in the epiregolith of airless bodies. Simulating the lunar environment allows us to measure TIR spectra that are directly comparable to remotely sensed TIR observations from the Diviner Lunar Radiometer (Diviner) instrument aboard the Lunar Reconnaissance Orbiter (LRO).

Here we characterize the TIR emission spectra of two- and three-component silicate mineral mixtures with the endmembers plagioclase, pyroxene, and olivine. These uniform composition and particle-size endmembers bound the typical mineral compositions of the lunar surface (***Figure 1***). By understanding the TIR characteristics of these mixtures, we can better interpret Diviner and future TIR datasets and their implications for surface compositions on the Moon and other airless bodies. In addition, we will revisit compositional maps of the Moon normalized to illumination conditions similar to those produced in our laboratory experiment and compare them to mineral mixture and lunar soil spectra.

Simulated Lunar Environment: In nearly 50 years of laboratory experiments, it has been established that thermal emission spectra measured in a simulated lunar environment (SLE) are significantly altered from spectra measured under terrestrial conditions [e.g. 1-4]. The data for this study were collected in the Simulated Airless Body Emission Laboratory (SABEL) chamber at the Johns Hopkins Applied Physics Laboratory. The lunar environment is simulated by (1) pumping the chamber to vacuum pressures (<10^{-4} mbar), which is sufficient to simulate lunar heat transport processes within the sample, (2) cooling the chamber with liquid nitrogen to simulate a surface radiating into a cold space environment, and (3) simultaneously heating the sample with cup heaters and illuminating the surface with a lamp to set up thermal gradients similar to those experienced in the top 100s of microns of the lunar regolith. This study used the environmental conditions described in [5], which through groundtruthing of Diviner observations and laboratory experiments on Apollo soils found the best consistency by matching the illumination to the expected flux for the given chamber incidence angle (~50 degrees).

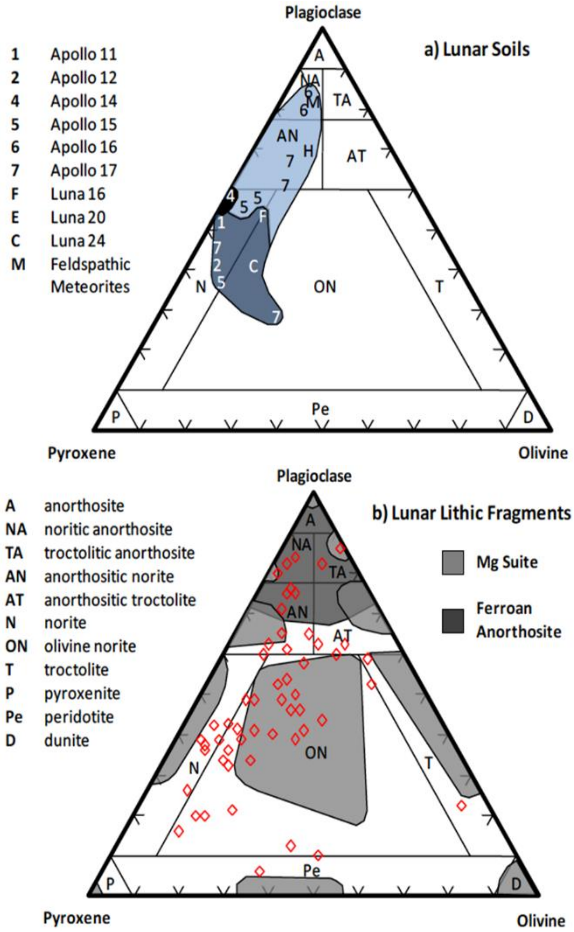

Figure 1: Lunar mineralogy is well-represented with a ternary of three silicate minerals (plagioclase, pyroxene, and olivine). Lunar soils are generally found to have noritic compositions (top; modified after [6]). However, lithic fragments and observations of crater central peaks (red diamonds) span the full range of compositions (bottom; modified after [7]).

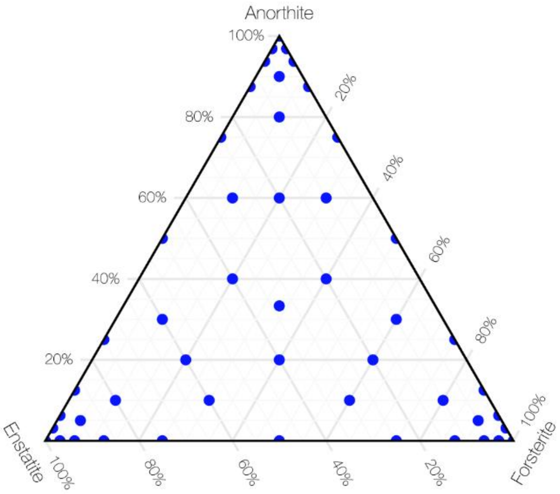

Figure 2: This study includes 49 total samples: 3 endmembers, 27 two-component mixtures, and 19 three-component mixtures (blue dots). All mixtures are shown in vol% of the endmembers.

Samples: Our sample suite is composed of terrestrial minerals with reasonably similar chemistries to lunar minerals. For plagioclase, we use Miyake Jima anorthite (~An95) that was manually picked and magnetically purified to remove basaltic coatings. For pyroxene, we use gem-quality Tanzanian enstatite (~Mg90). And for olivine, we use gem-quality San Carlos olivine (~Fo90). All minerals were crushed and sieved to particle size fractions less than 32 microns. A CAMSIZER was used to verify similar particle size distributions for each mineral endmember. Mixtures with 49 unique compositions were produced (***Figure 2***) and measured using SABEL.

Results: We found that the position of the Christiansen feature (CF), a TIR emissivity maximum, in the two- and three- component mixtures followed smooth, generally linear trends across most compositions (***Figure 3***). The trends became non-linear at the highest olivine compositions. Additionally, the slope across the ternary was significantly different between endmember interpolations and mixture interpolations. An incomplete understanding of these factors could lead to an underestimate of olivine abundances, especially in olivine-rich lithologies. Importantly, the uniformity of these measurements lead confidence that mineral compositional constraints can be enhanced when both near-infrared and TIR data are included. Work to interpret the mineral mixtures as analogs to the lunar soil and determine actionable spectral trends relevant to producing new compositional constraints is ongoing.

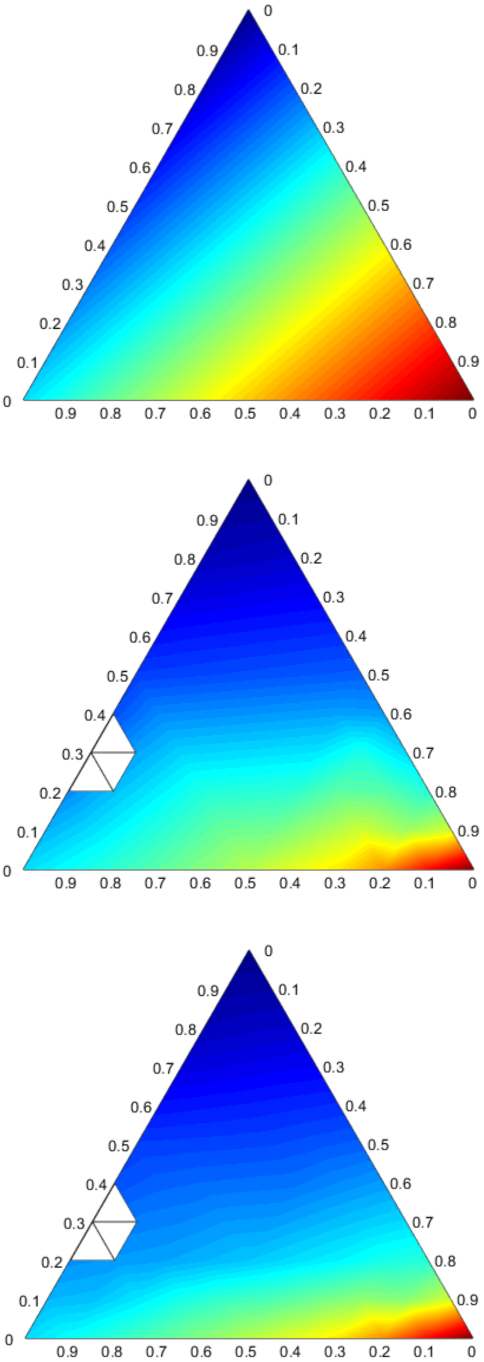

Figure 3: Top panel shows a linear interpolation of endmember CF positions. Middle panel shows a linear interpolation of all two-component mixtures (i.e. edges of the ternary). Bottom panel shows a linear interpolation including two- and three-component mixtures (i.e. edges and interior of the ternary). Endmembers and axes match ***Figure 2***.

References: [1] Henderson B.G. et al. (1996) *JGR*, 101. [2] Logan L.M. et al. (1973) *JGR,* 78, 4983. [3] Thomas I.R. et al. (2012*) Rev.Sci.Inst.*, 83 (12), 124502. [4] Donaldson Hanna K.L. et al. (2017) *Icarus*, 283, 326-342. [5] Greenhagen B.T. et al. (2019) *LPSC 50*, Abstract #2751. [6] Lucey P.G. et al. (2004) GRL, 31, L08701. [7] Cahill J.T.S. et al. (2009) JGR, 114, E09001.

DETERMINING LUNAR REGOLITH WATER CONTENT USING PERMITTIVITY MEASUREMENTS WITH THE LUNAR VOLATILES SCOUT.

C. Gscheidle[1], S. Sheridan[2], L. Richter[3] and J. Biswas[1], [1]Institute of Astronautics, Technical University of Munich, Boltzmannstr. 15, 85748 Garching, Germany (c.gscheidle@tum.de), [2]School of Physical Sciences, The Open University, Milton Keynes, MK7 6AA, United Kingdom, [3]OHB System AG, Manfred-Fuchs-Straße 1, 82234, Weßling, Germany.

Introduction: In recent year, missions to the Moon have indicated that significant amounts of hydrogen and potentially water could be found there [1]. Especially the Lunar Crater Observation and Sensing Satellite (LCROSS) has measured a water content of 5.6±2.9 w% for the Cabeus crater [2]. Nevertheless, confirmation of these findings requires ground-truth data. The Lunar Volatiles Scout (LVS), which is currently developed at the Technical University of Munich (TUM), can potentially provide this valuable ground-truth data [3].

Lunar Volatiles Scout: The LVS is an instrumented drill designed for future mobile in-situ extraction, detection and analysis of lunar volatiles. A schematic of the instrument is given in Figure 1. By heating the regolith to high temperatures, water and other volatiles can be extracted and identified with an integrated mass spectrometer. However, accurately determining the abundance of water in the regolith remains difficult. To address this issue, a lunar regolith permittivity measurement could be added to the LVS' capabilities. In principal, the change in moisture content can be detected by comparison of the LVS' capacitance between heating rod and drill shell before and after heating the regolith. Both liquid water and water ice have a significantly higher static relative permittivity ($\varepsilon_{r,w} \approx 80$ [4]) than both lunar regolith ($\varepsilon_{r,s} \approx 5$ [5]) and vacuum ($\varepsilon_{r,v} = 1$), which results in a measureable change in capacitance when water has been extracted from the probe volume. The usage of permittivity measurements to analyze water content is also included in ESA's PROSPECT instrument package [6] and has been used for various applications [7,8].

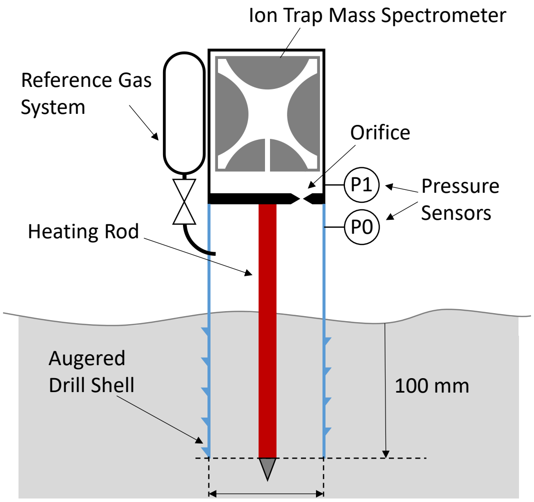

Figure 1: LVS Schematic. Drill Shell (blue) and Heating Rod (red) form the capacitive system.

Theoretical Considerations: In this context, the LVS functions a cylindrical capacitor with the heating rod and drill shell as electrodes (see Figure 1). The capacitance of the system is proportional to the interior material's permittivity ε [9], which is a function of the interior's components individual permittivity. Multiple mixing rules for the permittivity exist [10]. For simplicity, the ideal permittivity of a mixture $\varepsilon = \sum_i \varepsilon_i \varphi_i$ was chosen with φ_i being the volume fraction of component i [11]. The capacitance C of the LVS system is then

$$C = 2\pi \frac{1}{\ln({}^{r_O}/_{r_I})} \left(z_s \left(\varphi_s \varepsilon_{r,s} + \varphi_w \varepsilon_{r,w} \right) + z_v \varepsilon_{r,v} \right) \quad (1)$$

with component height z, inner radius r_I, outer radius r_O, and s denoting sand, w denoting water and v denoting vacuum (or air). When charging the capacitive system with voltage U_0, the ideal capacitor voltage over time is described by

$$U(t) = U_0 \left(1 - e^{-t/\tau} \right) \quad (2)$$

with $\tau = RC$ being the time constant. Here, R is the charging resistance. The water content can then be determined by measuring the transient charging curve and using Equation 1 and 2 to calculate φ_w.

Experimental Setup: The experiment setup is depicted in Figure 2. It consists of a concentric metal tube and metal rod, which is hold in place by a non-conductive 3D-printed structure. The rod is insulated

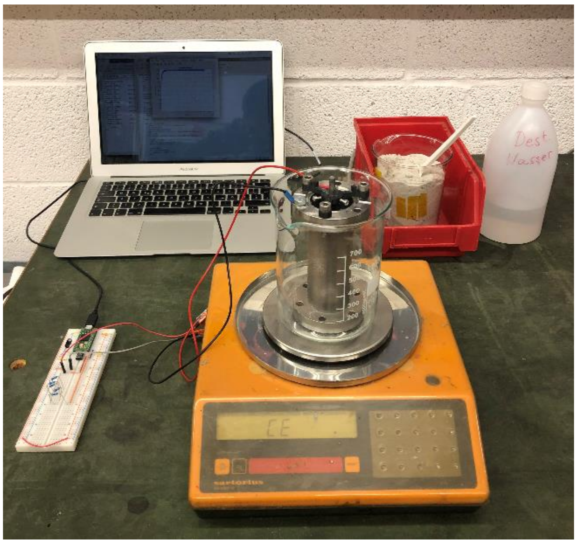

Figure 2: Experimental Setup: LVS system connected to read-out electronics and on precision scale. Quartz sand and distilled water in the background.

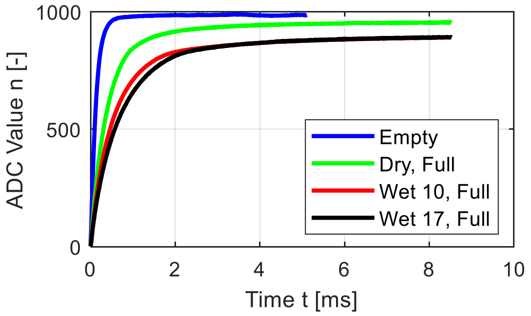

Figure 3: Preliminary Results: Charging Curves. ADC read-out over time of the LVS system for different materials. 'Empty' and 'Full' refers to sand filling, 'Dry' and 'Wet' to its water content with the numbers indicating water content.

towards the interior to prevent parasitic currents. The interior of the tube can be filled with material of interest. For simplicity and better availability, we used quartz sand as analogue material for the pretests and tracked the amount of water in the probe with a precision scale. Water content was chosen to be in the same magnitude as the LCROSS measurements (see Table 1, [2]). Experiments with lunar regolith simulants are planed.

The electronics consist of a commercial microcontroller charging the system with 3.3 V and reading a buffered 10-bit analog input, which returns ADC values n. We used a 5.0 MΩ charging resistance.

Experiments were conducted where the LVS system was filled with different components. Four cases have been selected to demonstrate functionality: (1) empty, (2) filled with dry sand and (3) filled with wet sand. For each experiment, ten measurements were made. Figure 3 shows mean charging curves of the system resembling the LVS. Additionally, exponential curves of form $n(t) = n_0(1 - \exp(-{}^{t}/_{\tau}))$ have been fitted to the data using a Nonlinear Least Square method to get the time constants of the system.

Results: Mean values and standard deviations for the time constants from selected experiments are given in Table 1, alongside analytically calculated values. Time constant correlates with both more mass and higher water content. The experiments' charging curves also display distinct differences (see Figure 3). A linear fit to measured over calculated time constants returns a nearly unity slope and an offset of around 80 µs, possibly due to the measurement technique. The linear dependency clarifies that the geometry of the LVS can be adapted to function as capacitive system with a dependency of the time constant to the capacitance of the contained material. This should in principal hold true for moist lunar regolith. By measuring relative change in capacitance instead of absolute values, the system is also quite insensitive to external disturbances and uncertainties, such as geometric misalignments due to launch.

Table 1: Experiment data: Measured sand mass m_s and water content φ_s. Measured (τ_m) and calculated (τ_c) time constant for experiments depicted in Figure 3.

Case	m_s [g]	φ_w [%]	τ_m [µs]	τ_c [µs]
Empty	0	0	134±3	43
Dry	154	0	426±1	345
Wet 10	154	10	582±5	499
Wet 17	154	17	719±3	624

Additionally to measuring the water content, the capacitance of the empty LVS system could be used to determine the amount of regolith in the LVS. Regolith and vacuum themselves have different permittivities which result in different capacities for different filling heights. Experiments investigating this correlation show promising results, while this relevant property is otherwise hard to determine.

In general, the experiments show that the investigated method works and that it can be applied to the LVS. By measuring the permittivity before and after the heating process, the LVS is able to determine the amount of water in lunar regolith.

Additional Investigations: Nevertheless, there are still major issues with the system, which are currently being analyzed with experiments and simulations. Firstly, proper integration of in the LVS is being investigated. Secondly, precise calibration of the system with internal parasitic resistances and initial conditions under thermal vacuum conditions can yield better insight. The current read-out electronics are neither flight ready nor capable of frequency dependent permittivity measurements. Including analyses of frequency behavior could also increase the science yield of the instrument. Finally, the selection of the mixing rules, especially with water ice, should be revised and a reliable model for the permittivity of lunar regolith are being developed to ease result interpretation.

References: [1] Crawford I. A. (2015*) Progress in Physical Geography: Earth and Environment, 39,* 137-167. [2] Colaprete A. et al. (2010) *Science, 330,* 463–468. [3] Biswas J. et.al. (2020), *Planetary and Space Science, 181*, 104826. [4] Uematsu M. and Frank E. U. (1980) *Journal of Physical and Chemical Reference Data, 9,* 1291-1306 [5] Chung D. H. et al. (1972) *Lunar and Planetary Science Conference Proceedings, 3,* 3161-3172. [6] Sefton-Nash E. et al. (2018) *European Lunar Symposium* [7] Soltani M. and Alimardani F. (2012) *Journal of Food Science and Technology, 51,* 3500-3504 [8] Lethuilier A. (2016) *PhD Thesis* [9] Lehnert G. (2018) *Elektromagnetische Feldtheorie* [10] Amooey A. A. (2013) *Journal of Molecular Liquids, 108,* 31-33 [11] Reis J.C.R. et al. (2009) *Chemical Physics, 11,* 3977–3986

ASSESSING BIOMARKER SURVIVAL IN TERRESTRIAL MATERIAL IMPACTING THE LUNAR SURFACE.

S. H. Halim[1], I. A. Crawford[1], G. S. Collins[2], K. H. Joy[3]. [1]Birkbeck, University of London, UK (shalim03@mail.bbk.ac.uk). [2]Imperial College London, UK. [3]University of Manchester, UK.

Introduction: The Moon's rich impact history is exemplified by an epoch circa 3.9 Gyr ago when the terrestrial planets are thought to have experienced frequent, large-scale impact bombardment [1-4]. During this time, Earth would have experienced numerous, giant, hypervelocity impacts [5], potentially ejecting terrestrial material into Moon-crossing orbits [6]. This has led to the proposal that such ejecta could be preserved on the lunar surface as terrestrial meteorites [7-10]. These could provide a geological record of terrestrial biomarkers predating the period for which the earliest evidence of life exists on Earth. Here, we have used the iSALE-2D shock-physics code [11-13] to determine the pressure and temperature regimes of simulated terrestrial meteorites impacting the lunar surface, in order to gauge the survivability of biomarkers in the projectiles. Previous impact modelling has used specific peak pressure thresholds as a proxy for survivability, with peak temperature from shock heating assumed to correlate with peak pressure. Here, we assess the additional influence of shear heating, which has been shown to be important, or even dominant, in raising temperatures within the projectile at lower impact velocities [14]. If this were the case, survivability of projectiles and their organic or hydrated mineral constituents would be less favourable than previously thought.

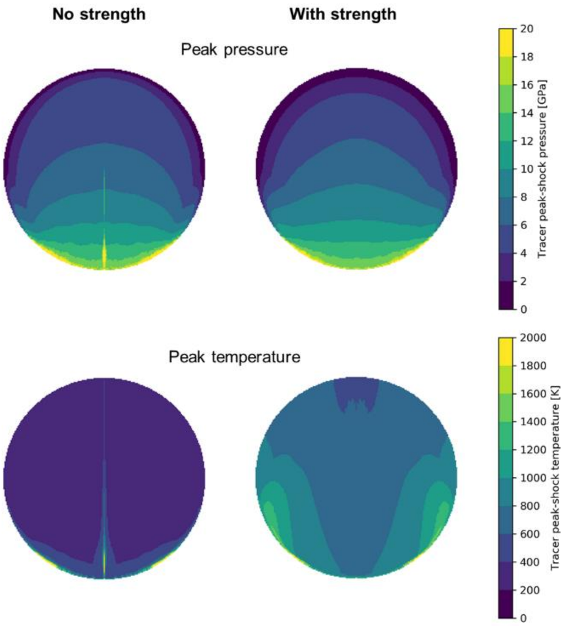

Fig. 1: *Contour maps of peak pressure (top) and temperature (bottom) for solid projectiles impacting a solid target at 2.5 km/s. Left projectile maps used no strength model (hydrodynamic), right projectile maps used a Collins strength model [12].*

Methods: We simulated non-porous and porous sandstone and limestone projectiles (dia. = 0.5 m), vertically impacting a basalt target at 2.5 and 5 km/s, the most likely and upper limit of the vertical velocity component found via analytical methods by [7,8] for terrestrial meteorites impacting the Moon, respectively. Oblate and prolate projectiles were also investigated but without porosity. Initial porosity [13] of the target basalt layer was varied between 0-70%, based on various locations across the lunar surface [15,16] and the porosity of the impactor was varied between 0-40%, to investigate a variety of sedimentary materials. The strength of the materials was modelled using the method described in [12], important for resolving both shock and shear heating. Simulations used lunar gravity (1.62 m/s^2) and a surface temperature of 273 K. Each model used 100 cells per projectile radius (cppr), improving resolution on [10]. Tracer particles recorded pressure and temperature in the projectile material during the simulation. Pressure and temperature regimes were then compared to known thermal degradation parameters for some example biomarkers (arginine, valine, glutamine, tryptophan [17], and lignin [18]), using a modified version of the Arrhenius equation and the method described by [19]. Pressures and temperatures for which lycophyte megaspore microfossils have survived in metamorphosed rocks were also used for comparison [20]. To investigate the influence of shear heating, we compared simulations of a solid sandstone projectile impacting a solid basalt target at 2.5 and 5 km/s, both with a strength model and without (hydrodynamic).

Results: In each simulation, pressure and temperature regimes were taken from tracers in the materials to create survival contour maps for each projectile in the figures going forward.

The influence of material strength: Projectiles displayed very similar peak pressure contours across the projectile for simulations with and without strength at both impact velocities. The top of Fig. 1 shows this for the 2.5 km/s velocity projectile. However, there is a marked increase in the peak temperatures experienced (bottom, Fig. 1) when a strength model is included. This highlights the importance of a strength model that can resolve shear heating, which provides additional heating to the projectile material at these velocities.

Sandstone projectiles: Fig. 2 shows the most favourable conditions for survival of biomarkers, in the simulations we modelled. Maximum temperatures in most of the projectile reach only 600 K. In terms of thermal degradation of biomarkers, there is

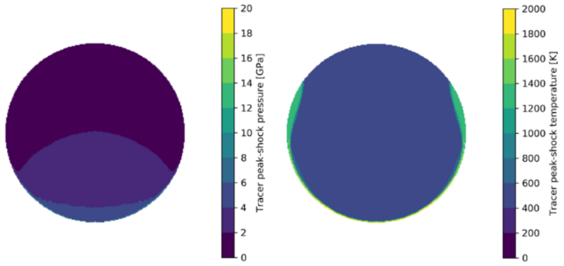

Fig. 2: *Contour maps of peak pressure (left) and temperature (right) for a solid (0% porosity) sandstone projectile impacting a 70% porous target at 2.5 km/s.*

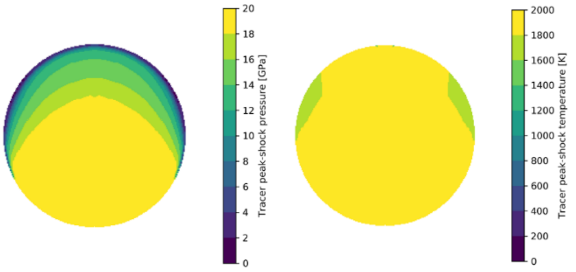

Fig. 3: *Contour maps of peak pressure (left) and temperature (right) for a 40% porous sandstone projectile impacting a solid (0% porosity) target at 5 km/s.*

essentially no degradation on the timescale of shock and shear heating. Therefore, the severity of thermal degradation will depend on the post-shock temperature and cooling rates of projectile fragments. Small impactor fragments on the lunar surface will undergo quick, radiative cooling into space, therefore experiencing the least thermal degradation. Conversely, large fragments buried in the well-insulated regolith will take longer to cool and biomarkers will undergo much greater degradation at prolonged high temperatures. Towards the rear of the projectile in Fig 2., lycophyte megaspores would survive with little alteration, according to the survival pressures/temperatures (<1 GPa/630 K) of metamorphosed examples over timescales of millions of years [20]. Fig. 3 shows the least favourable conditions for biomarker survival. In this case, temperatures are too high (>2000 K) for any substantial proportion of amino acids to survive and pressures are too great for lycophytes to survive. Results for spherical projectiles between these extremes show a range of biomarker survival.

Limestone projectile comparison: Limestone projectiles showed comparable results for their sandstone counterparts. Peak-shock pressures in the limestone projectiles were almost identical to those in the sandstone projectiles, but peak-shock temperatures are lower in the limestone projectiles relative to the sandstone projectiles, with the most noticeable difference in solid projectiles impacting solid targets at 2.5 km/s (Fig. 4).

Conclusions: With the aid of numerical modelling, we show that including strength in the simulation materials is important for accurately assessing the temperature in a projectile impacting at velocities expected for terrestrial meteorites. Nevertheless, in spite of the higher temperatures that result, we have shown that biomarkers within terrestrial meteorites can probably survive after impact with the Moon, especially at the lower end of the range of impact velocities. Increasing projectile porosity is detrimental to the survival of biomarkers, whereas increasing porosity in the target increases the chances of surviving projectile material. Comparing sandstone and limestone projectiles shows similar temperature and pressure profiles for the same simulation, with limestone providing slightly more favourable conditions for biomarker survival.

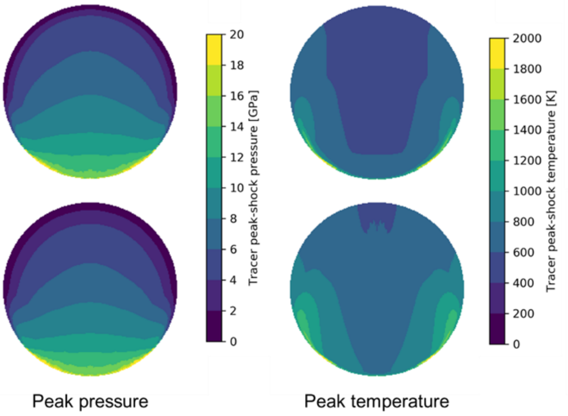

Fig. 4: *Contour plots comparing pressure and temperature regimes in limestone (top) and sandstone (bottom) projectiles. Both sets of plots are the result of a solid projectile impacting a solid target at 2.5 km/s.*

Acknowledgements: We gratefully acknowledge the developers of iSALE-2D and STFC for funding.

References: [1] Turner G. (1973) *4th Lunar Sci. Con.* 1889–1914. [2] Hartmann W. (1975) *Icarus*, 24, 181-187. [3] Stöffler D. et al. (2006) *Rev. Min. Geochem.*, 60, 519-596. [4] Marchi S. et al. (2012) *EPSL*, 325-326, 27-38. [5] Marchi S. et al. (2014) *Nature*, 511, 578-582. [6] Beech M. et al. (2019) *American Journal of Astronomy & Astrophysics*, 7, 1-9. [7] Armstrong et al. (2002) *Icarus*, 160, 183-196. [8] Armstrong J. (2010) *Earth, Moon, & Planets*, 107, 43-54. [9] Gutiérrez J. L. (2002) *ESA SP-518*, 187-191. [10] Crawford I. A. (2008) *Astrobiology*, 8, 242-252. [11] Amsden A. et al. (1980) *LANL Report*, LA-8095. [12] Collins G. S. et al. (2004) *MAPS*, 38, 217-231. [13] Wünnemann K. et al. (2006) *Icarus*, 180, 514-527. [14] Kurosawa K. & Genda H. (2018) *GRL*, 45, 668-679. [15] Heiken G. H. et al. (1991) *Cambridge University Press*, ISBN 0-521-33444-6. [16] Schultz P. H. et al. (2010) *Science*, 330, 468-472. [17] Rodante F. (1992) *Thermochimica Acta*, 200, 47-61. [18] Brebu, M. & Vasile C. (2010) *Cellulose Chemistry and Technology*. 44. 353-363. [19] Pierazzo E. & Chyba C. (1999) *MAPS*, 34, 909-918. [20] Bernard S. et al. (2007) *EPSL*, 262, 257-272.

Hawai`i - High Fidelity Lunar Analog Field testing sites.

J. C. Hamilton[1], [1]University of Hawai'i – Hilo (PAaR - Planetary Astrogeology & Robotics, Dept of Physics & Astronomy, 200 W. Kawili St., Hilo, Hawai`i 96720, jch@hawaii.edu).

Introduction: The "Big Island" of Hawai`i has been shown to be an ideal terrestrial location as a analog field testing site for the Moon, Mars and other basalt-covered rocky bodies. Recent volcanic terrain creates high fidelity science and technical analog sites with comparable geomorphology, regolith simulants and geochemistry.

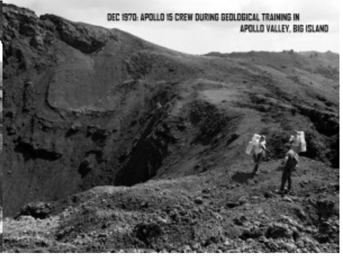

Heritage from the 1960s into the next century: Dating back to the early Apollo mission training in the late 1960s, equipment and geology field training brought astronauts to the island. After the shuttle missions, when the Return to the Moon paradigm was operative, NASA conducted its only In-Situ Resource Utilization (ISRU) field tests in the early 2008-10, successfully extracting oxygen, water and creating methane rocket propellant from the volcanic tephra. Internatioal in scope, the participants included CSA and ESA via DLR. Trials of the RESOLVE/Lunar Prospector robotic polar mission followed.

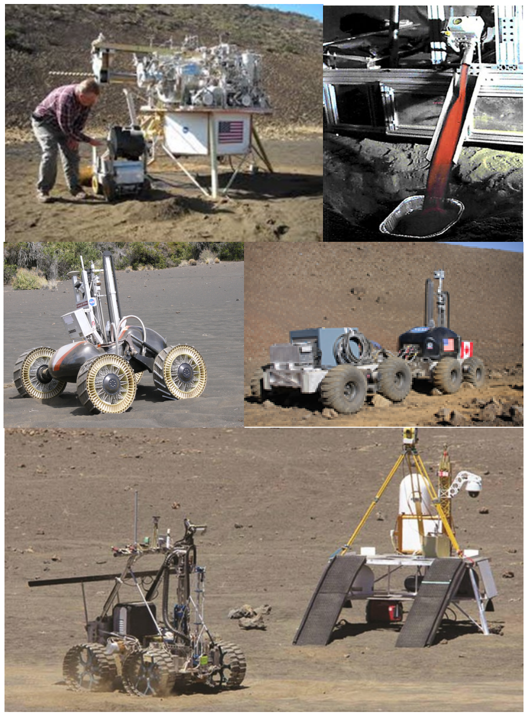

Commercial space made its mark with the Google Lunar X-Prize teams and field tests for milestones by Hungary and Japan teams.

Combined Moon and Mars missions: Volcanoes National Park was well suited for serveral trials and two deployments of BASALT, a Mars Ops-Sim with geobiochemistry sampling protocols. Instruments for Lunar Prospector such as NIRVSS were brought onto the lava flows.

The successful Mars habitat food-study program HI-SEAS on Mauna Loa yielded many long duration missions. It has now transitioned to two-week lunar campaigns managed by the Internationa MoonBase Alliance.

References:

[1] Lim, Darlene et.al. (2019) AGU proceedings.

[2] Hamilton, J. (2015) SSERVI Polar Relogith Workshop Without Walls.

[3] Sanders, G.B. & Larson, W.E. (2011) Advances in Space Research Vol 47, Issue 1, 20-29.

[4] ten Kate, et al (2011) Geochemistry, Geophysics, Geosystems.

[5] Sanders, Larson, Picard & Hamilton (2011) EPSC_DPS 20111Vol 6.

CHLORINE IN BRECCIATED LUNAR METEORITE NWA 12593: IMPLICATIONS FOR LUNAR VOLATILE HISTORY.

T. S. Hayden[1], T. J. Barrett[1], X. Zhao[1], M. Anand[1,2], G. Degli-Alessandrini[1], I. A. Franchi[1] [1]The Open University (School of Physical Sciences, The Open University, Walton Hall, Milton Keynes MK7 6AA, UK; [2]Department of Earth Sciences, The Natural History Museum, London, SW7 5BD, UK; tara.hayden@open.ac.uk)

Introduction: Pristine lunar samples returned by the Apollo and Luna missions in the 1960s and 1970s have significantly broadened our understanding of the geological history of the Moon. The material these missions returned to Earth, however, were collected from an area that represents only a small proportion (~5 %) of the entire lunar surface [1]. Until new lunar material is returned from the upcoming Artemis, Luna and Chang'e missions, lunar meteorites are the only samples that may have originated from outside of the Apollo and Luna-sampled regions. These samples, therefore, provide less biased representation of the lunar surface's chemical and lithological diversity.

Northwest Africa (NWA) 12593, is a lunar fragmental breccia [2]. The rock is clast-rich, with mineral and lithic clasts embedded in a fine-grained vesicular impact melt matrix. Within the lithic clast population are crystalline impact-melt breccias, highlands, and basaltic clasts. The main minerals comprising this rock, in both clastic and isolated matrix mineral populations are anorthite, pigeonite, augite, olivine, with minor amounts of chromite, ilmenite, zircon, apatite and merrillite. The apatite grains in this sample are of considerable size (up to 70 µm in the longest dimension) and in texturally pristine condition within both lithic clasts and the matrix. As a major volatile-bearing phase in lunar samples, apatite in this sample could reveal new insights into the distribution and isotopic composition of volatile elements in areas of the Moon not sampled previously. Of the highlands lithologies preserved in NWA 12593, a number of them show affinities to ferroan anorthosites (FAN) sampled during the Apollo missions, but with slight chemical variance (more Ca-rich plagioclase (An_{98}) and Mg-rich mafic silicates (Mg# = ~73). There are also highlands-type clasts compositionally distinct from Apollo highlands sampled material, re-affirming a greater compositional diversity in lunar crustal rocks [3]. In this context, chlorine in the apatites of NWA 12593 could potentially be used to explore the heterogeneity in the distribution and isotopic composition of volatiles, as has been highlighted through recent work on Apollo samples [4].

Methods: Apatite grains in NWA 12593 were identified using an FEI Quanta 200 Scanning Electron Microscope (SEM) fitted with an Oxford Instruments Energy Dispersive X-ray detector, with an accelerating voltage of 20kV and beam current of 0.60nA. The chlorine content (Cl wt. %) and isotopic composition (δ^{37}Cl) of the apatites were then measured using the CAMECA NanoSIMS 50L at The Open University, using a 20pA probe current. Following a protocol adapted from [5-10], negative secondary ions of ^{13}C, ^{18}O, ^{35}Cl, ^{37}Cl and ^{40}Ca^{19}F were acquired simultaneously on electron multipliers in scanning ion imaging mode. Regions of interest (ROIs) were selected within the acquired images based on greater Cl abundance and homogeneity in ^{18}O and Cl images . The isotopic ratio of ^{37}Cl/^{35}Cl of the ROIs were then used to calculate the δ^{37}Cl and Cl abundances. For calibration of Cl content and isotopic ratios three terrestrial apatite standards Ap004, Ap005, Ap018 were used [11]. The isotopic composition of Ap020 standard, which has the lowest chlorine content among all the standards used [11] was analysed to assess reproducibility of the results for apatite with low Cl abundances (see [8]). This was found to be within error of typical terrestrial values reported for Ap004. There is, consequently, no evidence of an extreme background isotopic composition of the SIMS. Background Cl abundances of the system were considered the same as those measured in San Carlos olivine (~1ppm). The lack of an extreme isotopic composition and low abundance of background Cl would result in an inappreciable difference in the measured isotopic composition of apatite grains in NWA 12593, and therefore no correction for background contribution was applied.

Results: There appears to be two groups of Cl isotopic composition in NWA 12593 apatite: a heavy δ^{37}Cl group (of ~+55‰) and a lighter δ^{37}Cl group (ranging between +10‰ and +24‰) (Fig. 1). It should be noted that most of these apatites are present within the matrix as isolated grains, with the majority of these displaying δ^{37}Cl values between +10‰ and +24‰ and, therefore, are assumed to represent a similar source region. There is no correlation between measured δ^{37}Cl and Cl contents.

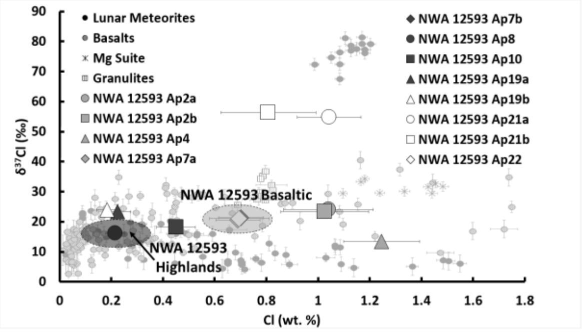

Fig. 1: Cl abundances (wt. %) vs δ37Cl (‰) of apatites in NWA 12593 compared to literature data [5-7, 12-15]. 2σ errors on δ37Cl are smaller than the symbol sizes.

Discussion: Given the elevated Cl contents of the heavier δ^{37}Cl group (Ap21a, b in Fig. 1), magmatic degassing is unlikely to be the primary fractionation mechanisms. Since Ap21 is not associated with any clast, and occurs as an isolated grain in the matrix, its geological context is not known. Although such heavy Cl isotopic compositions have not yet been reported from Apollo material, much heavier δ^{37}Cl values have been measured in apatite in lunar meteorite Dhofar 458 [12] (Fig. 1). This large isotopic fractionation was attributed to the giant impact which formed the Moon, followed by an extensive evaporation of the lunar magma ocean [12, 15]. The Moon coalesced from an enriched vapor, as ^{35}Cl would be preferentially lost from the vapor phase by Rayleigh distillation [12, 17], followed by an extended LMO liquidus phase that persisted for 10 – 200 Myr, inducing further isotopic fractionation by metal chloride evaporation [12]. It is possible that the isotopic composition of Ap21 is indicative of its source region, which may have recorded this process. The influence of shock effects on the Cl isotopes of the apatite grains in NWA 12593 should be further assessed (e.g. using Raman spectroscopy [12]), as petrographic analysis that has concluded the sample is moderately shocked. Notably, Ap21 exhibits irregular outlines indicating some degree of high-temperature interaction with an external melt/fluid source, possibly during shock events which formed the impact melt matrix. Similarly ^{37}Cl-enriched values (up to ~+40‰) in Apollo 14 rocks have been attributed to vapor metasomatism associated with an impact event [14], and it may therefore be reasonable to suggest a similar process is responsible for the heavy signature in NWA 12593. Further work is required to test these hypotheses further.

Of lithic-clast associated apatites, there is a clustering of values for basaltic apatites around +21‰, whereas highlands-type clasts record lower values (+16‰) (see ellipses in Fig. 1). The basaltic apatites are consistent with the literature data (which range from +2‰ to +40‰ [5, 7, 14-15], whereas typical highlands rocks are known to have heavier δ^{37}Cl (+25‰ to +36‰ [5] than those in NWA 12593 (Fig. 1). The matrix associated apatites mainly show lighter δ^{37}Cl values (+13‰ to +24‰). Some of these apatites plot very close to those with highlands clastic associations (see Fig. 1), which could indicate that these isolated apatites may represent the same highlands signature, with the difference in isotopic composition (~+24‰ compared to +16‰ for matrix- and clast-associated, respectively) resulting from magmatic crystallization or source heterogeneity. Other isolated apatites have similar δ^{37}Cl values to those mentioned above (+13‰ to +18‰), but with elevated chlorine contents (0.69 to 1.25 wt. % vs ~2000pm). Further analysis of the mineral chemistry of the lithic clast with which some of the apatites are associated is required to define which highlands lithology this signature represents.

Apatite grains associated with a basaltic clast have Cl abundances of ~7000 ppm and δ^{37}Cl values of +20‰ to +22‰. A number of isolated apatites show comparable δ^{37}Cl (+23‰ to +24‰) but greater Cl abundances (1.02 to 1.04 wt. %). Cl concentration variation likely reflects partitioning behavior in the source region of these apatites, with a limited δ^{37}Cl range reflecting the isotopic composition of this region.

Conclusion: The measured δ^{37}Cl and Cl contents of apatites in lunar meteorite NWA 12593 indicate the possibility of multiple fractionation events and lithologies recorded in this rock. Possible highlands apatites show lighter δ^{37}Cl than previously recorded. Further investigations are ongoing to better constrain the nature of the heavy δ^{37}Cl reservoir on the Moon.

References: [1] Warren, P. H., et al. (1989) *EPSL, 91(3-4)*, 245-260. [2] The Meteoritcal Bulletin, no. 108 (2019) https://www.lpi.usra.edu/meteor/metbull.php?sea=nwa+12593&sfor=names&ants=&nwas=&falls=&valids=&stype=contains&lrec=50&map=ge&browse=&country=All&srt=name&categ=All&mblist=All&rect=&phot=&strewn=&snew=0&pnt=Normal%20table&code=69536 [3] Gross, J. et al. (2014) *EPSL, 388*, 318-328. [4] Boyce, J. W., et al. (2018) *EPSL, 500*, 205-214. [5] Barnes, J. J., et al. (2019) *GCA, 266*, 144-162. [6] Tartèse, R., et al. (2014) *MaPS, 49(12)*, 2266-2289. [7] Barnes, J. J., et al. (2016) *EPSL, 447*, 84-94. [8] Barrett, T. J., et al. (2019) *GCA, 266*, 582-597. [9] Stephant, A., et al. (2019) *EPSL, 523*: 115715. [10] Barrett, T. J., et al. (2020) *LPSC LI, Abstract #2879.* [11] McCubbin, F. M. et al. (2012) *Geology, 40*, 683-686. [12] Wang, Y., et al. (2019) *Scientific Reports, 9:5727.* [13] Stephant, A., et al. (2019) *GCA, 266*, 163-183. [14] Potts, N. J., et al. (2018) *GCA, 230*, 46-59. [15] Boyce, J. W., et al. (2015) *Science Advances, 1,* e1500380. [16] Sharp, Z. D., et al. (2010) *Science, 329*, 1050-1053. [17] Warren, P. H. (1985) *An. Rev. Earth Planet. Sci, 13*, 201-240.

SPECTRAL DIVERSITY OF EXPLOSIVE VOLCANIC DEPOSITS IN SCHRODINGER BASIN WITH MOON MINERALOGY MAPPER DATA.

M.J.B. Henderson[1] B. Horgan[1] L.R. Gaddis[2] and K.A. Bennett[2]. [1]Purdue University, 610 Purdue Mall, West Lafayette, IN (marie@purdue.edu), [2]Astrogeology Science Center, U.S. Geological Survey, Flagstaff, AZ.

Introduction: Schrödinger is a 320 km diameter Imbrium-aged (~3.8 billion years old) impact crater located within South Pole-Aitken (SPA) basin on the lunar far side at 138ºE and 75ºS [1]. It is believed to be the second youngest basin on the lunar surface [2]. Pre-Nectarian-aged SPA basin is a 2400 km by 2050 km impact structure centered at 53°S, 191°E on the far side [3]. Schrödinger is a target for future human or robotic exploration as sampling its diverse lithologies would address a variety of high priority lunar science goals. Sample sites might include a conical edifice raised 415 m above the floor and an associated pyroclastic deposit with an area of 1250 km^2 located near the crater peak ring [4]. Pyroclastic deposits on the Moon represent a primitive material that could help to characterize the lunar interior and to expand our understanding of lunar basaltic magmatism and have resource potential in future exploration [5,6]. The proximity of these deposits would allow a robotic or human mission to answer questions about the history of both volcanic and impact processes in a single mission, which would address goals outlined in the Decadal Survey [7]. Outstanding knowledge gaps at Schrödinger include the relationship between the volcanic deposits and the extent of the pyroclastic deposit. In this study we use spectroscopy and inferred mineralogy to assess these properties and their implications for the volcanic eruption style and history of the deposits.

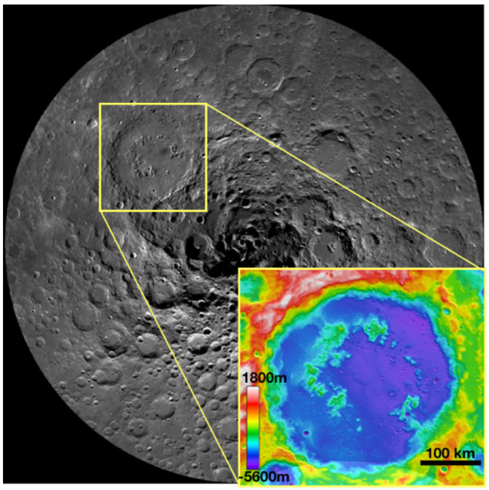

Figure 1: LROC WAC mosaic of the South Pole showing the location of Schrödinger basin. The inset displays the topography of the basin from LOLA data.

Background: Visible wavelength images [8](*Figure 1*) reveal that the pyroclastic deposits within Schrödinger crater may be relatively complex, with multiple pyroclastic deposits and an unusually high albedo compared to other lunar pyroclastic deposits [LPDs, 5]. Kramer *et al.* (2013) previously examined the Schrödinger basin with Level 1 M^3 hyperspectral data [9,10] by studying fresh material exposed by impact craters. The pyroclastic deposit was interpreted to be glass-rich, but the inner-Schrödinger mare could not be spectrally distinguished from the surrounding basin floor material [9]. Here we use Level 2 M^3 products (which include thermal and photometric corrections), incorporate spectra from more diverse range of sites, and use advanced mineral diversity and mapping methods to expand on these earlier results and to assess the mineralogy and likely eruption style of Schrödinger pyroclastics.

Methods: M^3 was an imaging spectrometer on the Chandrayaan-1 lunar orbiter operating in the visible to near-infrared (0.42-3.0 μm). M^3 observations of Schrödinger have a resolution of 280 m/pixel in 86 spectral channels [10]. M^3 collected data during two operational periods distinguished by changes in instrument temperature and orientation; Schrödinger data were obtained in optical period 2B. A M^3 mosaic of the basin was constructed with bounds 110-155ºE and 82-67ºN in an orthographic projection (*Figure 2*). The spectral continuum was removed using a linear convex hull with two segments between 0.6-2.6 μm. Spectral noise was reduced using a median filter and a boxcar smoothing algorithm, both with widths of 5 channels [11,12]

Spectral diversity maps were created by parameterizing the shape, position and depth of the 1- and 2-μm absorption bands in the M^3 mosaic. A glass spectral parameter (average band depth below the continuum at 1.15, 1.18, and 1.20 μm) detects the wings of the glass iron absorption band, which is centered near 1 μm, at much longer wavelengths than other Fe-bearing minerals [11]. This parameter does not uniquely detect glass but along with other spectral parameters, detailed spectral interpretation, and geologic context can infer the presence of glass.

Results: Spectral mapping of the glass band depth, 1-μm and 2-μm band centers are mapped as red, blue, and green respectively in a composite image (*Figure 2*) which highlights the mineralogical diversity of the Schrödinger units. Analysis of these data reveals that the volcanic terrains of the pyroclastic and the inner mare are spectrally distinct from impact features as well as the basin floor. The potential LPDs also have a notably lower albedo.

The M^3 extracted spectra (*Figure 3*) for Schrödinger units show distinctive iron-bearing absorption bands near 1- and 2-μm. The inner-peak ring floor exhibits bands centered near 0.93 and 1.8 μm that are consistent with orthopyroxene (OPX), typical of highlands. In comparison, the inner peak-ring mafic units and distinct linear ridges on the floor exhibit bands shifted to near 0.97 μm and 1.9-2.0 μm, which can be attributed to increased influence of clinopyroxene (CPX). Some areas on the ridges and within the inner mare show stronger absorption at longer wavelengths within the 1-μm band that suggest the presence of glass. The conical edifice in Schrödinger basin has bands centered near 1.1 and 1.9-2.0 μm, and strong shoulders on the 1 μm band representative of a mixture of glass and pyroxene [11, 13].

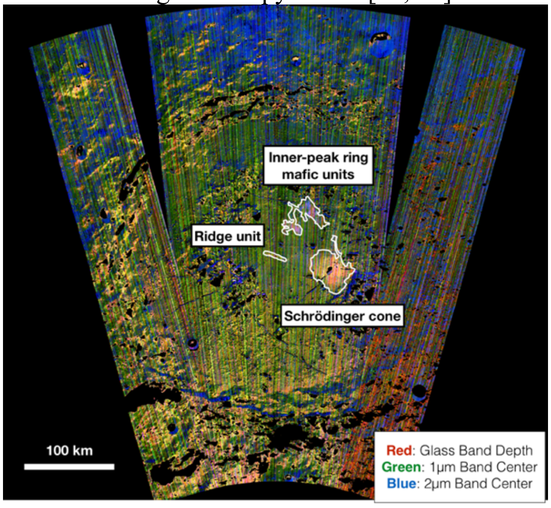

Figure 2: Composite color image of Schrodinger crater. Shades of yellow are inferred to indicate significant glass, blue indicates CPX, magenta indicates glass/CPX mixtures, and greens are dominated by orthopyroxene.

Discussion: The broad absorption bands in the M^3 spectra of the Schrödinger volcanic cone are consistent with a pyroxene and glass mixture, supporting an explosive origin. Inner-peak ring mafic units were previously hypothesized to be mare-like deposits based on the presence of flow-like morphologies. Spectral results show the units are likely dominated by CPX, which suggests that they were emplaced by a more effusive eruption than the cone, perhaps originating as a smaller fissure eruption. Some glass may be present in the inner mare, so they may still have an explosive component. Ridge units exhibit similar colors as the LPD (Figure 2), suggesting a contribution from glass, possibly emplaced as a thin mantle. This possibility is supported by the similarity of the ridge spectra to the inner peak-ring mare, suggesting a limited spectral contribution from glass.

There are multiple hypotheses for how the smaller mafic units are connected to the large conical pyroclastic deposit. A single volcanic vent may have produced a large explosive volcanic edifice before transitioning to effusive flows that were later segmented by impacts. Alternatively, Schrödinger deposits could result from multiple volcanic vents, similar to the multiple volcanic pyroclastic deposits ranging in crystallinity observed in Oppenheimer crater, located farther north within the SPA basin [12]. While the largest deposit in Oppenheimer is comparable in size to the large deposit in Schrödinger, it is flat compared to the 415 m conical edifice in Schrödinger. This could be consistent with eruption of a similar volume of magma from one vent compared to seven. The inner mare deposits of Schrödinger have spectral properties consistent with CPX mixed with glass, similar to some Oppenheimer floor deposits; both LPDs may have formed during a fire fountaining or Strombolian event where large blebs of molten magma accumulated near the vent and formed a lava flow and crystallized [12]. These results suggest that complex volcanic eruption styles may be typical among SPA pyroclastic deposits.

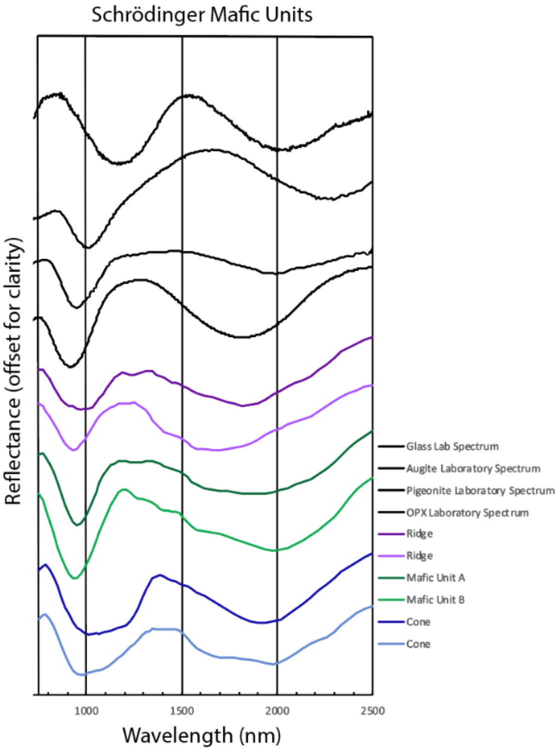

Figure 3: M3 spectra extracted from the Schrödinger pyroclastic deposit, inner- peak ring mafic deposits, and ridge unit deposits compared to laboratory spectra.

Future work will examine the band parameter maps and spectra for the pyroclastic deposit in more detail to assess their distribution relative to vents and local topography. Additionally, we will use Diviner [14] derived iron content and CF feature position to evaluate whether or not the smaller volcanic deposits are related to the large LPD in Schrödinger.

References: [1] Wilhelms & McCauley (1971) [2] Shoemaker *et al.* (1994) *Science*, *266*(5192), 1851-1854. [3] Bethell & Zuber (2005) *GRL*, *32*(13), 2347 [4] Potts *et al.* (2014) *LPSC,* 1835. [5] Gaddis, L.R. et al. (2003) Icarus, 161:2, 262-280. [6] Allen *et al.* (1996) *JGR Planets*, 101(E11) 26085-26095 [7] National Research Council (2011) [8] Robinson, M. S. *et al.* (2010) Space Sci Rev, 150(1-4), 81-124. [9] Kramer *et al.* (2013) *Icarus*, 223, 131-148 [10] Pieters *et al.* (2009) *Science,* 326, 568-572 [11] Horgan et al. (2014) Icarus, 234(C), 132–154 [12] Bennett et al. (2016) *Icarus*, 273, 296-314 [13] Cloutis & Gaffey (1991b) Earth Moon Planet, 53(1), 11–53 [14]Paige *et al.* (2009) Space Sci Rev, 150(1-4), 125–160.

A FRESH LOOK AT AN OLD FUNCTION: THE LUNAR CHRONOLOGY.

H. Hiesinger[1], C. H. van der Bogert[1], W. Iqbal[1], T. Gebbing[1]. [1]Institut für Planetologie, Westfälische Wilhelms-Universität, Wilhelm-Klemm-Str. 10, 48149 Münster, Germany (hiesinger@uni-muenster.de).

Introduction: The Moon is the single most important planetary body for calibrating the impact record of the inner Solar System with absolute ages derived from the returned samples. Overall, the Soviet Luna and the American Apollo programs returned almost 400 kg of lunar samples. Thus, the Moon is unique in that it allows us to groundtruth and calibrate remote-sensing data at the landing sites (e.g., crater size-frequency distributions [CSFDs], crater degradation, mineralogy, composition) with these well-documented samples (e.g., ages, geologic context, composition, mineralogy) [e.g., 1,2]. On the basis of such studies, a lunar chronology function (CF) was derived, which links the CSFD at a certain reference diameter (determined for example via the lunar production function [PF]) with the radiometric and exposure ages of lunar samples [e.g., 3-10]. Commonly, the lunar chronology is shown as the cumulative number of the craters ≥1 km in diameter per km^2, i.e., the $N(1)$ value (y-axis), plotted against the laboratory-derived sample ages (x-axis) (Fig. 1).

CSFD measurements enable us to not only study the geology of unsampled regions on the Moon, but also to derive absolute model ages (AMAs) of surfaces on other planetary bodies. Thus, the lunar chronology function and its extrapolation to other planetary bodies is a prerequisite for dating planetary surfaces and understanding the geologic history and evolution particularly for inner Solar System objects. Although it is known that SNC meteorites originated from Mars and that HED meteorites very likely came from asteroid Vesta, these samples do not have known provenance, making it impossible to link their radiometric ages with CSFDs, i.e., to directly derive chronology functions for these planetary objects.

Ideally, the derivation of the chronology function would yield only one uniquely accepted solution. However, in the process of deriving the chronology function, several assumptions (e.g., importance of secondary craters, target properties, count area size, etc.) have to be made. Consequently, several lunar chronology functions have been proposed over the last 50 years since the Apollo and Luna samples have been brought to Earth [e.g., 5,6,8,10]. Some of these chronologies are drastically different from each other. The largest discrepancies among the chronologies manifest themselves in the time period between about 1 and 3.2 Ga, resulting in drastically different model ages for the same crater frequency (Fig. 1). Although the chronology of [5,6] is widely used, we recognized that many aspects of it are not sufficiently documented in the literature. One important piece of information that is missing for some landing sites are the exact positions and sizes of the count areas for the CSFD measurements that were originally linked with the sample ages. Furthermore, since the derivation of the original lunar chronology of [5,6], our understanding of the samples, their geologic context, and their ages has greatly improved. Considering the importance of the CF for dating planetary surfaces, it is high time to reevaluate the proposed chronologies.

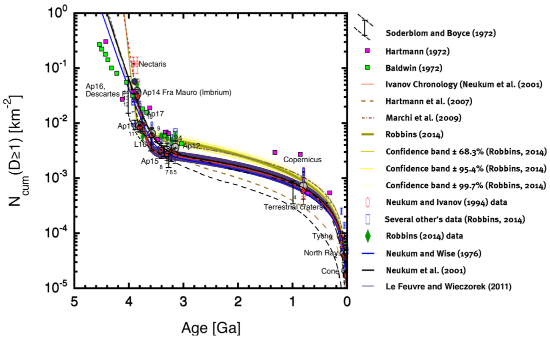

Fig. 1. Proposed lunar chronologies

Results: At the meeting, we will report on our work reevaluating the lunar chronology. Our study has produced and is producing new geologic maps, on which we selected updated and new homogeneous geologic units for new CSFD measurements. Our geologic mapping effort has allowed us to accurately attribute samples to a specific geologic unit. On the basis of our literature review of laboratory-derived sample ages, we correlated these ages with our new CSFDs. Were available, we also recounted the count areas of [5,6] to gauge the quality of the original counts with modern high-resolution imaging data. This also allowed us to detect and investigate possible differences with our newly defined count areas. So far, we re-investigated the data points for Copernicus, Tycho, North Ray [11], and Cone craters [12], as well as the Apollo 11, 12, 14, 16, and 17 landing sites [13-18]. For Apollo 15 we have available a preliminary geologic map.

Cone Crater: On the basis of our new CSFD measurements on LROC images, we derived older $N(1)$ values than previous CSFDs [e.g., 19]. Our results are more similar to the older CSFDs than to those of [20] and are within the error bars of [21]. The newly derived $N(1) = 3.26 \times 10^{-5}$ km^{-2} is very close to the $N(1)$ of 3.36 x 10^{-5} km^{-2} of [10].

North Ray Crater: CSFD measurements for North Ray crater were performed by two independent researchers to test potential effects introduced by different crater recognition, diameter measurements, number of counted craters, etc. Both CSFD measurements agree very well with each other and yielded an $N(1)$ of 3.94×10^{-5} km^{-2} and 3.90×10^{-5} km^{-2}, respectively for count areas defined by [5,6]. In [22], we also report on

CSFD measurements for count areas that were slightly adjusted on the basis of our new geologic maps. These CSFD measurements resulted in an *N*(1) of 4.26x10^{-5} km^{-2}, hence slightly older.

South Ray Crater: In [22], we also describe the results of our CSFD measurements for South Ray crater. For this crater, we derived *N*(1) values that are somewhat younger than previously reported. Our new CSFD measurement indicate an *N*(1) value of 8.95x10^{-7} km^{-2}.

Tycho Crater: In our 2012 paper [11], we determined an *N*(1) value of 7.12x10^{-5} km^{-2} for several count areas on the ejecta blanket of Tycho and an *N*(1) value of 2.72x10^{-5} km^{-2} for several Tycho melt pools.

Copernicus Crater: In [5,6], the data point of Copernicus showed an N(1) that was significantly higher than one would expect from the lunar chronology, which long puzzled researchers. Inspection of the original count area revealed that it is heavily contaminated with secondary craters. Thus, it seems most likely that the high *N*(1) value of [5,6] resulted from the inclusion of secondary craters. Consequently, in [11] we used Lunar Reconnaissance Wide Angle (WAC) and Narrow Angle Camera (NAC) images to adjust the count area location carefully and derived *N*(1) values of 66.8x10^{-5} km^{-2} and 65.3x10^{-5} km^{-2}, respectively. Kaguya Terrain Camera images yielded a slightly lower *N*(1) of 56.8x10^{-5} km^{-2}. These *N*(1) values fit the original chronology of [5,6] much better.

Apollo 11: On the basis of WAC images, Iqbal et al. [13] re-investigated CSFDs at the Apollo 11 landing site. As a result, we determined an *N*(1) value of 6.47x10^{-3} km^{-2} for the original count area of [5,6]. However, we also recognized that the original count area is affected by the deposition of ray material. Taking this into account, we defined new more appropriate count areas. Our new *N*(1) values are 6.42x10^{-3} km^{-2} (NAC) and 6.88x10^{-3} km^{-2} (WAC). On the basis of NAC CSFD measurements, [13] determined an *N*(1) of 5.74x10^{-3} km^{-2}.

Apollo 12: Our CSFD measurements yielded an *N*(1) of 2.81x10^{-3} km^{-2} for the mare unit containing the Apollo 12 landing site and an *N*(1) of 6.67x10^{-4} km^{-2} for the Copernicus ray material [14]. The *N*(1) values published by [5,6] for this landing site are 3.61x10^{-3} km^{-2} and 1.3x10^{-3} km^{-2}, respectively. [10] determined an *N*(1) of 5.68x10^{-3} km^{-2}.

Apollo 14: For the count area of [5,6], we determined an *N*(1) value of 4.31x10^{-2} km^{-2}, thus slightly older than the *N*(1) value of 3.7x10^{-2} km^{-2} of [5,6]. Our new WAC count area yielded an *N*(1) of 4.5x10^{-2} km^{-2} and our NAC counts, which combined several smaller count areas show an *N*(1) of 5.39x10^{-2} km^{-2}. All our *N*(1) values are older than the *N*(1) values of [8], i.e., 2.595-2.672x10^{-2} km^{-2}.

Apollo 15: Preliminary work on the Apollo 15 landing site was presented in [15] and in a companion abstract. For the count areas A and B defined by [5,6], we found *N*(1) values of 2.99x10^{-3} km^{-2} and 2.98x10^{-3} km^{-2}. The *N*(1) given by [5,6] is 3.2±1.1x10^{-3} km$^{-2\cdot}$ Our study also showed that count area C is heterogeneous, consisting of several geologic units. After adjustment of the count area, we determined an *N*(1) of 1.72x10^{-3} km^{-2}. Count area E exhibits two *N*(1) values of 3.55x10^{-3} km^{-2} and 7.88x10^{-3} km^{-2}, representing two mare units.

Apollo 16: Previous studies determined *N*(1) values of 3.4±0.7×10^{-2} km^{-2} [5] and 2.490×10^{-2} km^{-2} to 2.509×10^{-2} km^{-2} [8] for the three count areas of [5,6]. We re-counted these areas and obtained an *N*(1) value of 1.84x10^{-2} km^{-2}. However, re-inspecting these count areas with modern LROC WAC data, we found the count areas to be heterogeneous. Thus, we defined new count areas for which preliminary CSFD measurements indicate an *N*(1) value of 1.84x10^{-2} km^{-2}. Our NAC CSFD measurements of several smaller count areas within the WAC count areas show *N*(1) values of 5.35×10^{-3} km^{-2} to 1.66×10^{-2} km^{-2} [16]

Apollo 17: Recently, [11,18] dated the light mantle material at the Apollo 17 landing site. As a result, [18] derived an *N*(1) value of 7.04x10^{-5} km^{-2}. For the mare unit and pyroclastics around the landing site, an *N*(1) value of 1.06x10^{-2} km^{-2} was found, which is close to the *N*(1) value of [18,23].

Conclusions: On the basis of our new CSFD measurements on carefully characterized count areas at the Apollo landing sites and at some additional anchor points, we do not find large discrepancies in the lunar chronology of [5,6]. Thus, on the basis of our CSFDs, we do not see the necessity to substantially change the lunar chronology function. For the first time, all count areas and measured CSFDs are documented in the literature, which has not been the case for some measurements in the publications of [5,6].

Acknowledgments: W. Iqbal was funded by the German Research Foundation (Deutsche Forschungsgemeinschaft SFB-TRR170, subproject A2).

References: [1] BVSP, 1981, Pergamon New York, 1286 pp.; [2] Nyquist et al., 2001, Kluwer Academic Publishers, 1325-1376; [3] Hartmann, 1970a, Icarus 13, 299-301; [4] Hartmann, 1970b, Icarus 12, 131; [5] Neukum, 1983, Habilitation thesis Univ. Munich; [6] Neukum et al., 2001, Space Sci. Rev. 96, 55-86; [7] Stöffler et al., 2006, Rev. Mineral. Geochem. 60, 519-596; [8] Marchi et al., 2009, Astron. J. 137, 4936-4948; [9] Hiesinger et al., 2011, Geol. Soc. Am. Spec. Pap. 477, 1-51; [10] Robbins, 2014, Earth Planet. Sci. Lett. 403, 188–198; [11] Hiesinger et al., 2012; [12] Hiesinger et al., 2015, LPSC 46, 1834; [13] Iqbal et al., 2019a, Icarus 333, 528-547; [14] Iqbal et al., 2019b, LPSC 50, 1070 [15] Iqbal et al., 2020, LPSC 51, 1073; [16] Gebbing et al., 2019, LPSC 50, 2337; [17] Borisov et al., 2019, LPSC 50, 2323; [18] Iqbal et al., 2019c, LPSC 50, 1005. [19] Moore et al. (1980) Moon and Planets 23, 231–252. [20] Plescia and Robinson (2011) LPSC 42, 1839. [21] Williams et al. (2014) Icarus 235, 23–36. [22] Gebbing et al., 2020, LPSC 51, 1871; [23] van der Bogert et al., 2016, LPSC 47, 1616.

IN ORBIT EXPLORATION OF RESOURCES IN PERMANENTLY SHADOWED LUNAR POLAR REGIONS

M. Horanyi[1,2](horanyi@colorado.edu), E. Bernardoni[1], S. Kempf[1], Z. Sternovsky[1,2], J. Szalay[3], [1]Institute for Modeling Plasmas, Atmospheres, and Cosmic Dust (IMPACT), U. of Colorado, Boulder, CO, USA, [2] Laboratory for Atmospheric and Space Physics (LASP), U. of Colorado, Boulder, CO, USA, [3] Princeton University, Princeton, NJ, USA

Introduction: The Moon is continually bombarded by on the order of 10^6 kg/y of interplanetary dust particles (IDP) that are micrometeoroids of cometary and asteroidal origin. Most of these projectiles range from 10 μm to about 1 mm in size and impact the Moon with speeds in the characteristic range of 10 to 72 km/s. At Earth, the passage through the atmosphere ablates most of these particles turning them into "shooting stars". However, they directly reach the surface of the Moon, generate secondary ejecta particles and leave a crater record on the surface from which the micrometeoroid size distribution has been deciphered [1]. Most of the ejecta particles have initial speeds below the escape speed from the Moon (2.4 km/s) and following ballistic orbits return to the surface, blanketing the lunar crust with a highly pulverized and impact gardened regolith with $\gg$ 1 m thickness. Micron and submicron sized secondary particles that are ejected at speeds up to the escape speed form a highly variable, but permanently present, dust cloud around the Moon. Such tenuous clouds have been observed by the Galileo spacecraft around all lunar-sized Galilean satellites at Jupiter [2]. Our understanding of the lunar dust exosphere is based on NASA's Lunar Atmosphere and Dust Environment Explorer mission (Fig.1) [3]. The findings provide a unique opportunity to map the composition of the lunar surface from orbit and identify regions that are rich in volatiles, providing opportunities [4] for future in situ resource utilization (ISRU).

In Situ Resource Utilization is a key element in establishing human habitats on the Moon. The expected availability of water ice, and other volatiles, in Permanently Shadowed Regions (PSR) makes the lunar poles of prime interest. However, the relative strength of the various sources, sinks, and transport mechanisms of water into and out of PSRs remain largely unknown. The quantitative characterization of the temporal and spatial variability of the influx of IDPs to the polar regions of the Moon is critical to the understanding the evolution of volatiles in PSRs. A dust instrument onboard a polar orbiting lunar spacecraft could make fundamental measurements to assess the availability and accessibility of water ice in PSRs. Water is thought to be continually delivered to the Moon through geological timescales by water-bearing comets and asteroids and produced continuously in situ by the impacts of solar wind protons of oxygen-rich minerals on the surface. IDPs are an unlikely source of water due to their long UV exposure in the inner solar system, but their high-speed impacts can mobilize secondary ejecta dust particles, atoms and molecules, some with high-enough speed to escape the Moon. Other surface processes that can lead to mobilization, transport and loss of water molecules and other volatiles include solar heating, photochemical processes, and solar wind sputtering. Since the efficiency of these are reduced in PSRs, dust impacts remain the dominant process to dictate the evolution of volatiles in PSRs.

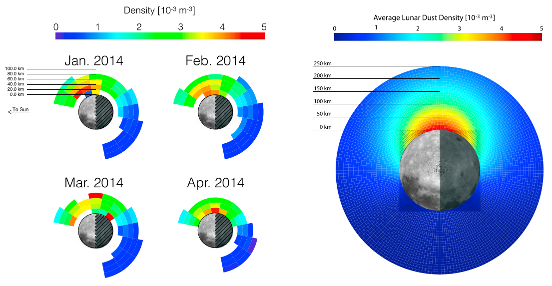

Fig.1 *The dust ejecta cloud observed by LDEX for each calendar month LADEE was operational in 2014 (left), and the modelled average lunar dust density distribution for particles with radii* ≥ 0.3 *μm (right panel) shown in a reference frame where the Sun is on the left [5].*

In the absence of an atmosphere, each incoming IDP directly hits the lunar surface and generates a copious number of secondary particles, with sufficient speeds, reaching over 200 km altitude before most of them returns to the surface. The continually present dust ejecta cloud was observed by LADEE/LDEX. A more capable dust instrument, in addition to the size and speed of an impacting particle, can also measure the composition of secondary ejecta particles, resulting in a surface composition map with a spatial resolution comparable to the height of the spacecraft. This talk will describe the available instrumentation, its testing and calibration using the SSERVI /IMPACT dust accelerator facility at the University of Colorado, Boulder.

Summary: A polar-orbiting spacecraft could directly sample the lunar ejecta, providing the critical link between IDP bombardment and the evolution of water ice in PSRs.

References: [1] E. Grün, et al., *Icarus*, 62:244, 1985. [2] H. Krüger, et al., *Icarus*, 164:170, 2003. [3] R. C. Elphic, et al., Space Sci. Rev., 185:3, 2014. [4] F. Postberg, et al., Planet. Space Sci., 2011. [5] J. R. Szalay and M. Horányi. *Geophys. Res. Lett.*, 42:10,580, 2015.

DIVERSE ROCK TYPES DETECTED IN THE LUNAR SOUTH POLE-AITKEN BASIN BY THE CHANG'E-4 LUNAR MISSION.

Jun Huang[1,2*], Zhiyong Xiao[3,2,4*], Long Xiao[1,2,4*], Briony Horgan[5], Xiaoyi Hu[1], Paul Lucey[6], Xiao Xiao[1], Siyuan Zhao[1], Yuqi Qian[1], Hao Zhang[1], Chunlai Li[7], Rui Xu[7], Zhiping He[7], Jianfeng Yang[8], Bin Xue[8], Qi He[1], Jie Zhong[9], Hongyu Lin[10], Changning Huang[10], Jianfeng Xie[11]. [1] State Key Laboratory of Geological Processes and Mineral Resources, Planetary Science Institute, School of Earth Sciences, China University of Geosciences (Wuhan), China. [2] CAS Center for Excellence in Comparative Planetology, China. [3] Planetary Environmental and Astrobiological Laboratory, School of Atmospheric Sciences, Sun Yat-sen University, China. [4] State Key Laboratory of Lunar and Planetary Sciences, Space Science Institute, Macau University of Science and Technology, China. [5] Department of Earth, Atmospheric and Planetary Sciences, Purdue University, USA. [6] Hawai‘i Institute of Geophysics and Planetology, University of Hawai‘i at Manoa, Honolulu, USA. [7] Key Laboratory of Space Active Opto-Electronics Technology, CAS Shanghai Institute of Technical Physics, China. [8] CAS Xi’an Institute of Optics and Precision Mechanics, China. [9] CAS Institute of Optics and Electronics, China. [10] CAST Beijing Institute of Space Mechanics and Electricity, China. [11] Beijing Aerospace Flight Control Center, China (junhuang@cug.edu.cn).

Introduction: South Pole-Aitken (SPA) basin, located between the South Pole and Aitken crater on the far side of the Moon, is the largest confirmed lunar impact structure. The pre-Nectarian SPA basin is a 2400-km-by-2050-km elliptical structure centered at 53ºS, 191ºE, which should have exposed lower crust and upper mantle due to enormous excavation depth. Olivine, the dominant mineral in the Earth’s mantle, has only been identified in small and localized exposures in the margins of the SPA basin and the dominant mafic component is, instead, pyroxene. The mineralogical characteristics could be explained by the recent hypothesis that the lunar upper mantle is dominated by low-calcium pyroxene (LCP), not olivine. Here we present observations from imaging and spectral data of China’s Chang’E-4 (CE-4) mission in the first 4 synodic days, especially the first in-situ visible/near infrared spectrometer (VNIS) observation of an exposed boulder. We have identified a variety of rock types, but not the recently reported olivine-rich materials in the landing region. The results are consistent with orbital observations. The obtained mineralogical information provides a better understanding of the nature and origin of SPA materials.

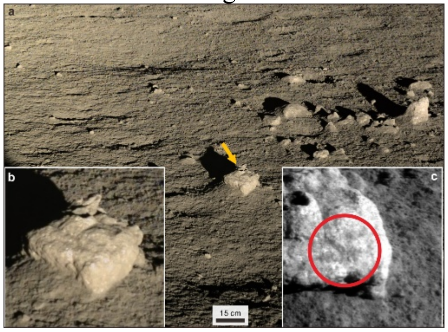

Figure 1. PCAM and VNIS visible observations of Qi Yuan(meaning “unexpected encounter” in Chinese), the first lunar rock for which a VNIS spectrum was obtained. (a) A group of relatively light-toned rocks. The half-buried rocks are likely exposed due to long-term mass wasting. Qi Yuan is indicated by the yellow arrow. (b) A blow-up view of Qi Yuan. It looks like a coherent igneous rock, and the bright spots on its relatively fresh surface are plagioclase phenocrysts or pits created by micro meteorite impacts. (c) VNIS visible image of Qi Yuan. The red circle indicates the footprint of the VNIS SWIR detector.

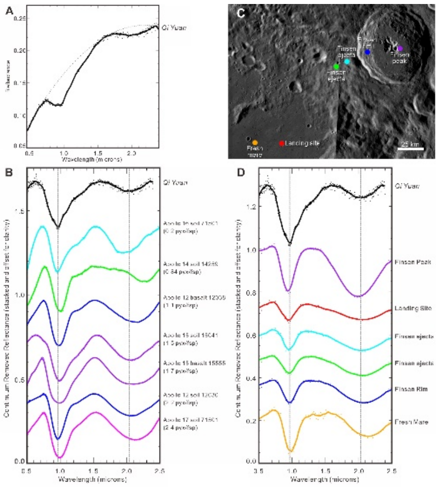

Figure 2. VNIS spectrum of Qi Yuan compared to Apollo samples and M3 spectra. (A) Reflectance spectrum of Qi Yuan, showing parabolic continuum fit (dashed line). (B) Comparison of continuum removed spectra of Qi Yuan and spectrally similar Apollo samples. Dashed vertical lines indicate band centers for Qi Yuan. (C) Regional NAC mosaic showing locations where M3 spectra were extracted. (D) Comparison of continuum removed spectra of Qi Yuan and M3 spectra from locations shown in (C). Qi Yuan is most similar to M3 spectra from the crater rim and proximal ejecta.

Notes: For the full text of this study, please refer to Huang et al., (2020). Diverse Rock Types Detected in the Lunar South Pole-Aitken Basin by the Chang’E-4 lunar mission. Geology, accepted. doi: 10.1130/G47280.1

NEW GEOLOGICAL MAPS OF THE APOLLO LANDING SITES.

W. Iqbal[1], H. Hiesinger[1], C. H. van der Bogert[1], D. Borisov[1], and T. Gebbing[1], [1]Institut für Planetologie, Westfälische Wilhelms-Universität, Wilhelm-Klemm-Str. 10, 48149, Münster, Germany, iqbalw@uni-muenster.de.

Introduction: Historical data from the Apollo program improved knowledge of lunar geology tremendously in many aspects. Nevertheless, the geological maps that were completed before the missions can and should now be updated with new data [1-6] and revisited with knowledge regarding geological processes that has been gained in the ~50 years since the mission [e.g., 7]. As part of a large project, we are using recent lunar datasets to produce comprehensive geological maps around the Apollo landing sites. These new maps are being used to test the calibration [8] of the lunar cratering chronology [9,10] by pinpointing the sampling sites of the collected samples [11] and reevaluating their position within and relevance for lunar stratigraphy. The maps can also be used for planning future missions [e.g., 12].

Methods: Detailed mapping is achieved using data with different spatial resolutions. Albedo differences are mapped using images from the Lunar Reconnaissance Orbiter (LRO) Wide Angle (WAC; 100 m/pixel) and Narrow Angle (NAC; ~0.5-1.2 m/pixel) cameras [1], as well as Selene/Kaguya Terrain Camera image mosaics. We use various digital elevation models (DEM) to map structures with topographic differences. These DEMs include the LRO WAC-derived (100 m/pixel) [2], LOLA (100 m/pixel), and LOLA/Kaguya merged (60 m/pixel) [3] DEMs. Geological units are also mapped on the basis of spectral differences in Clementine [4], Chandrayann-1 Moon Mineralogy Mapper (M^3) [5], and Kaguya Multiband Imager (MI) data [6].

The stratigraphic system of Wilhelms (1987) [7] is adapted in our new geological maps. The symbology used for geological units follows the standards of the Federal Geographic Data Committee (2006) [13] and harmonized with the PlanMap mapping standards, and the nomenclature is adapted from the Gazetteer of Planetary Nomenclature (1999) [14].

Geological units: The highlands contain units such as *IpIt*-Imbrian pre-Imbrian terrains (which are Nectarian terrains covered or mixed with the Imbrian materials), Fra Mauro Formation Imbrium basin ejecta units (*Ifm*-Imbrian Fra Mauro formation and *Ifs*-Imbrian Fra Mauro smooth plains), and *Ip*-Imbrian plains. Mare units are mapped on the basis of spectral differences [e.g., 4-6] using the same approach as [15], thus the contacts between the mare units are mapped as approximate spectral boundaries. In a few places, the stratigraphy of the mare units was identified through crater densities derived from crater size-frequency distribution (CSFD) measurements [e.g., 16-18]. The different generations of craters are mapped as *Cc*-Copernican craters, *Ec*-Eratosthenian craters, *Ic*-Imbrian craters, and *Nc*-Nectarian craters or *pIc*-preImbrian craters.

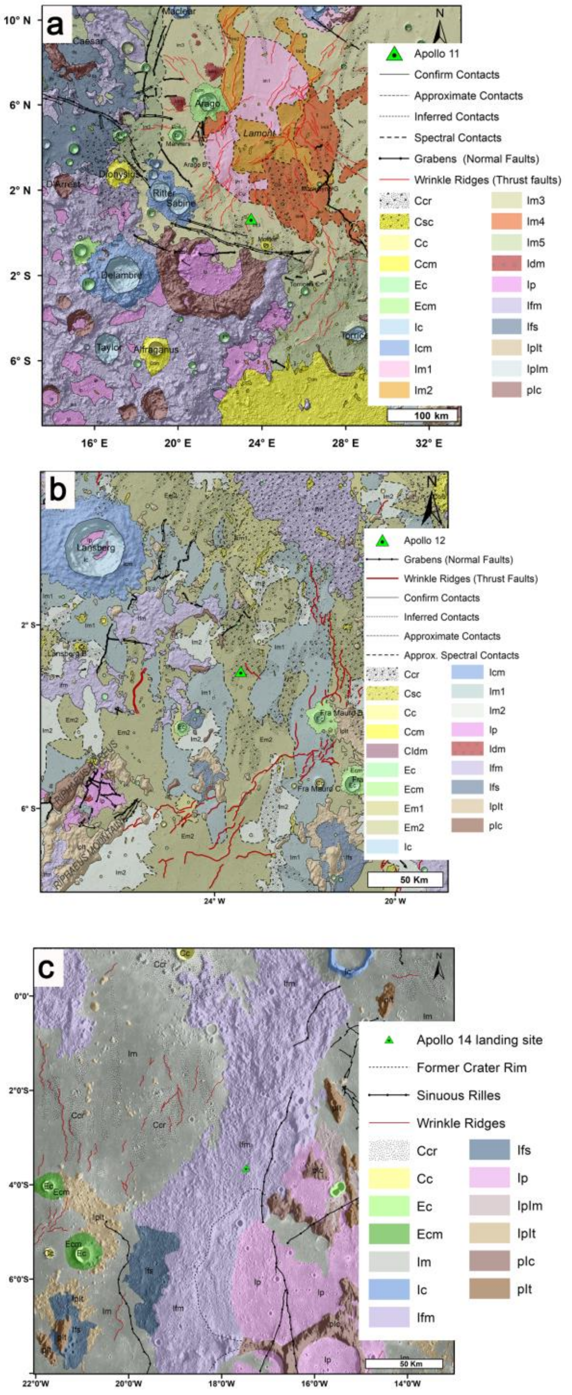

Figure 1. *The detailed geological maps of the Apollo 11[16], 12 [17], and 14 landing sites [19]. (a) The Apollo 11 landing site lies in southwestern Mare Tranquillitatis. (b) The Apollo 12 landing site lies south of Copernicus crater in Oceanus Procellarum. (c) Preliminary geological map of the Apollo 14 landing site on the Fra Mauro formation (Ifm), east of the Apollo 12 landing site. Locations of the landing modules are marked by green triangles.*

Implications: The lunar cratering chronology is based on CSFD measurements that are calibrated with the radioisotopic and exposure ages of the lunar samples [9,10]. It is used to derive absolute model ages (AMAs) of unsampled geological units across the Moon, as well as on planetary bodies throughout the Solar System [e.g., 15]. On the basis of our new geological maps [16-21], we defined and refined homogeneous geological counting areas for measuring CSFDs and deriving accurate $N(1)$ reference values and AMAs, which are necessary to test and improve the lunar cratering chronology [9].

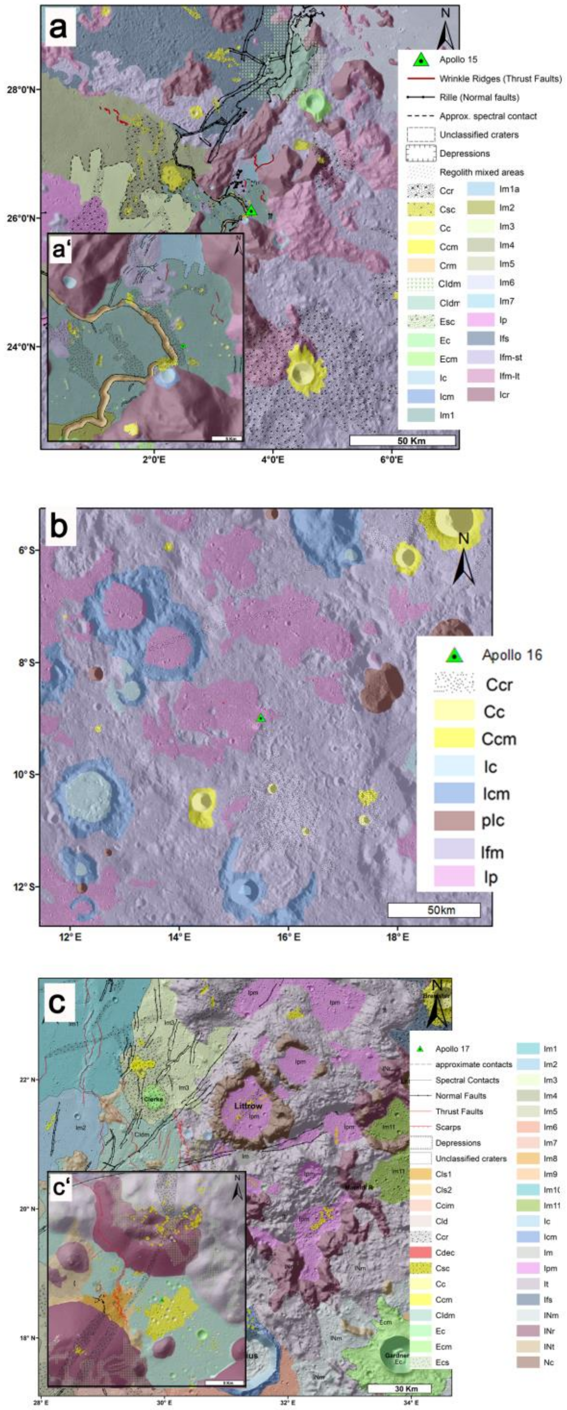

Figure 2. *Preliminary new geological maps of the Apollo landing sites 15 [21], 16 [20], and 17 [18]. (a) The Apollo 15 landing site lies at the eastern rim of the Imbrian Basin. (a’) Inset shows a local geological map around the Apollo 15 landing site. (b) Map around the Apollo 16 landing site. (c) The Apollo 17 landing site near the eastern rim of the Serenitatis basin. (c’) The local geological map of the Taurus Littrow valley around the Apollo 17 landing site. The green triangles show the locations of the landing sites.*

In addition, the new geological maps can be used to examine and understand potential landing sites for technology demonstration missions. For example, van der Bogert (2020) [12] used our detail geological map [18] in an analysis of landing sites for an end-to-end in situ resource utilization demonstrator mission concept for ESA.

The new geological maps provide new and refined perspectives on the locations and relationships between the Apollo samples and remotely-sensed compositional and morphological differences. Our geological maps can be used to investigate the exact origin of the collected samples [e.g., 11] and further enhance our knowledge about the history of the geological processes that took place on the Moon.

Acknowledgements: WI and HH were funded by the German Research Foundation (Deutsche Forschungsgemeinschaft SFB-TRR170, subproject A2) and CvdB was supported by EU H2020 project #776276, PLANMAP.

References: [1] Robinson et al (2010) *Space Sci. Rev. 150*, 81-124. [2] Scholten, et al. (2012). *JGR. 117*, E00H17. [3] Barker et al. (2016) *Icarus 273*, 346-355. [4] Pieters et al. (1994) *Science 266*, 1844-1848. [5] Isaacsom, et al. (2013). *JGR Planets. 118*, 369-381. [6] Ohtake, et al (2013) *Icarus 226*, 364-374. [7] Jolliff, et al. (2006) *New Views of the Moon 60* [8] Hiesinger et al. (2020) *LPSC 51*, 2045. [9] Neukum, (1983) *Habil. thesis, U. of Munich.* [10] Neukum, et al. (2001) *Space Sci. Reviews 96*, 55-86. [11] Haber, et al (2018) *AGU*, P31G-3785. [12] van der Bogert, et al. (2020) *LPSC 51*, #1876. [13] FGDC (2006). *FGDC-STD-013-2016.* [14] Blue, J. (1999) Gazette. of Planet. Nomen. *USGS.* [15] Hiesinger, et al. (2000) *JGR 105*, 29239-29275. [16] Iqbal, et al (2019) *Icarus 333*, 528-547. [17] Iqbal, et al (2018) *LPSC 49,* 1002. [18] Iqbal, et al (2019) *LPSC 50,* 1005. [19] Borisov, et al (2019) *LPSC 50,* 2323. [20] Gebbing, et al (2019) *LPSC 50,* 2337. [21] Iqbal, et al (2018) *LPSC 51,* 1073.

NEW GEOLOGICAL MAPS AND CRATER SIZE-FREQUENCY DISTRIBUTION MEASUREMENTS OF THE APOLLO 15 LANDING SITE.

W. Iqbal[1], H. Hiesinger[1], and C. H. van der Bogert[1], [1]Institut für Planetologie, Westfälische Wilhelms-Universität, Wilhelm-Klemm-Str. 10, 48149 Münster, Germany, (iqbalw@uni-muenster.de).

Introduction: We are testing and improving the the lunar cratering chronology [1,2] within a series of studies [3-8] where we are performing detailed investigations of the geology, sample collection, and crater size-frequency distribution (CSFD) measurements at Apollo landing sites. The correlation of CSFD measurements with radioisotopic and exposure ages of Apollo and Luna samples form the basis for the lunar cratering chronology, which is used to derive absolute model ages (AMAs) of unsampled surfaces of planetary bodies throughout the inner Solar System [e.g., 1-11].

The Apollo 15 landing site is located at the rim of the Imbrian basin, is covered by mare units from late Imbrian to Eratosthenian period, and provides a wide range of samples from various geological periods. Using recent data, we produced a new geological map of this site and updated CSFDs for the described geologic units. The newly derived $N(1)$ (cumulative number of the craters ≥1 km in diameter) values will be correlated with updated sample ages [e.g., 12], resulting in a reevaulated calibration point for the lunar cratering chronology [1].

Methods: The used image data include LROC Wide Angle (WAC; 100 m/pixel) and Narrow Angle Camera (NAC; ~0.5 m/pixel) images [13] with incidence angles between 55-80°, and SELENE (Kaguya) Terrain Camera morning, evening, and ortho mosaics. The topographic features were mapped using a LOLA/SELENE merged digital elevation model (DEM) [14] and LRO NAC-derived DEMs. The spectral boundaries were defined on Clementine data [15] and Kaguya Multiband Imager (MI) data [16]. The geologic units were mapped using ArcGIS. The CSFDs of the mapped units were measured using CraterTools [17] in ArcGIS, and were plotted and fit in cumulative and relative plots using pseudolog binning in Craterstats [18]. Randomness analyses [19] were used to avoid contamination from clusters and chains of secondary craters.

Geological Events: The Apollo 15 landing site contains geologic units of Imbrian, Eratosthenian, and Copernican ages. Previous studies [e.g., 20,21] identified the massifs in highlands as preImbrian material, in contrary, we identified them as a part of Imbrium basin rim. The highlands in the mapping area exhibit the Imbrium basin rim (*Icr*), Imbrium basin ejecta units (*Ifm-lt, Ifm-st, and Ifs,* which are topographically different), and Imbrian plains (*Ip*). The mare units in the mapping area belong to the

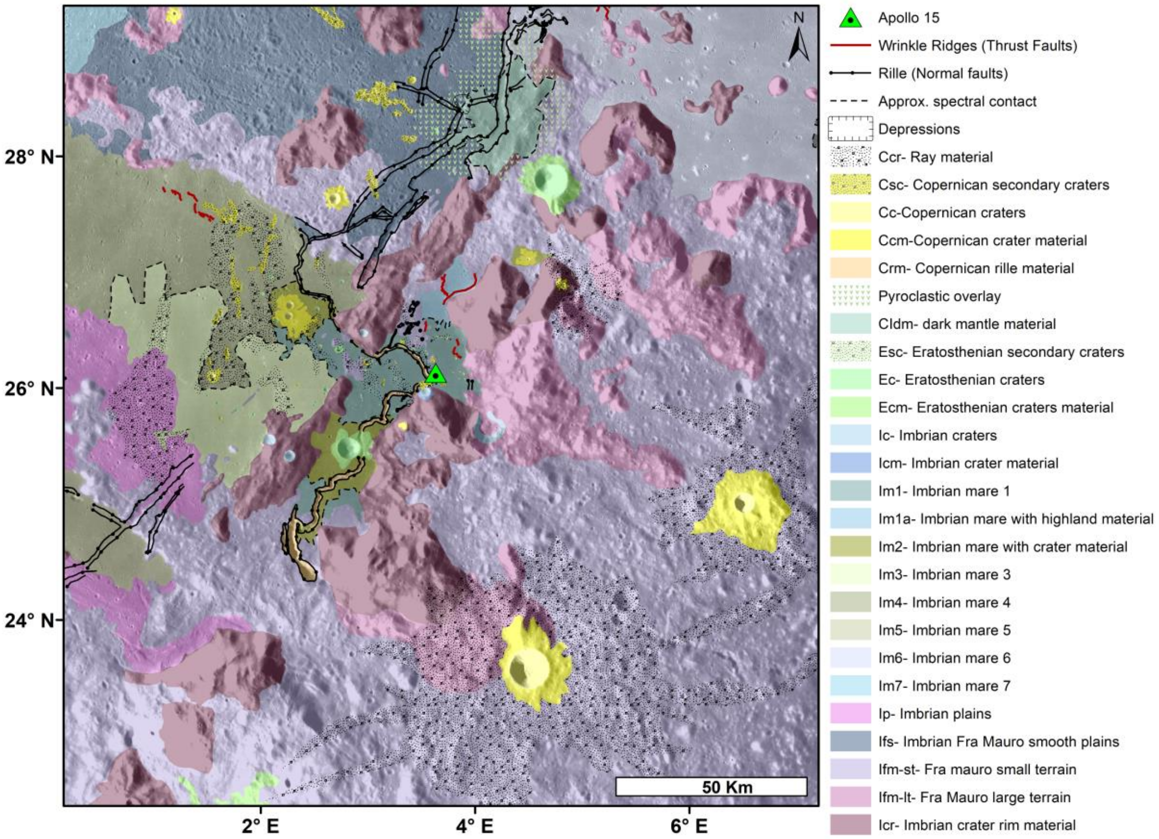

Figure 1. *Preliminary geological map of the Apollo 15 landing site showing Imbrium basin units such as: Imbrian basin rim (Icr), Imbrium basin ejecta (Ifm-lt. Ifm-st), a few mare units, young material in Hadley Rille, a network of the rilles and various generations of craters and their materials. The green triangle represents the position of the landing site.*

Eratosthenian and Imbrian periods [22]. The Copernican-aged Aristillus crater and apparently Eratosthenian Autolycus crater [21,22] rays and secondary craters cover a large area around the landing site. The young Copernican-aged crater to the southwest of the landing site also contributed to the resurfacing of the study area. The section of the Hadley rille to the west of the landing site is morphologically younger than the rille in the north. Other rilles in the mapping area are older than the deposited mare units.

CSFD Measurements: Count areas were carefully selected on the basis of our new geological map. First, we modified the areas selected by Neukum (1983), because his areas were found to cross geological unit boundaries in some cases, and discussed the results in [6]. The CSFD of this area (blue, *Fig. 2a*) was measured using LRO WAC data, which resulted in an $N(1)$ value of $2.98\text{x}10^{-3}$ km^{-2} and an absolute model age (AMA) of ~3.22 Ga. Next, we used the Kaguya ortho-image mosaic to measure the CSFD around the landing site (magenta, *Fig. 2a*), which gives an $N(1)$ value of $3.07\text{x}10^{-3}$ km^{-2} and an AMA of ~3.25 Ga. The CSFD measured on LRO NAC data (black, *Fig.* 2a) resulted in an $N(1)$ value of $2.94\text{x}10^{-3}$ km^{-2} and an AMA of ~3.21 Ga. The three measured values are consistent with the $N(1)$ value of $3.2\pm1.1\text{x}10^{-3}$ km^{-2} and age ~3.28 Ga, which was used by Neukum (1983) to calibrate the lunar cratering chronology [3]. Moreover, the recently determined isotopic age for the olivine normative basalts found at the landing site is ~3.26 Ga [12], which is also consistent with the obtained AMAs. Our measured $N(1)$ values and the recently determined isotopic ages of the samples can be used to confirm and slightly update the calibration point for the lunar cratering chronology [3,4].

Acknowledgements: WI and HH were funded by the German Research Foundation (Deutsche Forschungsgemeinschaft SFB-TRR170, subproject A2) and CvdB was supported by EU H2020 project #776276, PLANMAP.

References: [1] Neukum (1983) *NASA TM-77558*. [2] Neukum et al. (2001) *Space Sci. Rev. 96*, 55-86. [3] Iqbal et al (2019) *Icarus 333*, 528-547. [4] Iqbal et al (2018) *LPSC 49*, 1002. [5] Iqbal et al (2019) *LPSC 50*, 1005. [6] Iqbal, et al. (2020) *LPSC 51*, # 1073. [7] Borisov, et al (2019) *LPSC 50*, 2323. [8] Gebbing, et al (2019) *LPSC 50*, 2337. [9] Hartmann (1970) *Icarus 13*, 299-301. [10] Robbins (2014) *EPSL 403*, 188-198. [11] Stöffler et al. (2006) *Rev. Min. Geochem. 60*, 519-596. [12] Snape et al (2019) GCA. 266, 29-53. [13] Robinson et al (2010) *Space Sci. Rev. 150*, 81-124. [14] Barker et al. (2016) *Icarus 273*, 346-355. [15] Pieters et al. (1994) *Science 266*, 1844-1848. [16] Lemelin et al (2016) LPSC 47, 2994. [17] Kneissl et al. (2011). *PSS 59*, 1243-1254. [18] Michael et al. (2016) *Icarus 277*, 279-285. [19] Michael et al. (2012) *Icarus 218*, 169-177. [20] Howard (1971) USGS, I-723 [21] Carr et al (1971) USGS, I-723. [22] Hiesinger et al (2000) JGR 105, 29239-29275.

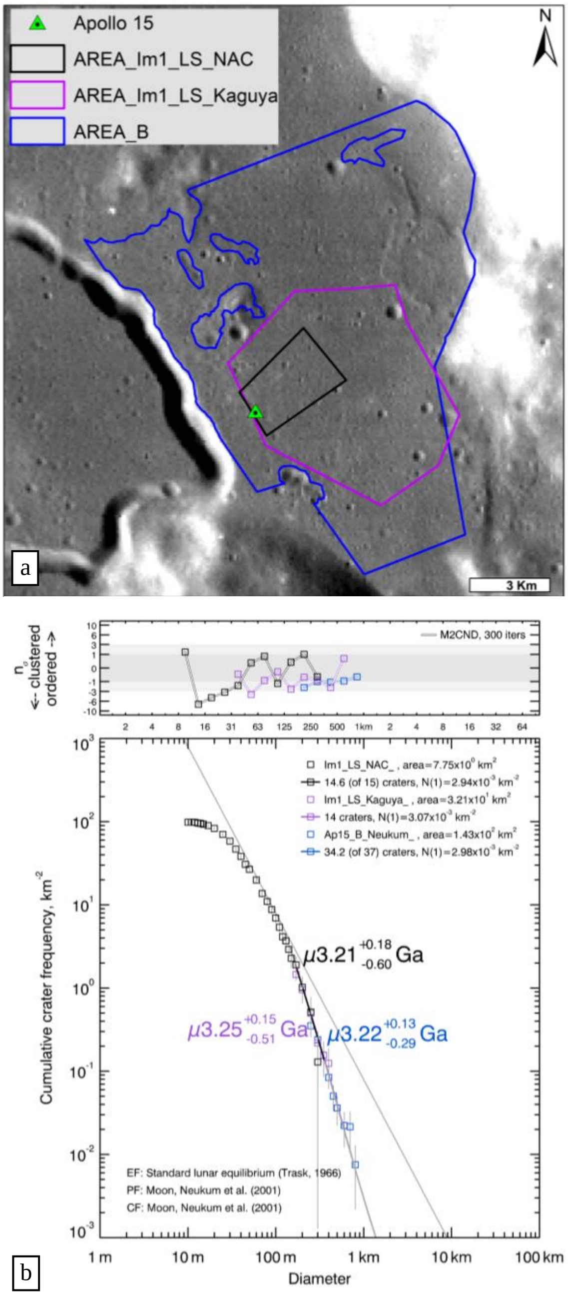

Figure 2. *Selected counting areas and the resulting absolute model ages around the Apollo 15 landing site. (a) The blue area was measured on the LRO WAC mosaic, the magenta area on the Kaguya mosaic, and the black area on an LRO NAC image. (b) CSFD measurements and absolute model ages of selected areas are shown in cumulative form. The panel above shows the randomness analysis of the count area, which is used to avoid contamination by clusters of secondary craters at the smallest diameters.*

Synthesis of Water from Intrinsic Solar Wind on the Moon.

B. M. Jones[1], A. Aleksandrov[1], T. M. Orlando[2], [1]Department of Chemistry, Georgia Institute of Technology, Atlanta, GA 30332, [2]Department of Physics, Georgia Institute of Technology, Atlanta, GA 30332, (thomas.orlando@chemistry.gatech.edu).

Introduction: The existence of physisorbed water (H_2O) [1] or the water equivalent in the form of solar wind implanted hydroxyls (-OH) [2] in lunar surface soils and rocks was postulated decades ago. Regrettably, initial analysis of Apollo samples indicated that water was absent and that previous observations of water were a result of atmospheric contamination [3]. However, attention to water on the moon was revived in response to latest remote sensing data culminating in the identification of OH/H_2O by the Moon Mineralogy Mapper (M3) [4], Visual and Infrared Mapping Spectrometer (VIMS) [5], and Deep Impact Extended Investigation (DIXI) [6]. In general, the sources of lunar water widely accepted by the community include: primordial water, water delivered via comets and meteorites, released during an impact event, and implantation from solar wind. However, we propose that an additional source term of water is prevalent and occurs on a daily basis on the lunar surface. Here, a small amount of molecular water is formed thermally (either diurnally or from an impact event) from recombinative desorption of -OH defects from implantation of solar wind protons.

Experimental Details: Second order (water formation) recombinative desorption activation energies of highland Apollo sample 15221 were determined utilizing temperature program desorption studies. Desorption at the grain/vacuum interface with re-adsorption as water transports though the porous medium and activated sub-surface diffusion/penetration were found to reproduce the experimental TPD signal. Signal from the grain/vacuum interface yielded the second order desorption activation energies and site probability distributions. The sample analyzed was Apollo 15 lunar sample 15221 and is a highland reference. Sample 15521 is considered mature with an I_s/FeO = 63. Briefly, sample 15221 has an average grain size 54 µm with olivine and pyroxene as the dominate minerals with a large percentage (37%) of agglutinate glass.

Results: Water production via recombinative desorption was assumed to have coverage dependent activation energies. Highland sample 15521 exhibited a broad distribution of binding site energies peaking at 120 kJ mol^{-1} extending to 300 kJ mol^{-1} at zero coverage limit with 100 kJ mol^{-1} at full coverage, as shown in Figure 1, corresponding to an onset temperature of 350 K for water production. The development and progression of the 2.8 µm optical signal on the Moon was simulated employing the measured experimental temperature driven water formation and desorption data. The results are shown in Figure 2 and display a latitude dependent OH signal with a very minor diurnal change.

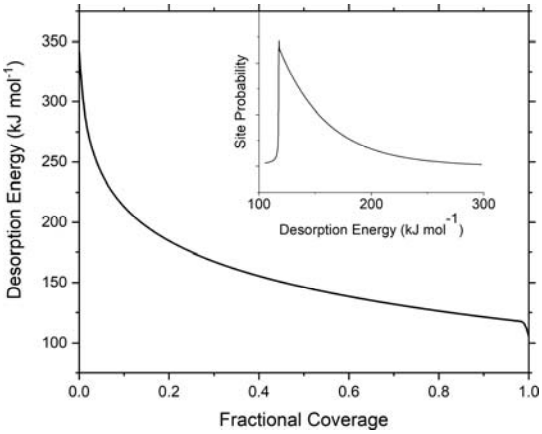

Figure 1: Recombinative desorption energies for Apollo Sample 15521. Inset displays site probability distribution.

Summary: The second order desorption activation energies were measured for lunar regolith samples. Utilizing a chemical kinetics model and the determined recombinative desorption energies, the evolution of –OH on the Moon was simulated and is shown in Figure 1. A balance between the second-order thermal processes and the proton implantation rate from the solar wind is the prevailing mechanism directing the latitude-dependent signal. Overall, the model is consistent with spatial (latitude) trends in the observed 2.8 µm feature on the Moon (Figure 2).

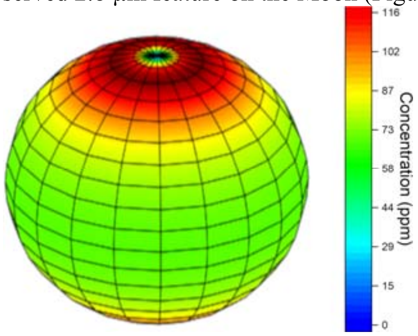

Figure 2: Hydroxyl concentration after simulating the solar wind-induced water cycle 3600 lunar days.

References: [1] Housley, R. M, et al. (1973) *LPS, IV*, 2737-2749. [2] Zeller, E. J, et al. (1966). *JGR,20*,4855-4860. [3] Taylor, S. R. (2016). Lunar science: A post-Apollo view. [4] Pieters, C. M, et al. (2009), *Science 326*, 568-572. [5] Clark, R. N. (2009). *Science*, *326*, 562-564. [6] Sunshine, J. M., et al. (2009). *Science*, *326*, 565-568.

Acknowledgments: This work was directly supported by the NASA Solar System Exploration Research Virtual Institute (SSERVI) under cooperative agreement numbers NNA17BF68A (REVEALS) and NNA14AB02A (VORTICES).

The Real Reasons We Explore Space and the Moon – We are today's Cathedral Builders

R. M. Kelso[1]
[1]Planetary Transportation Systems GmbH (PTS), Germany, robert.kelso@pts.space,

Introduction: I am convinced that if ESA and NASA were to disappear tomorrow, if we never put up another Hubble Space Telescope, never put another human being in space, people in Europe would be profoundly distraught. Americans and Europeans would feel that we had lost something that matters, that our best days were behind us, and they would feel themselves somehow diminished. Yet I think most would be unable to say why.

There are many good reasons to continue to explore space, which most Europeans have undoubtedly heard: for purposes of scientific discovery, economic benefit, and national security.

But these are not reasons that would make Europeans would miss our space program. They are merely the reasons we are most comfortable discussing. I think of them as "acceptable reasons" because they can be logically defended. When we contemplate committing large sums of money to a project, we tend to dismiss reasons that are emotional or value-driven or can't be captured on a spreadsheet. But in space exploration those are the reasons—what I think of as "real reasons"—that are the most important.

The return the cathedral builders made on their investment could not have been summarized in a cost/benefit analysis. They began to develop civil engineering, the core discipline for any society if it wishes to have anything more than thatched huts. They gained societal advantages that were probably even more important than learning how to build walls and roofs. For example, they learned to embrace deferred gratification, not just on an individual level, where it is a crucial element of maturity, but on a societal level, where it is equally vital. The people who started the cathedrals didn't live to finish them. The society as a whole had to be dedicated to the completion of those projects. We owe Western civilization as we know it today to that kind of thinking: the ability to have a constancy of purpose across years and decades.

It is my contention that the products of our space program are today's cathedrals. The space program satisfies the desire to compete, but in a safe and productive manner, rather than in a harmful one. It speaks abundantly to our sense of human curiosity, of wonder and awe at the unknown. Who can watch people assembling the greatest engineering project in the history of mankind—the International Space Station—and not wonder at the ability of people to conceive and to execute the project?

EUROPE’S COMMERCIAL LUNAR LANDER ALINA: INNOVATIONS FROM PLANETARY TRANSPORTATION SYSTEMS (PTS)

R. M. Kelso[1] and J. Eyer[2], [1]Planetary Transportation Systems GmbH (PTS), Germany, robert.kelso@pts.space, [2]Planetary Transportation Systems GmbH (PTS), Germany, jesse.eyer@pts.space

Introduction: Germany’s commercial lunar lander company, Planetary Transportation Systems (PTS) GmbH is developing its next iteration of our lunar lander in the ALINA lunar spacecraft series. ALINA will be capable of transporting 150 kg of commercial payloads from GTO to the lunar surface. Several key enabling technologies are employed on ALINA-2. A newly designed propulsion system provides the necessary thrust for the Power Descent Maneuver (PDM) to the lunar surface and a total v of 3700 m/s for all maneuvers. The motors can be pulsed to vary the thrust level and improve the controllability of the lander. During the PDM, ALINA’s GNC utilizes a combination of radar, laser altimeters, and crater navigation technology to facilitate a soft and accurate landing. Carbon fibre reinforced polymer is used strategically to lower the weight of ALINA’s main structure and landing legs, while phase changing materials are employed on units with high heatloads.

This important presentation will new updates to the community on the PTS’ current status of lunar landers and Moon missions within Europe.

AUTOMATIC PLANNING OF ROVER TRAVERSES. M. Killian[1], [1]Chair of Astronautics, Technical University of Munich, Boltzmannstr. 15, 85748 Garching, Germany (m.killian@tum.de).

Introduction: Currently, lunar poles are in focus of future exploration missions to the Moon. Recent investigations of remote sensing data suggests the presence of volatiles and water ice at or near the surface at the poles. [1-3]. In-situ measurements can provide precise data about volatile species on the Moon and their chemical composition. These measurements are important for both, science and exploration purposes. Sending exploration rovers to the poles of the Moon is the obvious choice in order to access different locations at the vicinity of a landing site for in-situ measurements. Sophisticated selection of waypoints is mandatory for a successful mission. However, planning of a feasible traverse along those waypoints represent a demanding challenge. Illumination conditions may vary drastically throughout a mission as well as the thermal environment for a rover. Consequently, an automatic optimisation of a traverse, which considers the thermal and energy state of the rover dynamically along the traverse, promises great potential to increase the chances of success of a mission.

Method: At the chair of Astronautics at the Technical University of Munich, a tool exists for the thermal simulation of the surface of the Moon (TherMoS) [4]. Its capabilities have been extended with a traverse optimisation of a rover system powered by solar energy (TherMoS-X). It can determine a short traverse between two points at a given start time under consideration of the energy state of a rover system. This includes amongst others the energy needed for thermal control as well as the energy needed for driving. This chapter describes the method for derivation of a near-optima traverse.

Simulation of temperatures of the lunar surface.

The first step is the simulation of temperatures of the lunar surface during the intended period of the investigated mission. An implementation of the thermal model of Hayne et al. [5] allows TherMoS-X to calculate those temperatures with topographic data from LRO LOLA for a selected region on the surface of the Moon. A more precise topography of co-registered LRO LOLA data is available for simulation at the south pole [6, 7]. A mesh of triangles represents the shape of the topography and a ray tracing defines the solar heat load on the triangles and their net infrared radiation. Resulting temperatures are stored at an interval of 30 min during the simulation.

Creation of optimisation maps

The second step is the creation of maps that the optimisation algorithm requires. Infrared heat fluxes and solar heat fluxes are calculated for a sphere that is placed on every centre of the triangles of the topography. TherMoS-X determines these heat fluxes at every position in the map every 30 min during the period of investigation. The shape of the rover defines how those heat fluxes are distributed amongst its geometry.

Creation of rover model

In the third step, the user has to define a thermal and power model of the rover. The power model can consider power demand for on board computer, for communication, and for driving where power depends on the mass of the rover, its speed, the amount of wheels, and the slope of the rover [8]. Solar cells provide energy to the rover system that consist also of rechargeable batteries. The thermal model is a standard lumped parameter model and depends on the rover system. The chosen approach for creation of maps with a sphere restricts the outer geometry of the rover to simple shapes.

Run optimisation

The last step is to run the optimisation algorithm. TherMoS-X uses the classic approach A* [9] for optimisation in an adapted version where the algorithm loses its capability to find the global optimum in favour of handling dynamic states of the rover system. Solutions converge to the shortest traverse possible by varying the capacity of the battery in steps. All solutions fulfil the criterion that the rover has sufficient power along the entire traverse.

Results and Discussion:

A region of interest between Faustini and Nobile [10] is investigated in this chapter. Figure 1 shows the region as used by TherMoS-X with the slope colouring the terrain.

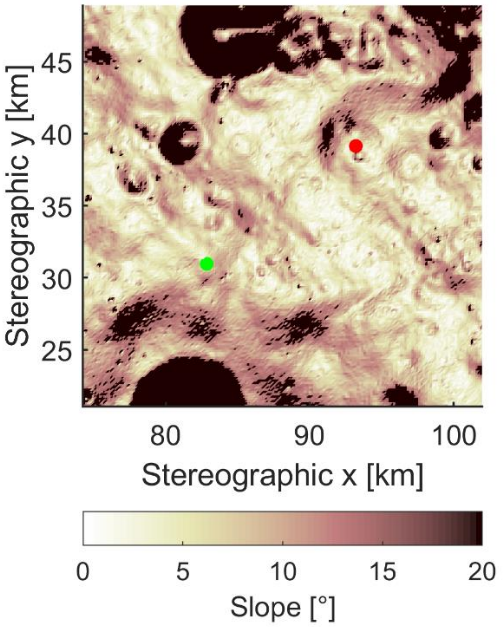

Figure 1: Investigated region between craters Shoemaker, Faustini and Nobile

Overall, slopes are benign in the area between start and goal point where slopes are below 10° most of the time. The solar powered rover drives with constant speed of 0.1388 m s^{-1}. It has a mass of 200 kg, solar cells with the size of 0.96 m^2 and varying battery capacity. The start date of driving is set to 9th of March 2022 at 16 o´clock. Investigation of illumination conditions during the year 2022 at the landing site revealed that this is a preferred period with favourable lighting conditions. TherMoS-X defines the traverse between the start point (green) and the goal point (red) if one exists where enough energy is provided to the rover system at any given time.

Figure 2 highlights resulting traverses of the optimisation algorithm. The green line is the shortest traverse possible when the energy state of the rover is neglected. It is the same that A* produces. All red lines are traverses determined by TherMoS-X with the adapted version of A*. They belong to different battery capacities. The one marked with white circles is the traverse with the lowest battery capacity possible for driving between both points. White crosses mark the second shortest traverse possible. It serves for comparison to the shortest traverse with respect to total distance and required battery capacity. The shape of traverses looks quite similar and so is the total length of them all. This is because the region has benign slope conditions together with nearly overall solar illumination in the investigated period. However, no traverse exist with permanent solar illumination of the rover. As a result, the rover requires having a battery of at least 70 W h.

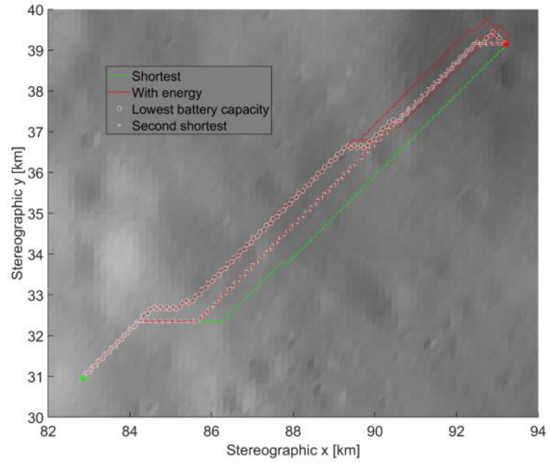

Figure 2: Resulting traverses of optimisation with TherMoS-X

Comparison of data in Table 1 shows that the lowest battery capacity needed to drive from start to goal is 70 W h whilst 260 W h are required to follow the shortest traverse. However, the shortest traverse is only 160 m shorter than the one with the lowest battery capacity. TherMoS-X even finds a traverse that is equal in total length to the shortest on but the required battery capacity is only 110 W h.

Table 1: Results of traverse optimisation

Traverse	Battery capacity [W h]	Total length [km]
Shortest (=A*)	≥ 260	14.93
Lowest Capacity	70	15.09
Second shortest	110	14.93

Conclusion: With the presented method, it is possible to find short traverses under consideration of the energy state of the rover. Results prove that sometimes a small detour of only ~1% of total length can reduce the required battery capacity tremendously. This is especially true at the lunar south pole with its rough topography and extreme lighting conditions. A careful selection of start date of operation seems to be mandatory for a mission to the lunar poles. Accurate and automated traverse planning represents a novel and beneficial addition to mission planning. The optimisation process within TherMoS-X will be able to handle multiple waypoints with time slots for operation in the future rendering TherMoS-X an even more powerful tool.

References:

[1] Paige et al. (2010), *Science*, 330, 479–482. [2] Hayne et al. (2015) *Icarus*, 255, 58–69. [3] Li et al. (2018) *Proceedings of the National Academy of Sciences of the United States of America*, 115, 8907–8912. [4] Hager, P. B. et al. (2014), *Planetary and Space Science*, 92 101-116. [5] Hayne et al. (2017) *J. Geophys. Res. Planets* 122, 2371–2400. [6] Gläser, P.; Haase, I.; Oberst, J.; Neumann, G. A. (2013) *Planetary and Space Science*, 89,111–117. [7] Gläser et al. (2014) *Icarus*, 243, 78–90. [8] Bekker, M. G. (1964) *SAE Transactions*, 72, 549–569. [9] Hart, Peter; Nilsson, Nils; Raphael, Bertram (1968) *IEEE Trans. Syst. Sci. Cyber*. 4, 100–107. [10] Flauhaut, J. et al. (2016) *European Lunar Symposium*, 19-20.

DIRECTLY MEASURING THE DISTRIBUTION OF SURFACE HYDROXYL/WATER ON THE MOON WITH LUNAR TRAILBLAZER.

R.L. Klima[1], B.L. Ehlmann[2,3], L. Bennett[4], D. Blaney[2], N. Bowles[5], S. Calcutt[5], M. Cannella[6], J. Dickson[2], K. Donaldson Hanna[7], C.S. Edwards[8], R. Evans[5], W. Frazier[3], R. Green[3], G. Helou[4], M.A. House[9], C. Howe[10], B. Marotta[6], J. Miura[2], C. Pieters[11], M. Sampson[6], E. Scire[4], R. Schindhelm[6], C. Seybold[3], K. Shirley[5], D. Thompson[3], J. Troelzsch[6], T. Warren[5], J. Weinberg[6]. [1]JHU Applied Physics Lab, Laurel, MD, [2]Div. Geological & Planetary Sciences, California Institute of Technology, Pasadena, CA, [3]Jet Propulsion Laboratory, California Institute of Technology, Pasadena, CA, [4]IPAC, California Institute of Technology, Pasadena, CA [5]Univ. of Oxford, United Kingdom, [6]Ball Aerospace & Technologies Corp., Boulder, CO [7]Univ. of Central Florida, Orlando, FL [8]Northern Arizona Univ., Flagstaff, AZ [9]Pasadena City College, Pasadena, CA, [10]Science & Technology Facilities Council, RAL Space, Didcot, United Kingdom [11]Brown Univ., Providence, RI

Introduction: Water on the Moon was one of the most exciting discoveries of the late 2000s. In 2008, [1] measured Apollo lunar glasses indicating magmas enriched in water. In 2009, OH and potentially H_2O were detected on the sunlit surface of the Moon by shortwave-infrared (SWIR) spectrometers, Chandrayaan-1/Moon Mineralogy Mapper (M^3), EPOXI/HRI-IR and Cassini/VIMS [2,3,4]. The LCROSS mission impact into a permanently shadowed region (PSR) in Cabeus crater detected H_2O ice [5], confirming inferences from a variety of remote sensing measurements and modeling [summarized in 6].

Key questions remain about lunar water, as well as the water cycle on airless bodies more generally, highlighted in the Decadal Survey [7]. Some PSRs have water ice, including those directly detected with M^3 using terrain-scattered light [8], while others show detections in some datasets and not others [6]. M^3 provided the best spatially-resolved (70-280 m/pixel) coverage for OH/water detection; however, because the discovery of water on the sunlit Moon was not expected, M^3 was not optimized to rigorously quantify its abundance. M^3's 3-µm cutoff wavelength results in ambiguities in the strength, shape, and exact position of the absorption band, which are critical for quantifying the abundance and form of hydrated species. Thermal emission further complicates the data, as thermal radiance needs to be removed from reflectance to accurately quantify the water band depth. Discrepancies exist between different thermal correction techniques, leading to conflicting results about whether the species is more likely water or hydroxyl, where it is concentrated, its abundance and whether it migrates over the course of the lunar day [e.g., 9-13].

Mission Objectives: In June 2019, NASA selected the SIMPLEx mission Lunar Trailblazer for Phase A/B development, culminating in a Preliminary Design Review in September 2020 and follow-on decision to proceed to flight. Lunar Trailblazer is optimized to make targeted measurements of the infrared properties of the lunar surface to directly measure the form, distribution, abundance and possible migration of water/OH on the lunar surface by acquiring compositional data to distinguish hydrated materials at the same time as data to derive surface temperature (Fig. 1). Lunar Trailblazer's objectives are to (1) detect and map water on the lunar surface at key targets to determine its form (OH, H_2O, or ice), abundance, and distribution as a function of latitude, soil maturity, and lithology; (2) assess possible time-variation in lunar water on sunlit surfaces; and (3) map the form, abundance, and distribution of water ice in the PSRs, finding any operationally useful deposits of lunar water and locations

Figure 1. Graphic of the simultaneous composition and temperature data that will be acquired by Lunar Trailblazer. The HVM^3 imaging spectrometer acquires data in 100's of infrared channels (0.6-3.6 µm) and nested within are simultaneous 14-channel LTM thermal IR multispectral data for temperature and silicate composition.

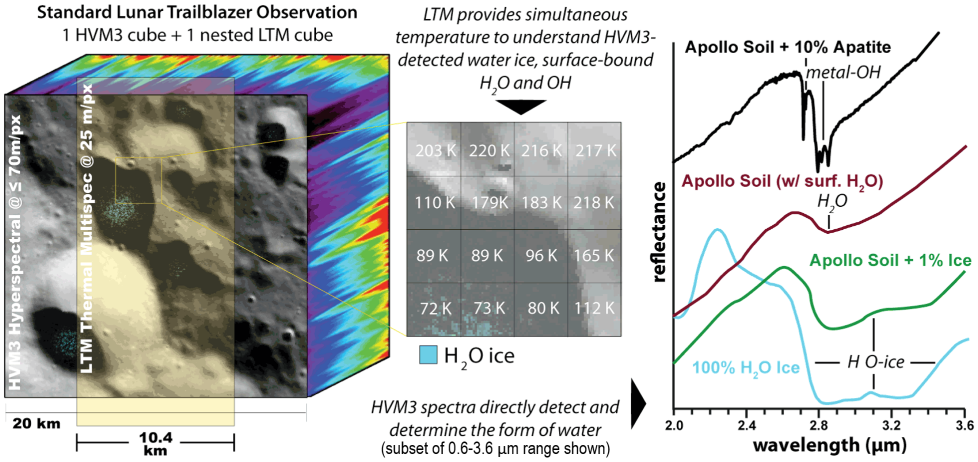

where it is exposed at the surface for sampling. In all cases, Lunar Trailblazer simultaneously (4) measures surface temperature to quantify the local gradients and search for small cold traps. These measurements advance understanding of volatiles on airless bodies by study of the lunar water cycle and incorporation of water into the lunar crust. Trailblazer will also—particularly if NASA selects a proposed communications system enhancement option—provide reconnaissance for candidate landing sites and provide the highest spatial and spectral resolution shortwave infrared and mid-infrared maps of lunar lithologies across the surface (e.g., irregular mare patches, silicic domes, spinel-rich locations, “dunite regions”, pyroclastic deposits).

Spacecraft, Mission Design & Instruments: Lunar Trailblazer is the first generation of ride-along planetary smallsats, selected under SIMPLEx. An ESPA Grande craft, compatible with most ESPA Grande rideshare opportunities to GTO/GEO and beyond, Lunar Trailblazer's schedule baseline is to be delivered for launch by end of 2022. During the Phase A/B study, NASA directed Trailblazer to baseline a launch opportunity with NASA's Interstellar Mapping and Acceleration Probe (IMAP), launching in 2024. From its separation with the primary, Trailblazer uses its solar electric propulsion system to enter into a ~100-km polar orbit around the Moon. In pushbroom mode, the spacecraft acquires data with its two science instruments: the High-resolution Volatiles and Minerals Moon Mapper (HVM^3), similar to M^3 but explicitly designed to measure hydrated materials, as well as the Lunar Thermal Mapper (LTM), a thermal infrared (TIR) mapping instrument to measure the temperature, composition, and thermophysical properties within each HVM^3 pixel (Fig. 2; Table 1).

Table 1. Current best estimate Lunar Trailblazer science observing parameters from 100±30 km orbit

HVM^3	
Spatial Sampling	≤ 100 m/pixel
Swath Width	≥ 20 km
Spectral Range	0.6 – 3.6 μm
Spectral Sampling	10 nm
SNR	>200 at 3-μm for low sun (85°) scene
Uniformity	>90% cross track
# Data Cubes*	1000
LTM	
Spatial Resolution	≤ 35 m/pixel
Spatial Width	≥ 10 km-swath
Thermal	Temp. retrieval 110-400K (± <5 K) 4 broad bands, 6-100 μm
Composition	7-10 mm 11 channels; < 0.5 mm
SNR	> 50 when sunlit
# Data Cubes*	1000

*optional greater (near-global) coverage under Data Enhancement Option

HVM^3 is a MatISSE-developed, JPL-built, modernized version of the successful M^3 imaging spectrometer and has been optimized to identify and quantify water [14]. LTM is a UK-contributed, University of Oxford/STFC RAL Space-built miniaturized TIR multispectral imager optimized to simultaneously measure temperature, composition, and thermophysical properties [15]. Over Trailblazer's 1-year primary science mission, each instrument will acquire ≥1000 targeted images. Targets include measurements to determine the composition of all PSRs using terrain-scattered light, and coverage of multiple latitudes at 3 times of lunar day.

Lunar Trailblazer is a PI-led mission at Caltech, managed by JPL with industry partner Ball Aerospace integrating the spacecraft. Science and mission operations will be led from Caltech. A student collaboration at Caltech and Pasadena City College involves undergraduate students—as well as graduate students and postdocs of the Co-Is—in all aspects of mission design and operations.

Acknowledgements: Thanks to the NASA SIMPLEx program and project offices and the entire team and staff contributing to the success of Lunar Trailblazer at Caltech, JPL, Ball, Oxford, RAL Space, UKSA, NASA, and other partners. For more information, see trailblazer.caltech.edu. Lunar Trailblazer is funded under NASA contract #80MSFC19C0042.

Figure 2. A schematic of the Lunar Trailblazer observing geometry, HVM^3 instrument, and LTM instrument.

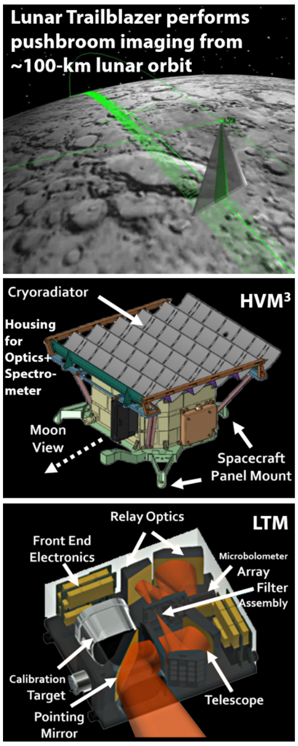

References: [1] Saal et al., 2008, Science [2] Pieters et al., 2009, Science [3] Sunshine et al., 2009, Science [4] Clark et al., 2009, Science [5] Colaprete et al., 2012, Science, [6] Hayne et al., New Approaches to Lunar Ice Detection and Mapping, KISS Study report, 2014 [7] Squyres et al., 2013, Visions & Voyages, [8] Li et al., 2018, PNAS, [9] Li and Milliken, 2016, JGR, [10] Li and Milliken, 2017, Sci. Adv. [11] Klima and Petro, 2017, Phil. Trans [12] Wöhler et al, 2017, Sci. Adv. [13] Bandfield et al., 2018, Nat. Geosci. [14] Thompson et al., 2020, LPSC. [15] Bowles et al., 2020, LPSC.

EXPLORING THE CONSEQUENCES OF BALLISTIC SEDIMENTATION ON POTENTIAL SOUTH POLAR ICE DEPOSITS ON THE MOON.

David A. Kring[1,2], [1]Center for Lunar Science and Exploration, Lunar and Planetary Institute, Universities Space Research Association, 3600 Bay Area Blvd., Houston TX 77058 USA (kring@lpi.usra.edu), [2]NASA Solar System Exploration Research Virtual Institute.

Introduction: Several competing processes would have affected the deposition and survival of volatile constituents, such was water ice, in the polar regions of the Moon. Here I briefly examine the consequences of ballistic sedimentation of impact ejecta into potential volatile-bearing regolith surfaces.

Evolving Volatile Sources: Sources of volatiles currently being explored are (i) impacting asteroids and comets, including micrometeoritic fractions, (ii) volcanic venting of lunar interior volatiles in flood basalt and pyroclastic eruptions, (iii) leaking of volatiles from the crust following moonquakes and impact events, and (iv) the solar wind.

Those sources operate on different timescales and/or operated at different times in lunar evolution.

Impact bombardment of asteroids and comets was more frequent during the first billion years of lunar evolution, although smaller objectis, including micrometeoritic debris, continues to pelt the surface today. (See sidebar for other impact cratering processes relevant to *in situ* resource utilization.) Volcanic venting occurred >4 Ga based on cryptomare and may have had two large surges of activity 3.8 and 3.5 Ga. Crustal leaking has occurred throughout lunar history, as has solar wind emplacement.

Evolving Catchments: Volatiles are potentially trapped in permanently shadowed regions (PSRs) where temperatures are below 100 K. PSRs are concentrated in the polar regions where dramatic topography shields areas from a Sun that is always low on the horizon. The floors of craters are often shadowed and suspected sites of volatiles are Haworth, Shoemaker, Faustini, de Gerlache, Amundsen, Cabeus, and Shackleton craters. Those craters do not have the same age. They were produced sequentially over about one billion years and, thus, were not always available to "catch" volatiles that were transported to the south polar region.

Potential Stratigraphy of Polar Ice Deposits: Because the sources of volatiles evolved over time and because catchments were created as a function of time, a stratigraphy of volatile deposits may have been created. A notional sequence is illustrated in **Figure 1** for the craters Haworth, Shoemaker, and Faustini.

Let's examine Faustini as an example. The crater was produced in the midst of the late heavy bombardment of the Moon. Once it had formed, volatiles delivered by impacting objects may have been trapped on its floor – if at that time Faustini was in the south polar region – over a period of about 200 Myr. Subsequently, the Amundsen crater was produced. It deposited ejecta over a broad region, including Faustini. Ice potentially accumulated again for about 100 Myr, possibly from a combination of sources (bombardment and volcanism), before ejecta from the Nobile impact event blanketed the area. Ice accmumulation may have resumed during an interval of about 650 Myr, before a trace of ejecta from the Shackleton crater landed on the floor of Faustini. Since that time, any volatile deposition was probably dominated by solar wind and sporadic impact events.

Missing from that notional stratigraphic picture is the consequences of ballistic sedimentation, when ejecta from younger, nearby craters lands. In **Figure 2**, the speed of impacting ejecta is plotted as a function of ballistic flight distance. Three cases are shown: for ejecta landing in Haworth, Shoemaker, and Faustini. Continous ejecta blankets may be expected if those craters are within one crater diameter of source craters. For example, Faustini may have been within the continuous ejecta fields from Amundsen and Nobile (green lines) and possibly within the continuous ejecta fields from Scott and Cabeus craters (yellow lines).

The speeds of the ejecta are of order 1000 km/hr, which should have eroded and mixed underlying material (i.e., ballistic sedimentation). When the impact debris landed at such high speeds, did it vaporize any volatiles in the regolith? If so, did the volatiles escape and get trapped elsewhere in the polar region? Or were the volatiles incorporated into the mixed ejecta blanket?

Discontinuous ejecta from more distant impact craters landed at higher velocitites. In the case of Faustini again, ejecta from Idel'son and Cabeus B landed with speeds between 2000 and 3000 km/hr.

The thickness of the continuous ejecta blankets were not inconsequential relative to the thickness of any ice-bearing regolith that may have accumulated between those events. Simple calculations suggest that in Haworth, ejecta layers from Shoemaker and Cabeus were 22^{+11}_{-8} m and 61^{+23}_{-17} m thick, respectively, before mixing with the substrate. In Shoemaker, ejecta layers from Faustini, Amundsen, and Nobile were 14^{+9}_{-5}, 28^{+17}_{-10}, and 33^{+17}_{-10} m thick, respectively. In Faustini, ejecta layers from Amundsen, Nobile, and Slater were 108^{+28}_{-22}, 36^{+17}_{-11}, and 4^{+3}_{-2} m thick, respectively. Those are thicker than regolith horizons that would probably have been <5 m thick, if not <1 m thick, based on a standard production rate and taking into account it may have been higher ~4.1 to 4.2 Ga when the craters formed.

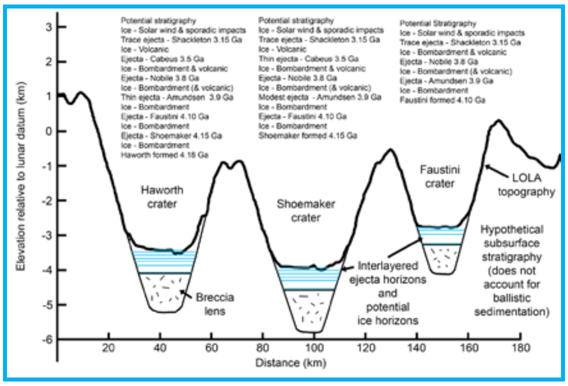

Figure 1. Notional stratigraphy of ice deposition and impact ejecta on the floors of three south polar craters: Haworth, Shoemaker, and Faustini. The topography is derived from LOLA data. A breccia lens is assumed to underly the original surface of the crater floor, based on observations of terrestrial craters.

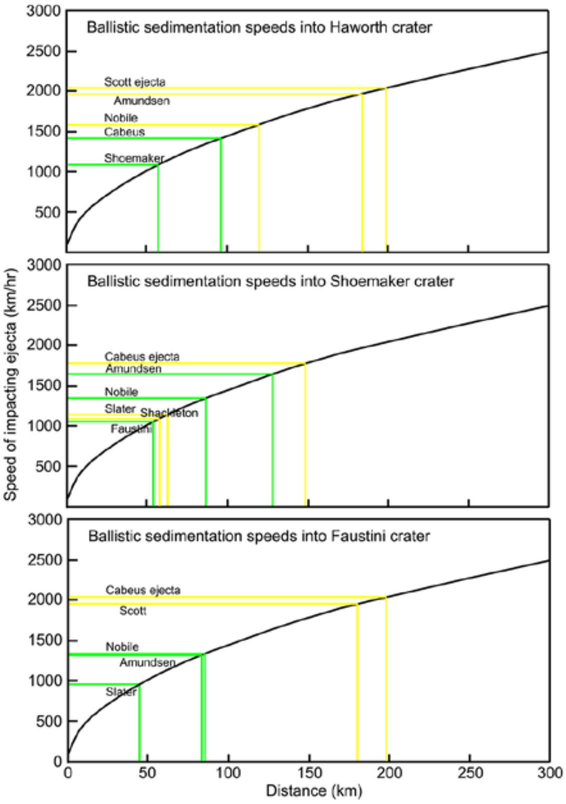

Figure 2. Speeds of ballistically emplaced ejecta in Haworth, Shoemaker, and Faustini craters from nearby craters (Scott, Amundsen, Nobile, Cabeus, Slater, and Shackleton). If a receiving crater is within a crater diameter of a source crater, a continuous ejecta blanket is likely and indicated with a green line. If a receiving crater is within two crater diameters of a source crater, then it is indicated with a yellow line. Speeds are scaled in kilometers per hour. For those who prefer to think in kilometers per second, 0.1 km/s is 360 km/hr and 1 km/s is 3600 km/hr. The escape velocity of the Moon is ~2.4 km/s

Impact cratering is the single most important geologic process affecting ISRU prospects.

1. The topography of impact craters in the polar regions produces the permanently shadowed regions (PSRs) where volatiles can be trapped.
2. Impacting asteroids (and, to a lesser degree, comets) were a source of the volatiles that could be trapped in those PSRs.
3. The largest impact events altered the spin axis of the Moon and, thus, the locations of PSRs where volatiles could accumulate.
4. The largest impact basins thinned the crust, allowing large volumes of magma to reach the surface and vent volatiles, providing another source of volatiles that could be trapped in PSRs.
5. Impact ejecta from cratering events covered (and potentially reworked via ballistic sedimentation) horizons of ice deposited in PSRs, producing a stratigraphic succession.
6. Ancient impact basins provided catchments for flood basalts (mare) that contain ilmenite that can be chemically modified to produce oxygen.
7. Ongoing impacts, including micrometeoritic impacts, have infused the regolith with meteoritic-derived volatile abundances. Those volatiles, when combined with volatiles from the solar wind, provide a recoverable reservoir everywhere on the Moon. They have also infused the soil with meteoritic metal, which is another potential resource for a sustainable exploration program.
8. The largest of the impacts produced melt sheets that may have differentiated, potentially forming ore deposits of metal and sulfide.

LUNAR X-RAY AND GAMMA-RAY SPECTROSCOPY WITH MINIATURIZED DETECTOR ON CUBESAT PLATFORM

M.Lavagna[1], F.Fiore[2], [1]Politecnico di Milano,Aersopace Science & Technology Department, michelle.lavagna@polimi.it, via La Masa 34, 20156 Milano, Italy,[2]Istituto Nazionale di Astrofisica, Osservatorio Astronomico di Triestre, Via Tiepolo 11, I-34143 Trieste, Italy

Introduction:

Assessing the chemical composition of the Moon is a key part of its investigation. Elements can be grouped according to their condensation and geochemical behavior, and thus chemical abundances of key elements can be used to asses both the origin and the evolution of the body.

The relative abundance of the surface (down to a few μm) major elements with atomic number ≤20 can be estimated using X-ray fluorescence, using solar X-rays to excite element's atoms (both quiescent Sun X-ray emission, in particular during solar maxima, and solar flares).

Only an handle of successful X-ray fluorescence experiments have been flown so far, including Apollo15 XRFS, Chandrayaan-1 C1XS, SMART-1 D-C1XS at the Moon, Messanger-XRS, BepiColombo-MIXS at Mercury, and NEAR-XRS at EROS, Hayabusa-XRS at Itokawa, OSIRIS-REX/REXIS at Bennu (Allen et al. 2013, arXiv:1309.6665 and refs. therein).

The main goal of fluorescent X-ray spectroscopy of asteroids is to determine the intensity of Fe-L, Fe-K, Al-K, Mg-K, Si-K complexes and S-Ka, S-Kb fluorescent lines. From these lines mass abundance ratios can be determined [Mg/Si], [Fe/Si]. The comparison of these abundance ratio to those of meteorites can understand whether the surface of the Moon resembles a particular chondritic meteorite.

Gamma-ray spectroscopy of nuclear lines can also be used to assess abundances of elements in the planetary surface (down to 10-20cm, e.g. Reedy et al. 1978, Proc. Lunar Planet Sci. Conf. 9th 1978). The main source of gamma-ray lines are: decay of natural radionuclides, reaction induced by energetic cosmic rays, capture of low-energy neutrons, and solar-proton induced radioactivity. Gamma-ray spectroscopy can provide information on many elements, including those with high atomic number, hardly accessible to X-ray fluorescence spectroscopy. Several successful gamma-ray experiment have been performed so far, including early spectroscopy of the Moon (Luna10, Apollo15, 16), Mars (Mars-5). More recently, Kayuga gamma-ray spectrometer obtained a detailed mapping of radioactive elements on the Moon (K, Th, U), as well major elements, O, Al, Mg, Si, Ca, Ti, Fe (Yamashita et al. EPSC Abstracts Vol. 5, EPSC210-580, 2010, Hasebe et al. Proc. Int. Workshop Advances in Cosmic Ray Science J. Phys. Soc. Jpn. 78, 2009). Other lunar experiments include Lunar prospector and Chang'E. Other experiments include more Mars spectroscopy (MARS Odyssey) Mercury (Messenger) and the asteroids EROS (NEAR) and 4 Vesta (Dawn).

The K/Th ratio is a diagnostic of the body bulk composition and provide information about where and when the body was formed.

The collecting area of most X-ray and gamma-ray spectrometers used for planetary observations is quite small, a few cm2. The REXIS instrument working today at Bennu as a collecting area of 25cm2. The largest instrument flown so far is the Kaguya-XRS with a collecting are of 100cm2.

A new miniaturize payload is here proposed, currently under development for astrophysics goals and to be installed on a 3U cubesat platform; the sensors uses GAGG scintillator crystals and Silicon Drift Detectors to both detect direct X-ray photons and optical photons produced in the scintillators by interaction with gamma-rays, and can cover a unique wide band, from a few keV to several MeV, providing at the same time both X-ray fluorescent spectroscopy and gamma-ray spectroscopy. The collecting area of a compact instrument (~3-4kg) can be conservatively ~100cm2. A passive collimator can shield the SDD from most Cosmic X-ray Background, reducing the background at energies <20keV, where it is largely dominated by the CXB. Laboratory calibration in the next few months will provide more precise numbers on the resolution achievable.

The gamma-ray line sensitivity of this instruments with collecting area ~ 100 cm2 and active anticoincidences (efficiency $\epsilon \approx$ twice that of Kayuga spectrometer) should therefore be a factor several better than that of other planetary gamma-ray spectrometers.

The paper shows the proposed scientific mission goals around which the miniaturized payload is designed, and its possible embarking on a cubesat like space segments, 6U large; the whole feasibility study for a smallsat scientific mission is presented, showing the generality of the approach and its applicability also for small bodies exploration as well.

NU-LHT-2M LUNAR SIMULANT CHARACTERISATION AND REACTIVITY MODELLING FOR RESOURCES EXTRACTION

M.Lavagna, G.Zanotti, I.Troisi, Politecnico di Milano,Aersopace Science & Technology Department, michelle.lavagna@polimi.it, via La Masa 34, 20156 Milano, Italy

Introduction: At the end of this decade the world is preparing to come back to the Moon with more specified scientific interests and with the perspective to bring humans back to the lunar surface to perform exptensive exploration of our satellite.

To this end a well structured techonology development shall be put in place which, to be credible, must include activities focused on verifying and validating on ground many different aspects of the lunar scenario.

Surface activities and science on the Moon are strongly affected by the regolith features, the peculiar material the lunar surface is made of. It is, then, obvious that the ground verification asks first for a simulant material availability which replicates the real planetary sand at te most. This is the case, for the highlands regions, of the NU-LHT-2M, considered in this paper, the production of which is standardised from both mineralogic composition as well as granularity.

However, many activities foreseen to occur on the Moon surface, ask for a more detailed soil features definition as a obliged step to run reliable tests on ground.

In particular, soil movimentation and interaction with robotics asks for the reology and electrical features regolith characterisation; volatiles or oxygen and metal extraction, as well as 3D printing performing, ask for the thermo-mechanical and electrical properties identification.

At Politecnico di Milano, together with the support of many different external labs, the NU-LHT-2M simulant has been fully characterized in terms of granularity, mineralogy,chemical composition, electrical and thermal conductivity and permissivity and floability to address at the best a facility implementation for different lunar surface activities feasibility assessment, technological challenges addressing and science goals reachability verification.

In particular, the information got from the simulant characterisation, drove the design of a plant and its operational procedures, for oxygen extraction from regolith with reduction processes. Each critical aspect of this kind of plant, risen by the feedstock characteristics, is discussed and the rationale for a specific plant component design highlighted.

The paper starts presenting the performed characterisation tests and discussing the results in terms of most relevant effects in driving anyt tool in strinct interaction with the soil.

Then, the charbothermal and hydrogen reduction processes fot oxygen extraction are introduced, toghether with their kinetic numerical modelling, and Gibbs free energy identification. This analysis, which consider the real feedstock mineralogy composition, helps understanding how to tune the different processes in terms of feedstock preparation, reactant (if any) fluxes, process temperature to maximize the yield.

NASA MOON TREK APPLICATIONS IN LUNAR EXPLORATION AND SCIENCE. E. S. Law[1], B. H. Day[2], and the NASA Solar System Treks Team[1], [1]Jet Propulsion Laboratory, California Institute of Technology. M/S 168-200. 4800 Oak Grove Dr. Pasadena, CA, USA 91109. (Emily.S.Law@jpl.nasa.gov, +01-818-354-6208), [2]NASA Solar System Exploration Research Virtual Institute. NASA Ames Research Center. M/S 17-1. Moffett Field, CA, USA. 94035. (Brian.H.Day@nasa.gov, +01-650-604-2605).

Introduction: NASA's Moon Trek (https://trek.nasa.gov/moon/) is one of a growing number of interactive, browser-based, online portals for planetary data visualization and analysis produced by NASA's Solar System Treks Project (SSTP). Moon Trek continues to be enhanced with new data and new capabilities enabling it to facilitate the planning and conducting of upcoming lunar missions by NASA, its commercial partners, and its international partners.

A Comprehensive Online Web Portal: Developed at NASA's Jet Propulsion Laboratory (JPL) and managed as a project of NASA's Solar System Exploration Research Virtual Institute (SSERVI) at NASA Ames Research Center, Moon Trek is a browser-based web portal. There is nothing additional to buy or install. Moon Trek provides a suite of interactive tools that incorporate observations from past and current lunar missions, creating a comprehensive lunar research Web portal. The online Web portal allows anyone with access to a computer to search through and view a vast number of lunar images and other digital products. The portal provides easy-to-use tools for browsing, data layering, data product blending, and feature search, including detailed information on the source of each assembled data product and links to NASA's Planetary Data System. Interactive maps, include the ability to overlay a growing range of data sets including topography, mineralogy, abundance of elements and geology. In 2020, SSTP introduced a new and improved release of Moon Trek featuring capabilities such as spatial search, tools and layers that are now consistent across polar and global projections, and a more intuitive layout for interfacing with Trek data.

A Diverse Lunar Analysis Toolkit: Moon Trek features a generalized suite of tools facilitating a wide range of activities including the planning, design, development, test and operations associated with lunar sortie missions; robotic (and potentially crewed) operations on the surface; planning tasks in the areas of landing site evaluation and selection; design and placement of landers and other stationary assets; design of rovers and other mobile assets; developing terrain-relative navigation (TRN) capabilities; deorbit/impact site visualization; and assessment and planning of science traverses.

Its baseline visualization and analysis tools, available to all users, allow users to measure the diameters, heights and depths of surface features. Users can plot Sun angles (altitude and azimuth for user-specified points over user-specified time/date ranges and time intervals). Custom 2D visualizations can be easily rendered based on polar and equatorial projections. Visualizations in 3D are equally easily rendered and provide the capability for interactive flyovers of lunar terrain. A virtual reality component allows the user to draw a path using the web client, and then fly along that path in virtual reality using VR goggles. User-specified bounding boxes can be used to generate STL and/or OBJ files to create physical models of surface features with 3D printers. In addition to visualizing a vast range of data products in multiple ways, users can access the metadata for the individual data products and can download any of our served data products for use in other applications.

More advanced account-level tools allow users to perform more computationally-intensive analyses. These include ray-traced lighting analysis for user-specified areas over user-specified time/date ranges and time intervals. Lighting analyses also produce maps of watts per square meter for the area specified. Electric surface potential analyses can also be generated for user-specified areas and intervals. Machine learning-based hazard analyses include boulder detection and distribution, crater detection and distribution, and slope analysis. Large data products can be subsetted, allowing users to download regions of specific interest. The LRR/LLR Geometry Calculator will allow researchers to find, visualize, and analyze images taken by the Lunar Reconnaissance Orbiter (LRO) that are applicable to Lunar Laser Retro-Reflector (LRR) and Lunar Laser Ranging (LLR) studies and planning [1].

Important new tools are currently being integrated into Moon Trek. A Convolutional Neural Network (CNN) is being implemented, trained to automatically detect rockfalls in LRO NAC imagery, and integrated into Moon Trek. Such rockfalls are interesting because they enable remote analysis of tectonic activity, surface evolution, and mechanical surface properties [2]. A new line-of-sight tool will support detailed studies of solar illumination, line-of-sight communications with the Earth, and communications with assets in lunar orbit.

Significant advantages are afforded by Moon Trek's features facilitating collaboration among members of distributed teams. Team members can share visualizations and add new data to be shared either with the entire Moon Trek community or only with members of their own team. Sharing of multi-layered visualizations is made easy with the ability to create and send URL-encoded visualization links.

Moon Trek continues to be enhanced with the addition of additional data products and new tools. Enhanced integration with the growing number of other portals of SSTP has been provided by its incorporation into the new SSTP home site (https://trek.nasa.gov). This site provides a common entry point into the various Trek portals as well as a number of additional supporting features.

Diverse Applications for Lunar Exploration: Moon Trek is being used for growing number of mission planning, mission support, technology development, and lunar science applications. Using an in-house stereo workflow, SSTP is able to produce new NAC-based high-resolution mosaics (Fig 1) and DEMs. These are particularly useful in our work with Commercial Lunar Payload Services (CLPS) providers using Moon Trek in site characterization for landing and surface operations. Moon Trek is able to significantly enhance the value and utility of mission data by putting it in the context of a vast collection of other data products gathered from many instruments on many missions. We are taking advantage of this as we plan specific enhancements optimizing Moon Trek for use as a support tool for the science backroom of NASA's upcoming VIPER mission. SSTP continues to work with the Italian National Institute of Nuclear Physics in enhancing Moon Trek's capabilities for LRR/LLR studies. The South Korean Space Agency is planning the use of Moon Trek as a mission planning tool for their Korean Pathfinder Lunar Orbiter, and as a testbed for development of terrain relative navigation systems. SSTP is working with NASA's Astromaterials Acquisition and Curation Office to integrate their database of Apollo lunar samples into Moon Trek. This will allow researchers to enter a catalogue number for a specimen into Moon Trek, and have the portal take them to the collection site where they can study the sample's setting and geological context. We are currently extending the capabilities of the Solar System Treks to facilitate terrestrial analog studies that support human lunar exploration missions. Moon Trek is the direct successor to the Lunar Mapping and Modeling Portal (LMMP). While LMMP was built to support landing site characterization for the Constellation Program, Moon Trek greatly enhances those capabilities and extends that heritage into the age of Artemis.

Acknowledgments: The authors would like to thank the Planetary Science Division of NASA's Science Mission Directorate, the Science Engagement and Partnerships Division of NASA's Science Mission Directorate, and the Advanced Explorations Systems Program of NASA's Human Exploration Operations Directorate for their support and guidance in the development of Moon Trek.

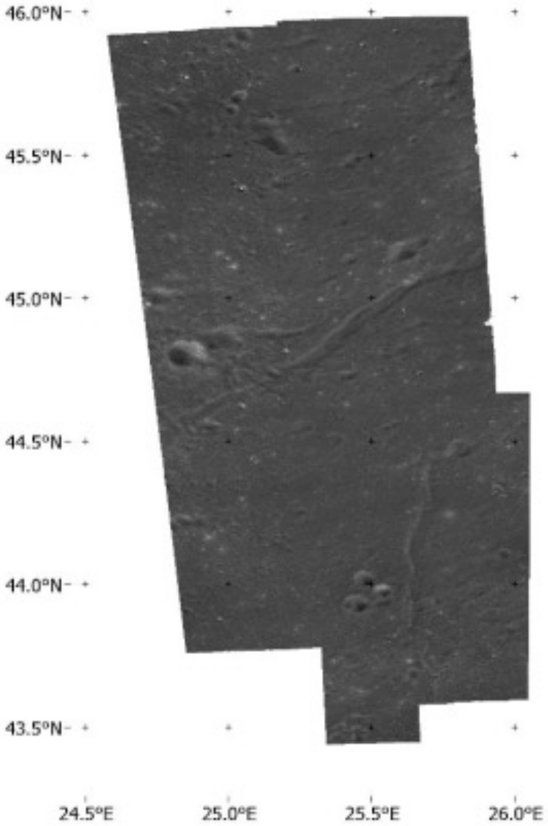

Fig. 1. Moon Trek Orthophoto mosaic of the Lacus Mortis CLPS target site

References:

[1] Law E. S. et al (2019), Applications and Planning for Lunar Laser Retroreflector Studies, European Lunar Symposium 2019

[2]Bickel V. T., Law E. S., Day B. H. (2019), A Big Lunar Data Application: Deep Learning-Driven Rockfall Detection and Mapping with NASA's Moon Trek, NASA Exploration Science Forum 2019

A MICROWAVE HEATING DEMONSTRATOR (MHD) PAYLOAD CONCEPT FOR LUNAR CONSTRUCTION AND VOLATILE EXTRACTION.

S. Lim[1] (sungwoo.lim@open.ac.uk), S. Reeve[2], A. D. Morse[1], A. Garbayo[2], J. Bowen[3], and M. Anand[1,4], [1]School of Physical Sciences, The Open University, Milton Keynes, MK7 6AA, [2]Added Value Solutions UK Ltd., [3]School of Engineering and Innovation, The Open University, Milton Keynes, MK7 6AA, [4]Department of Earth Sciences, The Natural History Museum, London, UK.

Introduction: A sustainable and affordable exploration of the Solar System cannot rely solely on Earth's resources and must use materials obtained and processed *in situ*. The current Solar System exploration road map, put together by a consortium of international space agencies envisage a longer-term presence on the Moon by 2028. Thus, the development of *In-Situ* Resource Utilisation (ISRU) to offset the need to transport all materials from the Earth is essential and timely. Based on our expertise in lunar science and building space instrumentation at the Open University, and by working in partnership with our industrial partners, we have established a consortium to develop a microwave heating-based 3D printing technique as a fabrication method for extra-terrestrial construction process and resource extraction, including oxygen, water and metal (e.g. iron). Alignment of our proposed work with the Global Exploration Roadmap (GER) is shown in Figure 1.

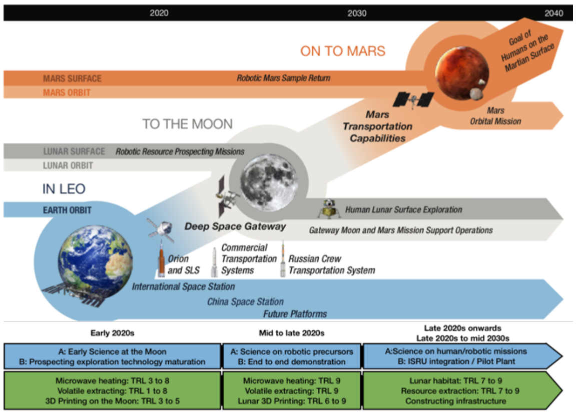

Fig 1: Alignment of our proposed research on lunar construction and ISRU activities (green) with GER and ESA's ISRU mission roadmap (blue boxes).

For an extended stay on the Moon, humans will require habitation with substantial shielding for protection from radiation and micrometeorites. Lunar regolith (soil) is a readily available *in-situ* resource, which can be thermally treated to extract oxygen and water, as well as for construction. For example, lunar habitats and infrastructure can be built by robots using additive manufacturing techniques [1]. Due to the volumetric heating characteristic, intrinsic to microwave heating, it is a more energy-efficient process than solar or laser sintering for large-scale manufacturing and construction purposes. Proof of concept experiments [2-4] have demonstrated that microwaves couple efficiently with lunar regolith simulants; therefore, microwaves could be an efficient mechanism to sinter and melt lunar regolith to build 3D structures, and also enable the extraction of volatiles.

These experiments are based on simulated conditions and materials; thus, there is missing information on microwave heating of lunar regolith, which includes the effects of nanophase iron (np-Fe^0) produced via space weathering, the highly electrostatic nature of the particles, and irregular particle geometries of the real lunar soil. Through a UK Space Agency (UKSA) grant (NSTP GEI) we are developing a conceptual design of the Microwave Heating Demonstrator (MHD) payload that could be delivered to the lunar surface for *in-situ* experiments via the ESA's HERACLES mission or NASA's CLPS programme. Here, we provide further details of our conceptual design of a MHD payload.

Microwave heating of lunar regolith: Our simulation [2] and lab experiments [3,4] have demonstrated that lunar regolith (highlands and mare) and simulant JSC-1A can be sintered and melted using as low as ~200-250 W input power under ambient atmospheric conditions while experiencing severe thermal runaway. It was found that (i) microwave energy couples well with both highlands and mare lunar regolith (numerical modelling) and their simulants JSC-1A (numerical modelling and experiments), and (ii) the temperature threshold of thermal runaway exists between 600 and 700 °C depending on the phase transition of the material. Further, through lab experiments under various input powers, it was confirmed that temperature (but not input power) is the main criterion for thermal runaway in microwave heating.

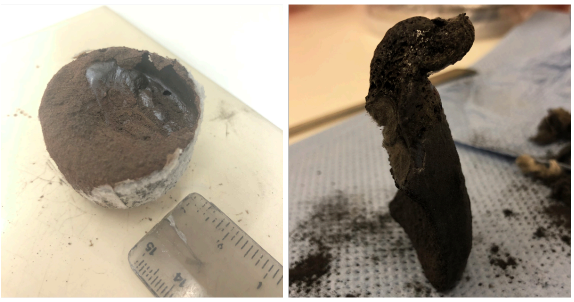

(a) (b)

Fig 2: Microwave heated JSC-1A under (a) ambient pressure, and (b) low-pressure (4.6e^{-5} hPa).

In the context of a MHD operating at the lunar surface, it is important to investigate the microwave heating behaviour of lunar material under reduced pressues. In this respect, our preliminary lab experiment involving microwave heating of lunar simulant JSC-1A under lower-pressure generated plasma due to the ionized volatiles, and a highly porous molten specimen, resulting in a lower yield rate of the sintered and melted specimen (13 g out of 50 g) than that of the specimen treated under a standard ambient pressure (50 g out of 50 g) as shown in Fig 2. Somewhat speculative, but possible, reasons include (i) less microwave energy absorption due to the plasma formation, and (ii) severe porosity of the specimen due to the rapid release of volatiles which possibly restricts the spread of the hotspot region due to poorer heat transfer through the porous regions.

Microwave Heating Demonstrator (MHD): In order to design the MHD, the payload requirements were first reviewed. These included the available power, interface, and mass/volume of the payload, from a potential lunar ISRU lander. Pre-defined computational simulations using COMSOL Multiphysics software were also conducted to determine the optimal input power, heating time, specimen mass and crucible shape for the experiment, which maximises the energy absorption while minimising the total energy input between room temperature and melting point. Then, a sequential operation of each experiment was carefully planned, followed by developing a conceptual hardware design for the MHD payload based on the functional diagram of MHD (Fig. 3). The MHD payload consists of a solid-state microwave generator, bespoke cavity, mass spectrometer, pyrometer, data logger, telemetry and crucible delivery unit with an optional material collection unit.

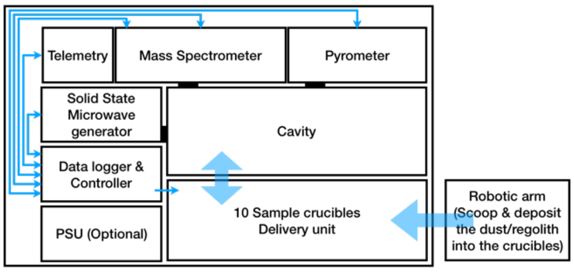

Fig 3: Functional diagram of MHD

The main functions of MHD and the sequence of experiment are to (i) collect up to ten lunar regolith samples (50 g each) depending on the lander mission and the lander path/destination, (ii) heat each specimen with 250 W of input power for up to 60 minutes, and (iii) measure the temperature of the specimen and released volatile profiles every second. The measurement of the specimen temperature is continued until it is cooled down to ambient temperature. More specific functions and a 3D CAD model of a MHD conceptual design of MHD will be presented at the meeting.

The MHD payload will produce scientifically invaluable findings in their own right. The outcomes of the experiments would also fill the knowledge gaps in Space Science and Engineering disciplines by revealing the physicochemical characteristics of thermally treated lunar regolith using microwave energy under the real lunar environment. It will provide useful insight into the properties of materials which have been thermally treated material properties by microwave energy on the Moon and potential opportunities on other airless bodies with near-vacuum atmospheres, e.g. Martian moons and asteroids, which are of interest to exploration communities worldwide. Ultimately, our research will lead us to realise lunar construction and ISRU mission activities, as indicated in Figure 1.

Acknowledgement: The authors acknowledge the funding from the UKSA's National Space Technology Programme (NSTP), Grants for Exploratory Ideas (GEI2-037) and support from the Open University's Space SRA.

References: [1] Lim, S. et al. (2017) *Adv. in Space Research J.*, 60(7), 1413-1429. [2] Lim S. and Anand M. (2019) *Special Issue on Space Resources, Planet. and Space Sci J.,* 179(104723). [3] Lim S. et al. (2019) *Lunar ISRU2019*, Abstract #5047. [4] Lim, S. et al. (2019) *ELS2019,* Session 6: Prospecting and ISRU.

INVESTIGATION OF MICRO-TEXTURES AND STRENGTHS OF MICROWAVE HEATED SAMPLES OF LUNAR SIMULANT JSC-1A UNDER DIFFERENT INPUT POWERS.

S. Lim[1] (sungwoo.lim@open.ac.uk), J. Bowen[2], M. Anand[1,3], G. Degli-Alessandrini[1], V. LevinPrabhu[1], A. D. Morse[1], and Aidan Cowley[4], [1]School of Physical Sciences, The Open University, Walton Hall, Milton Keynes MK7 6AA, [2]School of Engineering and Innovation, The Open University, Walton Hall, Milton Keynes MK7 6AA, [3]Department of Earth Sciences, The Natural History Museum, London, UK, [4]European Astronaut Centre, Germany.

Introduction: At the Moon, the regolith (soil) is a readily available resource, which can be thermally treated for extracting oxygen and water, as well as, for fabricating construction components [1]. Due to the volumetric heating characteristic, intrinsic to microwave heating, it is considered as a more energy-efficient process than solar or laser sintering for large-scale manufacturing and construction purposes. Proof of concept experiments and numerical modelling [2-4] have demonstrated that microwaves couple efficiently with lunar regolith simulants. Therefore, microwaves could be an efficient mechanism to sinter and melt lunar regolith to build 3D-printed structures, while also enabling the extraction of volatiles. In the context of *In-Situ* Resource Utilisation (ISRU) to offset the need to transport all materials from Earth, it is highly desirable and timely to align with the current Solar System eploration road maps of international space agencies.

At the Open University we have been leading the development of a microwave heating-based 3D printing technique to be used as a preferred fabrication method in extra-terrestrial construction processes and resource extraction, including oxygen, water and iron. As part of this research, a series of experiments were conducted to understand the microwave sintering/melting behaviour of lunar regoith [2] and simulants [3,4]. In this contribution, we describe different microtextures that were observed in microwave heated lunar simulant JSC-1A specimens under different input powers. This is important because it would allow us to utilise a specific input power of microwave for specific applications.

Comparison of heated specimens by input power: Although a higher input power of microwave energy will cause a faster and higher yield of sintered/melted part from a specimen, the differences in micro-structures as a function of input power has not been previously investigated. In this study, we have used five different input powers for heating JSC-1A with the same total input energy of 900 kJ, allowing for a meaningful comparison. The heating conditions for each input power were (a) 900 seconds at 1,000W, (b) 1,125 seconds at 800 W, (c) 1,500 seconds at 600 W, (d) 2,250 seconds at 400 W, and (e) 3,600 seconds at 250 W. The thermally treated specimens were analysed using a Quanta200 SEM equipped with Oxford Instruments EDS technique for textural/mineralogical analysis. In addition to examining specific areas/zones at high-resolution (e.g. ~5,000-10,000x magnification), the Large Area Mapping (LAM) feature of SEM (Figure 1) was also utilised to image the whole sample while maintaining a high resolution.

As mentioned above, adjusting input power causes the change in yield rate (sintered/melted mass). For example, with a starting mass of 50 grams in each case, for condition (a) the resultant sintered/melted specimen weighed 50 g (i.e. 100 % yield) at 1,000 W. Similarly, for condition (b) 45 g (90 % yield) at 800 W, condition (c) 41 g (82 % yield) at 600 W, condition (d) 35 g (70 % yield) at 400 W, and condition (e) 22 g (44 % yield) at 250 W. Based on this dataset, we infer that the longer heating time leads to higher energy loss to the surroundings, resulting in a poorer yield.

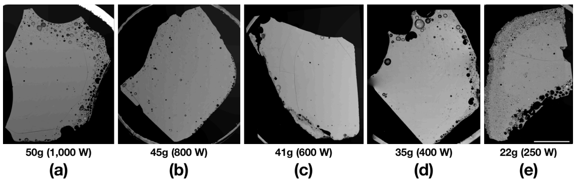
50g (1,000 W) (a)
45g (800 W) (b)
41g (600 W) (c)
35g (400 W) (d)
22g (250 W) (e)

Figure 1: Backscatter Electron images with 5 mm scale bar (Large Area Map) of microwave heated JSC-1A under various input power. (a) 1,000 W, (b) 800 W, (c) 600 W, (d) 400 W, (e) 250 W.

The density of the molten specimens vary from 3.01 g/cm^3 (1,000 W) to 2.82 g/cm^3 (250 W) showing a linear trend, while the bulk density of JSC-1A used in this experiment is 1.54 g/cm^3 with 47 % of porosity. The Young's Modulus and hardness measured using a nano-indentation method are from 85.2 GPa / 8.4 GPa (800 W) to 40.7 GPa / 3.4 GPa (250 W). The 1,000 W specimen shows lower strength than 800 W specimen despite the higher density because the 1,000 W specimen experienced thermal runaway for one minute less than 800 W specimen. Due to the high temperature of thermal runaway, 1,700 ~ 2,200 °C for the lunar regolith according to our simulation [2], the specimen could achieve higher strength when it experiences thermal runaway for a longer period of time even if the input power is slightly lower.

The micro-textural features of thermally treated JSC-1A using microwave energy can be categorised in three parts: fully-melted, partially-melted and sintered zones, as shown in Figure 2. Several unique features have been identified across the three categories. Notably, a feature was observed in the partially-melted with less temperature zone of the 250 W specimen in the form of abundant iron oxide (magnetite/haematite) particles arranged in a roughly circular pattern (Fig 3), which is not seen in other specimens with higher input powers. Interestingly, this observation suggests that microwave heating could also be used to beneficiate/extract iron from lunar regolith.

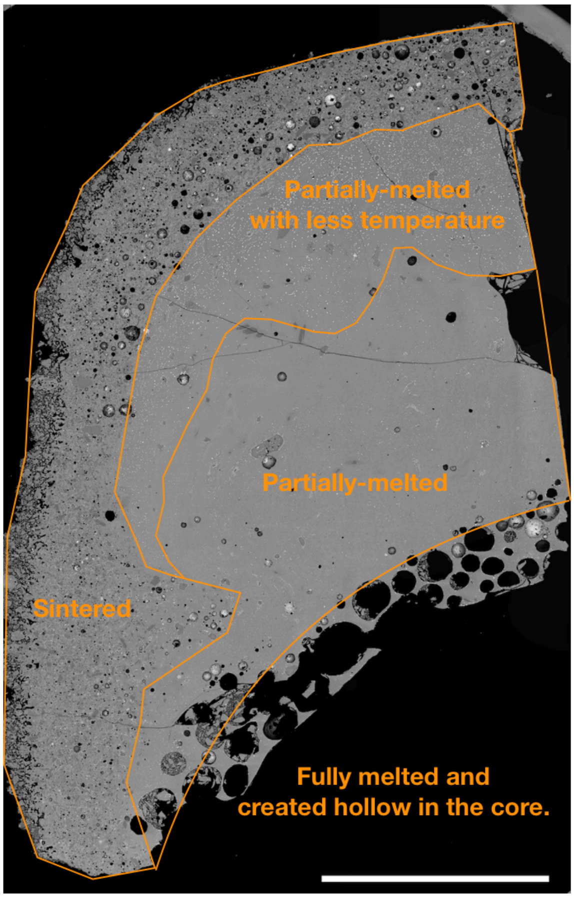

Figure 2: Backscatter Electron images with 5 mm scale bar (Large Area Map) of microwave heated JSC-1A at 250 W of input power.

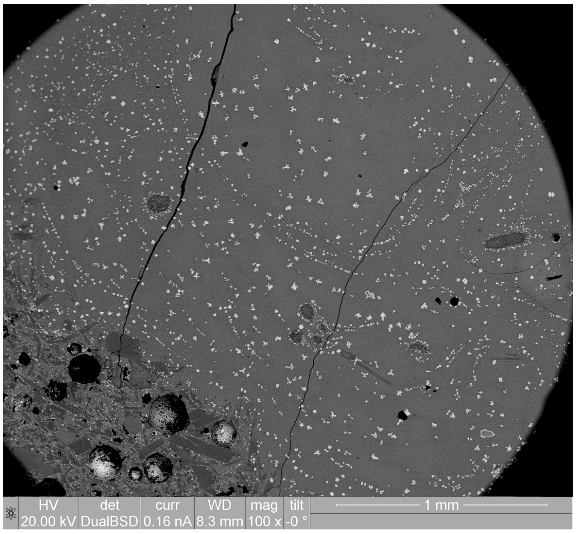

Figure 3: A circular pattern exhibited by iron oxides in the partially-melted area of the 250 W specimen.

Discussions: While several interpretations and hypotheses could be developed from the above observations, a few issues need further investigation.

Firstly, thermal runaway is a phenomenon that needs to be avoided in industrial applications, in general, due to the uncontrollable, rapid and extreme temperature increases. In our case, however, thermal runaway seems favourable as it allows instant sintering/melting at a 'hotspot'. Moreover, it was found that thermal runaway can be predicted or even controlled by a temperature threshold, which could be applied for other industrial applications.

Secondly, the circular patterned iron oxides in the partially-melted with less temperature area of the 250 W specimen could possibly have happened due to the magnetic field created by a microwave generator. When the iron oxides are formed out of other minerals such as olivine and pyroxene, and the partially-molten area is still not solidified, the iron-oxides could easily align to a magnetic field. Alternatively, the circular pattern could have formed as a result of convection currents in the melted material. If true, then this phenomenon is not expected in the lunar environment.

Thirdly, the above findings indicate that a different input power can potentially be used for different purposes, e.g., higher input power for fabricating construction components, and lower input power for mining/beneficiating metallic elements and extracting oxygen.

Acknowledgement: The authors acknowledge the funding from the Open University's Space SRA.

References: [1] Lim, S. et al. (2017) *Adv. in Space Research J.*, 60(7), 1413-1429. [2] Lim S. and Anand M. (2019) *Special Issue on Space Resources, Planet. and Space Sci J.,* 179(104723). [3] Lim S. et al. (2019) *Lunar ISRU2019*, Abstract #5047. [4] Lim, S. et al. (2019) *ELS2019,* Session 6: Prospecting and ISRU.

Preparing for telerobotic geological exploration: Science Support for ESA's Analog-1 project

Erica Luzzi[1], Matteo Massironi[2], Riccardo Pozzobon[2], Samuel Payler[3, 4], William Carey[3], Francesco Sauro[5], Loredana Bessone[3], Kjetil Wormnes[3], Thomas Krueger[3], Angelo Pio Rossi[1]
[1]Jacobs University Bremen (e.luzzi@jacobs-university.de), [2]Università degli Studi di Padova, [3]European Space Agency, [4]Agenzia Spaziale Italiana, [5]Università di Bologna

The Analog-1 (A1) project is aimed at testing telerobotic geological exploration. It focuses on a lunar-gateway scenario, where a rover on the surface of the moon would be controlled from an orbiting station. As an analogue for this scenario, a rover was operated from ISS by ESA astronaut, Luca Parmitano, who had to complete several science objectives such as collecting rocks that had been exposed to volatiles.

To prepare for this experiment, the A1 field campaign and data collection started in November 2018, within the ESA PANGEA-X campaign [1] in Lanzarote (Canary Islands). During the campaign, several sites were identified that could act as exploration points for the rover (one of the sites shown in Fig. 1). The sites, including prospective sample locations, were documented in 3D through photogrammetric and Lidar data (Fig. 4). Compositional and spectral analyses were performed on collected samples [2] using VNIR TerraSpec Halo spectrometer, raman Inspector300, LIBS Z-300, and XRF Epsilon 1.

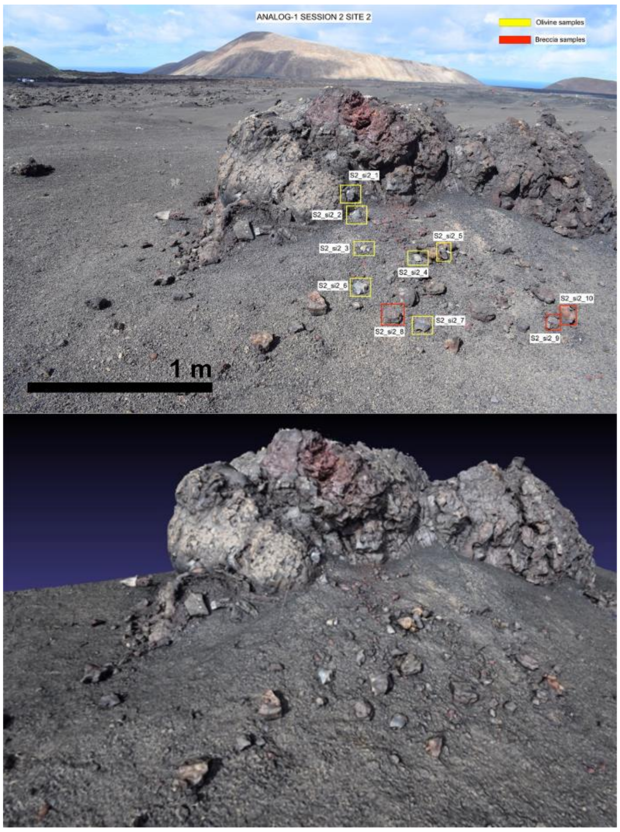

Figure 1: Above: Field setup with samples characterised during the Pangaea-X 2018 campaign. Below: Rendering of the digital outcrop model reproducing the outcrop and sample locations.

Based on this field experience and setup [see 3], as well as characterised samples, an artificial geological environment was then set up in an indoor hangar facility of the former Valkenburg airfield (Katwijk, NL), in the vicinity of ESA ESTEC, for the implementation of the project on November 25th 2019. The hangar was set up to reproduce some aspects of the Moon , characterized by boulders and other possible obstacles (Fig. 2). Three sites were prepared with a variety of samples (Fig. 3) including massive, amygdaloidal or vesicular basalts, scorias, gabbros, anorthosites, peridotites with xenoliths, impact breccias and pyroclastic materials as regolith.

Figure 2: Top view of the ESTEC hangar in Valkenburg. The three sites are indicated.

Figure 3: Samples available in the three sites (above) and collected samples (below).

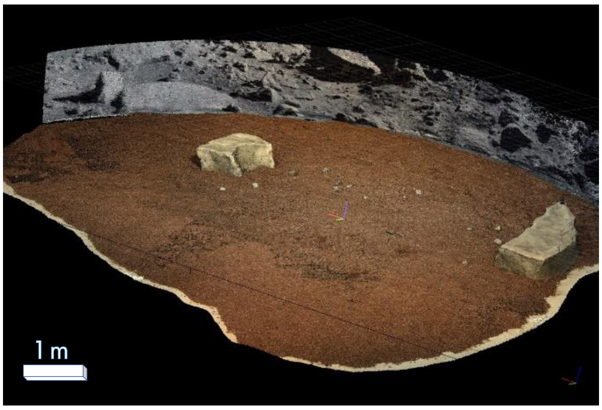

Figure 4: 3D model of site 1

The astronaut on board the space station Luca Parmitano was given a set of science objectives to help guide his sample collection efforts. These were to collect different types of basaltic material, degassing structures, xenoliths and rocks that looked out of context. Supporting Luca was a science backroom team located at the European Astronaut Centre (EAC) in Cologne, who interacted with the astronaut discussing the most interesting samples to collect. The actual sample nature and location was unknown to both the science backroom personnel and operating astronaut. The in-scenario team on site had independently placed samples in advance.

The minimum success threshold of the experiment was to have Luca navigate to the first site and collect two specimens there within the allotted time period (90 minutes). The experiment exceeded this expectation, with Luca being able to collect two samples from each of the three sites (Fig. 3, 5).

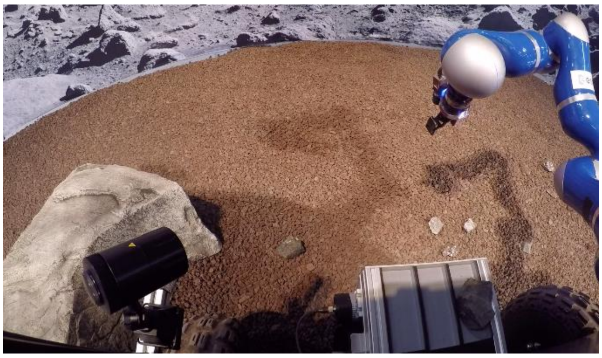

Figure 5: the view from the rover's head camera showing part of the first geological site. The arm is opened and approaching the sample to collect.

Collected samples from the first geological site (Site 1) were a vesicular and a massive basalt; the samples from the Site 2 were a welded scoria and a gabbro with large feldspars; in the third and last site Luca collected an impact breccia and, as suggested by the Science Team, the representative loose pyroclastic materials of the regolith for the context (Fig. 3).

Interactions both internally in the science backroom and between the crew and ground teams is being analysed and recommendations made for future work. Some examples include improving the ability for the science backroom to accurately point out a particular sample and easily relay that to the astronaut without excessive voice communications, and improvements to the camera system to enable better image quality in high contrast scenarios.

Overall, the performance of the astronaut matched and exceeded expectations, from the high quality voice descriptions of the sites and samples to the choice and logical order of sampling, all demonstrating effective geologic training has been received [4]. In addition, the efficiency and speed of the experiment was enhanced by the user interface of the robot control station and astronauts proficiency with it.

References: [1] Bessone, L., et al. (2018). Gepphysical Research Abstracts, Geophysical Research Abstracts, Vol. 20, EGU2018-4013 [2] Drozdovskiy, I., et al., (2019). Geophysical Research Abstracts Vol. 21, EGU2019-18250-2. [3] Rossi, A. P., et al. (2019) EPSC Abstracts, Vol. 13, #EPSC-DPS2019-1614-4. [4] Sauro et al. (2018) Geophysical Research Abstracts, Vol. 20, EGU2018-4017-1

ABSENCE OF EJECTA ROCKINESS IN COPERNICAN CRATERS AND IMPLICATIONS TO INFERRED MODEL AGES FROM ROCK-ABUNDANCE

P. Mahanti[1], J.D. Clark[1], H. Meyer[1], M.S. Robinson[1], [1]Lunar Reconnaissance Orbiter Camera, School of Earth and Space Exploration, Arizona State University, Tempe, Arizona (pmahanti@asu.edu)

Introduction: During crater formation ballistic excavation of ejecta covers the surrounding impact plane with rock fragments, granular material, glass, and melt [1, 2, 3]. The excavation physics ensures that larger rocks overlie the continuous ejecta close to the rim (up to a distance of one-diameter (D) from the crater rim), with ejecta thickness and rock sizes decreasing radially outwards [4]. Exposed to micrometeorite bombardment and thermal stresses, rocks break down into smaller rocks till finally they comminute to regolith fines. As rock sizes decrease, so do their bulk thermal properties - larger rocks preserve heat longer than smaller rocks, and are more thermally visible during nighttime. The discrepancy between nighttime brightness temperatures for warmer rocks and cooler lunar soil is observed in the thermal channels of the LRO Diviner instrument [5], leading to model based estimation of the areal fraction of each scene in the Diviner FOV occupied by exposed rocks 1 m and larger (termed rock abundance, or RA) [6]. Since large rocks break down to fine regolith particles over time, RA at the crater ejecta decreases with time. A relationship between estimated RA and crater size-frequency distribution (CSFD) based absolute model age (AMA) can be thus derived for young craters [7] with known, independently estimated AMAs. In this work, we show examples of Copernican craters Wiener F and Lalande whose RA statistics do not follow the description above and their (RA, AMA) values strongly deviate from proposed models. We then offer possible reason for the discrepancy and outline implications of such cases.

Methods and Observations: RA obtained from the Diviner global rock-abundance map [6]is used here to show the high RA regions ($RA > 0.01$) for six craters (Figure 1). In Giordano Bruno, Moore F and Tycho the high RA regions appear over the proximal ejecta while for Wiener F , Lalande and Kepler the high RA regions are mostly limited within the crater rim. All numbers for the RA statistics represent the 95^{th} percentile values.

LROC NAC images with incidence angles between 65°to 75°were considered [8] to obtain AMA estimates. CSFD measurements were obtained using CraterTools [9] and and fit in Craterstats [10], using the techniques described in [11, 12]. The derived AMAs are based on the production and chronology functions [13], valid for lunar craters $D >$ 10m and $D <$ 100km. Previously, [14] conducted CSFD measurements on three different types of rock material: ejecta blanket, melt ponds on the wall terraces, and the hummocky crater floor of Lalande. The melt ponds ($\sim 38Ma$) and crater floor ($\sim 44Ma$) CSFDs were close in age however, the age determined for the ejecta blanket was twice as old ($\sim 90Ma$). The differences in ages could be due to target properties [15] or because the ejecta blanket near the crater rim has been heavily populated by self-secondary craters [16]. Furthermore, the two ejecta count areas hug the crater rim where there is an abundance of rock populations. RA and AMA for the craters are compared (Figure 3) against the power law regression [7] to show the two outliers Wiener F and Lalande. The predicted age for Lalande is from another related work [17].

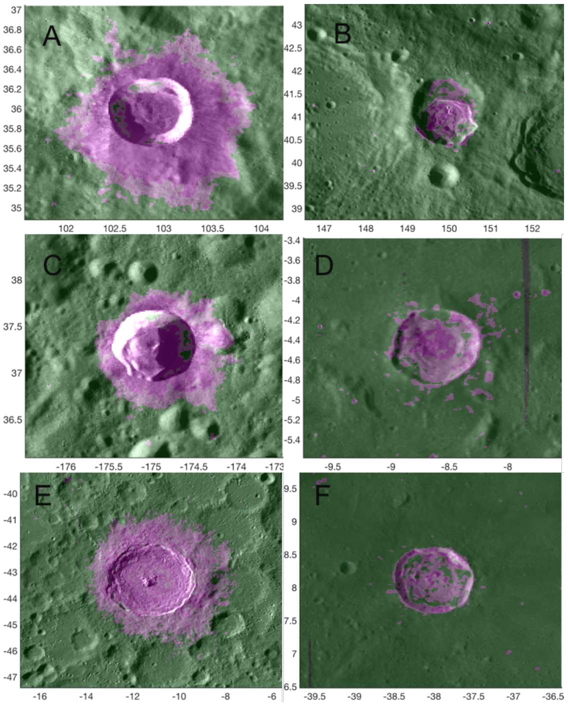

Figure 1: Rock abundance shown for Giordano Bruno (A), Wiener F(B), Moore F (C), Lalande (D), Tycho (E), and Kepler (F). RA of higher than 0.01 is shown in magenta. Giordano Bruno, Lalande, and Kepler are all similar in size of 20km.

Results and Discussions: The craters Lalande and Moore F are nearly similar in size, the RA on Moore F is higher than Lalande. Kepler, which is a Copernican but older crater, shows a ejecta RA spatial distribution similar to Lalande but the estimated age of Kepler is more than an order of magnitude larger than Lalande. Clearly, the RA statistics for Lalande is not representative of its young age. At AMA ¡ 50 My, majority of meter-sized rocks should still be visible on the ejecta and close to the rim of Lalande [18], but this is not the case. Wiener F,

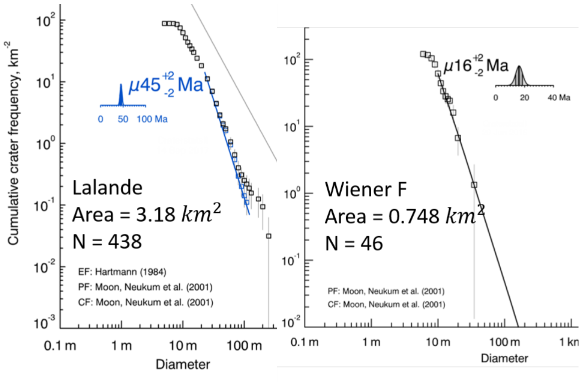

Figure 2: CSFD plots for craters Lalande and Wiener F

twice as large as Lalande shows similar behavior and the 95th percentile statistics outside the rim is lower than Lalande and close to the typical background RA values of impact craters [7].

In the case of Wiener F, it formed over a larger, older crater, and its northern rim is substantially lower than the southern rim. The spatial distribution of rocky ejecta could have been effected due to the tilt in the pre-impact plane, or from the melt spills, particularly at the northern rim. Still this does not justify an overall low RA. Lalande is formed over a flat pre-impact topography, yet has low RA. Target properties could be one of the contributing factors for these anomalies. If the pre-impact subsurface has low rock concentration, the excavation process would also yield less rocks. Neither the subsurface rock size distribution below the lunar regolith nor the regolith thickness is expected to be globally uniform, and can moderate the excavated rock size frequency and spatial distribution. For example, frequencies of rocks larger than one meter across are higher on rough mare than on smooth mare [19]. Burial of rocks during the crater formation or immediately after formation by melt flow, volcanic or tectonic processes is also possible, altering the RA statistics. Low RA statistic (< 0.01) does not necessarily mean an $AMA > 200My$ (conservative, with a margin of approximately 100 My).

High RA within the proximal ejecta boundary does not necessarily indicate excavated rocks either, and arises over impact melts. Typically, impact melt is found deposited over the proximal continuous ejecta, and the RA computed over impact melts is low (e.g. extensive impact melt at King crater [6, 7]). At places where RA is high, excavated rocks are generally visible over melt deposits. Accordingly, in studies involving RA measures, impact melt areas are typically excluded to preserve the overall statistics [7]). However, fractures in relatively thin layers of impact melt are found to be spatially correlated with large values of RA and appears to distinguish between fractured and relatively smooth impact melt [20]. Fractured sections of impact melt veneers show similar response as other areas on the continuous ejecta with higher rock populations.

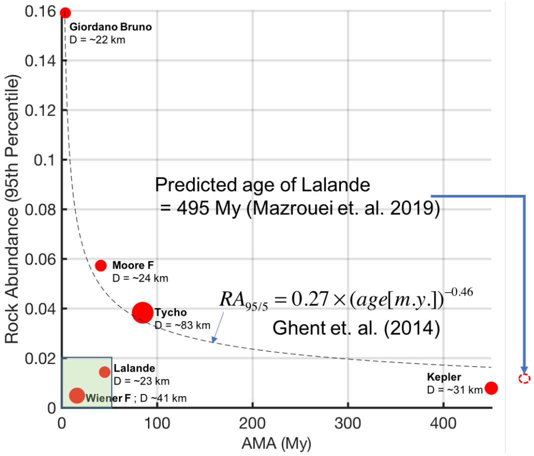

Figure 3: Chart showing RA (95^{th} percentile) versus AMA. The green shaded region indicates $RA < 0.02$ and an $AMA < 50Ma$.

Conclusion: Rock abundance over the proximal ejecta and crater model ages are related, but the relationship is complex and effected by pre-impact topography and target properties. AMA predictions from simple RA vs. AMA models can have large deviations. Inclusion of additional variables like spectral maturity, crater size and target properties in modeling the crater age can be useful and will be discussed in our future work.

References: [1] M. R. Dence (1971) *Journal of Geophysical Research* 76(23):5552. [2] R. A. Grieve, et al. (1977) in *Impact and explosion cratering: Planetary and terrestrial implications* 791–814. [3] R. Grieve, et al. (1992) *Meteoritics* 27(5):526. [4] H. J. Melosh (1989) *Research supported by NASA New York, Oxford University Press (Oxford Monographs on Geology and Geophysics, No 11), 1989, 253 p* 1. [5] D. Paige, et al. (2010) *Space Science Reviews* 150(1-4):125. [6] J. L. Bandfield, et al. (2011) *Journal of Geophysical Research: Planets* 116(E12). [7] R. R. Ghent, et al. (2014) *Geology* 42(12):1059. [8] L. Ostrach, et al. (2011) in *Lunar and Planetary Science Conference* vol. 42 1202. [9] T. Kneissl, et al. (2011) *Planetary and Space Science* 59(11-12):1243. [10] G. Michael, et al. (2010) *Earth and Planetary Science Letters* 294(3-4):223. [11] G. Neukum (1984) . [12] G. Michael, et al. (2016) *Icarus* 277:279. [13] G. Neukum, et al. (2001) in *Chronology and evolution of Mars* 55–86 Springer. [14] B. Li, et al. (2018) *Planetary and Space Science* 151:85. [15] C. H. Van derBogert, et al. (2017) *Icarus* 298:49. [16] M. Zanetti, et al. (2017) *Icarus* 298:64. [17] S. Mazrouei, et al. (2019) *Science* 363(6424):253. [18] A. Basilevsky, et al. (2013) *Planetary and Space Science* 89:118. [19] K. Di, et al. (2016) *Planetary and Space Science* 120:103. [20] P. Mahanti, et al. (2020) in *Lunar and Planetary Science Conference* vol. 51.

MERTIS SEEING THE MOON IN THE TIR: RESULTS FROM THE FIRST BEPICOLOMBO FLYBY.

A. Maturilli[1], J. Helbert[1], H. Hiesinger[2], G, Alemanno[1], S. Schwinger[1], M. D'Amore[1], A. Neumaier[1], [1]Institute for Planetary Research, German Aerospace Center DLR, Rutherfordstr. 2, 12489 Berlin, Germany (alessandro.maturilli@dlr.de), [2]Wilhelms Universität Münster, Germany.

Introduction: The Mercury Radiometer and Thermal Infrared Spectrometer (MERTIS) is part of the ESA BepiColombo Mercury Planetary Orbiter (MPO) payload and consists of a push-broom IR-spectrometer (-TIS) and a radiometer (-TIR) [1]. MERTIS-TIS and -TIR make use of the same optics, electronics, and in-flight calibration components [2, 3]. MERTIS-TIS operates at wavelengths of 7-14 µm, has 78 spectral channels, and a spectral resolution of $\lambda/\Delta\lambda$=78-156. The radiometer operates between 7 and 40 µm with 2 spectral channels. Depending on surface characteristics, MERTIS spectral resolution is adapted to optimize the S/R ratio. Thus, the instrument is capable of resolving weak spectral bands with less than 1% contrast.

During the long cruise to Mercury, and before its arrival on December 5th 2025, BepiColombo will perform 9 flybys: among them, the Earth/Moon flyby on April 10th 2020. Due to the flight configuration, not all the instruments onboard BepiColombo are able to operate during cruise and flybys. Among the instruments that can operate is MERTIS. The MERTIS imaging spectrometer will provide the first hyperspectral observation of the Moon in the thermal infrared (TIR) wavelength range from space.

At the Planetary Spectroscopy Laboratory (PSL) of DLR in Berlin, a spectral library for lunar analog rocks in the TIR spectral range, measured under simulated Moon surface conditions, has been built to help the interpretation of MERTIS' Moon spectra.

BepiColombo Earth/Moon flyby: Shortly after launch, MERTIS underwent a Near-Earth Commissioning Phase on Nov. 13-14 2018 during which the instrument was turned on for the first time in space. The goal of this phase was to verify the instrument functionality and science performance by using the in-flight calibration devices and to verify their performance. As a result of the commissioning, MERTIS was found to be fully operational [4]. The radiometer was also found fully functional with an excellent correspondence of the 2013 preflight sensitivity measurements and the 2018 in-flight measurements.

Although most instruments on the BepiColombo MPO are blocked by the Mercury Transfer Module (MTM) during cruise and flyby operations, including the MERTIS planetary baffle, MERTIS will be able to acquire data through its space baffle. In fact, the MERTIS pointing device allows viewing the planet (planet-baffle), deep space (space-baffle), and two internal black bodies at 300 K and 700 K temperature, respectively. We adapted the MERTIS operations software to allow for this unique opportunity. Especially the Earth/Moon fly-by is of interest, as the surface composition of the Moon and Mercury have been frequently compared in the literature [5-10]. Observing the Apollo and Luna landing sites with MERTIS, in combination with laboratory studies, will provide extremely valuable ground truth for our MERTIS measurements.

The attitude profile for the flyby has been already generated by ESA Mission Control. The time allocated for MERTIS pointing to the Moon is 4 hours and starts 1 day before closest approach. During this slot it is feasible to have the Moon in the FoV of MERTIS. The 4 hours visibility slot is divided in 4 segments of 1 hours approximately connected by short slews. The attitude in each segment will be quasi inertial (no tracking, keeping the Sun within illumination constraints) with the Moon slowly drifting in the FoV such that it is aligned with the boresight right in the middle of the segment. Within the 4 hours allocated for observations the Moon is nearly fully illuminated; the angle between Moon and Earth (from limb to limb) is 8.5 in the beginning and increases up to 10.64 degrees; the apparent size of the Moon starts at 0.268 degrees and increases up to 0.2927 degrees. The Moon moves 1.6 degrees in these four hours.

Lunar surface analogs: In the last decades orbital spectroscopic observations of the lunar surface have greatly advanced our understanding of the global distribution of different rock types and their chemical compositions. This vast dataset is now complemented by the first in situ reflectance spectra from the lunar surface obtained by the recent Chang'E 3 and current Chang'E 4 missions, which provide more detailed information about the mineralogy of local surface materials and the geological context of the landing sites.

The material analyzed by Yutu-2 at the Chang'E 4 landing site includes not only regolith but also a fragment of rock with a small- to medium grained plutonic texture, that has most likely been excavated by a nearby impact crater [11]. Due to its deep-seated origin, the composition of such a rock fragment is of particular importance for understanding the underlying stratigraphy of the landing site.

A reliable quantification of mineral modal abundances from measured reflectance spectra requires the availability of laboratory spectra of comparable samples. However, current spectral databases primarily contain spectra measured on powder samples, while spectra of coarse grained rock samples are rare. Since reflectance spectra are sensitive to grain size and surface roughness [12], the available powder spectra might not be sufficient for a quantitative interpretation of measured rock spectra.

Rock samples obtained during the Apollo missions indicate that lunar anorthosites are typically coarse grained and can reach grain sizes of more than 1 cm. Hence, the global abundance of anorthosite as the dominant rock type of the lunar surface suggests that such coarse grained rocks are ubiquitous.

Therefore the extension of the current spectral databases by new spectral data of whole rock samples is crucial for the interpretation of current remote and in-situ measurements.

Set-up description: The Planetary Spectroscopy Laboratory (PSL) of DLR in Berlin is a spectroscopy facility providing spectral measurements of planetary analogues from the visible to the far-infrared range for comparison with remote sensing spacecraft/telescopic measurements of extraterrestrial surfaces [13-17]. Three identical FTIR instruments are operating at PSL, in an air-conditioned room (Figure 1). The spectrometers are Bruker Vertex 80V (high-end model) that can be evacuated to ~.1 mbar. One spectrometer is equipped with aluminum mirrors optimized for the UV, visible and near-IR, the second features gold-coated mirrors for the near to far IR spectral range.

Spectral measurements: External simulation chambers are attached to the FTIR spectrometer to measure the emissivity of solid samples. One chamber features a high efficiency induction system to heat the samples under vacuum to temperatures from 320K up to above 900K, while keeping the chamber at almost ambient temperature. A shutter allows separating the spectrometer from the external chamber. Sample cups are made of stainless steel and have elevated rims enclosing the samples heating it from all sides, effectively supressing thermal gradients within. A sample carousel driven by a highly precise stepper motor allows measuring several consecutive samples without breaking the vacuum. A large number of temperature sensors in the emissivity chamber are allocated to measure the sample temperature as well as monitoring the range of equipment and chamber temperatures. A webcam is mounted in the emissivity chamber to monitor the heated sample and its vicinity.

With the Bruker A513 accessory bi-directional reflectance of samples, with variable incidence and emission angles between 0° and 85° (minimum phase angle is 26°) is measured. Integrating spheres (with gold or PTFE mirrors) allow for hemispherical reflectance measurements. Bi-directional and hemispherical reflectance are measured under purging or vacuum conditions, covering the 0.2 to above 200 µm spectral range.

Sample preparation and measurements: The initial suite of samples selected for this work includes: -slabs and stone chunks of plagioclases bearing rocks such as anorthosite, diorite, monzodiorite, gabbro and diabas; several basalts, rhyolite, olivine, granite, andesite, labradorite, obsidian.

Samples are placed in the emissivity chamber at PSL and heated in vacuum slowly and gradually up to 400° C. Measurements were taken at 100° C, 200° C, 300° C and 400° C in the MIR and FIR spectral ranges.

Each sample has been cooled in vacuum down to T_{room}. Thermally processed samples are measured in hemispherical and bi-directional reflectance in the full spectral range from UV to FIR.

A sample of graphite measured in emissivity at increasing T, adopting the same configuration and procedure used for the samples was used as blackbody for emissivity calibration.

Conclusion: MERTIS on ESA BepiColombo will be the first instrument to obtain hyperspectral measurements of the Moon in the TIR spectral range from space. Here we present the first results combined with a spectral library of emissivity for lunar analog rocks measured under simulated Moon conditions.

References: [1] Hiesinger, H., Helbert, J., and MERTIS Co-I Team (2010). *PSS*, 58, Issues 1–2, 144-165. [2] Arnold, G.E., Hiesinger, H., Helbert, J., Peter, G., Walter, I. (2010). *Proc. SPIE* 7808, Infrared Remote Sensing and Instrumentation XVIII, 78080I. [3] D'Amore, M., Helbert, J., Maturilli, A., Varatharajan, I., Ulmer, B., Säuberlich, T., Berlin, R., Peter, G., Walter, I., Hiesinger, H., Martinez, S., Landaluce, I.O.d., Casale, M. (2018). *Proc. SPIE* 10765, Infrared Remote Sensing and Instrumentation XXVI, 107650G. [4] D'Amore, M., Helbert, J., Maturilli, A., Varatharajan, I., Ulmer, B., Säuberlich, T., Berlin, R., Peter, G., Hiesinger, H., and Arnold, G. (2019). *Proc. SPIE* 11128, Infrared Remote Sensing and Instrumentation XXVII, 111280U. [5] McCord, T.B. and Clark, R.N. (1979). *JGR* 84, 7664-7668. [6] Vilas, F. (1988). *Mercury*. The University of Arizona Press, 59-76. [7] Robinson, M., Lucey, P. (1997). *Science* 275, 197-200. [8] Blewett, D.T., Lucey, P.G., Hawke, B.R., Ling, G.G., Robinson, M.S. (1997). *Icarus* 129, 217-231. [9] Warell, J. (2002). *Icarus* 156, 303-317. [10] Warell, J. (2003). *Icarus* 161, 199-222. [11] Gou, S., et al. (2019). *EPSL, 528*, 115829. [12] Salisbury, J et al. (1985). *Icarus 64(3)*, 586–588. [13] Maturilli, A. and Helbert, J (2006) PSS, Vol. 54, pp. 1057-1064 [14] Maturilli, A., Helbert, J., and Moroz L. (2008) PSS, Vol. 56, pp. 420-425, at http://figshare.com/articles/BED_Emissivity_Spectral_Library/1536469. [15] Helbert, J. and Maturilli, A, EPSL, Vol. 285, pp. 347-354, 2009. [16] Maturilli A, Helbert J., Journal of Applied Remote Sensing, 2014. [17] Maturilli A, et al (2014). EPSL, Vol. 398, pp. 58-65.

TESTING GRAVITY WITH LUNAR LASER RANGING

L. Mauro[1,2], L. Porcelli[1,3], S. Dell'Agnello[1], S. Capozziello[4,5].

[1] INFN Laboratori Nazionali di Frascati, 00044 Frascati, Italy,
[2] Dipartimento di Matematica e Fisica, Università degli Studi "Roma Tre", Roma, Italy,
[3] Dipartimento di Fisica, Università della Calabria, Cosenza, Italy,
[4] Dipartimento di Scienze Fisiche, Università di Napoli "FedericoII", Napoli, Italy,
[5] INFN Sez. di Napoli, Compl. Univ.di Monte S.Angelo, Edificio G, Via Cinthia, I−80126, Napoli, Italy.

Einstein's theory of General Relativity provides a comprehensive and coherent description of space, time, gravity and matter at the macroscopic level. Classical tests of General Relativity (such as perihelion precession of Mercury, deflection of light and gravitational redshift) have affirmed that the theory is well founded. But they are valid essentially in a weak field. In the last thirty years several shortcomings of Einstein's theory were found and scientists began wondering whether GR is the only fundamental theory capable of successfully explaining the gravitational interaction, at all scales. This new point of view comes mainly from the study of cosmology and of quantum field theory. Therefore, various alternative gravitational theories were proposed which attempt to formulate at least a semiclassical scheme in which GR and its successes could be replicated [1]. There are possible many experiments for testing General Relativity and its extensions but most of them are complex (atomic clocks, interferometers, etc.). Hence, it is very important to work within the best possible theoretical framework to compare models with observations. An example is the Parametrized Post Newtonian (PPN) formalism. It contains a set of ten parameters whose values differ from one theory to another [2]. Solar System experiments, like Laser Ranging, allow us to measure some of these PPN parameters, and thereby to determine which theory of gravity best describes the observed physical phenomena (GR, scalar tensor theories, f(R) or something else).

Over the past 50 years, Lunar Laser Ranging (LLR) to the Apollo Cube Corner Retroreflector (CCR) arrays have supplied almost all the significant tests of General Relativity in the Solar System, just providing the PPN parameters, as we said before. The LLR technique consists in a ToF (Time Of Flight) measurement of short laser pulses fired by stations of the ILRS (International Laser Ranging Service) on Earth to payloads of CCRs on the Moon. However, arrays with a multi-CCR structure located on the lunar surface have some limitations. The main problem that affects the Apollo arrays in longitude is the lunar librations, that result from the eccentricity of the Moon's orbit around Earth. Then the accuracy of the ranging measurements cannot go below few centimeters (for a single normal point). In order to solve this problem, the SCF (Satellite/lunar laser ranging/altimetry and cube/microsat Characterization Facility) group, in collaboration with the University of Maryland, indicates a new design of lunar CCR whose performance is unaffected not only by lunar librations, but also by regolith motion, due to its very large thermal cycle. MoonLIGHT (Moon Laser Instrumentation for General relativity High accuracy Tests) CCR has the same design style as the Apollo cubes but with a diameter of the front face of 100 mm. In this way, final ranging accuracy is improved by a factor ten [3], [4].

MoonLIGHT is the result of an international collaboration among LNF, UMD, ASI-CGS (Centro di Geodesia Spaziale), the University of California at San Diego (UCSD) and the Harvard-Smithsonian Center for Astrophysics (CfA). The latter provides an open source sophisticated software package, named PEP (Planetary Ephemeris Program), to estimate the orbits of the Solar System natural bodies and of many artificial satellites. But it is also used to compare model with observations, by placing limits on the PPN parameters β and γ, geodetic precession and the variation of the gravitational constant.

INFN-LNF built a new operative experimental apparatus and created a new industry-standard test procedure (SCF-Test) to characterize and model the detailed thermal behaviour and the optical performance of CCRs in space conditions accurately simulated in the laboratory, for industrial and scientific applications. The key experimental innovation is the concurrent measurement and modelling of the optical Far Field Diffraction Pattern (FFDP) and the temperature distribution of retroreflector payloads under thermal conditions produced with a solar simulator [3], [4].

Optical simulations of the CCR response is performed with Code V. It is an optical design software used to model, analyse and simulate optical systems.

The combined use of Code V and MatLab allows us to obtain the FFDP and the Optical Cross Section (OCS) plot of the CCR in analysis. In particular, for MoonLIGHT simulation, a laser beam with a wavelength of 532 nm was considered. The position of the first minimum in the OCS plot is in agreement with the value given by the Airy disk equation. Furthermore, since MoonLIGHT CCR is uncoated, the intensity is calculated taking into account that the resulting far-field diffraction pattern has a central intensity only 26% that of the perfect reflector case [5]. These simulations allow us to check the results obtained in the laboratory with the SCF-test. But above all, they allow us to understand what the behavior of the CCR could be once launched into space. At the moment, there is agreement between optical simulations and laboratory tests.

Therefore, a good theoretical framework, simulations and precise laboratory tests are the fundamental ingredients for the success of a space mission.

References:

[1] S. Capozziello, V. Faraoni. (2011) *Beyond Einstein Gravity. A Survey of Gravitational Theories for Cosmology and Astrophysics*, Springer Netherlands, Series ISSN 0168-1222. [2] C. W. Misner, K. S. Thorne, J. A. Wheeler. (1973) *Gravitation*, W. H. Freeman and Company, ISBN-10: 0691177791.

[3] D. G. Currie, S. Dell'Agnello, G. O. Delle Monache, B. Behr, J. G. Williams. (2013) *A Lunar Laser Ranging Retroreflector Array for the 21st Century*, Nuclear Physics B (Proc. Suppl.), *243-244*, 218-228.

[4] M. Martini et al. (2012). *MoonLIGHT: A USA–Italy lunar laser ranging retroreflector array for the 21st century*, Planetary and Space Science *74*, 276–282. [5] T. W. Murphy, Jr., S. D. Goodrow. (2013) *Polarization and far-field diffraction patterns of total internal reflection corner cubes*. Applied Optics *52*, 117-126.

NEW CONSTRAINS ON THE TIMING AND MANTLE SOURCES OF LUNAR MAFIC MAGMATISM FROM METEORITES.

R. E. Merle[1], A. A. Nemchin[2], M. J. Whitehouse[1], J. F. Snape[3], G. G. Kenny[1], J. J. Bellucci[1], J. N. Connelly[4], M. Bizzarro[4], [1]Swedish Museum of Natural History (Stockholm, Sweden), [2]Curtin University (Perth, Australia), [3]Vrije Universiteit Amsterdam (Amsterdam, The Netherlands), Centre for Star and Planet Formation (Copenhagen, Denmark).

Introduction:

The duration of mafic magmatic activity on the Moon,which is essential to understand the chemical evolution of the lunar mantle through time, remains poorly constrained. As a consequence, determining precise and reliable ages and initial isotopic compositions of mafic lunar meteorites is a critical step in defining the periods of magmatic activity that occurred during the history of the Moon and to constrain the chemical characteristics of mantle components involved in the sources of the magmas.

Samples and methods:

To achieve this goal, we investigated lunar gabbros and basalts using the in-situ Pb–Pb SIMS approach demonstrated in previous studies [1]. Analyses of K-rich feldspars, phosphates and sulphides present in the samples allow us to use the $^{204}Pb/^{206}Pb$ vs $^{207}Pb/^{206}Pb$ isochron method, which has the advantage of yielding precise ages, constraining initial Pb initials while also screeninf for the presence of terrestrial Pb contamination. In this study we have analysed lunar meteorites from the Northwest Africa (NWA) 773 clan (NWA 2727, NWA 3333, NWA 2977, NWA 773 and NWA 3170), LAP 02224, NWA 4734 and Dhofar 287A. These samples have been selected because they all belong to the dominant chemical group of low-titanium mare basalts for which there has, to date, been no clear agreement on their age.

Results:

We have obtained ages of 2978 ± 13 Ma for LAP02224, 2981 ± 12 Ma for NWA 4734 and 3208 ± 22 Ma for Dhofar 287. Four samples of the NWA 773 clan (NWA 2727, NWA 773, NWA 2977, NWA 3170) yielded isochron ages that are identical within uncertainty with an average age of 3086.1 ± 4.8 Ma. The gabbro NWA 3333 yielded an age of 3038 ± 20 Ma suggesting that two distinct magmatic events are recorded in the meteorites of the NWA 773 clan. Finally, we obtained a reliable age of 3882. 9 ± 0.6 Ma for the coarse grained basalt MIL 05035 (Figure 1). To establish a reliable time frame of the mafic magmatism, the entire published age dataset from lunar mafic meteorites was screened to identify data that are problematic from an analytical viewpoint and/or show evidence of resetting and terrestrial contamination.

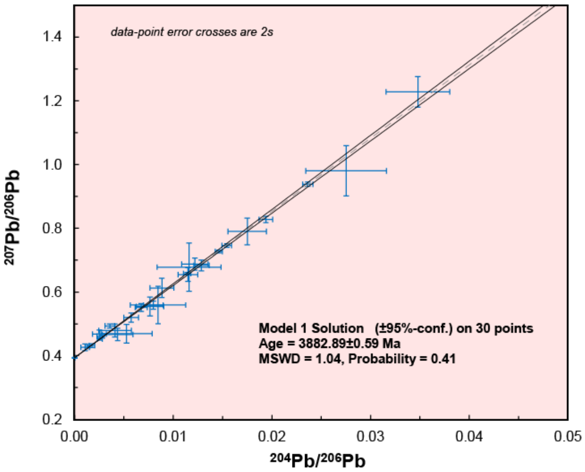

Figure 1: $^{204}Pb/^{206}Pb$ vs $^{207}Pb/^{206}Pb$ isochron for MIL05035 meteorite.

Interpretations and conclusions:

The new and refined dataset combines the ages of mafic lunar meteorites and Apollo samples and suggests pulses in magmatic activity, with two main phases between 3350 and 3100 Ma and between 3900 and 3550 Ma followed by a minor phase at ~3000 Ma (Figure 2).

The evolution of the Pb initial ratios of the low-Ti mare basalts between 3400 ma and 3100 Ma can be interpreted as a progressive mixing of a compenant represented by the 3400 Ma low-Ti basalts (low-Ti mantle component) with a KREEP-like component. This suggests that a KREEP component can be traced in the lunar mantle for at least 800 myrs (3900 Ma-3100 Ma).

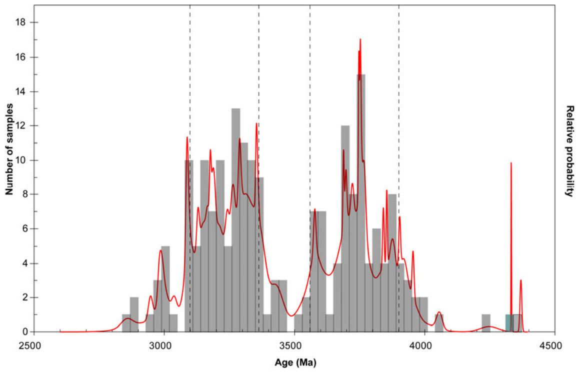

Figure 2: Probability density plot representing the age distribution of mafic lunar rocks (meteorites and Apollo samples). Age dataset for Apollo samples after [2] and meteorite ages filtered database from [3].

References: [1] Snape J. F. et al. (2016) *Earth Planet. Sci. Lett.* 451, 149-158. [2] Snape J. F. et al., (2019) *Geochim. Cosmochim. Acta* 266, 29-53. [3] Merle et al. (2020) *MAPS*, submitted.

MOLTEN SALT ELECTOLYSIS OF LUNAR SOIL SIMULANTS.

A. Meurisse[1], B. Lomax[2], M. Symes[2], and J. Carpenter[1], [1]European Space Agency, ESTEC, Keplerlaan 1, 2201 AZ Noordwijk, The Netherlands, [2] University of Glasgow, Glasgow G12 8QQ, UK.

Introduction: Sustainability of space exploration is bound to the development of technologies and processes that can make use of space resources. In-situ Resource Utilisation (ISRU) could potentially create the paradigm of the production of resources at the point of need, changing the way we design space exploration missions today, starting with the lunar surface missions.

In this context, extracting the oxygen present in the lunar soil would be extremely valuable for life support systems and refuelling rockets. Past studies have mainly focussed on gas/solid reactions at high temperature, using hydrogen or methane to reduce ilmenite and potentially other iron-bearing minerals [1-4]. Yet, thermodynamics limits the amount of oxygen recoverable by hydrogen and carbothermal processes at temperatures <1000°C. These processes cannot reduce major lunar minerals such as plagioclase and pyroxene, thus leaving a lot of oxygen in the processed material. In this work, the authors will present the latest experimental results of a molten salt electrolysis process for reducing lunar soil simulants. This process is based on the FFC-Cambridge process and has demonstrated a full reduction of lunar regolith simulants [5].

FFC-Cambridge process: The Fray-Farthing-Chen process is an electrochemical process working with molten salts as electrolyte, typically $CaCl_2$ at 900°C. The oxides to reduce are placed in a basket or pelletised to form the cathode. The anode is made of carbon or of an inert material (e.g. SnO_2). As current is applied to the electrodes, direct de-oxidation of the oxides occurs. O^{2-} evolves at the anode to form CO and CO_2 with a carbon-cased anode, or O_2 with an inert one.

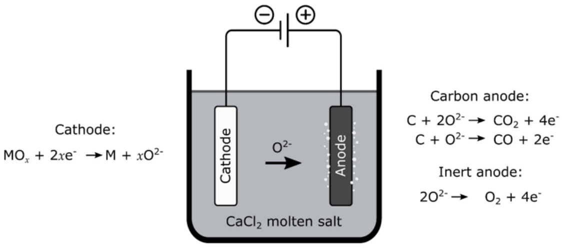

Figure 1: *A diagram showing the basic concept of the FFC-Cambridge process, whereby a metal oxide (MO_x) is reduced to the corresponding metal with the co-generation of CO/CO_2 (at a graphite anode) or O_2 at an inert anode [5].*

Towards a use in space: Research work at ESA-ESTEC aims at developing the FFC process further towards an application on the lunar surface. On-going work is focussing on materials selection, electrolyte composition, anode and cathode configuration, salt and regolith ratios, and scalability. Analysis of the extracted gas by mass spectrometry provides information regarding the purification system required for larger systems (e.g. pilot plant). Results of this work are expected to refine the requirements for the oxygen production demonstration mission planned to launch in 2025.

Understanding reduction mechanisms: More fundamental research is also targeted. Full and partial reduction of LMS-1 and LHS-1 lunar soil simulants by molten salt electrolysis allow for investigation of the reduction pathways of major lunar minerals/phases and their respective intermediates. A better understanding of these reduction mechanisms will help with optimisation of electrolysis parameters for a given location and characterisation of the by-product of the process, a mix of metal alloys that could potentially be used for additive manufacturing.

References: [1] Allen et al. (1996), Journal of Geophysical Research, 101, E11. [2] Hegde U. et al. (2011), *AIAA*, 0608. [3] Rice E. E. et al. (1996), *AIAA*, 0487. [4] Balasubramaniam et al. (2010), *International Journal of Mineral Processing*, 96 (1-4), 54-61. [5] Lomax B. A. et al. (2020) *Planetary and Space Science*, 180, 104748.

MOSCOVIENSE BASIN: POTENTIAL LANDING SITE FOR FUTURE LUNAR MISSIONS.

S. Mikolajewski[1], H. Hiesinger[1], and C. H. van der Bogert[1], [1]Institut für Planetologie, Westfälische Wilhelms-Universität Münster, Wilhelm-Klemm-Str. 10, 48149 Münster, Germany (sascha.mikolajewski@uni-muenster.de)

Introduction: Although we have more than 400 kg of lunar samples that were either brought back by the Apollo astronauts, Luna robotic sample return, or were delivered in the form of lunar meteorites, new lunar samples are required to expand our knowledge of the geological history and evolution of the Moon. Mare Moscoviense, especially the eastern mare unit, is a good candidate landing site for future rover-based sampling missions, similar to the previously proposed young mare basalts NE of Mons Rümker, and the sites close to the lunar South Pole [1-5]. Moscoviense basin is located on the northern hemisphere of the lunar farside at 27°N, 148°E with a diameter of 445 km [6]. Mare Moscoviense largely fills the impact structure with volcanic material of Eratosthenian age.

Data/Methods: Prior studies have used multispectral data and images [6-18] to examine the nature and origin of mare volcanism. We used recent Lunar Reconnaissance Orbiter Camera (LROC) datasets to generate a new geological map for the Moscoviense basin and to examine possible landing locations for future lunar missions. With Clementine [6, 7] and Kaguya [8, 9] spectral data we examined compositional differences in the exposed rocks and regolith. Kaguya mineral maps [9], multispectral Clementine FeO and TiO_2 data [6], and LROC datasets [12] were used to define morphological and compositional units within the Moscoviense basin. Using digital terrain models [13], slope maps, and LRO Diviner rock abundances [11,18], we examined the topography and rock distributions inside Mare Moscoviense. We also derived absolute model ages (AMAs) from crater size-frequency distributions (CSFDs) measurements for one of the prominent dark plains (mare) units and an old impact crater between two mare units using the production and chronology functions of [14].

Results: Moscoviense basin is located in a heavily cratered undivided pre-Nectarian region on the lunar farside (*pNtm*). The basin itself can be divided into two sub units. The first subunit contains the units associated with the rim of Moscoviense and the basin forming units. The second subunit is associated with the younger dark materials, which fill the basin floor of Moscoviense. Both units are also affected by cra-

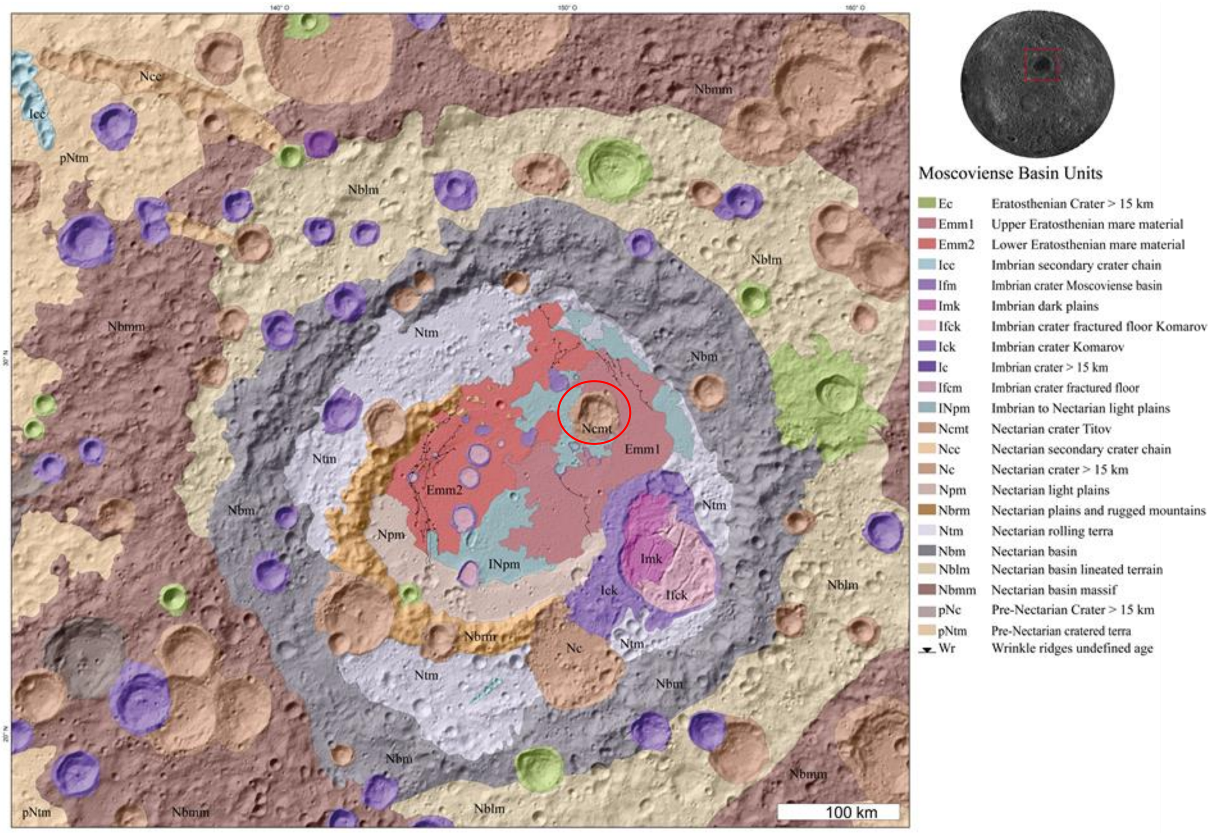

Figure 1.: *Geological map of the Moscoviense basin in the northern hemisphere of the lunar farside. The red circle marks the Nectarian crater Titov between the INpm and Emm1 units.*

ters and secondary crater chains of different ages.

Moscoviense Rim and basin forming units. The oldest part of the basin is the steep, heavily cratered outermost rim of Moscoviense (*Nbmm; **Fig. 1***). This unit is superposed by the less steep *Nblm* unit (*Fig. 1*). *Nblm* consists of mainly landslide material and blocks and lineated features at the western edge of the basin. The next unit, *Nbm*, overlays the older *Nblm* unit. *Nbm* (***Fig. 1***) is steeper and rougher than the aforementioned unit and consist of mainly blocks and massif material. The *Nbm* unit marks the second ring of the Moscoviense basin. *Nbm* is superposed by the younger and less steep *Ntm* unit(***Fig. 1***). *Ntm* is dominated by landslide material and has a smooth surface. The steep and rough *Nbrm* unit overlays the *Ntm* unit (***Fig. 1***). The *Nbrm* unit is presumably the central ring of Moscoviense basin.

Moscoviense basin floor and basin filling units. The first unit associated with the basin floor is the *Npm* unit (***Fig. 1***). It is characterized by a smooth surface and cratered with secondaries. It consists of mainly anorthositic material. The unit is superposed by a younger light plains unit (*INpm*; ***Fig. 1***). The unit is flat, consist of small craters and has a higher anorthosite compostion than the *Npm* unit. The dark plains unit *Emm2* (***Fig. 1***), which overlays the *INpm* unit is characterized by a smooth surface with few craters and a FeO-rich, TiO_2-poor composition. The *Emm2* unit also fills some of the older craters inside the basin (*Ifm; **Fig. 1***). The CSFD measurement for this unit results in an AMA of 3.0 Ga (***Fig 2***). The *Emm2* unit is superposed by the younger *Emm1* unit (**Fig. 1**). It is characterized by a FeO-rich and TiO_2-high compostion. The surface is smooth and butcratered and the albedo is lower compared to the *Emm2* unit. *Emm1* also embays a large Nectarian impact crater, Titov, inside Mare Moscoviense (*Ncmt*; ***Fig. 1, Fig. 3***).

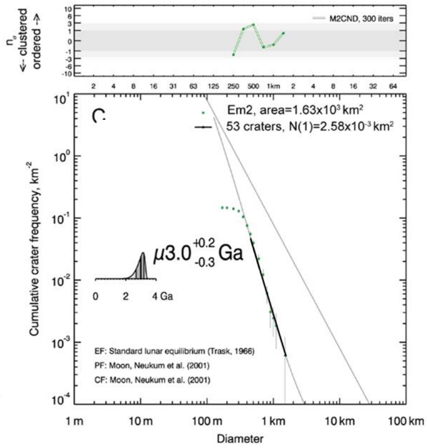

Figure 2. *Crater size-frequency distribution and absolute model age for the eastern Eratosthenian mare unit Emm2 of Mare Moscoviense.*

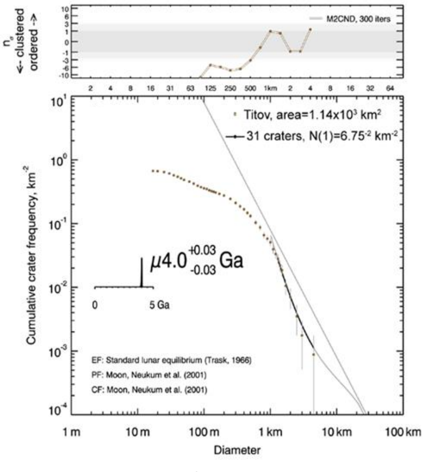

Figure 3. *Crater size-frequency distribution and absolute model age for the Nectarian crater Titov inside Mare Moscoviense.*

Impact crater, secondary crater and crater chains. All of the previous mentioned units are affected by impact craters, secondary impact craters and also secondary crater chains of different geological age (***Fig. 1***).

Discussion: Although the southeastern part of *Emm1* has the lowest abundance of rocks compared to the other flows and is better suited as a landing site with a rock abundance of ≤0.05 %, the eastern part of the *Emm1* unit is the more scientifically interesting landing site. Spectral data reveal that the eastern part is covered by a mare unit with different mineralogical composition than the underlying older unit. The eastern flow also provides access to older impact craters, e.g., Titov, a 25 km wide Nectarian crater that may expose parts of the original basin floor (*Ncmt*; ***Fig. 1,Fig. 3***). A landing site on the eastern part of *Emm1* provides access to at least two different mare units, ray material on one of the mare units, several wrinkle ridges and would allow insights in the small scale mare volcanism on the lunar farside as shown by [16, 17, and this work].

Conclusion/Future work: We identified at least three mare units inside Moscoviense basin and dated two of them in this updated geological map of the Moscoviense basin region. As our next step, we will investigate several possible landing ellipses on the *Emm1* unit of the eastern part of Mare Moscoviense and will define a rover traverse for potential missions. Access to several mare units, possible old crater material and the vicinity of wrinkle ridges makes the eastern part of Moscoviense basin a promising site for getting a better understanding in the timing of young mare volcanism, examination of lunar cooling processes, and the formation of wrinkle ridges.

References: [1] Hiesinger et al. (2019) LPSC *L*. #1327. [2] Morse et al. (2019) LPSC *L*. #2886. [3] Hiesinger et al. (2000) JGR, 105.
[4] Hiesinger et al. (2010) JGR, 115. [5] Qian et al. (2018) JGR, 123.
[6] Lucey et al. (1998) JGR, 103, 3679-3699. [7] Chevrel. et al. (2000) *JGR*. 107, NO. E12, 5132. [8] Lemelin et al. (2016) 47th LPSC #2994. [9] Morota et al. (2009) GRL, 36, L21202. [10] Morota et al. (2011) EPS, 63, 5-13.
[11] Bandfield et al. (2011) Icarus, 116. [12] Sato et al. (2017) Icarus, 296, 216-238. [13] Scholten et al. (2012) JGR, 117(3). [14] Neukum et al. (2001) *Space Sci. Rev. 96*, 55–86. [15] Kramer et al. (2008) *JGR*, 113.
[16] Pasckert et al. (2015) Icarus, 257, 336-354. [17] Pasckert et al. (2018) Icarus, 299, 538-562. [18] Williams et al. (2017) Icarus, 283, 300-325.

Experimentally Exploring Factors Affecting Water Ice Sublimation Rates to Inform Development of ESA's PROSPECT Package.

J. I. Mortimer[1], H. Chinnery[1], S. J. Barber[1] and M. R. Leese[1], [1]School of Physical Sciences, The Open University, Walton Hall, Milton Keynes, Buckinghamshire, United Kingdom, MK7 6AA, UK. (James.Mortimer@open.ac.uk).

Introduction: ESA's PROSPECT package, which is due to fly to the south polar region of the Moon on board Russia's Luna 27 mission in 2024, consists of two main elements: the ProSEED sample drill, and the ProSPA volatile analysis instrument [1]. After drilling down to a depth of up to 1 metre, the ProSEED drill will then collect icy regolith material and bring it up to the lunar surface, before transferring it to the ProSPA oven carousel. From there, it will be rotated and positioned under a sample imaging system (SamCam) to work out the volume of the sample material in the oven, then rotated again to a tapping station, where it will be sealed, ready for heating and thus volatile release for analysis in the ProSPA instrument mass spectrometers. However, these processes of sample retrieval, positioning, transfer, imaging, and sealing all take time, during which the icy regolith sample is exposed to radiative and conductive heat sources, thereby potentially raising the temperature of the icy sample. Exposed to the high vacuum conditions of the lunar surface environment, such temperature rises may result in ice mass loss caused by sublimation, and this is important to quantify with some confidence in advance of lunar surface operations.

Previous studies conducted in support of PROSPECT have indicated that significant isotopic fractionation of the remaining water ice is unlikely until more than approximately 30% of the starting water ice mass has been lost [2]. Despite this, it is still necessary to have as much ice content remaining for analysis as is reasonably possible, whilst not overly constraining the volatile preservation requirement such that it excessively drives the associated engineering requirements (such as temperature control and speed of operations). This limit on the amount of permissible mass loss then provides constraints on the maximum temperatures of different parts of the PROSPECT systems and so is of high importance to the thermal design of the entire package. Computer numerical simulation can model the expected water ice mass losses at various stages of this sample handling pathway, but these need to be verified by an experimental approach. This abstract outlines some of the laboratory experiments already conducted at The Open University in order to inform the inputs to the modelling efforts being undertaken elsewhere, and highlights the ongoing activities in this area being conducted through the PROSPECT Science Team.

Experimental Procedure: In brief, the set-up comprises a large vacuum chamber with a side-mounted hinged quick access door, on top of which is affixed (*via* a hermetic seal) a microbalance (CI Precision Recording Microbalance). The microbalance can take loads up to 5 g and is capable of measuring differences in mass between the counterbalance and the sample of up to a maximum of 500 mg to an accuracy of 0.1 μg. The microbalance is controlled *via* its associated electronics and display box, or through its computer software, through which mass and temperature data (from a K-type thermocouple) are recorded at chosen time intervals (up to 60 measurements per minute) for any user-set experimental duration. Hanging down into the chamber from the microbalance head are two fine NiCr wires, one of which supports the counterbalance, and the other the sample weighing pan, containing an aluminium sample crucible manufactured to replicate the internal size and geometry of a ProSPA oven. This is suspended mid-way into a temperature-controlled copper jacket (cooled by liquid nitrogen and heated by a PID-controlled waterproof heating wire circuit) and is cooled from above by a liquid nitrogen cooled copper canopy. Both the jacket and the canopy are thermally isolated from the room-temperature metal walls and floor of the chamber as much as practical by the use of PTFE stilt legs and sheets of multi-layer insulation.

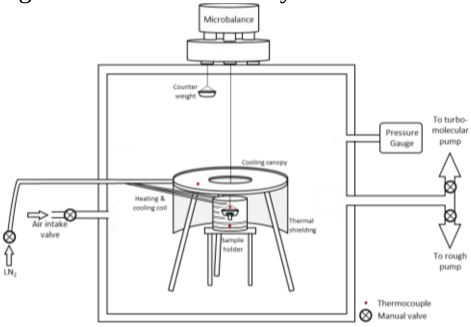

Figure 1: Schematic Diagram of the Sublimation Chamber and Microbalance Set-up

Results: Water ice losses as percentages of the starting ice mass, for various experimental conditions, conducted with both JSC-1A and NU-LHT-2M regolith simulants display much higher loss rates than the current models predict. Crucially, there is also variation in the scale of the difference between laboratory tests and model iterations, of up to an order of magnitude. Therefore, a series of different experimental campaigns was carried out in order to examine both the potential sources of unintended variability within the experimental samples, and also to derive 'real-world' measured values for key aspects of the model, such as the diffusivity coefficient of water vapour through the lunar simulants used, at different densities (since the models were constructed using several initial assumptions for certain factors and assume physical properties derived from Apollo lunar soil core data rather than those of the NU-LHT-2M simulant used for experiments).

Sample Temperature Tests

It was important to first constrain how accurately the experimental set-up measures the temperature of the subliming icy regolith sample; if the sample turned out to be much warmer than the measured value, then this could account for the discrepancy between what the model predicts and what is measured in the laboratory. Accepting that mass loss measurements would be compromised in order to investigate this potential temperature issue, a series of experiments was conducted using two thermocouples, one in the original position above the sample, and the other embedded a few mm into the sample. This revealed that both thermocouples agree, with only a slight offset of a maximum of 4K between the two (Fig.2); this therefore cannot explain the much higher rates of mass loss measured in the experiments.

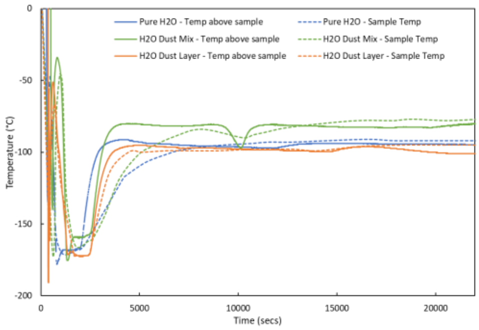

Figure 2: Comparing icy regolith sample temperatures as read above the sample, and within the sample mass

Effect of oven filling level on water ice loss rates

It was observed that, for multiple experiments at similar temperatures, mass loss rates varied considerably. Looking further at the data, this is correlated with how much of the total oven crucible volume the sample takes up; crucibles with more in them lose water ice faster than those with less inside. This can be explained by the cold trapping effect of the crucible walls extending upwards around the sublimation surface of the sample; a lower level of filling means a greater area of cold crucible wall is exposed, which in turn traps some of the sublimating water vapour and so reduces the overall mass loss rate.

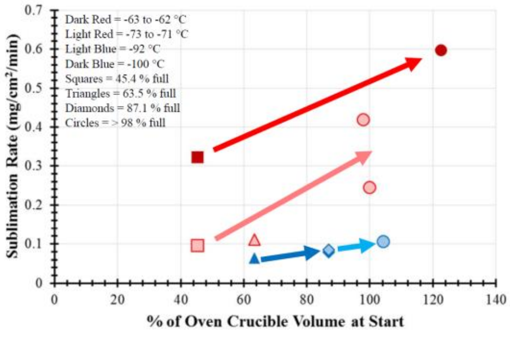

Figure 3: Effect of crucible filling on net mass loss rate

Effect of dry regolith density on diffusion.

The models use Apollo lunar soil values for particle size distributions, porosity, and regolith densities. Although these are the most relevant values to use when considering the true lunar mission scenario, they may not be applicable to laboratory experiments conducted using NU-LHT-2M simulant. If, for example, the experimental samples are of a lower density than the model assumes, then the diffusion of a water molecule through the sample could be much faster, giving rise to much more rapid ice loss rates than the model would predict. A suite of experiments was conducted where the crucible was half filled with pure water ice, overlain by dry regolith simulant compacted to different densities.

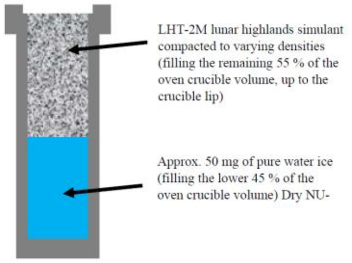

Figure 4: Layered samples to investigate diffusion

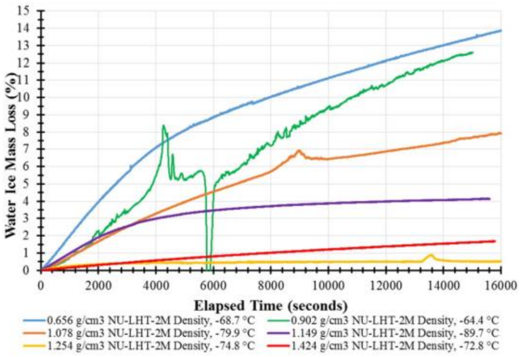

Figure 5: Water ice mass loss at varying densities of regolith simulant

Using these data, diffusion coefficients were derived for the experimental samples; some were close to the Apollo values already in use in the models, and so this alone cannot explain the discrepancy seen between mass loss rates in the models and lab tests.

Next Steps: As the development of PROSPECT enters the next phase, it is vital that a more comprehensive understanding of likely water ice losses from lunar surface operations is reached, requiring the models to be more confidently backed up by laboratory data. Therefore, the PROSPECT Science Team plan to target specific aspects of this question over the coming months, with laboratory tests tailored specifically to measure desorption and diffusivity of water vapour through regolith, and to experimentally asses sublimation rates using mass spectrometry to corroborate the mass loss data recorded by the microbalance set-up.

References: [1] Trautner R. et al. (2018) 69th International Astronautical Congress, Paper ID: 42773 [2] Mortimer J. et al. (2018) *Planet. Space Sci.*, *158*, 25-33.

NEW MEASUREMENTS OF THE HYDROGEN ISOTOPIC COMPOSITION OF APOLLO LUNAR SOILS.

James Mortimer[1], Mahesh Anand[1,2], Sasha Verchovsky[1], Simona Nicoara[1]. [1]School of Physical Sciences, The Open University, Walton Hall, Milton Keynes, Buckinghamshire, United Kingdom, MK7 6AA, UK. (James.Mortimer@open.ac.uk), [2]The Natural History Museum, London SW7 5BD, UK.

Introduction: In the context of widespread renewed interest in the exploration of the Moon and the volatile inventory of the lunar surface, it seems timely to reassess the existing returned lunar soil samples for evidence of not only their volatile content, but also the isotopic composition of such volatiles, from which can be inferred their likely sources. Such information may prove highly useful to future missions intending to utilize such volatiles as resources to support human activity at the lunar surface in the coming decades. Although similar studies of the hydrogen content and isotopic compositions of lunar soils were conducted in the years following the return of the Apollo samples, new instrumentation available in the laboratory today means that around 30x less material is needed to make a measurement, enabling a wide-ranging study to be performed whilst using minimal irreplaceable sample mass.

Samples: In this study, we have focused on a suite of Apollo lunar soils, covering a range of missions and collection sites, and representing different lithologies and regolith maturities. Most samples were run at least 3 times, however, soils 12070 and 69921, having previously been analysed for C. N, He, Ne, and Ar at the Open University, only had enough sample mass remaining for one run each.

Mission	Sample	I_s/FeO (maturity)	No. of runs	Total Sample Mass Used (mg)
Apollo 11	10010	75 (mature)	3	76.25
	10084	78 (mature)	3	128.21
Apollo 12	12070	47 (submature)	1	30.59
Apollo 14	14163	57 (submature)	4	168.20
	14259	80 (mature)	3	81.66
Apollo 15	15030	68 (mature)	3	90.32
	15040	94 (mature)	3	87.66
Apollo 16	60500	80 (mature)	3	101.05
	61221	9.2 (immature)	3	151.28
	69921	90 (mature)	1	17.10

Table 1: Apollo lunar soil samples analysed in this study. I_s/FeO values taken from [12] and maturity indices from [13].

Given the relatively low hydrogen contents expected based on historical studies [1-9, 11], and taking into account the known H content of standard materials and their associated mass spectrometer signal strength, it was decided to use 25-40 mg of soil per subsample run, although for very immature soil 61221, a larger sample load of around 50 mg per run was used in order to ensure a sufficiently strong signal on the mass spectrometer.

Sample Preparation: Bulk soil samples were handled and weighed out in a cleanroom environment, using tools (spatulas, tweezers etc) that had first been cleaned by sonicating in isopropyl alcohol for 45 minutes, followed by further sonication in deionised water for 45 minutes, and then baked out in an oven at 100 °C overnight prior to use. Tools were wiped clean between use with different samples using lint-free cloths and isopropyl alcohol, gloves were replaced, and any benchtop surfaces the weighed samples might come into contact with were covered with fresh aluminium foil sheets to avoid the possibility of cross-contamination between different soil samples.

Using a spatula, small amounts of bulk soil were transferred from the main sample mass vial into a premade silver foil capsule, and then, using tweezers, the filled capsule was placed onto the weighing pan of a sensitive balance and the mass recorded to an accuracy of 0.0001 mg. When the desired sample mass had been added to the silver foil capsule, the final mass was noted and the silver foil capsule sealed by folding over the open top edge using tweezers. The filled capsule was then crushed into a small (≤ 2 mm diameter) round pellet using two sets of tweezers, ready for loading into the autosampler of the analytical instrument.

Analytical Method: A Thermo Flash HT Elemental Analyser, coupled to a Thermo Conflow IV and a Thermo MAT 253 mass spectrometer was used to measure the bulk hydrogen content and isotopic composition of the prepared lunar soil subsamples. The Thermo Flash HT EA consists of an autosampler, which sits on top of a furnace containing an outer ceramic tube, with layers of silver wool, quartz wool, and glassy carbon chips at the base, and into which is inserted a glassy carbon tube, also containing silver wool and glassy carbon chips at its base. Into this whole assembly is placed a small removable graphite crucible, into which the samples drop from the autosampler. The furnace is held at 1450 °C and has a flow of helium carrier gas through it of 250 ml/min during an analysis. The high temperature of the furnace tube, in the presence of so much carbon, releases any H-bearing species from the solid sample materials and reduces them to pure H_2 gas. This hydrogen gas is then carried by the flow of helium, through a GC column held at 85 °C, and into the MAT 253 mass spectrometer for analysis. Hydrogen reference gas, from a lab tank determined to have a δ^2H value of -157.00 ‰ compared to VSMOW, is also fed into the mass spectrometer interspersed with sample gas, with the flow being controlled by the ConFlow IV and held at 100 ml/min. The H_3 factor is determined at the start of each analytical sequence using this reference gas and the mass spectrometer's performance when measuring it. In addition to assessing the mass spectrometer performance using the hydrogen reference gas, a set of known isotopic and abundance reference materials and standards are run alongside the samples; this permits a 3-point (or more) isotopic calibration, and an abundance regression to be calculated for each sequence of samples run in the EA, and to monitor for any memory effects or anomalous measurements by the mass spectrometer during the analysis of a suite of different soil samples. Standards and reference materials used in these analyses include USGS57 (Biotite), USGS58 (Muscovite), EMA-P2 (sourced from Elemental Microanalysis Ltd), IAEA-CH-7 (polyethylene), and IA-R002 (laboratory standard, mineral oil, sourced from Iso-Analytical).

Results:

	I_s/FeO	δ^2H (‰)	±	Total H Content (ppm)	±
10010	75	-225.6	26.2	195.0	28.5
10084	78	-377.1 -385.1*	11.4 34.1*	119.0 136.8*	6.0 6.4*
12070	47	-314.3	-	112.3	-
14163	57	-405.2	13.8	59.3	23.1
14259	80	-348.8	14.6	177.8	9.7
15030	68	-334.8	16.3	153.7	4.2
15040	94	-355.4	5.4	146.7	9.5
60500	80	-392.5	10.5	130.7	12.1
61221	9.2	-156.2	8.0	84.8	2.0
69921	90	-269.3	-	194.6	-

Table 2: Measured δ^2H and Total H contents for all samples in this study. *calculated from data in [1]

In general, there is a weak positive correlation between total hydrogen content and δ^2H values; samples with the lowest total hydrogen content also have the lightest, most D-depleted isotopic compositions (Fig.1). This may suggest that a small contribution for an extremely isotopically-light source of hydrogen is being progressively masked by mixing with at least one and maybe more isotopically heavier sources of hydrogen. There is also a weak positive correlation between total H content and soil maturity, with more mature soils generally containing greater abundances of total H., although there is no correlation between soil maturity and δ^2H. A notable exception to these trends is Apollo 16 soil 61221, which has both an anomalously heavy isotopic composition of -156.2 ± 8.0 ‰ for its H content, and also an unexpectedly high total H content of 84.8 ± 2.0 ppm, considering its extreme immaturity (I_s/FeO = 9.2). 61221 has long been noted to be an unusual soil sample, with its unusually high volatile abundances (considering its immaturity) and the unusually low release temperatures of said volatiles leading researchers to suggest it may contain cometary or chondritic volatiles [10, 4]. 61221 was collected from the bottom of a trench, below 30 cm depth [12], and was thus had been shielded from isotopically-light solar wind H contributions; this could explain its unusually heavy isotopic composition compared to the other, mostly surface, soils in this study. Furthermore, it was brought back to Earth in container ALSRC#1, which did not seal properly and so was exposed to the moisture-bearing atmosphere inside the spacecraft and Pacific Ocean air back on Earth; this may have enabled the sample to adsorb much more water than it initially contained when collected, explaining both the relatively high total H content of 61221 and its terrestrial atmospheric-like isotopic composition.

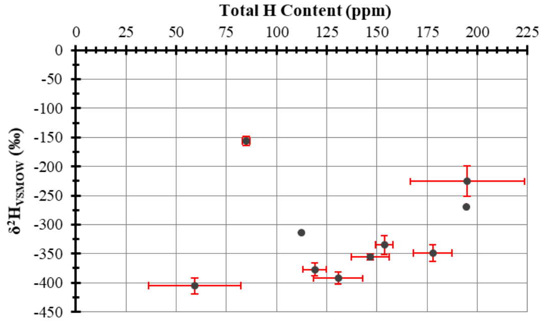

Figure 1: Positive correlation between measured isotopic composition and measured total H content of Apollo soil samples.

Since this technique permits only bulk total H to be analysed, the next step is to analyse the same soil samples using a recently established quantitative evolved gas method (Q-EGA; Verchosky et al., 2020), in order to measure the exact contributions from molecular H_2 gas *vs.* H_2O (and any other H-bearing species) to the total H contents measured so far. This will then permit the mixed isotopic compositions measured here to be deconvoluted *via* multiple component mixing calculations, to assess the likely source(s) of the various H-bearing compounds present.

Acknowledgements: The authors thank CAPTEM for allocation of lunar samples, and The Open University for supporting this work *via* the Space SRA.

References: [1] Epstein, S., Taylor, H. P. (1970) Proc. Apollo 11 Lunar Sci. Conf., **2**, 1085-1096. [2] Epstein, S., Taylor, H. P. (1971) Proc. 2nd Lunar Sci. Conf., **2**, 1421-1441. [3] Epstein, S., Taylor, H. P. (1972) Proc. 3rd Lunar Sci. Conf., **2**, 1429-1454. [4] Epstein, S., Taylor, H. P. (1973) Proc. 4th Lunar Sci. Conf., **2**, 1559-1575. [5] Epstein, S., Taylor, H. P. (1974) Proc. Lunar Sci. Conf. 5th, 1839-1854. [6] Epstein, S., Taylor, H. P. (1975) Proc. Lunar Sci. Conf. 6th, 1771-1798. [7] Friedman, I., Gleason, J. D., Hardcastle, K. G. (1970) Proc. Apollo 11 Lunar Sci. Conf., 1103-1109. [8] Friedman, I., O'Neil, J. R., Gleason, J. D., Hardcastle, K. (1971) Proc. 2nd Lunar Sci. Conf., **2**, 1407-1415. [9] Friedman, I., Hardcastle, K. G., Gleason, J. D. (1974) J. Res. US Geological Survey, **2**, 7-12. [10] Gibson, E. K., Moore, G. W. (1973) Science, **179**:4068, 69-71. [11] Merlivat, L., Lelu, M., Nief, G., Roth, E. (1974) Proc. Lunar Conf. 5th, 1885-1895. [12] Meyer, C (2010) Lunar Sample Compendium, https://curator.jsc.nasa.gov/lunar/lsc/. [13] Morris, R. V. (1978) Proc. Lunar Planet. Sci. Conf. 9th, 2287-2297.

Lunar elemental abundances from X-ray spectroscopy: Chandrayaan-2 Large Area Soft X-ray Spectrometer

S. Narendranath, Netra S Pillai, K. Vadodariya and the CLASS team

Space Astronomy Group, Indian Space Research Organisation

Lunar surface composition has been studied remotely and insitu primarily by the techniques NIR spectroscopy, X-ray spectroscopy and gamma ray spectroscopy. Each of these have different ways of estimating the abundances. X-ray fluorescence spectroscopy is one of the most direct approaches to mapping surface elemental abundances . Solar X-rays trigger X-ray fluorescence (XRF) lines from the lunar surface. Major elements (>1 wt%) can be detected unambiguously and quantitative abundances derived using fundamental equations (Shirawai and Fujino, 1969). The X-ray spectra are not sensitive to environmental factors like surface temperature and space weathering.

The mare-highland dichotomy in composition was clearly observed by the Apollo 15 and 16 XRS experiments in the service command module (Adler et al, 1973). DCIXS on SMART-1 measured Mg, Al, Si, Ca, Ti and Fe during intense solar activity (Grande et al, 2003, Swinyard et al, 2009). C1XS (Grande et al., 2009) on Chandrayaan-1 using the same technique provided elemental maps (Narendranath et al, 2011, Weider et al, 2012, Athiray et al, 2014) of 50 km to several hundred kilometers for ~ 5% of the Moon. Chandrayaan-2 Large Area Soft x-ray Spectrometer (hereafter CLASS) (Radhakrishna et al, 2020) is a continuation of C1XS but with about four times the geometric area. From the 100 km altitude polar orbit, the instantaneous ground pixel is 12.5 km x 12.5 km, the best spatial resolution ever flown. A Solar X-ray Monitor (XSM) (Shanmugham et al, 2019) simultaneously measures the varying solar X-ray spectrum in the 1- 15 keV energy range which is a crucial input for determining the elemental abundances from the lunar surface. During the six months of operations, CLASS has mapped O, Mg, Al and Si in several regions including high latitude and far side highlands. Na is also detected at several regions. We will present these initial results from CLASS and also highlight its capabilities for the benefit of potential users.

References

1. Adler, I., Trombka, J.I., Lowman, P. et al.., 1973. Apollo 15 and 16 results of the integrated geochemical experiment, The Moon, 7, 1973, 487-504
2. Athiray P. S. et al, 2014, C1XS results—First measurement of enhanced sodium on the lunar surface, Planetary and Space Science, Volume 104, Part B, Pages 279-287.
3. Grande, M., et al., 2003. The D-CIXS X-ray mapping spectrometer on SMART-1. Planet, Space Sci., 51, 427-433.
4. Grande, M., et al., 2009. The C1XS X-ray Spectrometer on Chandrayaan-1. Planet. Space Sci., 57, 717-724.
5. V. Radhakrishna, et al, 2020, Chandrayaan-2 Large Area Soft X-ray Spectrometer, CURRENT SCIENCE, VOL. 118, NO. 2, Page 219-225.
6. Shanmugam, M. et al,, 2012,The solar X-ray monitor on Chandrayaan-2. In 43rd LPSC, abstr. no. 1858.
7. Swinyard, B. M. et al., 2009, X-ray fluorescence observations of the Moon by SMART-1/D-CIXS and the first detection of Ti-Ka from the lunar surface. Planet. Space Sci., 57, 744–750

8. Shirawai, T., Fujino, N., 1966. Theoretical calculation of fluorescent X-ray Intensities in fluorescent X-ray spectrochemical analysis. Jpn. J. Appl. Phys. 5, 886-899
9. Narendranath, S. et al., 2011. Lunar X-ray fluorescence observations by the Chandrayaan-1 X-ray Spectrometer (C1XS): Results from the nearside southern highlands. ICARUS, 214, 53-66.
10. Weider, S. Z., et al., 2012. The Chandrayaan-1 X-ray Spectrometer: First results. Planet Space Sci., 60, 217-228.

SPACE WEATHERING AND VOLATILE FORMATION VIA SIMULATED MICROMETEORITE IMPACT EVENTS,

T. M. Orlando[1,2], R. A. Brennan[1], I. P. Dowding[3] and B. M. Jones[1], [1]School of Chemistry and Biochemistry, [2]School of Physics, [3]School of Materials Science and Engineering, Georgia Institute of Technology, Atlanta, GA 30332, (thomas.orlando@chemistry.gatech.edu).

Introduction: It is well known that space weathering of solar system bodies in the inner and outer solar system involves medium velocity (> 3 km/sec) micrometeorite impact events, solar wind electron and ion bombardment, magnetospheric plasma interactions, cosmic ray irradiation, and thermal excursions [1]. Investigating these energetic and thermal processes at a fundamental level is crucial to developing an understanding of the chemical and physical transformations of the surface materials typically observed in spectroscopic campaigns. In addition, space weathering and impact events can produce volatiles such as water that can be present in both the regolith and the exosphere.

In the past, interactions with energetic ions and electrons have been easily simulated in the laboratory and high power pulsed laser irradiation is purported to simulate impact events. Though the thermal spike and melting can be simulated with lasers, the momentum transfer, initial electronic excitations, and subsequent chemistry involving the impactor may not be simulated with this approach. It is therefore useful to compare the results of experiments using laser irradiation and particle impact approaches directly using the same "table-top" apparatus and the same sample.

Experimental Details: Though developing table-top micrometeorite bombardment systems remains a challenging task, laser-based technique that can dynamically accelerate grains exist [2-4]. Specifically, a laser induced microparticle accelerator (LIMA) or laser induced particle impact testing (LIPIT) system utilizes a high energy pulsed 1064 nm Nd:YAG laser to irradiate the backside of a thin nanostructured foil target or a thin metal foil/film covered with an elastic polymer as shown in Figure 1. Mineral and lunardust grains that are deposited on the front face of the launching target are accelerated off the substrate toward a collision target of interest, e.g. a lunar mare or highland slab. The velocity distributions of the grain projectiles are measured either directly using a fast-frame camera or optically using a stroboscopic approach. The latter utilizes a second 532 nm laser that passes through an optical delay.

The molecules produced and desorbed during a laser and particle impact are detected by either phase-locked detection quadrupole mass spectrometry or laser resonance-enhanced multiphoton ionization time-of-flight mass spectrometry (REMPI-TOF). The latter has detection sensitivities of ~10^6 or 10^8 molecules per quantum state depending upon the optical transitions used.

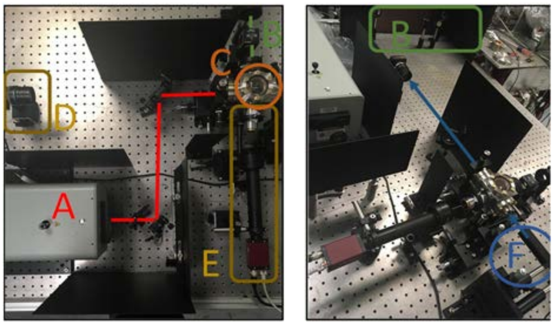

Figure 1: Left side: photo of the LIMA set-up showing the YAG laser (1064 nm) used to launch particles (A), part of the beam path for the second laser (532 nm) used for velocity measurements (B), main chamber with the launching substrate inside (C), the ancillary camera (D) used to image the substrate through a dichroic mirror, and the detection camera to photograph the moving particles (E).

Results: The experimental design of LIMA and its first results involving comparing laser irradiation and silicate grain impact events on lunar regolith are presented. Laser irradiated lunar breccia produces vibrationally excited molecular water with a cross section of 6.4×10^{-20} cm^2 [5]. This process likely occurs via a process known as recombinative desorption and should be prevalent during impact [6]. The water, oxygen and hydrogen formed during impact will desorb, however, depending upon the recrystallization rate in the impact zone, some water can be trapped within the glassy agglutinate. The relative ratios of these will be probed using direct analysis of the desorption products and optical probing of the laser irradiated and particle impact zone with micro-FTIR and micro-Raman microscopy.

Overall, the laser and microparticle acceleration testing system will allow quantitative measurement of the production of gas phase water, hydroxyl, oxygen and hydrogen during realistic grain impact events involving both mare and highland samples that are saturated with solar wind hydrogen. Being aware of the chemical evolution of the volatiles on the Moon will help further the understanding of how to find, process and utilize in situ resources such as water, hydrogen and methane.

References: [1] Bennett *et al. Chem. Rev.* 2013, **113**, 9086; [2] Lee *et al. Nat. Commun*. 2012, **3**, Article number: 116; [3] Lee *et al. Science* 2014, **346**, 1092; [4] Veysset *et al. Sci. Rep.* 2016, **6**, 25577; [5] DeSimone and Orlando, *JGR*, 2014, **119**, 884; [6] Jones, *et. al.GRL*, 2018, **45**, 10,959

Acknowledgments: This work was directly supported by the NASA Solar System Exploration Research Virtual Institute (SSERVI) under cooperative agreement numbers NNA17BF68A (REVEALS).

PERSPECTIVES FOR RADAR REMOTE SENSING OF THE MOON. R. Orosei[1], E. Flamini[2] and G. Mitri[2], [1]Istituto Nazionale di Astrofisica, Istituto di Radioastronomia, Bologna, Italy (roberto.orosei@inaf.it), [2]Università degli Studi "G. D'Annunzio", International Research School of Planetary Sciences, Pescara, Italy.

Background: Radars in planetary exploration have been employed to map topography, to measure properties such as dielectric permittivity and roughness, to produce images of the surface, and to probe the subsurface down to depths of a few kilometers. The first radar orbiting around the Moon was the Apollo 17 Lunar Sounder Experiment (ALSE) [1], operating at 5, 16, and 158 MHz for subsurface probing and surface imaging. This experiment detected geologic structures beneath the surface down to depths of 1.6 km. Beginning in 2007, the Lunar Radar Sounder (LRS) onboard the SELENE (Kaguya) Japanese mission, operating at 5 MHz, revealed the existence of subsurface stratification at depths of a few hundred meters in several lunar maria [2].

In the following years, the mini-synthetic aperture radar (Mini-SAR) onboard the ISRO Chandrayaan-1 spacecraft at 13 cm wavelength and the Lunar Reconnaissance Orbiter (LRO) Mini-RF at 13 and 4.2 cm wavelengths have been imaging the lunar polar areas searching for ice deposits in permanently shadowed craters, through the study of the polarization properties of surface echoes [3]. More recently, data from LRS have been analyzed to detect lava tubes a few tens of meters below the surface [4]. The Moon has also been imaged from Earth by transmitting radar signals at 12.6 cm from the Arecibo radio telescope, and by receiving echoes either through Mini-RF [5] or terrestrial radio telescopes [6].

Perspectives: Past experiments have probed the subsurface down to depths of more than a kilometer at MHz frequencies, and measured the properties of the first meters of Lunar regolith in the GHz frequency range. The full capabilities of radar experiments have yet to be realized, however, as illustrated for example by the SHARAD sounder at Mars [7]. A radar sounder with capabilities similar to those of SHARAD would be able to penetrate deep enough in the subsurface to detect lava tubes, and would have the resolution to characterize them in much greater detail compared to LRS. Also, it would be capable to map the layering of the lunar regolith and the interface between regolith and bedrock at a global scale, but with resolution and penetration comparable to those of the ground penetrating radars on board the Yutu and Yutu 2 rovers [8].

A global SAR imaging of the Moon has not yet been achieved. The use of SAR at higher frequencies compared to Mini-SAR and Mini-RF would allow the characterizaton of small-scale surface roughness and near-surface regolith density, at scales that are relevant to human exploration. Also, data acquired by radars operating at different frequencies in the GHz range can be used to characterize the upper meters of the regolith at different horizontal and vertical scales, allowing the study of its properties as a function of depth. As SAR is capable of imaging areas in permanent shadow such as polar craters, such information would also help characterizing the distribution of volatiles at depths that are accessible to human explorers. Interferometric SAR is now being proposed for the exploration of Venus [9]. Such technique has the potential to map the Lunar topography at much greater resolution than that of existing datasets, and repeated observations of the same area in different epochs can potentially measure millimeter-scale deformations of the surface occurring over time.

Several mission concepts based on radar instruments for the remote sensing of the Moon have been proposed in the last years, although none has been yet approved. Current plans for the return of humans to the Moon and the building of a permanent outpost there provide several types of opportunities for flying such experiments in the coming years.

References: [1] Porcello L. J. et al. (1974) *Proc. IEEE, 62,* 769-783. [2] Ono T. et al. (2009) *Science, 323,* 909-912. [3] Spudis P. D. et al. (2013) *JGR Planets, 118,* 2016-2029. [4] Kaku T. et al. (2017) *GRL, 44,* 10,155-10,161. [5] Patterson G. et al. (2018) *AGU Fall Meeting,* Abstract #P51G-2952. [6] Carter L. M. et al. (2015) *AGU Fall Meeting,* Abstract #P51C-2072. [7] Seu R. et al. (2007) *Science, 317,* 1715-1718. [8] Lai J. et al. (2019) *GRL, 46,* 12,783-12,793. [9] Smrekar S. et al. (2016) *AAS/DPS Meeting,* Abstract #48 216.07.

SURFACE DENSITY AND SIZE-FREQUENCY DISTRIBUTION OF BOULDERS IN LINNÉ CRATER'S EJECTA (MARE SERENITATIS – MOON).

Maurizio Pajola[1], Riccardo Pozzobon[2], Alice Lucchetti[1], Sandro Rossato[2], Emanuele Baratti[3], Valentina Galluzzi[4], Gabriele Cremonese[1], [1]INAF-Astronomical Observatory of Padova, Vic. Osservatorio 5, 35122 Padova, Italy (maurizio.pajola@inaf.it); [2]Geosciences Department, University of Padova, Padova, Italy; [3]Department of Civil, Chemical, Environmental and Material Engineering, University of Bologna, Bologna, Italy; [4]INAF-Istituto di Astrofisica e Planetologia Spaziali, Roma, Italy.

Introduction: The first boulders discovered on a non-terrestrial surface were observed on the Moon in 1965, thanks to the Ranger probe photographs [1]. In 1977, the Viking spacecraft photographed the first Martian boulders [2], hence suggesting that they might be present on other solid planetary surfaces too. Afterwards, by means of an increasing number of high resolution images of different Solar System targets it has become clear that boulders surrounding impact craters are present not only on the surface of the Earth [3], Moon [4] or Mars [5], but also on icy satellites [6], asteroids [7], as well as on the actively reshaping cometary surfaces [8]. By studying the boulder size-frequency distribution (SFD) it is possible to investigate a wide range of processes that occurred or are still occurring on a planetary/minor body surface. Indeed, boulders are the remnant of the excavated rocky interiors showing the underlying mineralogical composition [9] and their SFD, as well as the maximum generated sizes, are directly related to the impactor composition and velocity, to the impact site morphological, geological and mechanical properties. or the Moon's case, the study of the boulder SFD identified on different maria is a fundamental mean to study the distribution and layering thickness of the lunar volcanic basalts [10] and the superimposed regolith thickness present at the impact site [11].

The Linné crater: The Linné crater is located at 27.74° latitude and 11.8° longitude in northwestern Mare Serenitatis, a basaltic smooth basin located on the nearside of the Moon (Fig. 1). It is a simple crater with a diameter D of 2.194 km, a depth d of 0.52 km and a d/D ratio of 0.237 [12]. It likely formed in the late Copernican period, within the last 10 Ma [13], and lays on top of a complex stratigraphic sequence of distinct volcanic events that piled up to form an homogeneous unit, as shown in the geological map reported by [10]. The Mare Serenitatis stratigraphic sequence is characterised by piled up lava flows that could reach a few kilometers of depth from the maria surface, and each of these geological units can be up to several hundred metres thick [14].

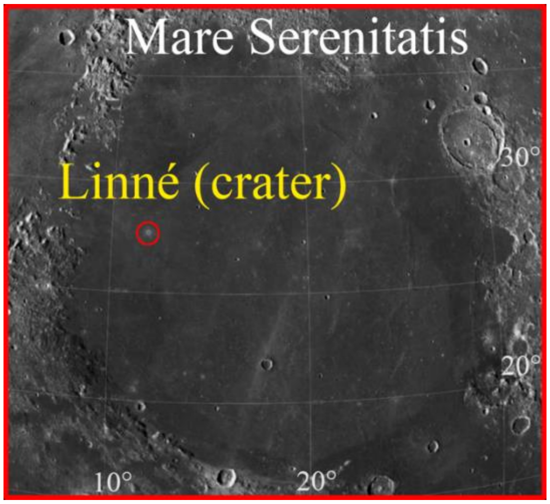

Figure 1: Context image showing the location of the Linné crater (2.2 km diameter, centred at 27.74° latitude, 11.8° longitude) in the Mare Serenitatis.

In order to identify and map the ejected boulders surrounding the Linné crater we used two publicly available (http://wms.lroc.asu.edu/lroc/) Lunar Reconnaissance Orbiter Camera (LROC) mosaics made of two Narrow Angle Camera (NAC, [15]) images each characterised by a spatial resolution ranging between 1.1-1.3 m. For the global boulder SFD analysis, we considered a circular area with a radius of 5.3 km outside the craters' rim, i.e. 6.4 km from the crater's centre. Beyond this distance the identifiable boulders are so few that a statistical analysis would be hardly meaningful. Over this area, 124.01 km^2 wide, we identified 46273 boulders ≥2.2 m, 12067 of which being ≥4.4 m (i.e. 4 pixels). The corresponding density of boulders ≥4.4m per km^2 is 137.85. As it is expected from impact cratering dynamics [16], the biggest sizes (>15 m) are all located in close proximity to the crater's rim, while their frequency radially decreases with increasing distances from the rim. At distances >3.5 km from the Linné's rim the ejected boulders are all <10 m in size. By studying the radial ejecta abundances, we found that, as the distance from Linné's rim increases, the boulder SFD power-law index steepens, ranging from -3.42 in the first 500 m to -3.82 at distances 10 times larger. This means that the relative abundance of the biggest sizes is largest within the first km from the rim, hence resulting in a shallower power-law index. On the other hand, at bigger distances the relative abundances of the smaller boulder sizes increases, becoming dominant

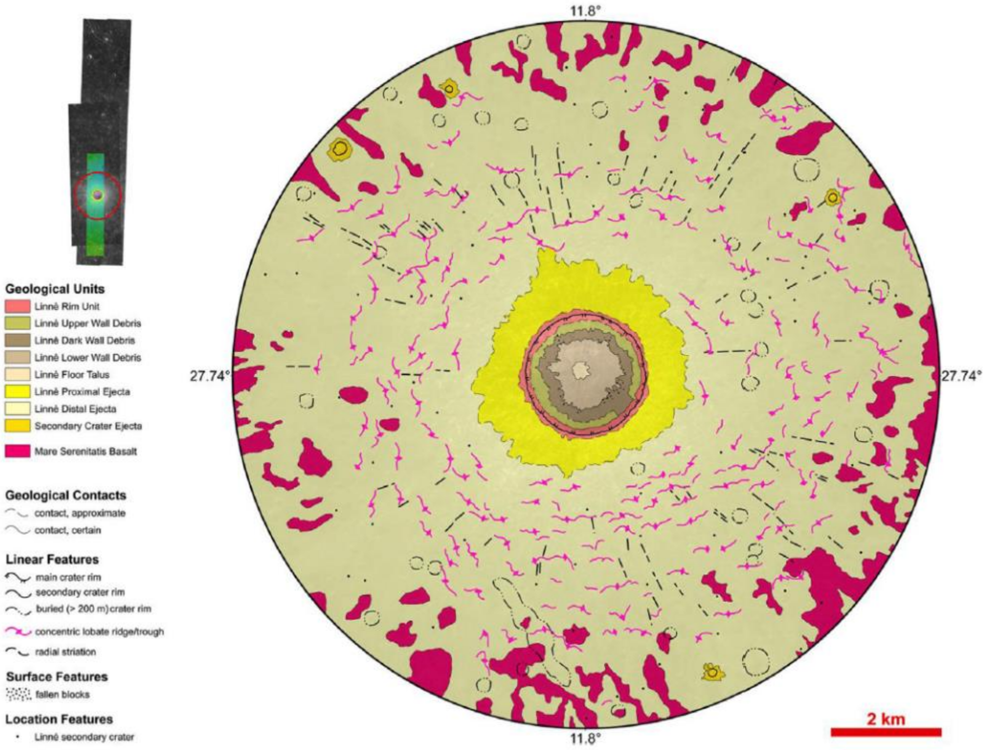

Figure 2: Geological map of the Linn_e crater showing the different identified units. Stereographic projection centred at 27.74_N; 11.8_E. Top-left: Extent of the NAC_ROI_LINNECTRHIA_E279N0118 image, the NAC_ROI_LINNECTRLOA_E282N0119 image, and the NAC_DTM_LINNECRATER_E280N0120 with the red circle indicating the extent of the geological map.

with respect to the full statistics and hence steepening the SFD.

The Linné high-resolution geological map we prepared (Fig. 2) shows that its proximal ejecta blanket is slightly asymmetrical in the NE-SW direction. This is confirmed by our boulder surface density analysis. Such behaviour can be either the result of an oblique impact emplacement of the original impactor, that ejected more boulders in the impact direction causing this preferential distribution, or the result of a perpendicular impact in the Mare Serenitatis location, but on a surface characterised by an interface between maria basalts with different local mechanical properties. We consider both scenarios equally likely to explain the ejecta distribution anisotropies we observe.

Eventually, we investigated the possible relation between the boulders ejecta distribution and the regolith thickness at the Linné impact site, since local variations of such blanket may affect the boulders' travel distance [11]. By exploiting our boulders statistics and our Linné geological map, coupled with Eq. 9 of [11], we estimated that the corresponding regolith thickness at the Linné impact site should be ~4.75 m [17], hence supporting the previously indicated Mare Serenitatis' evaluations [18].

Acknowledgments: This Paper is part of a project that has received funding from the European Union's Horizon 2020 research and innovation programme under grant agreement Nº776276 (PLANMAP). We gratefully acknowledge the NASA LROC Archive node for providing access to the LROC dataset used in this work.

References: [1] Kuiper, G.P., 1965. The Johns Hopkins Press, 99. [2] Binder, A.B. et al., 1977. JGR 82, 4439. [3] Senthil Kumar, P. et al., 2014. JGR Planets 119, 2029. [4] Cintala, M.J., McBride, K.M., 1995. NASA Technical Memorandum 104804. [5] Moore, H.J., Jakosky, B.M., 1989. Icarus 81, 164. [6] Martens, H.R. et al., 2015. Icarus 245, 162. [7] Michikami, T. et al., 2008. EPS 60, 13. [8] Pajola, M. et al., 2015. A&A. 583, A37. [9] Shoemaker, E.M., 1987. Meteor Crater, Arizona, GSA Field Guide - Rocky Mountain Section. [10] Hiesinger, H. et al., 2000. JGR Planets 105, 29239. [11] Bart, G.D., Melosh, H.J., 2010. JGR 115 (Issue E8). [12] Garvin, J.B. et al., 2011. LPSC 42 #2063. [13] Stickle, A.M. et al. 2016. Icarus 273, 224. [14] Weider, S.Z. et al. , 2010. Icarus 209, 323. [15] Klem, S.M. et al., 2014. LPSC 45 #2885. [16] Melosh, H.J., 1989. Impact Cratering. Oxford Univ. Press, New York, p. 245. [17] Pajola, M. et al. 2019, PSS, 165, 99-109. [18] Shkuratov, Y.G., Bondarenko, N.V., 2001. Icarus 149, 329.

VISTA: LOW MASS AND LOW POWER BUDGET INSTRUMENT FOR VOLATILES MEASUREMENT AND CHARACTERIZATION OF LUNAR DUST CHARGING AND LEVITATION PROCESSES.

E.Palomba[1], F. Dirri[1], A. Longobardo[1], D. Biondi[1], A. Galiano[1], A. Boccaccini, E. Zampetti[2], B. Saggin[3], D. Scaccabarozzi[3]; [1]INAF (National Institute for Astrophysics), Via Fosso del Cavaliere, 100, Rome, Italy (ernesto.palomba@inaf.it; fabrizio.dirri@inaf.it), [2]CNR-IIA, Via Salaria km. 29.300, 00016, Montelibretti, Rome, Italy; [3]Politecnico di Milano, Polo Territoriale di Lecco, Via G. Previati, 1/c, 23900, Lecco, Italy.

Introduction: The VISTA instrument, been developed by a consortium of institutes leaded by IAPS-INAF, plans to characterise the lunar environment and potential in situ resources to identify their implications for future human exploration. In the framework of Moon Exploration Programme, e.g. Artemis, Deep Space Gateway etc., VISTA can accomplish the following scientific objectives:

- measure the properties of lunar dust and the processes of charging and levitation by using a variable Electric Field and capacitors cascade;
- measure the volatiles content in the regolith (e.g. water ice and light organics) by using the TGA technique on accumulated samples;
- identify potential resources, which might be exploited in future exploration missions, such as water or organic rich material.

Scientific issues and VISTA working principle: the characterization of volatiles in lunar dust and the charging and levitation has significant implications both from the scientific point of view and for enabling future long-duration human lunar missions. In particular, the measurement of water and organic rich materials is extremely important to understand the resources available on the Moon and what kind of processes acts to originate and/or destroy Lunar volatiles. In addition, an instrument able to monitor the lunar dust inside the cabin leackege could be useful, specially to avoid problems to the crews in terms of safety and instrumentation [1] (during the Apollo missions it was noted that lunar dust, d<20 mm, easily entered the cabin after astronauts Extra Vehicular Activity).

VISTA is based on two micro-oscillator modules whose detecting sensitive section is made up of piezoelectric crystals with a conductive electrode that acts as a collector of micron and sub-micron size particles. The Piezoelectric Crystal Microbalances (PCMs) are widely used chemical sensors in gas/particle, in biological applications [2,3] and are able to convert mass changes into fundamental resonance frequency variations, by following the Sauerbrey equation [4]:

$$\Delta f \propto \frac{f_0^2}{A}\Delta m$$

which states that the change in resonance frequency Δf of a thin quartz crystal is proportional to the additional mass Δm deposited on it, f_0 being the resonance frequency of the uncovered quartz and A the sensitive area.

The two main challenge of VISTA are:

1) the possibility to manage the PCM temperature by using bult-in RTDs and performing μ–Thermogravimetric analysis (μ–TGA): this technique allows to infer the abundance of the desorbed volatile compound (from the mass variation) and its composition (by desorption rates with temperatures and enthalpy of sublimation, ΔH_{sub} [5]) (Figure 1);

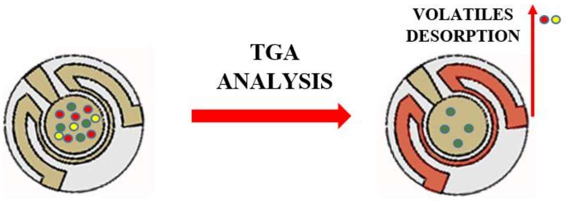

Figure 1: Volatiles desorption from PCM by using the built-in RTD.

2) the development of a new generation of microbalances able to attract charged dust grain by means of a variable Electric Field (EF), generated locally by the instrument itself: the EF will break the equilibrium between the Electric and the Gravity Fields on the Moon [6], allowing the electrically charged dust grains to be attracted toward the microbalance (Figure 2).

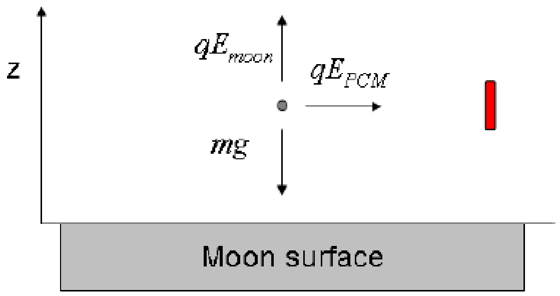

Figure 2: Dust deposition on the PCM (in red) when an electric field (E_{PCM}) is applied.

Instrument Concept and technical characteristics: VISTA is composed by three following units

1) *Unit 1:* the electronic box or MEU;

2) Unit 2: a Thermal-PCM (T-PCM), for measurements of volatile content in the regolith and water ice detection. PCM should be heated up to 280-330 K to allow desorption of water and light organics [7,8] while at low temperatures can be heated up to 160K to detect the water ice sublimation;

3) *Unit 3*, an Electric Field-PCM (EF-PCM) coupled with an electric field generator for measurements of electric properties of the dust. PCM placed inside a capacitor held at a voltage *V*. Dust particles passing through the capacitor will deposit on a PCM in a time depending on their charge-to-mass-ratio.

Unit 2 and *Unit 3* require low mass, low size and are low power-consuming. The *Unit 1 (Main Electronics)* can be easily shared with other instruments.

VISTA technical characteristics are summarized in Table 1.

Mass	<500g
Volume	< 300 cm^3
Average data rate	0.5 kbps
Average required power	< 2 W

Table 1: VISTA technical characteristics.

The heritage of **VISTA** [9] and the concept applied for Moon come from previous ESA ITT Projects and ESA Cosmic Vision 2015-2025 proposed mission:

- *Marco Polo* and *Marco Polo – R* (where VISTA was selected for Phase A): cometary-like activity of asteroids, water and organic content in the asteroid regolith, contamination assessing;
- *Penetrator for JUICE (JUpiter ICy moon Explorer)* [10]: organics and clathrate hydrates revelation, composition of non-ice materials of the Europa and Ganymede surfaces;
- *CAM (Contamination Assessment Microbalance)*, a ITT-ESA funded study for the development of a new QCM based device for contamination monitoring in space [11];
- *CAMLAB (Contamination Assessment Microbalance for LABoratory)*, a ITT-ESA funded study for the development of a quartz crystal microbalance for laboratory use.

Currently, the TRL is 6 for VISTA *Unit 2* while the TRL is 3 for the *Unit 3*. In particular, the technology for VISTA *Unit 2* is mature and has been tested in relevant environment while new improvements concerning the *Unit 3* are demonstrated in their basic principles and the performances will be evaluated experimentally.

References:

[1] Taylor L. A. et al. (2005), 1st Space Explor. Conf., AIAA; [2] Wood B.E. et al. (1996), Proc. SPIE 2864, 187-194; [3] Palomba E. et al. (2002), Adv. Spa. Res., 29, 8, 1155-1158; [4] Sauerbrey G. (1959), Z. Phys., 155, 206-222; [5] Dirri F. et al. (2016), AMT 8, 7127-7160; [6] Wang, J. et al. (2008), IEEE Transactions on Plasma Science, 26, 5, 2459-2466; [7] [7] Grady, M.M.; et al. (2002), *Met. Planet. Sci.*, 37, 713-735; [8] Sephton, M.A. et al (2002), *Nat. Prod. Rep.*, 19, 292-311; [9] Palomba E. et al. (2016), OLEB, 46(2-3), 273-81; [10] Gowen, R. A. et al (2010). Adv. Sp. Res.., 48, 8, 725-742; [11] E. Palomba et al. (2016), Metrology for Aerospace, IEEE Xplore Digital Library.

MINI-RF S- AND X-BAND BISTATIC OBSERVATIONS OF THE MOON. G. W. Patterson[1], L. M. Carter[2], A. M. Stickle[1], J. T. S. Cahill[1], M. C. Nolan[2], G. A. Morgan[3], D. M. Schroeder[4] and the Mini-RF team, [1]Johns Hopkins University Applied Physics Laboratory, Laurel, MD (Wes.Patterson@jhuapl.edu), [2]Lunar and Planetary Laboratory, Tucson AZ, [3]Planetary Science Institute, Tucson AZ, [4]Stanford University, Stanford CA.

Introduction: NASA's Mini-RF instrument on the Lunar Reconnaissance Orbiter (LRO) is currently operating in concert with the Arecibo Observatory (AO) and the Goldstone deep space communications complex 34 meter antenna DSS-13 to collect bistatic radar data of the Moon. These data provide a means to characterize the scattering properties of the upper meter(s) of the lunar surface, as a function of bistatic angle, at S-band (12.6 cm) and X-Band (4.2 cm) wavelengths. These data are being collected to address LRO science objectives related to: the vertical distribution of lunar water; the form and abundance of lunar water ice; how impacts expose and break down rocks to produce regolith on the Moon and other airless bodies; the present rate of regolith gardening; and how lunar volcanism has evolved over time.

Background: The transmitters for Mini-RF bistatic observations are AO (S-band) and DSS-13 (X-band). For each observation, the lunar surface is illuminated with a circularly polarized, chirped signal that tracks the Mini-RF antenna boresight intercept on the surface of the Moon. The Mini-RF receiver operates continuously and separately receives the horizontal and vertical polarization components of the signal backscattered from the lunar surface. The resolution of the data is ~100 m in range and ~2.5 m in azimuth but can vary from one observation to another, as a function of the viewing geometry. For analysis, the data are averaged in azimuth to provide a spatial resolution of 100 m. This yields an ~25-look average for each sampled location.

The data returned provide information on the structure (i.e., roughness) and dielectric properties of surface and buried materials within the penetration depth of the system (up to several meters for Mini-RF) [1-4]. The bistatic architecture allows examination of the scattering properties of a target surface for a variety of bistatic angles. Laboratory data and analog experiments, at optical wavelengths, have shown that the scattering properties of lunar materials can be sensitive to variations in bistatic angle [5-7].

Operations: Collecting data in the Mini-RF bistatic architecture requires significant advance planning with both the LRO operations team and ground-based facilities. As a result, no more than a few collects per month are feasible. The first Mini-RF bistatic campaign (2012-2015) included 28 AO S-band observations of the lunar surface – polar and nonpolar. Those observations provided data used to suggest the presence of water ice within floor materials of the crater Cabeus [8] and to characterize the weathering of Copernican crater ejecta [8,9].

The current bistatic campaign (2017-present) includes an additional 5 AO S-band observations and 48 DSS-13 X-band observations of the lunar surface (Figure 1). A variety of lunar terrains are being targeted to address science objectives for the ongoing LRO extended mission. They include collecting data of: the floors of south polar craters to search for signatures indicative of the presence of water ice; Copernican crater ejecta blankets to characterize rates of regolith breakdown/weathering; the ejecta of newly-formed craters to characterize the size-distribution and density of wavelength-scale scatters as a function of distance from the impact; mare materials within the Imbium basin to provide important information on the locations, extents, and depths flow units and deposits; and irregular mare patches (IMPs) and pyroclastic deposits to characterize their radar properties. In concert with the collection of these data, modeling work is being conducted to characterize the response of surface materials to variations in incidence angle and to address LRO science objectives with Mini-RF monostatic data.

Results: Initial analysis of south polar targets acquired at X-band do not appear to show the potential water ice signature detected at S-band [8]. This would indicate that, if water ice is present in Cabeus crater floor materials, it is buried beneath ~0.5 m of regolith that does not include radar-detectible deposits of water ice. Observations of Copernican crater ejecta materials at S- and X-band wavelengths continue to show variations that can be attributed to the age of the crater. Differences between S- and X-band observations of the same crater are also present, providing new insight into the size-distribution of radar scatters within the ejecta. Two craters that formed during the LRO mission have been identified in X-band Mini-RF data acquired in the current bistatic campaign. Analysis of these data suggest enhanced wavelength-scale surface roughness to radial distances of 100s of meters from the crater centers. S- and X-band observations of mare materials in the Imbrium basin and pyroclastic deposits in the Montes Carpatus, Aristarchus, and Taurus Littrow regions have been acquired and, combined with ground-based P-band observations, are providing important information on the locations, extents, and depths to individual flow units and deposits.

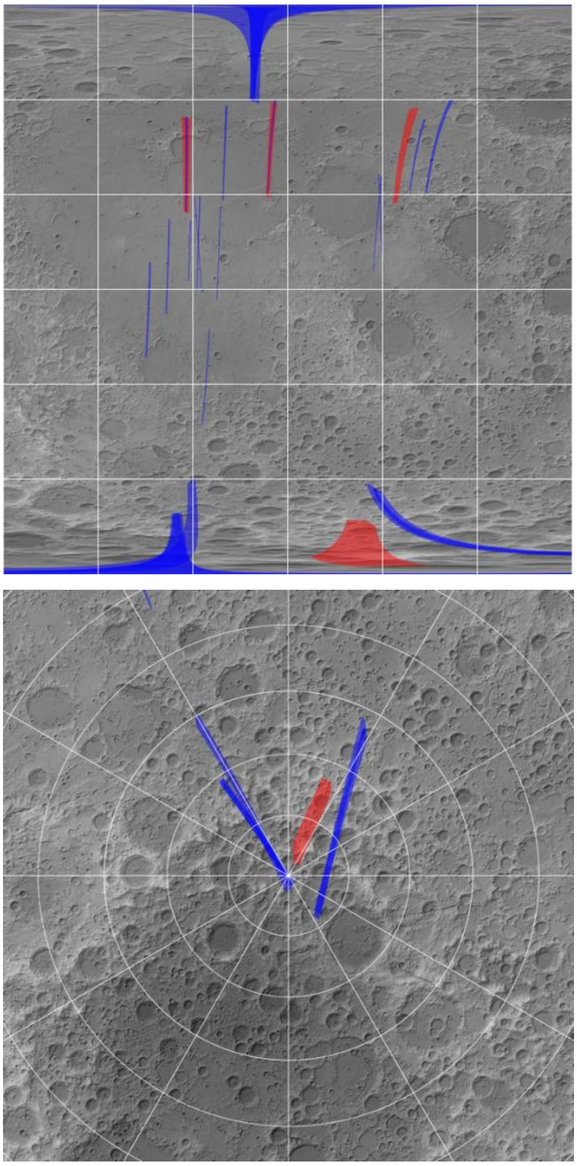

Figure 1: S-band (red) and X-band (blue) radar coverage in the second bistatic campaign for the lunar nearside (top; 90°W to 90°E) and south pole (bottom; 60°S to 90°S)

References: [1] Campbell et al. (2010), *Icarus*, 208, 565-573; [2] Raney et al. (2012), *JGR*, 117, E00H21; [3] Carter et al. (2012), *JGR*, 117, E00H09; [4] Campbell (2012), *JGR*, 117, E06008; [5] Hapke et al. (1998), *Icarus*, 133, 89-97; [6] Nelson et al. (2000), *Icarus*, 147, 545-558; [7] Piatek et al. (2004), *Icarus*, 171, 531-545. [8] Patterson et al. (2017), *Icarus*, 283, 2-19; [9] Stickle et al. (2016), *47th LPSC* #2928.

Comparison between shallow subsurface stratigraphy at CE-3 and CE-4 landing sites using high frequency Lunar Penetrating Radar data. Elena Pettinelli[1], Yan Su[2], Francesco Soldovieri[3], Sebastian Emanuel Lauro[1], Elisabetta Mattei[1], Barbara Cosciotti[1], Chunyu Ding[4], Chunlai Li[2]. [1]Mathematics and Physics Department of Roma Tre University, Roma 00146, Italy. [2] Key Laboratory of Lunar and Deep Space Exploration, National Astronomical Observatories, Chinese Academy of Sciences, Beijing, 100101, China. [3]Istituto per il Rilevamento Elettromagnetico dell'Ambiente, IREA-CNR, I-80124 Naples, Italy. [4]School of Atmospheric Sciences, Sun Yat-sen University, Zhuhai, 519000, China.

Introduction: Ground Penetrating Radar (GPR) is one of the most suitable geophysical techniques for Moon exploration, as it is potentially capable to image the shallow subsurface at great resolution. This instrument can be hosted onboard an orbiting spacecraft, be accommodated on a rover or directly used on the lunar surface by a human operator. The technique has been tested for the first time onboard the Command Module of the Apollo 17 during the Apollo Lunar Sounder Experiment (ALSE) [1]. ALSE was a coherent surface penetrating radar operating at three different frequencies band (5–5.5, 15–16.5, and 150–166MHz); it has been able to image the bottom of various buried craters and to detect several subsurface geological units like, for example, those located within Mare Crisium, up to a depth of about 1000–1400m [2]. More than thirty years later (2007), a new subsurface radar sounder equipped with a 5MHz antenna (the Lunar Radar Sounder—LRS) was hosted on board another spacecraft, during the Japanese SELENE mission (JAXA). LRS extensively explored the Moon subsurface for more than 2363 hours, reaching a maximum depth of about 2000m [3].

Yutu rovers: Recently, two surface coupling GPR instruments have been deployed on the Moon by CNSA. In 2013, Chang'e-3 (CE-3) landed on Mare Imbrium, deploying the Yutu rover that was equipped with two separated radar systems, a high frequency (500MHz) and a low frequency (60MHz) system [4]. On 3 January 2019, Chang'e-4 (CE-4) landed on Von Kármán crater within the South Pole-Aitken Basin, deploying Yutu-2 rover, which is equipped with the same radar systems employed for the CE-3 mission. The fate of the two rovers has been quite different: Yutu rover landed on Mare Imbrium and was able to only acquire about 100m of radar data, whereas Yutu-2 rover is still in operation and up to now have collected more than 300m of data.

Data and Methods: In this paper, we present and compare the data collected at the two landing sites using the high frequency antennas. Indeed, the low frequency antennas, installed on the back of the rovers, are electromagnetically coupled with the rover's metallic body. In this configuration, the antennas generate strong disturbances that largely overlap the signals coming from the subsurface preventing a reliable interpretation of the reflectors [5].

The signal penetration in the two sites is very different (with a maximum penetration in time that is about three time larger at Aiken Basin than at Mare Imbrium), suggesting a completely different geological context. Because both radar sections were affected by a large amount of volume scattering, we processed the data using an advanced approach based on microwave tomography [6]. This approach solves a linear inverse scattering problem and the buried features are estimated as "electromagnetic anomalies" with respect to the background (homogeneous soil). We obtained tomographic images of the subsurface where the buried targets (layers, localised objects) were detected, localized and geometrically outlined in terms of areas characterised by a significant contrast with respect to the electromagnetic properties of the subsoil.

Results: The tomographic approach allowed us to reconstruct the detailed stratigraphy of the first 40m of the subsurface at the CE-4 landing site. We found that the subsoil is primarily made of low-loss, highly porous, granular materials (regolith) with embedded boulders of different sizes distributed in a stratigraphic sequence that well represents an ejecta deposit [7].

For the CE-3 landing site, the tomographic reconstruction shows the presence of a very fine layer of regolith which covers a chaotic layer of large boulders and rocks having a dimension of 1m or larger. This layer has a thickness of about 2m and produces a strong signal attenuation that prevents the detection of the deeper structures. These results suggest that CE-3 radar data were collected above a field of large ejecta blocks (edge of a crater) or on a layer of fractured basalt.

References: [1] Porcello L. J. et al. (1974) *Proc. IEEE*, 62, 769-783. [2] Maxwell T. A. and Phillips R. J. (1978) *GRL*, 5(9), 811-814. [3] Ono T. et al. (2010) *Space Sci. rev.*, 154(1-4), 145-192. [4] Fang G. et al. (2014) *Res. Astron. & Astroph.*, 14, 1607-1622. [5] Li, C. et al. (2017) *IEEE TGRS* 56(3), 1325-1335. [6] Solimene et al. (2014) *IEEE Signal Processing Magazine*, 31, 90-98 [7] Li et al. (2020) *Science Advances*, in press.

COMPOSITION OF TERRAIN AT THE LUNAR SOUTH POLE.

C. M. Pieters[1] and P. G. Lucey[2],
[1]DEEPS, Brown University, Providence, RI 02912 (Carle_Pieters@brown.edu), [2]University of Hawaii at Manoa, 1680 East-West Rd, Honolulu, HI 96822 (lucey@higp.hawaii.edu).

Introduction: The character of the lunar poles and their potential resources (volatiles) are of great interest to space-faring countries and commercial organiztions as plans are made for future exploration of these enigmatic regions. At polar latitudes, average solar radiation onto the surface is weak since illumination is largely incident at near grazing incidence and some polar areas are in permanent shadow (**Figure 1**). Currently, useful compositional data derived from remote sensing spectroscopic techniques that rely on solar illumination is sparse to non-existant.

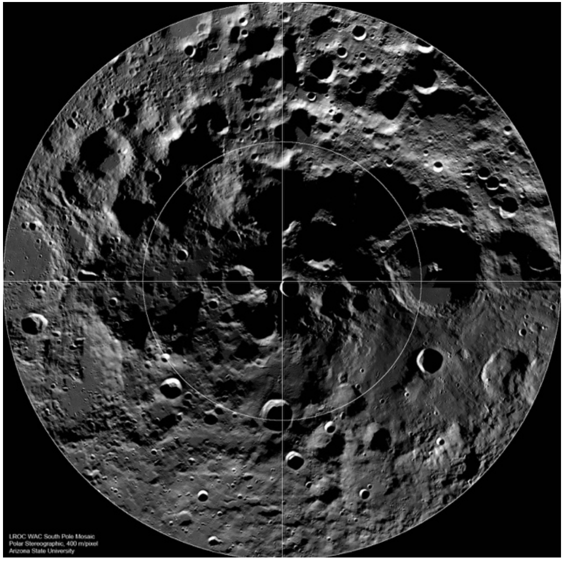

Fig. 1. LROC Wide Angle Camera (WAC) image mosaics of the lunar South Pole, width ~600 km, latitude ranges from 80° to the pole.

Nevertheless, two available data sources can be used to assess the bulk composition of lunar polar regions: a) LOLA global laser albedo maps (acquired with an active laser @ 1 µm) [1] and b) Lunar Prospector gamma ray iron abundance maps [2]. Both are relatively low spatial resolution, but are well suited to evaluate first-order composition properties based on knowledge from Apollo and Luna landed sample return sites at lower latitudes.

Integrated Data. Shown in **Figure 2** is a LOLA albedo map of the lunar nearside. This general view is very familiar to Earth-based observers measuring the Moon at 'Full-Moon' geometry when the sun is directly behind the observer and therefore casts no shadows visible from Earth. LOLA albedo maps are obtained at 1 µm, a slightly longer wavelength than typical optical albedo images (commonly acquired at 0.55-0.60 µm). Three fundamental types of lunar terrain are readily recognized: A) the low albedo basaltic maria (dark largely due to the presence of abundant Fe-bearing minerals), B) the high albedo 'highlands' that are now known to consist largely of low-iron feldspathic breccias [e.g. comparable to materials found at Apollo 16], and C) materials that have not been heavily affected by long exposure to the space environment (space weathering) and are relatively bright compared to surrounding materials. These unweathered areas typically have been recently exposed by events such as an impact crater (e.g. Tycho).

LOLA laser albedo maps can be prepared for other projections such as the hemisphere centered on the South Pole (**Figure 3**). Unlike solar illuminated polar images (Fig. 1), these shadow-free laser albedo maps now provide the same general compositional information as describd for Fig. 2. The feldspathic crustal terrain sampled at Apollo 16, although heterogeneously altered, is seen to extend across the entire South Pole region.

The compositional information associated with lunar albedo is largely dependent on the amount of FeO in lunar soils as well as the variety of ongoing local surface processes that alter the physical form of surface materials. This approximate relation between albedo and FeO provides a first order assessment of the entire south pole terrain composition as feldspathic in character. This interpretation is readily validated by fully independent measurements of FeO by gamma-ray spectroscopy [2] shown in **Figure 4**. The LOLA laser albedo map and the Lunar Prospector FeO measurements both show the lunar South Pole terrain to be low in mafic minerals (low FeO) and comparable to the feldspathic breccias sampled at Apollo 16.

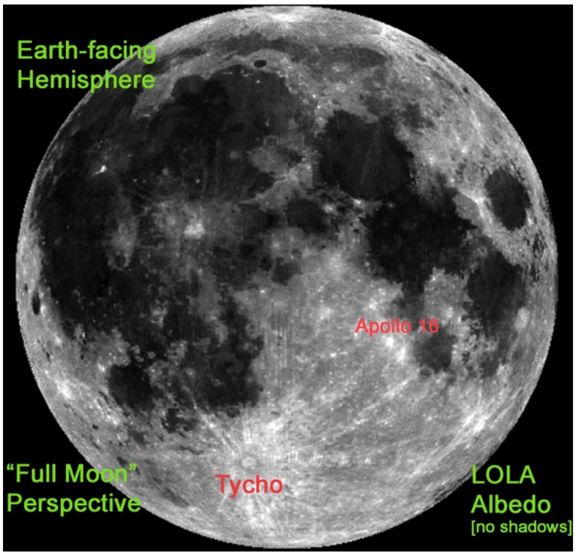

Fig. 2. LOLA laser albedo map (@ 1 µm) of the lunar nearside hemisphere [1] similar to a 'Full Moon' perspective.

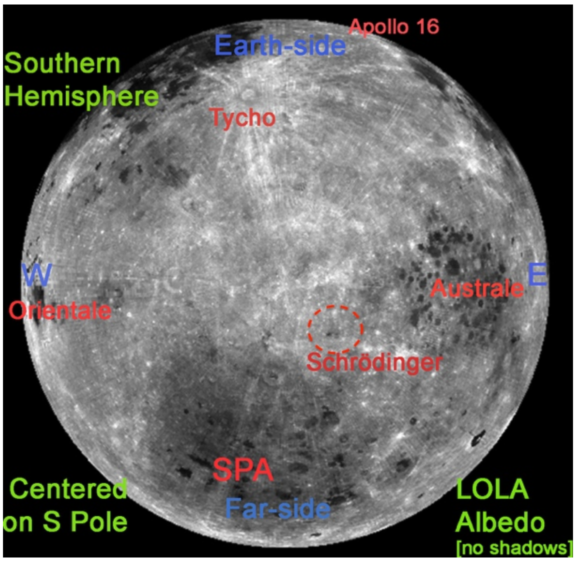

Fig. 3. LOLA laser albedo map [1] of the lunar hemisphere *centered on the South Pole*. The feldspathic Apollo 16 region is near the top. The south polar region is seen to be a continuation of the crustal feldspathic terrain.

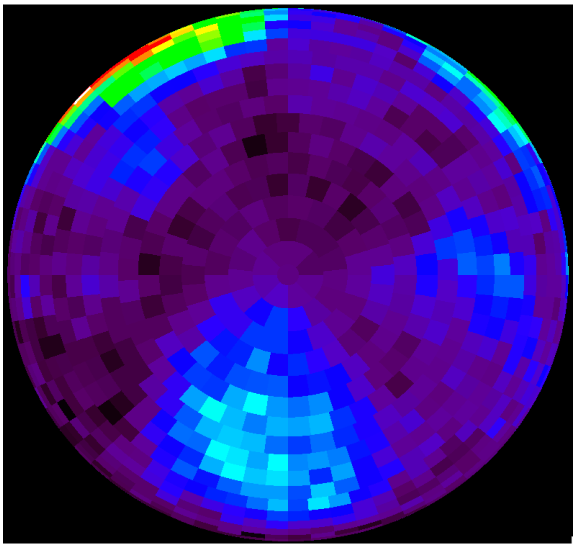

Fig. 4. Lunar Prospector FeO gamma ray data [2] for the hemisphere *centered on the South Pole* (same projection as Fig. 3). The lowest values of FeO are shown in dark purple shades.

Shown in **Figure 5** is a closer look at the LOLA laser albedo for the South Pole. The area within the black circle allows comparison to be made with the shadowed WAC optical image of Fig. 1. The bulk composition of the entire South Pole region is comparable to the feldspathic breccias sampled by Apollo and Luna. Although the low-albedo area of pyroclastic material in Schrödinger basin [e.g. 3] can be seen, it is readily recognized that mafic-rich materials associated with basaltic terrain or SPA are located several 100s km distant from the South Pole.

Given the extended impact history of the surface of the Moon, it is recognized that materials can be transported great distances and mixed with terrain of a different composition. For example, returned samples of Apollo 16 mature feldspathic soils show geochemical signatures of ~6% mare derived material [4]. Thus, a small amount of foreign materials from distal areas such as Tycho, SPA, or Australe basalts could occur in the South Pole region, but such materials will be quite rare. Identifying such exotic lithologies will require careful training of geologist-astronauts (as was done in Apollo) and adding capable 21st century tools and approaches, including modern higher spectral/spatial resolution *remote sensing* along with rapid *in-situ* assessment of rock and soil compositions.

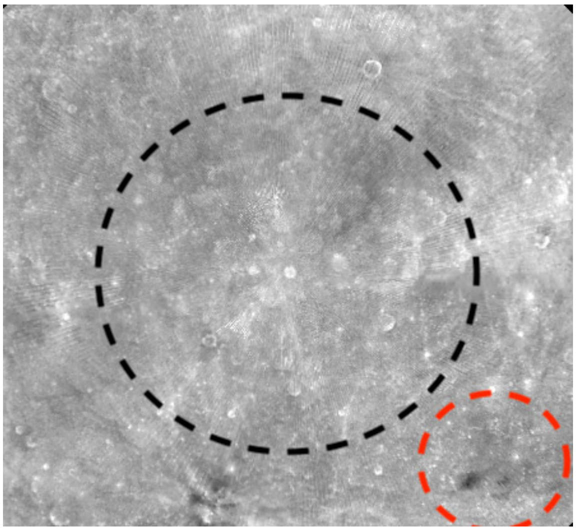

Fig. 5. LOLA laser albedo map centered on the unexplored lunar South Pole. The black circle outlines the 600 km WAC image of Fig. 1. The red circle outlines Schrödinger basin (as in Fig 3.).

References:

[1] Lucey, P. G., et al. (2014), The global albedo of the Moon at 1064 nm from LOLA, *J. Geophys. Res. Planets*, 119, 1665–1679,

[2] T. H. Prettyman et al. (2006), Elemental composition of the lunar surface: Analysis of gamma ray spectroscopy data from Lunar Prospector, *J. Geophys. Res.*, 111. E12007

[3] Kramer et al. (2013) Spectral and photogeologic mapping of Schrödinger Basin and implications for post-South Pole-Aitken impact deep subsurface stratigraphy, *Icarus*, 223, 131-148

[4] Korotev, R.L. (1997), Some things we can infer about the Moon from the composition of the Apollo 16 regolith. *Meteorit. Planet. Sci*. 32, 447–478.

OLIVINE DETECTION AND COMPOSITION DETERMINATION AT COPERNICUS AND ERATOSTHENES CRATERS.

P.C. Pinet[1,2], S.C. Chevrel[1,2] , Y.H. Daydou[1,2] and D. Dhingra[3], de Toulouse; UPS-OMP; IRAP; Toulouse, France, [2]CNRS/CNES; IRAP; 14, avenue Edouard Belin, F-31400 Toulouse, France, [3]Dept. Earth Sciences, Indian Institute of Technology, Kanpur, India. (patrick.pinet@irap.omp.eu)

Introduction:

We build on the previous works carried out [e.g.,1,2] to document at best the compositional variation of olivine from diagnostic absorption features across the visible and near-infrared wavelengths due to electronic transitions of Fe2+ in the crystal structure. Based on an advanced MGM deconvolution approach, the behavior of the three primary olivine absorptions near 1 μm (referred to as M1-1, M2, M1-2) is revisited. This improved modeling is then applied to orbital observations made with Chandrayaan-1 Moon Mineralogy Mapper (M3) over Copernicus and Eratosthenes craters.

MGM implementation:

The principle of the Modified Gaussian Model is to deconvolve overlapping absorptions of mafic mineral spectra into their fundamental absorption components. Spectra are modeled in the logarithm of reflectance space as a sum of modified Gaussian distributions superimposed on a baseline continuum [e.g., 3,4].The current procedure is described in [5,6].

Olivine Spectra Deconvolution / Methodology:

MGM inverse modeling provides with band center, band width and band depth estimates. Band centers are used to determine trend line equations for each individual absorption band, with an assessment on the regression performance (rms spectral distance between bandcenter estimate from MGM and the one from the trend line).

The olivine composition (Molar Forsterite Fo#) is then predicted based on minimizing the deviations in band centers from the established trends for the three absorptions simultaneously, using the integrated rms **s**pectral **d**istance to **t**rend quantity (**sdt**).

As presented in [5,6,7], our MGM procedure has been implemented on both synthetic and natural olivine samples spanning the forsterite – fayalite solid solution series [7].

Though not discussed here, the possible influence of the presence / absence of an absorption feature in the spectral range 600-700 nm linked to electronic transitions of minor elements Cr3+, Ni2+ and/or Fe2+/Fe3+ spin-forbidden crystal field transitions is assessed.

An example is given hereafter (Fig.1) for a synthetic spectrum (Fo#20 case) from [2].

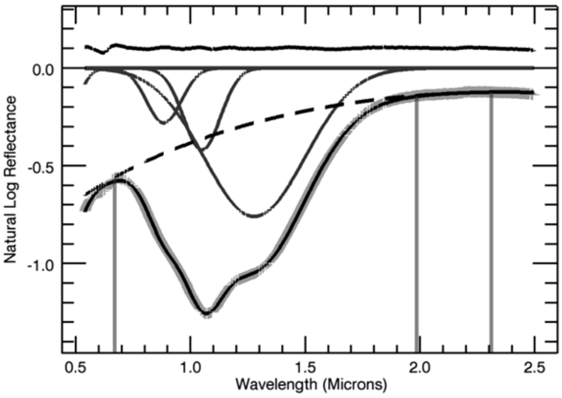

Figure 1. Case of C1DD96 (Fo#20). Measured spectrum (light grey crossed line) and MGM modeled one (thick black solid line) with the Gaussians (solid black lines) and polynomial (hatched line) and the residuals line along the spectral domain. Position of the local maxima along the spectrum used for the process of initialization (anchor points found at 670, 1985, 2310nm). For clarity, the residuals (observed – modeled quantity) are shifted by +0.1 which means that a perfect fit is displayed with a 0.1 flat line (rms : 0.005).

M3 orbital observations:

Copernicus: This procedure is then implemented on M3 spectra with the objective of documenting the petrology at Copernicus crater from spectra acquired over exposed outcrops (e.g., central peaks, inner walls and rims). The present study has been made on a subset of the M3G20090416T122951_V01_RFL hyperspectral image (140m/pixel) acquired during the OP2A optical period. Based on a previous selection of olivine-bearing spectra across Copernicus [5], we consider 5 spectra (Fig. 2) taken in the central peaks and northern wall and derive their composition (Molar Forsterite Fo#).

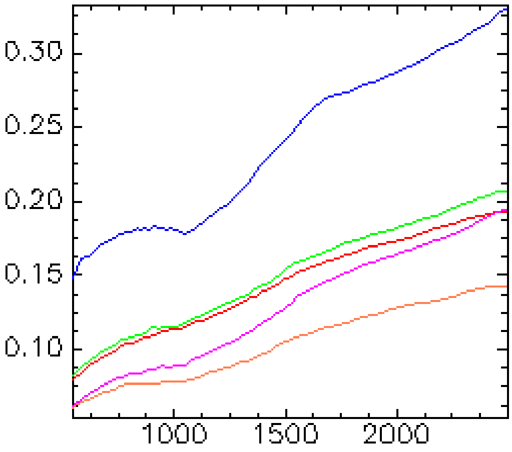

Figure 2. Selection of 5 spectra taken from the central peaks and the north wall of Copernicus crater.

As an example, the result of the MGM deconvolution for the blue spectrum (from Copernicus Pk3 peak, Fig. 2) is displayed and detailed (Fig. 3). From these deconvolutions, the olivine composition (Molar Forsterite Fo#).is derived for the 5 spectra (Fig. 4).

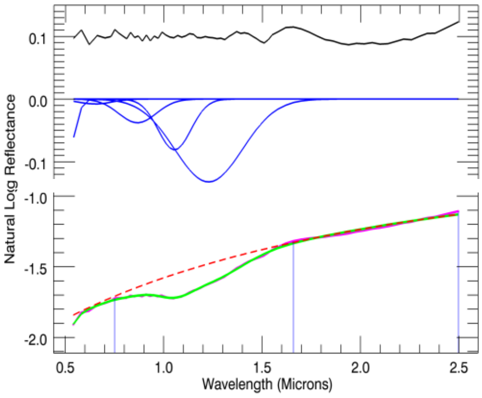

Figure 3. Copernicus Pk3 peak measured spectrum (light pink curve below the green one) and MGM modeled one (green solid line) with the Gaussians (solid blue lines) and polynomial (red hatched line) and the residuals line (black line) along the spectral domain. Position of the local maxima used for the process of initialization (anchor points found at 750, 1560, 2500nm). Residuals (see Fig.1) (rms : 0.007).

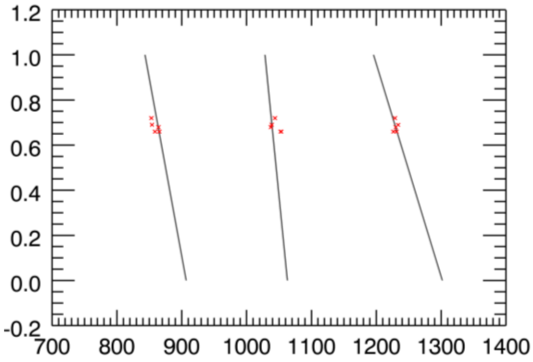

Figure 4. Olivine Composition estimates derived from our MGM for the 5 spectra shown on Fig. 2 in Molar % Forsterite vs band center (nm) graph.

A very interesting result is that for all spectra Fo# is found in the range of 0.70+/- 0.05 consistent with the idea that there is no obvious local/regional variability in the subsurface petrology of the target.

Eratosthenes: We perform the same type of analysis (Fig. 5) on spectra acquired, during the OP1B optical period of M3-Chandrayaan mission, over Eratosthenes crater [8], in its central peak region. This crater (diameter: 65km, depth: 6.5km) formed about 3.2 Ga and is located on the southern edge of Mare Imbrium, about 250 km N-E of Copernicus. From this modeling, we produce an olivine composition estimate (Fig.6). Fo# is found in the range of 0.68+/- 0.05.

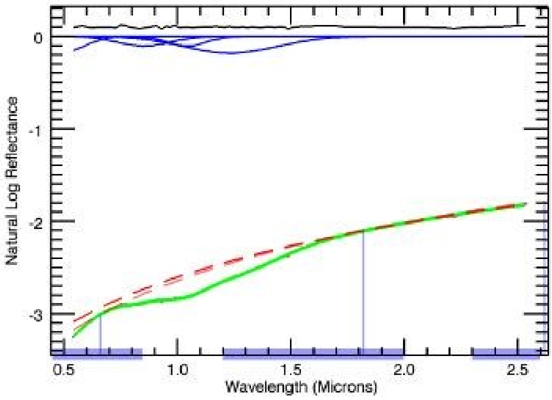

Figure 5. Eratosthenes measured spectrum (see fig. 3 caption). Position of the local maxima used for the process of initialization (anchor points found at 750, 1820, 2500nm). Residuals (see Fig.1) (rms : 0.008).

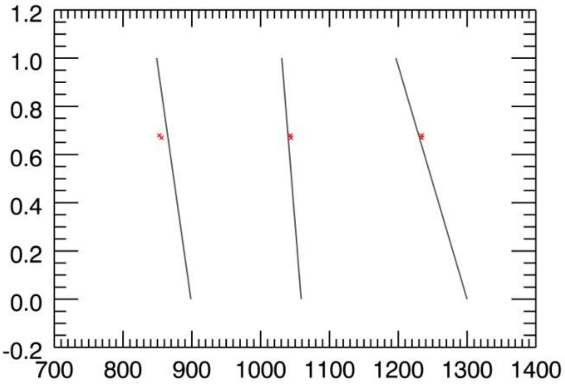

Figure 6. Olivine Composition estimates derived for the modeled spectrum shown on Fig. 5 in Molar % Forsterite vs band center (nm) graph.

Conclusions: The band center positions of the three primary olivine absorptions near 1 µm can be used simultaneously to produce a well-constrained prediction across an extended range of olivine solid solution composition from spectra measured on synthetic, natural samples and from orbital observations. The current results obtained for both Copernicus and Eratosthenes craters indicate that the olivine composition is rather Mg-rich and homogeneous, in favor of a plutonic origin with a single mantle source. This approach is of great interest for preparing the selection of potential landing sites and in situ characterization of samples to be collected for addressing the exploration and identification of primitive mantle lunar rocks (e.g., Heracles, Chang'e-4 mission and following ones, …).

References: [1] Sunshine J. M. and C. M. Pieters (1998) *JGR, 103*, 13,675–13,688. [2] Isaacson P.J. et al (2014) *Am. Miner*., *99*, 467-478. [3] Sunshine J.M. et al. (1990) *JGR, 95, B5*, 6955-6966. [4] Clenet, H. et al. (2011) *Icarus,* 213, 404-422. [5] Pinet et al. (2018) LPSC XLIX, #1899. [6] Pinet et al. (2019) LPSC L, #1806. [7] Pinet et al. (2019), ELS 7th *Proc.*, #25. [8] Kumaresan, P.R. et al. (2019), pss.2019.104817.

Acknowledgments : The support of CNES and CNRS to this project is duly acknowledged.

ITALIAN CUBESAT FOR MOON AND ASTEROID IMAGING: ARGOMOON AND LICIACUBE

S. Pirrotta[1] , M. Amoroso[1], G. Impresario[1], E. Dotto[2], V. della Corte[2], P. Tortora[3], M. Lavagna[4]
[1]Italian Space Agency (via del Politecnico snc, 00133 Rome, Italy. simone.pirrotta@asi.it), [2]Istituto Nazionale di Astrofisica INAF (via del fosso del cavaliere 100, 00133 Rome, Italy), [3]Università di Bologna (Dip. di Ingegneria Industriale, Via Fontanelle 40, Forlì, Italy), [4]Politecnico di Milano (Via La Masa 34, 20156 Milano – Italy)

Cubesats for Space Science missions have been recently conceived as important means to complement, and sometimes replace, the investigations performed by traditional larger probes. Modularity, standardization, intensive use of state-of-the art COTS technologies allow to manage cheaper missions in shorter timeframes, thus providing more opportunities to access near Earth and deep space, to a wider technical and scientific community. Since several years, the Italian Space Agency (ASI) has promoted, funded and coordinated the national initiatives in this promising sector, both for autonomous missions and in international cooperation. The first Italian satellite to the Earth-Moon environment will be ArgoMoon [1] [2], a 6U cubesat designed manufacture by the Italian company Argotec. It will be launched in November 2020, during the NASA Space Launch System (SLS) maiden flight "Artemis 1", with the aim to collect pictures of SLS Interim Cryogenic Propulsion Stage (ICPS) and of the other piggy-back nanosatellites. After the first mission phase, few orbital maneuvers will move the satellite in a geocentric highly elliptic orbit, with apogee high enough to allow flybys and imaging of the Moon and of the surrounding environment. Taking advantage of a Moon fly-by, after approximately six months this second part of the mission will be terminated with the injection into a heliocentric trajectory. A similar cubesat platform equipped with specific payloads, named "Light Italian Cubesat for Imaging of Asterods" (LICIACube), will join the NASA Planetary Defense mission "Double Asteroid Redirection Test" (DART) towards the binary asteroid system Didymos. The 6U cubesat, whose development is again under Argotec srl responsibility, will fly as DART piggyback and will separate from the main satellite five days before DART impact with Didymos B. Argotec srl is in charge of the satellite design, while Istituto Astrofisica e Planetologia Spaziali (INAF-IAPS) guides the payload customization and scientific case identification. The mission team is enriched by University of Bologna team, performing orbit determination and the satellite navigation, Polytechnic of Milan, for mission analysis and optimization. LICIACube on board optical payloads will capture images of impact effects, primarily the plume of ejecta, and of the non-visible side of the secondary body, thus supporting the validation of kinetic impactor technique for trajectory deflection. Both these cubesat-based initiatives will make use of the NASA Deep Space Network (DSN) stations for Ground Communications.

References:

[1] V. Di Tana et al., (2019) "ArgoMoon: there is a nano-eyewitness on the SLS" IEEE Aerospace and Electronic Systems Magazine, Vol. 34, Issue 4, 30-36.

[2] V. Di Tana et al., (2018) "ArgoMoon, a multipurpose cubesat platform for missions in Moon vicinity and orbit", European Planetary Science Congress 2018, held 16-21 September 2018 at TU Berlin, Berlin, Germany, id.EPSC2018-1181.

[3] P. Tortora et al., (2019) "LICIACube, the Italian Witness of DART Impact on Didymos", IEEE 5th International Workshop on Metrology for AeroSpace, 314-317.

[4] S. Pirrotta et al. (2019) "LICIACube, the Light Italian CubeSat for Imaging of Asteroid joining NASA DART mission to Didymos binary system", Geophysical Research Abstracts, Vol. 21, EGU2019-17780, 2019, EGU General Assembly 2019.

[5] A. Capannolo et al. (2019), "Challenges in LICIA CubeSat Trajectory Design to Support DART Mission Science" 70th International Astronautical Congress (IAC 2019), Washington DC, USA, Oct. 21-25, 2019.

A NEW MAP OF THE SOUTH POLE-AITKEN BASIN INCLUDING THE SOUTH POLE. C. M. Poehler[1], M. A. Ivanov[2], C. H. van der Bogert[1], H. Hiesinger[1], J. H. Pasckert[1], W. Iqbal[1], J. Wright[3], and J. W. Head[4], [1]Institut für Planetologie, Westfälische Wilhelms-Universität, Wilhelm-Klemm-Str. 10, 48149, Münster, Germany, c.poehler@uni-muenster.de, [2]Vernadsky Inst., RAS, Russia, [3]School of Physical Sciences, The Open University, Milton Keynes, MK7 6AA, UK, [4]Department of Earth, Environmental and Planetary Sciences, Brown University, Providence, RI 02912 USA.

Introduction: The South Pole-Aitken (SPA) basin is located on the lunar farside and is centered at ~53° S, 191° E. It is the largest [1-5] and oldest observable basin [6,7] on the Moon. Therefore, the timing of SPA formation gives valuable information on the formation and evolution of the lunar crust.

Here, we provide a comprehensive map (1:500K) of the SPA basin, including the South Pole region and parts of the Orientale basin, which is an extension of a map of the Apollo basin region [8]. The SPA basin and the South Pole are targets for future and ongoing robotic and human missions [e.g., 9–13], since the area potentially includes exposed mantle material [14, 15], sources of volatiles (e.g., pyroclastic deposits [6]), and permanently shadowed regions that may harbor ice or other volatiles [16]. For such missions, detailed studies of the geological history and setting of the region are necessary. Our map provides a comprehensive overview of the geology in the region (***Fig. 1***).

Methods: For large-scale mapping, we used the Lunar Reconnaissance Orbiter (LRO) Wide-Angle Camera (WAC) basemap (100 m/pixel). We used Narrow Angle Camera (NAC; 0.5 m/pixel) [17] and Kaguya (10 m/pixel) data for more detailed, smaller areas and for identifying specific features. We also used Clementine [18], M^3 [19], and Kaguya MI [20] data for spectral/compositional information. Topographic features were identified using Lunar Orbiter Laser Altimeter (LOLA) digital elevation products [21, 22] and a LOLA/Kaguya merged digital elevation model with a resolution of 59 m/pixel [23]. To mitigate the effect of low solar illumination angles at the pole, which cause significant shadows, we produced hillshade maps with various illumination conditions. We used PLANMAP mapping standards [24], an extension of USGS standards [25].

To begin with we used morphological appearance and albedo contrasts for identifying units and features. We determined relative ages for the units using morphological and stratigraphic evidence. In addition to relative dating of geologic units, we performed crater size-frequency distribution (CSFD) measurements and from these determined absolute model ages (AMAs) using the production and chronology functions of [26]. CSFD measurements were made using CraterTools [27] in ArcGIS, and we fitted the AMAs with Craterstats [28]. Detailed descriptions of the technique are given by [26, 29].

Geology: In our study area we defined three classes of geologic features: Basin materials, crater materials, and plains-forming materials.

Basin materials are related to the formation of the large basins in the area with the oldest and most dominant being the SPA basin. We also identified materials related to the Apollo, Schrödinger, and Orientale basins.

Crater materials are divided into different classes according to the state of degradation and shape of the craters. We dated several craters to obtain a framework for both the relative and absolute stratigraphy across the mapped area.

Plains-forming materials are characterized as relatively flat, smooth surfaces, and can be further divided into dark and light plains based on their albedoes.

SPA's rim is obscured by various later impacts and is degraded due to its old age. It appears most distinctively in the NW part of SPA, close to the Apollo basin. Here, we identify two topographic rings of SPA rim massifs. Around the South Pole, the morphological features become more difficult to interpret due to the low sun angle and extensive shadowing. We were able to find traces of the outer massif, but most of the inner massif seems to be destroyed by younger craters, if it existed in this area.

Acknowledgments: This paper is part of a project that has received funding from the European Union's Horizon 2020 research and innovation programme under grant agreement N°776276 (PLANMAP).

References: [1] Stuart-Alexander (1978) USGS Map I-1047, 1978. [2] Spudis et al. (1994) *Science 266*, 1835-1839. [3] Hiesinger and Head (2004) *PLPSC 35*, 1164. [4] Shevchenko et al. (2007) *Solar Sys. Res. 41*, 447-462. [5] Garrick-Bethell and Zuber (2009) *Icarus 204*, 399-408. [6] Wilhelms (1987*) USGS SP-1348*, 302. [7] Hiesinger et al. (2012) LPSC 43, 2863. [8] Ivanov et al. (2018) *JGR Planets, 123*, 2585–2612. [9] Flahaut et al. (2019) *PSS.*, in press. [10] Steenstraet al. (2016) *Adv. Space Res. 58*, 1050–1065. [11] Allender et al. (2018) *Adv. Space Res. 63*, 692–727. [12] Hiesinger et al. (2019) *LPSC 50*, 1327. [13] Huang et al. (2018) *J. Geophys. Res., 123*, 1684 – 1700. [14] Melosh et al. (2017) *Geology, 45*, 1063-1066. [15] Yamamoto et al. (2010) Nature Geoscience 3, 533-536. [16] Nozette et al. (2001) *J. Geophys. Res., 106*, 23253– 23266. [17] Robinson et al. (2010) *Space Sci. Rev., 150*, 81–124. [18] Pieters et al. (1994). *Science, 266*, 1844–1848. [19] Isaacsom et al. (2013). *JGR, 118*, 369–381. [20] Ohtake et al (2013*) Icarus, 226*, 364–374. [21] Smith et al. (2010) Icarus, 283, 70-91. [22] Smith et al. (2010) *Geophys. Res. Lett.*, 37, L18204. [23] Scholten et al. (2012) *JGR, 117*, E00H17. [24] wiki.planmap.eu/display/public/D2.1-public. [25] FGDC (2006). FGDC-STD-013-2016. [26] Neukum et al. (2001) *Space Sci. Rev. 96*, 55–86. [27] Kneissl et al. (2011) *PSS, 59*, 1243–1254. [28] Michael and Neukum (2010) *EPSL, 294*, 223–229. [29] Hiesinger et al. (2000) *JGR, 105*, 29239–29276.

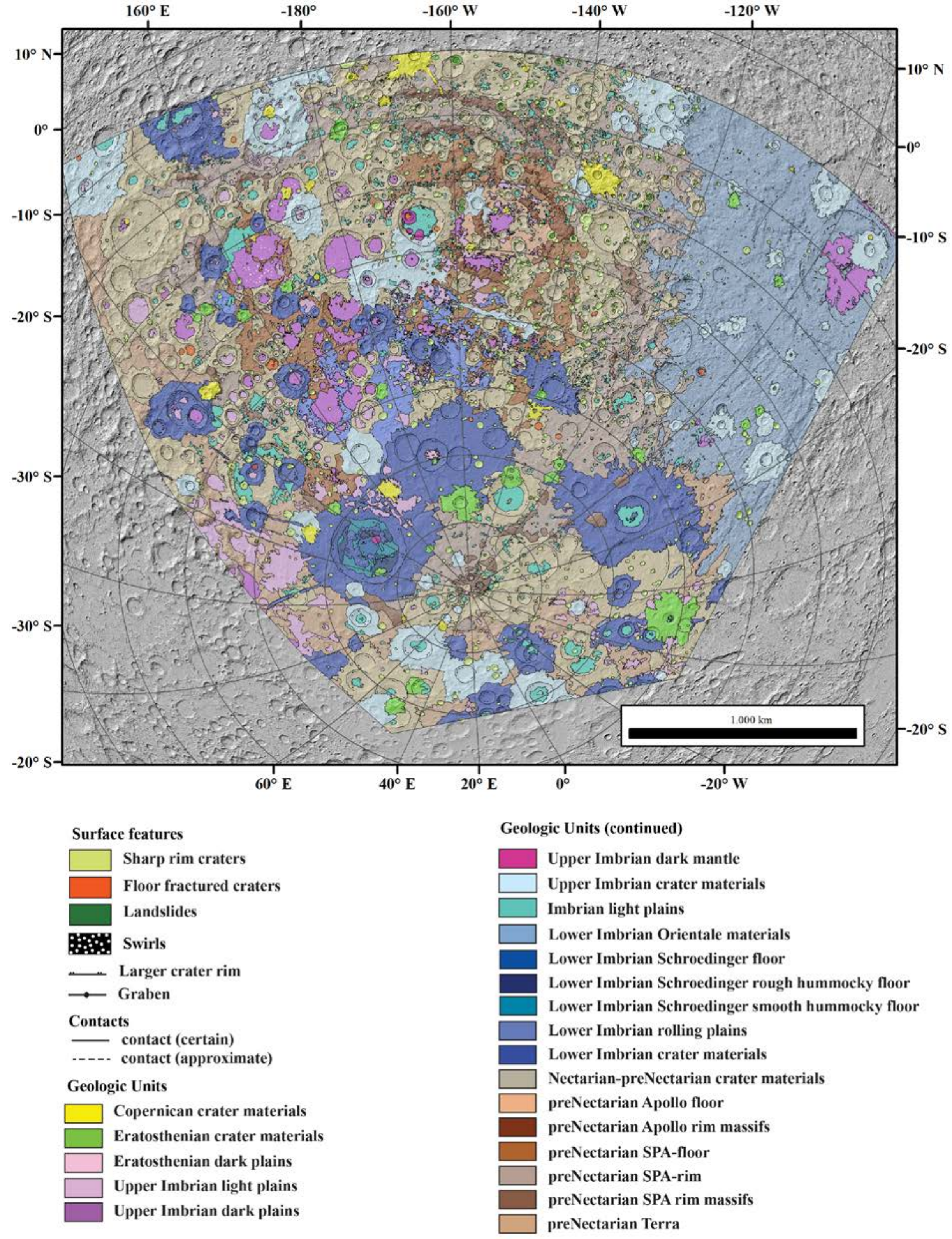

Figure 1. *Preliminary geological map of the lunar South Pole and the South Pole-Aitken basin at a scale of 1:500,000 in Lambert projection centered at 157.5° S and 53° E. The background image is a hillshade map compiled from a LOLA global DEM.*

GEOLOGIC MAP, LANDING SITE SELECTION AND TRAVERSE PLANNING IN COPERNICUS CRATER.

Riccardo Pozzobon[1], Filippo Tusberti[1], Maurizio Pajola[2], Matteo Massironi[1,3], [1]Department of Geosciences, University of Padova, Via Gradenigo 6, 35131, Padova (Italy), [2]INAF – Padova Astronomic Observatory, Vicolo dell'Osservatorio 5, 35122, Padova (Italy), [3]Center of Studies and Activities for Space "G. Colombo", University of Padova, Via Venezia 15, 35131, Padova (Italy).

Introduction: Copernicus Crater is a relatively young impact crater of ~800 Ma with a diameter of ~100 km and it is located on the lunar near side. Developed within the PlanMap H2020 project, we hereby present two geologic maps, at a broad and local scale, and the technical evaluation as a landing site with possible traverse paths and sampling sites. The scientific rationale guiding this study is that Copernicus is pivotal to refine the lunar time scale and because of its particular composition. Sample returns could provide absolute ages useful to improve both the lunar crater chronology and, by extrapolation, that of other inner solar system terrestrial bodies. Moreover, olivine spectral signature was detected [1], and this can provide information about the lunar crust and mantle. The whole central peak represents, in fact, exhumed deep olivine-rich troctolite [1]. This work is timely given the foreseen human assisted robotic missions proposal and Artemis programs that both can benefit from the outcomes of these analyses.

Data and methods: As base maps for broader scale geologic mapping of the crater we made use of the merged DEM of LOLA+Kaguya at 59 m of grid spacing and LROC WAC 100m/pixel mosaic. This was integrated with spectral observations in order to recognize lithological variations and to better define the geologic units.

To do that, the Clementine UVVIS color ratio mosaic was used: the band ratios combined in an RGB mosaic were used to determine the relative abundance in titanium, olivine and mafic minerals in general, and volcanic glasses.

Higher resolution geologic mapping, landing site and traverse definition analysis were carried out on mosaics of LROC NAC images, with high and low incidence angles scaled at 5 m/pixel.This resolution was chosen as a compromise between the need of high detail for landing and traverse definition and the need of a first screening of a relatively large area.The images with low incidence angles were used, together with the Clementine band ratio mosaic to identify the compositional units, whereas the higher incidence was used to better constrain the morphologies and obstacles.

Mapping and traverse definition: The geologic mapping was at first performed at a broad scale of 1:400.000 both on Clementine, WAC images, and DEM shaded relief in order to detect the broad geologic context in terms of smoothness of terrains, obstacles, general morphologies and potentially interesting areas in terms of composition. As a second step, to assess the possibility of landing in Copernicus maximizing safety and scientific return we used the LROC NAC mosaic. We mapped in higher detail landforms previously identified at a larger scale, aiming to plan rover traverses and scientific stops (for potential in-situ analysis and/or sampling) as well as to define possible obstacles and hazards. Therefore, a second geologic map at higher resolution (1:100.000) of NW quadrant of Copernicus was produced. We selected this location for its relatively high smoothness, low number of obstacles and significant hazards. Three different landing ellipses were selected: sizes were derived from the NASA Mars rovers MSL Curiosity and Mars2020, since to date no constraints are available for the Moon and their location was chosen in order to avoid obstacles and to be as meaningful as possible in terms of sites of interest in the surroundings.

Hazards related to rock abundance wew investigated within the landing ellipses according to [2] as well as for small impact craters together with overall surface slope. Following the constraints defined for Schrödinger crater exploration in the HERACLES program [3] six traverses were defined: three long and three short traverses, of 32 and 16 km respectively. The sampling sites/stops within all the foreseen traverses (from a minimum of 13 to a maximum of 19 per traverse with a variable time duration from 6 to 18 days [3]) were chosen to maximise the scientific return, following the future science goals in in situ lunar exploration [4].

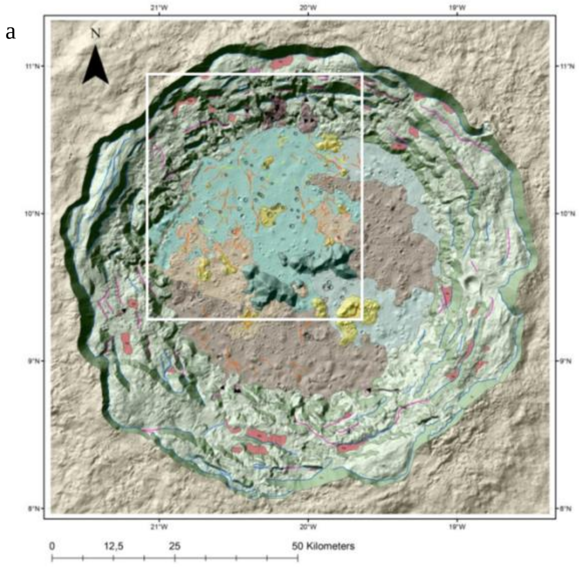

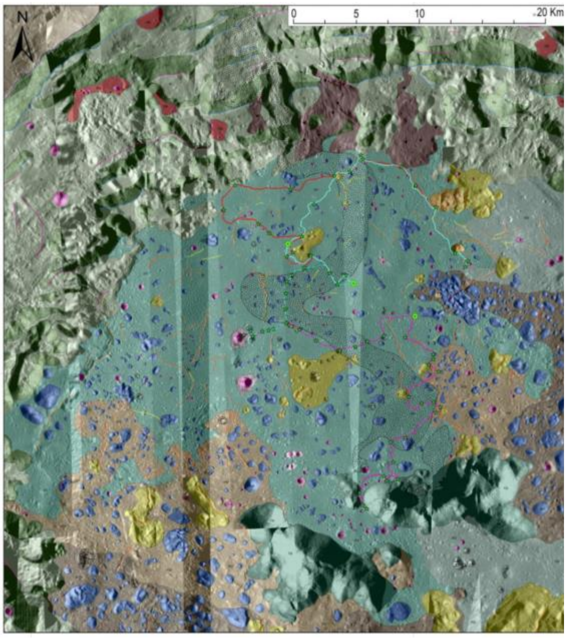

Figure 1: in a) the geomorphologic mapping of Copernicus crater at a scale of 1:400.000 overlaid in transparency on LOLA-Kaguya shaded relief DEM. For the units description we forward to the PlanMap data repository https://data.planmap.eu/pub/moon/PM-MOO-MS-Copernicus_01/. In white it is marked the area of higher resolution mapping at 1:100.000 shown in b). Here more landforms were characterized and proposed rover traverses are visible in red, cyan and pink. The dashed lines identify the short traverses.

Conclusions: This work represent a first assessment for landing on the near side of the Moon in a well-known location that would provide insights in the lunar crust composition and evolution as well as new constriaints to the lunar chronology. This investigation could provide a baseline for future and more detailed analyses as soon as more engineering and scientific constraints will be provided for unmanned or manned landings on the lunar near side both from the Heracles and Artemis programs aiming to return to the moon in this decade.

This research was supported by European Union’s Horizon 2020 under grant agreement No 776276-PLANMAP.

References: [1] Liu, F., Yang, R., Zhang, Y., Qiao, L., Wang, S., Yang, Y., & Wang, X. (2011). Distribution of olivine and pyroxene derived from Clementine data in Crater Copernicus. Journal of Earth Science, 22(5), 586–594. https://doi.org/10.1007/s12583-011-0209-2

[2] Pajola, M., Rossato, S., Baratti, E., Pozzobon, R., Quantin, C., Carter, J., & Thollot, P. (2017). Boulder abundances and size-frequency distributions on Oxia Planum-Mars: Scientific implications for the 2020 ESA ExoMars rover. Icarus, 296(May 2017), 1339–1351. https://doi.org/10.1016/j.icarus.2017.05.011

[3] Steenstra, E., Martin, D., Mcdonald, F., Paisarnsombat, S., Venturino, C., O’Hara, S., ... Kring, D. A. (2016). Analyses of Robotic Traverses and Sample Sites in the Schrödinger basin for the HERACLES Human- Assisted Sample Return Mission Concept. In Advances in Space Research. https://doi.org/10.1016/j.asr.2016.05.041

[4] Massironi, M., & Ferrari, S. (2019). Future science goals of in situ Lunar explorations. International Workshop on Metrology for AreoSpace.

LUNAR ISRU DEMONSTRATION MISSION PHASE-A: PAYLOAD FOR EXTRACTION OF OXYGEN FROM THE REGOLITH.

I. Pretto[1], R. Freddi[1], F. Venditti[1], M. Lavagna[2], M. Masi[2], A. Colagrossi[2]; P. Lunghi[2]; S. Silvestrini[2], L. Richter[3], A. Pilati[4], A. Rusconi[4], G. Sangiovanni[4], C. H. van der Bogert[5], D. Binns[6], [1]OHB Italia S.p.A., via Gallarate 150, 20151 Milano, Italy – *ipretto@cgspace.it*, [2]Politecnico di Milano, via La Masa 34, 20156 Milano, Italy – *michelle.lavagna@polimi.it*, [3]OHB System A.G., Manfred-Fuchs-Str. 1, D-82234 Weßling, Germany – *lutz.richter@ohb.de*, [4]Leonardo S.p.A., Viale Europa snc, 20014 Nerviano (MI), Italy – *alessandro.pilati@leonardocompany.com*, [5]Westfälische Wilhelms-Universität, Wilhelm-Klemm-Str. 10, 48149 Münster, Germany – *vanderbogert@uni-muenster.de*, [6]European Space Agency-European Space Research and Technology Centre, Keplerlaan 1, 2201 AZ, Noordwijk, The Netherlands – *david.binns@esa.int*.

Introduction: OHB Italia (OHB-I) and its partners have been participating in a Phase-A ESA study for the development of a payload to demonstrate the chemical extraction of oxygen from lunar regolith. The activities are part of a wider effort of the Agency for the definition of a set of lunar missions devoted to the development and testing of in situ resource utilisation (ISRU) technologies.

Here, we address a selection of possible ISRU processes that could be used on the Moon, mainly in terms of their implementation into a payload system. Aspects of these processes differ, such as yield performance and technical complexity, hence requiring dedicated investigations for determination of the most promising reactor configuration and the technological feasibility of each payload and mission. The work addresses, in a broader way, all aspects related to the payload definition, including regolith excavation, preprocessing and handling, thermal aspects such as the high temperatures required, the overall integration of an ISRU plant into a payload system, and the concept of operations.

Of particular interest are the challenging technological developments required by an ISRU demonstrator payload, for instance handling quantities of regolith on the order of kilograms, thermal issues deriving from reaction temperatures up to 1000 °C, mechanisms operating at unusual temperatures (some hundreds of °C) as part of the reactor unit, regolith flow valves to provide gas-tight sealing when closed, and handling of molten salt.

The reasons: The Moon has two primary geological regions: mare and highlands. The mare are dominated by four minerals: plagioclase (mostly anorthite $CaAl_2SiO_8$), orthopyroxene $(Mg,Fe)_2SiO_3$, olivine $(Mg,Fe)SiO_4$, and ilmenite ($FeTiO_3$). The highlands are dominated by anorthite with minor pyroxene and olivine. Seven elements represent ~98% of the lunar crust: O, Mg, Al, Si, Ca, Ti, and Fe. In all soils, oxygen and silicon concentrations are similar to within 10% [1]. Thus, regolith across the Moon possesses large amounts of oxygen which can be extracted and collected through selected thermochemical processes. In addition, extracting oxygen from metal oxides produces metal dust as a (waste) byproduct.

The capability for harvesting oxygen on the Moon is the foundation for establishing a future human settlement: oxygen (and consequently water) for life sustainment, and metals as a byproduct for fabrication of habitats and structures to host the settlers.

The processes: Separating oxygen from the metal species that constitute the oxides requires great amounts of energy, i.e. usually high temperatures. Three different processes have been identified as promising for this purpose: the Hydrogen Reduction process (HR), the Carbo-Thermal Reduction process with regolith in solid phase (CTR), and the Fray-Farthing-Chen (FFC) process. Each of these processes has distinguishing characteristics and peculiarities.

In the HR process, the ilmenite ($FeTiO_3$) fraction of the lunar regolith reacts with hydrogen at temperatures of 800-900 °C at 1 bar pressure, generating water as reaction byproduct. Because this process is restricted to the ilmenite fraction of the lunar regolith, it can only be used at ilmenite-rich mare basalt and pyroclastic deposits. The efficiency of the process is 1-3% of the feedstock mass [2].

The CTR process is a different technique which was investigated originally by Politecnico di Milano and OHB Italia in 2009/2010 in a modality which allows the extraction of oxygen without reaching the melting temperature of the minerals. The metal oxides fraction of the solid phase regolith are first reduced through the intervention of methane at a temperature of about 950 °C [3] and 1 bar pressure, then the resulting carbon oxides react with hydrogen (brought from Earth) at a lower temperature (~250 °C) in a second reactor named methanator. The resulting products are the process target – i.e. water – and methane again, which can therefore be recycled. The efficiency of the process with regards to water generation is of 5-7% of the feedstock mass [4].

The FFC process involves an electrochemical stage. Instead of processing gases flowing in the regolith bed, a molten salt of calcium chloride ($CaCl_2$) operates as process medium. The regolith feedstock is compacted and integrated in the reactor cathode. The application of a specific voltage at the anode reduces the metal oxides at the regolith cathode and oxygen ions are released in the molten salt bath. The reaction takes place at temperature of about 900-1000 °C. The extraction efficiency of oxygen in this case is the highest, potentially all the oxygen could be extracted, up to 40% by mass [5][6].

The missions: ESA has developed a framework plan for a sequence of missions with the goal of fully demonstrating the capability of extracting oxygen from lunar regolith. Three separate missions are foreseen in this framework and are reflected by a programme called “Commercial In-Situ Resource Utilisation Demonstration Mission Preparation Phase” under which OHB Italia and its partners are performing, since 2018, the development of a Phase-A payload. The three different missions are: a technological demonstration mission (TECH) aiming at demonstrating the capabilities of the implied critical technologies; a scientific characterization mission (CHAR) with the purpose of characterizing the compositional and geotechnical properties of previously unsampled feedstock materials; and an End-to-End mission (E2E) to demonstrate the feasibility of oxygen extraction on the Moon. For each of these missions, OHB Italia is coordinating the development of a payload solution to fulfill the purpose of the mission in partnership with Politecnico di Milano, Leonardo S.p.A, OHB System A.G., University of Münster. Participants at the University of Münster examined potential landing sites for both CHAR and E2E missions [7].

The technologies: Under said contract, the team led by OHB Italia is developing a Phase-A solution for each of the three missions, trading-off between the different processes and evaluating two different commercial landing platforms. The technological solutions identified in the frame of the project are suitable with little to no adaptation for two of the three chemical processes (HR and CTR), which requires the regolith to be heated up in a closed furnace with the oxygen consequently collected from the byproducts of the reaction. After a trade-off, the CTR was identified as the most promising to be further developed, because of certain characteristics, such as a lower required temperature and the possibility of using it on different mineralogical species besides ilmenite (thus relaxing certain requirements on the landing site). The team has therefore designed the payload solution that allows the implementation of the CTR process on the two considered landers. The heart of the payload is the reactor, which must operate under extremely harsh conditions. In particular the greatest challenges are the very high temperatures and lunar dust contamination, which strongly affects gas sealing capabilities. In order to perform the chemical reaction needed for the extraction to happen, a mixture of different gases must be used and fluxed into the crucible, and then recycled, analyzed or discarded (depending on the chemical species). To overcome these challenges, an innovative sealing mechanism, capable of providing gas tightness while dealing with regolith containment and dust resistance has been designed and developed. Over time, different designs have been considered and improved, reaching the current stage of development. This last design evolved in the frame of a contract OHB-I has in place with ESA called “ISRU System Demonstrator – Oxygen Extraction from Lunar Regolith” for which a reactor demonstrator is being constructed, based on the CTR process with solid phase. In this project, the sealing mechanism is being manufactured for a demonstration campaign which will take place in early 2020.

As per the third process (the FFC), OHB-I is now developing a payload design that takes into account several criticalities such as the contamination of the molten salt bath, the introduction/extraction of the regolith cathode, and the thermal environment.

By mid-2020, the Phase-A will be completed with a payload design for each of the three processes.

References:

[1] Schwandt, C., Hamilton, J. A., Fray, D. J., & Crawford, I. A. (2012). The production of oxygen and metal from lunar regolith. Planetary and Space Science, 74(1), 49-56.

[2] Lucey P., R. L. Korotev et al. (2006) Understanding the lunar surfaces and space-Moon interactions, In: Jolliff B. L., M. A. Wieczorek, C. K. Shearer, and C. R. Neal (eds) New Views of the Moon, Reviews in Mineralogy & Geochemistry 60, 83-220.

[3] Grasso M., Lavagna M., Della Torre A., Mailland F., La Plena D., Critical Analysis of ISRU Plants Inte-gration in Complex Architectures for Planetary Hu-man Colonies Development, 58th International As-tronautical Congress 2007, Hyderabad, India, 24-28 Sept. 2007, p. 1391-1402, IAC-07-A5.1.06.

[4] Monchieri E., Hovland S., Masi M., Sliepcevich A., Lavagna M., Hoppenbrouwers T., Venditti F., ESA Lunar in-situ Resource Utilisation (ISRU) Bread-boarding Activities and Conceptual Design for a Lu-nar Demonstrator, 62nd International Astronautical Congress 2011 (IAC 2011), Cape Town, South Africa, 3-7 Oct. 2011, p. 1611-1627

[5] Symes, M., Lomax, B., Conti, M., Khan, N., Bennett, N., & Ganin, A. (2019, September). Proving the Viability of an Electrochemical Process for the Simultaneous Extraction of Oxygen and Production of Metal Alloys from Lunar Regolith. In Meeting Abstracts (No. 57, pp. 2455-2455). The Electrochemical Society.

[6] Chen, G. Z., Fray, D. J., & Farthing, T. W. (2000). Direct electrochemical reduction of titanium dioxide to titanium in molten calcium chloride. Nature, 407(6802), 361-364.

[7] van der Bogert et al. (2020) Selecting landing sites for in situ resource utilization mission. ELS, this conference.

EMMIHS-III: EUROMOONMARS- INTERNATIONAL MOONBASE ALLIANCE-HI-SEAS SIMULATION CAMPAIGN. P. Rajkakati[1,2], M. V. Heemskerk[2,3], K. Edison[4], M. Musilova[5], L. Brasileiro[6], R. S. Heemskerk[7], and B. H. Foing[2,5,8], [1]ISAE Supaero, [2]ILEWG (International Lunar Exploration Working Group), [3]VU Amsterdam, [4]PISCES, [5]International Moonbase Alliance, [6]Université de Technologie de Troyes, [7]TU Delft, [8]ESA/ESTEC

Introduction: The present abstract describes the results and discussions of the EMMIHS-III lunar-analogue campaign, which took place between 18th January – 1st February, 2020, at the HI-SEAS Habitat on the Northern slope of the Mauna Loa Volcano (Hawai'i, USA). The crw onsisted of 6 members (3 males and 3 females, all under the age of 32). The mission focussed on scientific research on robotics and lava-cave exploration techniques.

Fig 1. *EMMIHS-III crew*

Background: The HI-SEAS (Hawai'i Space Exploration Analog and Simulation) is a Habitat on an isolated Mars-like site on the Mauna Loa side of the saddle area on the Big Island of Hawaii at approximately 8200 feet above sea level. HI-SEAS is unique, in its setting in a distinctive analog environment, where geological, physical, and psychological factors are as close to the Moon as possible. The International Moonbase Alliance (IMA)'s founder, Henk Rogers, is its owner. As of 2018, IMA, an organization dedicated to building sustainable settlements on the Moon, has been organising regular simulated missions to the Moon, Mars or other planetary bodies at HI-SEAS. Dr. Michaela Musilova is the Director of HI-SEAS and she also takes part in missions as a Crew Commander, Flights Director or CAPCOM.

Fig 2. *Analogue-astronaut with the HI-SEAS habitat in the background*

The International Lunar Exploration Working Group (ILEWG) is a public forum sponsored by the world's space agencies (including NASA and ESA) to support international cooperation towards the exploration and utilization of the Moon. As part of research efforts towards the colonization of the Moon and creation of a Moon Village, ILEWG founded the EuroMoonMars initiative, which comprises of field campaigns in Moon-Mars analogue environments. The EMMIHS campaigns are a collaboration between EuroMoonMars, IMA and HI-SEAS, and consist of scientific research, field tests, training and outreach activities.

Experiments and results: The The six crew members (M. Musilova, M. Heemskerk, K. Edison, L. Brasileiro, P. Das Rajkakati, R. Heemskerk) focused on different fields of investigation, depending on their fields of expertise, including domains such as geology, robotics, nutrition, crew psychology and cultural aspects. The main projects and investigations are described below:

Lunar-analogue Simuation. The crew proposed and tested novel methods of water conservation and was officially termed as the most water-efficient crew at HI-SEAS. The crew also simulated EVA protocols when quitting the habitat to go out into the "lunar terrain", including the use od spacesuits, helmets and adapted communication devices. Lastly, the crew worked on emergency protocols and waste-limitation. These activities are some of the active areas of research towards developing a sustainable Moon Village.

Fig 3. *Lava cave exploration and mapping during an EVA simulation*

Geosciences experiments. A magnetometer from GeoMetrics was used to read the magnetic profile of the subsurface and estimate cavities, notably by mapping the absence of magnetic conductors in the iron-rich basalts of Mauna Loa, which was then used to deduce the structure of the lava tubes. This was then verified through analogue-astronaut-style expeditions inside the lava tubes, and several new entrances and tunnels were hence discovered, successfully mapped and documented. An RGB-D (depth-sensor) camera was tested for usability inside the low-light environment of lava tubes.

Fig 4. *The GeoMetrics Magnetometer*

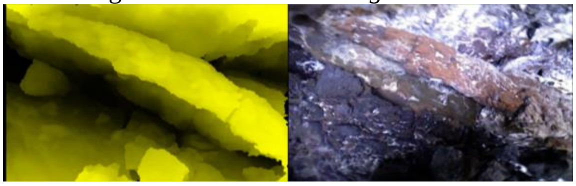

Fig 5. *RGB-D CAM depth image (left), 2D (right)*

Robotics. The crew tested three rovers for studies on autonomous navigation and human-robot interface. The Helelani, a rover loaned by the Pacific International Space Center for Exploration Systems (PISCES) and the Zebro rover, developed at TU Delft, were used for testing rover deployment for experimental human-robot interface,. Lastly, the Rover of EuroMoonMars (REMM) was used for outreach purposes, exploration, and Remote-Control tests.

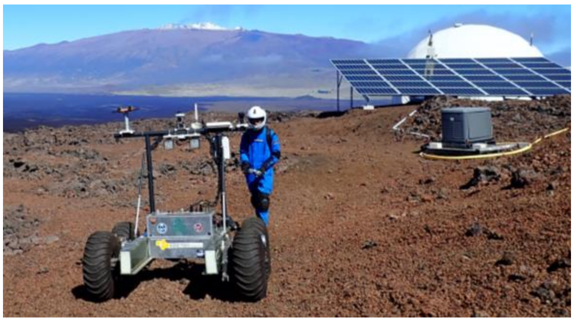

Fig 6. *Analogue-astronaut driving the Helelani rover*

Materials Science experiments. Studies regarding metallic material sciences in inter- and intra-habitat conditions were conducted., including sintering basalt at high altitudes to test the viability of sintering on the Moon and Mars. Characterization of Mauna Loa basalts based on mineral abundances was performed.

Human Factors. Several human-factor experiments and tests on crew psychology and crew dynamics were implemented, including medical wellbeing of the crew derived by basic body measurements such as heart rate and blood pressure.

Art-EMMIHS experiments. Cultural activities were carried out during the analogue mission and the impact of such activities on crew morale was investigated. The ILEWG MoonGallery, which aims to bring art to the Moon, was also exhibited for outreach purposes.

Fig 7. *Moon Gallery*

Outreach activities. The crew regularly shared their discoveries on multiple platforms, focusing on extending the EMMIHS-network and international scientific presence. The crew did a live session with MoonKids, a Netherlands-based outreach and educational platform to teach and inspire young kids from ages 4 – 11.

Fig 8. *Analogue-astronaut in lunar-simulation (outreach photo example)*

References: [1] 50th Lunar and Planetary Science Conference (2019), Abstract #1633 [2] 50th Lunar and Planetary Science Conference (2019), Abstract #1693[3] 50th Lunar and Planetary Science Conference (2019), Abstract #2416 [4] 50th Lunar and Planetary Science Conference (2019), Abstract #3090

LUNAR SURFACE ACCESS SERVICE (LSAS) – UPDATE ON THE FIRST OHB-IAI COMMERCIAL LUNAR LANDER MISSION.

L. Richter[1], E. Hayun[2], Y. Naimark[2], M. Nissim Nir[2], B. Ordoubadian[1], T. Stuffler[1], [1]OHB System AG, Manfred-Fuchs-Str. 1, D-82234 Wessling, Germany (Lutz.Richter@ohb.de, bjorn.ordoubadian@ohb.de, timo.stuffler@ohb.de), [2]Israel Aerospace Industries Ltd, Yehud, Israel (ehayun@iai.co.il, y-naimark@iai.co.il, mnir@iai.co.il).

Introduction: Continued exploration of our Moon will rely both on institutional missions, such as through national space programs and agencies, and on a strong commercial element. Several private actors are in advanced stages of developing lunar orbital and landing spacecraft for uncrewed missions. Of all these commercial lunar mission actors, SpaceIL, with Israel Aerospace Industries (IAI), was the first to launch a privately funded lunar landing spacecraft with their Beresheet lander [1]. In January 2019, OHB System and IAI signed a teaming agreement to offer a Lunar Surface Access Service (LSAS) based on the "Israeli Lunar Lander" (ILL) platform, itself derived from Beresheet [2].

The first LSAS mission: During the second half of 2019, the OHB-IAI consortium held a so-called "user's workshop" with lunar scientists and instrument developers and subsequently downselected a payload suite of technological and scientific instruments, amounting to roughly 40 kg in mass. This payload suite focuses on cutting-edge demonstrations of several new techniques intended to use the lunar regolith as feedstock for resource extraction and manufacturing physical components, achieving important In-Situ Resource Utilization (ISRU) milestones in the very near term. Since then, detailed accommodation of this payload suite was established, the necessary adaptations of the ILL platform addressed, and launch scenarios investigated with launch service providers. Talks with a commercial customer, private supporters, and with space agencies are at an advanced stage.

OHB will lead the project, manage the payload instrument teams, and integrate the payload suite into the platform at OHB's premises.

This talk will describe the LSAS first mission definition and its programmatic status.

The key advantage of the LSAS under the OHB-IAI collaboration is the already available flight heritage through Beresheet, providing a significant edge in terms of risk and schedule.

Fig. 1: Configuration of LSAS lander with payload of first mission accommodated

References:

[1] https://solarsystem.nasa.gov/missions/beresheet/in-depth/. [2] Hayun E. et al. (2019) *70th IAC, IAC-19-A3,2A,* Washington DC, Oct. 21-25.

AN EVALUATION OF LUNAR SIMULANT AND METEORITE AS A PROXY FOR LUNAR REGOLITH FOR IN SITU RESOURCE UTILIZATION EXPERIMENTS.

H. M. Sargeant[1], F. Abernethy[1], M. Anand[1,2], S. J. Barber[1], S. Sheridan[1], I. P. Wright[1] and A. D. Morse[1]. [1]School of Physical Sciences, The Open University, Walton Hall, Milton Keynes, UK. [2]The Natural History Museum, London, UK. Email: hannah.sargeant@open.ac.uk

Introduction: Water is one of the most critical resources required to enable long term space exploration. Lunar water could not only provide the life support needs of crew members, but its constituents hydrogen and oxygen can also be used as rocket propellant. The use of local resources such as water is known as *in situ* resource utilization (ISRU). Arguably, there are water ice deposits at the lunar poles. However, the majority of these ice deposits are thought to be in areas known as permanently shadowed regions (PSRs). These PSRs experience temperatures as low as 30 K and, therefore, accessing water-ice deposits in these regions will be technologically challenging. There are other potential ways of producing water on the Moon, such as through hydrogen reduction of iron-oxide-bearing minerals. Hydrogen can reduce iron-oxides such as ilmenite in an equilibrium reaction when heated to temperatures of at least 900˚C [1] as in eq. 1:

$$FeO_x + xH_2 \leftrightarrow Fe + xH_2O \qquad (1)$$

A hydrogen reduction experiment is to be performed on the lunar surface using the ProSPA instrument on-board Luna-27 in 2025 [2]. A breadboard of ProSPA was successfully used to produce water from the hydrogen reduction of ilmenite and the procedure was optimized [3]. ProSPA is expected to land in a highlands-like region which is likely to be ilmenite-poor. However, iron-bearing silicates such as pyroxene and olivine can also be reduced by hydrogen, although at much lower efficiencies than ilmenite [4].

A handful of previous studies have successfully produced water from lunar minerals [e.g. 1,5]. However, there is currently a resurgence in ISRU studies and Apollo soils are not available for routine large-scale destructive ISRU experiments. Therefore, lunar simulants are being used as a proxy for lunar materials [e.g. 6,7]. However, certain requirements must be met by a simulant to realistically replicate the behavior of lunar material for each type of extraction technique. In this study a highland simulant, a lunar meteorite, and two Apollo soils were reduced in a ProSPA breadboard to determine the feasibility of the reduction experiment on lunar soils and to identify any key differences between the samples that should be considered when performing ISRU studies.

Methodology: The ProSPA instrument is static in that it does not utilize a flow of carrier gas to remove reaction products from the reaction site. Instead, samples are reacted in a furnace which operates in a closed system that contains hydrogen. Produced water is condensed on a cold finger, and the resultant pressure gradient created ensures the diffusion of water away from the reaction site and towards the cold finger. Consequently, the equilibrium reaction can continue forwards and reduction can continue.

A breadboard model (ISRU-BDM) of the ISRU-relevant components of ProSPA was built at The Open University. Samples of ~45 mg were reacted in a furnace at 1000 °C for 4 hours in the presence of ~420 mbar of hydrogen, while the cold finger was set to -80 °C [3]. Quantification of the yield was determined by pressure changes within the system.

Materials: Four different materials were reacted in the ISRU-BDM. The FeO content of each material is shown in Table 1, along with the estimated maximum ilmenite content, as derived from the TiO_2 content.

Lunar Simulant: NU-LHT-2M is the chosen simulant which aims to replicate some of the characteristics of Apollo 16 highland soils [8]. The simulant contains only trace amounts of ilmenite so it will be used to represent the 'worse-case-scenario' material that could be expected on the lunar surface at the Luna-27 landing site. The NU-LHT-2M was also doped with 10% ilmenite ('Sim & Ilm' in Table 1) to understand how beneficiation would influence the yields.

Lunar Meteorite: Northwest Africa 12592 is classified as a fragmental breccia and chosen as a representative of the bulk lunar regolith at feldspathic lunar highlands terrain, albeit with no reported ilmenite [9]. To eliminate the effects of iron-oxide weathering products, some of the meteorite samples were treated with EATG which is commonly used to remove secondary iron-oxides [10].

Apollo Soils: 10084 is an Apollo 11 mare soil [11]. With high ilmenite concentrations of up to 14.33 wt.%, 10084 was considered suitable for an initial reduction experiment. If 10084 produced measurable yields of water, then a series of follow up experiments on 60500 were planned. The sample 60500 is from the Apollo 16 highland soils and has low ilmenite content of up to 1.14 wt.% [12]. The two Apollo samples analysed in this study represent two very different compositions of the major lunar terrains from which we currently have samples.

Results: The pressure rise from the release of water from the cold finger was used to quantify the yields. Yields are shown in Table 1 as the wt.% oxygen produced. The 1σ uncertainty was derived from the three repeats for each experiment. The results for a pure ilmenite sample are also shown, as taken from [3]. All samples were successful in producing water, with those containing high ilmenite contents producing the highest yields.

Table 1 Yields from the reduction of lunar simulant and samples, as compared to pure ilmenite

Sample	FeO (wt.%)	Est. Ilmenite (wt.%)	Avg. yield (wt.% O_2)
Ilmenite	45.0	95	3.43±0.14
NU-LHT-2M	3.59	0.7	0.29±0.04
Sim & Ilm	7.73	10.13	0.89±0.04
NWA 12592 - treated	3.89	0.32	0.07±0.02
NWA 12592 - untreated			0.08±0.01
10084	15.81	14.33	0.94±0.03
60500	5.53	1.14	0.18±0.02

Scanning electron microscope (SEM) images were obtained from a random selection of grains of each unreacted and reacted sample. Evidence of reduction was identified in all samples by the appearance of the pure iron (Fe^o) blebs in ilmenite, pyroxene, and olivine grains.

Discussion: A comparison of ilmenite content with yield is shown in Fig. 2 for the samples used in this work and other lunar or lunar-like materials reacted at 1000 °C with hydrogen in previous studies [1,5,6,7]. It should be noted that the results from literature were obtained from fluidized systems with various H_2 pressures. Generally, the more FeO rich a material, the higher the O_2 yield. However, if the FeO is bound mostly in ilmenite, it would produce higher yields. Therefore, ilmenite content is a more accurate predictor of yield of oxygen than FeO content alone. For example, the doped simulant (Sim & Ilm) contains less than half the FeO content of the Apollo 11 soil, however has similar ilmenite contents. Consequently, the doped simulant produces almost as much water as the lunar soil.

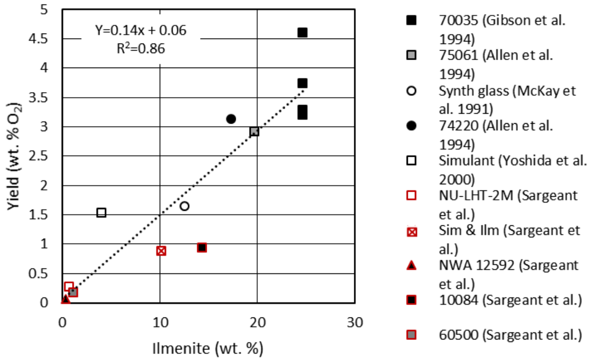

Figure 1. Experimental yields from lunar soils and simulants reacted with H_2 at 1000 ℃.

There was no significant difference between the un-treated and treated meteorite sample, suggesting minimal weathering products present that would influence the reaction. The meteorite samples produced particularly low yields, probably because they contain no ilmenite, but also because they have a larger average grain size than the other materials, a consequence of the manual crushing of the sample (i.e., smaller area/volume ratio compared to lunar soils). Larger grain sizes limit the movement of reactants and products to and from the reaction site.

Most lunar soils are a mixture of feldspathic and mafic components. As a result, ilmenite is often likely to be present as a component in lunar soils [6]. Also, finer soils contain more ilmenite than larger size fractions [13]. Thus, fine soils, even those found in more highland-like regions, are likely to produce higher yields than some lunar rocks, such as the genesis rock, that contains very little FeO and no ilmenite [14]

Conclusions: Ilmenite content is a good indicator for potential oxygen yields in hydrogen reduction experiments and should be considered when using simulants as a proxy for lunar material. Lunar simulant or crushed meteorite containing relatively low ilmenite contents would be recommended to represent the likely soils that will be sampled by ProSPA. As grain size also significantly influences reaction rates, the grain size distribution of any proxy material should also be representative of the expected lunar material at the proposed landing site.

Acknowledgments: The funding by STFC of a studentship for H.S. is acknowledged. ProSPA is a programme of and funded by the European Space Agency. Bulk analysis on NU-LHT-2M and NWA 12592 was performed by E. Humphreys-Williams and B. Schmidt at the Natural History Museum, UK, using Inductively Coupled Plasma Mass Spectrometry (ICP-MS).

References: [1] Allen et al. (1994) *JGR: Planets,* 99, 23173-23185. [2] Barber et al. (2017) *LPSC* XLVIII, Abstract #2171. [3] Sargeant et al. (2020) *PSS*, 180, 104751. [4] Allen et al. (1996) *JGR: Planets,* 101, 26085-26095. [5] Gibson 1994. [6] McKay et al. (1991) *LPSC XXII,* 881-882. [7] Yoshida et al. (2000) *Second Space Res. Roundtable,* 0704-0188. [8] Zeng et al. (2010) *J. Aerosp. Eng.,* 23(4), 213-218. [9] Met. Bul. Data. (2019) 'Northwest Africa 12592'. [10] Martins et al. (2007) Met. & Plan. Sci., 42, 1581-1595. [11] Meyer (2009) Lun. Samp. Comp. [12] Meyer (2010) Lun. Samp. Comp. [13] McKay & Williams (1979) 'A geologic assessment of potential lunar ores' in *Space resources and space settlements*, 243-255. [14] Meyer (2011) Lun. Samp. Comp.

Training astronauts for scientific exploration on planetary surfaces: F. Sauro[1], M. Massironi[2], R. Pozzobon[2], H. Hiesinger[3], N. Mangold[4], C.S. Cockell[5], J.M. Frias[6], S.J. Payler[7,8], L. Bessone[8]: [1]Department of Biological, Geological and Environmental Sciences, Italian Institute of Speleology, Bologna University, [2]University of Padua, Dipartimento di Geoscienze, [3]Institut für Planetologie, Westfälische Wilhelms-Universität Münster, [4]Laboratoire Planétologie et Géodynamique de Nantes, CNRS, France, [5]School of Physics and Astronomy, University of Edinburgh, [6]Instituto de Geociencias, IGEO (CSIC-UCM), [7]Agenzia Spaziale Italiana, Rome, Italy, [8]Directorate of Human and Robotics Exploration, European Space Agency.

Introduction: The Artemis programme aims to send astronauts back to the lunar surface by 2024. These missions, and other future Moon and Mars missions, will require astronauts to perform science-focused surface exploration in complex geological environments. Although astronauts currently participate in Extra Vehicular Activities (EVAs) and science experiments in low Earth orbit (LEO), scientific exploration of a planetary surface by humans has not been carried out since the Apollo missions. Consequently, much of the scientific expertise required for these activities has not been systematically trained at the same level into the astronaut corps. Moreover, many astronauts and mission developers participating in the planning of future missions to planetary bodies have limited knowledge of the scientific disciplines underpinning them. Field geology and astrobiology will be the focus of scientific exploration of Moon/Mars, meaning that for the individuals involved to effectively contribute to the preparatory and execution phases of these missions, varied levels of training in such disciplines is required. PANGAEA (Planetary ANalogue Geological and Astrobiological Exercise for Astronauts) is a geological and astrobiological field training course of the European Space Agency (ESA) that seeks to address some of these areas.


Fig. 1. *Cosmonaut, Sergey Kud-Sverchkov, examines an outcrop during PANGAEA training.*

Goals and structure: PANGAEA has been running since 2016, with participants including ESA and Roscosmos astronauts/cosmonauts, mission designers and engineers. The course forms part of the basic and pre-assignment training for European astronauts, and is open to trainees from other agencies. Whilst the course intends to impart core theoretical and practical knowledge of geology and geo-biology to the trainees, significant focus is given to skills in areas relevant to future missions, such as scientific decision-making, the ability to provide clear scientific descriptions of geological features and efficient documentation. For this reason, although minor portions of the course are taught in classrooms, significant focus is given to developing field skills in analogue geological environments, an important learning from the Apollo mission training [1, 2]. Trainees also have the opportunity to practice conducting field science under the additional constraints imposed by realistic spaceflight operational conditions.

A significant strength of the PANGAEA course is that it integrates both geology and astrobiology (including planetary protection) training into its field trips. As both disciplines inform each other, teaching them together enables overlapping concepts and ideas to be explored thoroughly.

Teaching in analogue sites: The primary field sites selected for the course are Permo-Triassic terrigenous sequences in the Italian Dolomites, impact lithologies in the Ries Crater, Germany, and a comprehensive suite of volcanic deposits in Lanzarote, Spain. Each is used as a base to deliver the main learning sessions, respectively; 1) Earth geology, rock recognition and sedimentology on Earth and Mars, 2) Lunar geology and impact cratering, and 3) volcanism on Earth, Moon and Mars, execution of geological traverses, and sampling techniques. This roster of analogues has been expanded to include a new field session in Lofoten, Norway, where anorthosites and other lunar highlands analogue rocks are present.

Fig. 2. *Science support team examining scientific data taken by astronauts in the field.*

Classroom lessons are conducted at these field sites using local facilities. For the field work component, trainees are initially shown the basics of field geology and astrobiology during the first two sessions. In the third session they begin a process of becoming independent field scientists. This is enabled by having trainees conduct geological traverses with realistic scientific goals, such as determine the contact relationship between geological units and the relative timing of events, recognise stratigraphic and tectonic structures, and sample rocks that were exposed to high temperature fluids. Trainees are initially accompanied by their instructors, to help them achieve these goals. The coaching is then progressively reduced until the field crew is supported by a remote science team, simulating a science back room in mission control, through voice communications.

Integrated testing for exploration beyond LEO: Whilst PANGAEA's primary focus is training, where appropriate and complementary, technologies being developed for future missions are used and tested by the trainees during geological traverses. This provides an opportunity to examine the performance of new equipment and software in analogue field environments, whilst also providing trainees with experience using technology that might support future missions. For example, trainee's use the Electronic Fieldbook (EFB) system to collect scientific data. This is a suite of hardware, software and networking tools being developed at the European Astronaut Centre (EAC) to support scientific fieldwork in the context of astronaut analogue field training and future missions beyond LEO.

__Fig. 3.__ Astronaut, Matthias Maurer, using the EFB during a mock EVA to transfer data back to the science team for analysis.

The logistical framework established by the training course also provided the opportunity for establishing a more extensive technological testing separate from the core training focus. This resulted in the creation of the PANGAEA-X (PANGAEA-eXtension) campaign, which focuses on testing technologies and operational concepts with applications to future Moon and Mars missions. To date, this has involved two campaigns in 2017 and 2018, with a host of research institutions, space agencies, commercial companies and ESA projects utilising the Lanzarote analogue for testing. This has included examining EVA science operations in preparation for lunar activities, and developing a geological test scenario for testing a tele-operated rover.

Conclusion: Preparations for human missions back to the Moon have already started. Improvements to surface mobility and extended surface exploration times enabled by the technological advancements made since Apollo, mean the time for scientific exploration will be extended significantly during future missions. It is therefore more important than ever to have astronauts capable of acting as independent field scientists, who can also understand and communicate efficiently with ground based science teams. These astronauts will also be heavily involved in the planning, preparation and implementation of such missions, meaning even if they do not actually travel to the Moon or Mars, proficiency in geology and astrobiology will help them perform in a variety of roles related to such missions. In order to get the best return from these expensive and high-risk endeavours, training key personnel in the scientific disciplines driving these missions will be essential to their success. Utilising terrestrial analogues will ensure the best training.

References: [1] Lofgren G. E. *et al*. (2011) Geological Society of America Special Papers, 483, 33-48. [2] Schmitt H. H (2011) Geological Society of America Special Papers, 483, 1-1

TRANSPORT AND CHEMICAL EQUILIBRIUM MODELING FOR ISRU APPLICATIONS.

G. L. Schieber[1], A. R. Clendenen[1], P. G. Loutzenhiser[1], B. M. Jones[2], and T. M. Orlando[2], [1]George W. Woodruff School of Mechanical Engineering and [2]School of Chemistry and Biochemistry, Georgia Institute of Technology (thomas.orlando@chemistry.gatech.edu)

Introduction: Lunar *in-situ* resource utilization (ISRU) is of great interest to the lunar exploration community since it is necessary for the sustained presence of humans on the Moon. ISRU requires a fundamental knowledge of the chemical compositions and transformations of lunar material and it is an immense engineering challenge. Several technologies have been proposed with some more advanced than others. Among the more important resources for human habitation are H_2, H_2O, O_2 and metals.

H_2O extraction research: A promising technology to harvest H_2O is by thermal extraction (thermal mining) [1]. Gas transport is an important aspect of thermal extraction of H_2O, and an experimental apparatus was fabricated to study gas transport in regolith under lunar-like conditions [2]. The study evaluated Ar and N_2 gas flow within JSC1A, a surrogate lunar medium. It provided a framework for moving towards complex volatiles like H_2O and showed that the advection diffusion model, typically applied to bulk volatile transport for ISRU, needs to be verified even for the simplified cases (Ar and N_2) studied. Currently, an experimental campaign is underway to study H_2O transport and a verifiable model is being developed as a critical system design component.

O_2 and metal extraction research: Lunar regolith consists of metal oxides that form complex minerals, resulting in regolith that is ~45% O by weight [3]. Thus, in addition to water, lunar regolith can also be a potential source of O_2 and reduced metals. Since O-metal bonds are strong and require high temperature and significant energy to break [4], a research effort is currently underway at Georgia Tech. to explore the thermal reduction of lunar regolith at elevated temperatures (also known as pyrolysis) [5]. Chemical equilibrium modeling was performed to forecast chemical compositions as a function of temperature and pressures on the Moon. Gibb's Free Energy minimization ($\Delta G = 0$) was used to predict equilibrium compositions for isobaric processes. The pressure on the Moon was ~ 3×10^{-15} bar, and the equilibrium compositions of each species were normalized per unit mass of regolith.

Equilibrium predictions for oxygen are shown in the Figure 1. A small temperature range is present for favorable $O_2(g)$ evolution due to the extremely low pressure. A dramatic increase in $O_2(g)$ favorability occurs at ~800°C and peak at ~ 950°C before dissociating to O(g). This corresponds to the thermolysis of $O_2(g)$ to O(g), where trace amounts of O(g) are predicted at 900°C, displacing the O_2 at equilibrium.

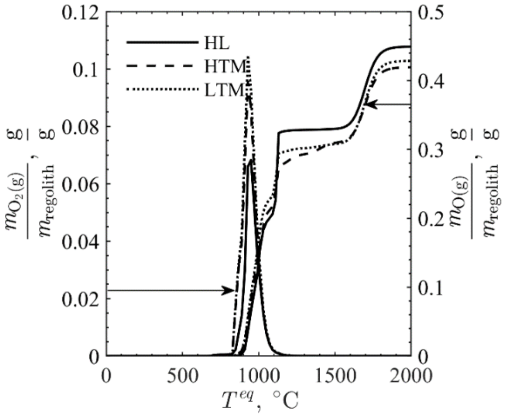

Figure 1. O(g) and $O_2(g)$ equilibrium predictions as a function of temperature at 3×10^{-15} bar. (HL-Highland, HTM and LTM –high and low titania samples)

Lunar solar mapping: ISRU methods will require heat to drive any proposed process. A promising approach utilizes concentrated solar irradiation. As there is no wind and less gravity, the infrastructure necessary to deploy a concentrating solar infrastructure on the Moon is likely significantly less than on Earth. Other advantages are no atmospheric reduction of solar radiation via attenuation (the direct-normal solar irradiation on the Moon is ~1365 W/m^2 compared to ~1000 W/m^2 on the earth); the declination angle on the Moon is small compared to on the earth, leading to very little seasonal variations; and a lunar day equals ~14 earth days. To optimize ISRU process efficiencies, locations on the Moon should be chosen considering both solar resources and regolith compositions. Using maps of lunar chemical and mineral spatial distributions, solar resources, and lunar topography, we have tried to identify the optimal locations for concentrated solar-driven ISRU.

Conclusions: A research effort is underway to study solar driven H_2O, O_2, and metal extraction. The multidisciplinary program involves modeling and experimental efforts to evaluate and develop lunar ISRU technology, specifically, solar mediated thermal extraction of volatiles and reduction of lunar regolith.

References: [1] P. Reiss (2018) *Icarus, 306*, 1-15. [2] G.L. Schieber, B.M. Jones, T.M. Orlando, P.G. Loutzenhiser (2020) *Acta Astronautica*, *169*, 32-39 [3] D.S. McKay, R.V. Morris, A.J. Jurewicz (1991) *LPSC, 22*, 4 [4] L.A. Taylor, W.D. Carrier III, (1992) *AIAA Journal*, *30*, 2858-2863 [5] C.C. Allen, R.V. Morris, D.S. McKay (1996) *JGR*, *101*, 26085-26095.

Acknowledgments: This work was directly supported by the NASA Solar System Exploration Research Virtual Institute (SSERVI) under cooperative agreement numbers NNA17BF68A (REVEALS).

The ARCHES Moon-Analogue Demonstration Mission: Towards Teams of Autonomous Robots for Collaborative Scientific Sampling in Lunar Environments.

M. J. Schuster[1], B. Rebele[1], M. G. Müller[1], S. G. Brunner[1], A. Dömel[1], B. Vodermayer[1], R. Giubilato[1], M. Vayugundla[1], H. Lehner[1], P. Lehner[1], F. Steidle[1], L. Meyer[1], K. Bussmann[1], J. Reill[1], W. Stürzl[1], I. von Bargen[1], R. Sakagami[1], M. Smíšek[1], M. Durner[1], E. Staudinger[2], R. Pöhlmann[2], S. Zhang[2], C. Braun[3], E. Dietz[4], S. Frohmann[4], S. Schröder[4], A. Börner[4], H.-W. Hübers[4], R. Triebel[1], B. Foing[5], A. O. Albu-Schäffer[1] and A. Wedler[1], [1]DLR-RM (German Aerospace Center (DLR), martin.schuster@dlr.de), [2]DLR-KN, [3]KIT-IRS, [4]DLR-OS, [5]ESA-ESTEC

Figure 1: Team of our Lightweight Rover Units (LRUs) [4] at a Moon-analogue site on Mt. Etna

Introduction: Teams of autonomous mobile robots operating on extraterrestrial surfaces will play a crucial role in future lunar and planetary missions. When exploring previously unknown hard-to-access environments, such as craters, pits, and subterranean caves, taking scientific samples is a challenging and expensive task. In contrast to past and ongoing single-robot missions, future teams of robots will increase the efficiency and scientific output via an extended level of autonomy and parallelization, improve robustness via functional redundancy, and benefit from collaboration in heterogeneous teams by exploiting the robots' complementary capabilities. Local robot autonomy is required to operate in the light of large communication round-trip times of several seconds (Moon) to minutes (Mars), as well as unreliable communication links. In the Helmholtz Future Project ARCHES [1], we aim to develop heterogeneous, autonomous, and interconnected robotic systems to operate in challenging environments. In the ARCHES space demonstration mission, we will deploy a team of flying and driving robots in two collaborative exploration and sampling scenarios at a Moon-analogue site on the volcano Mt. Etna (Sicily, Italy) in June and July 2020. In Figure 1, we give an impression of two of our rovers demonstrating their skills for autonomous exploration and sampling in previous experiments at the Moon-analogue site [2].

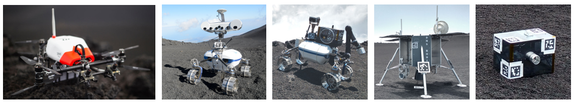

Figure 2: Robots and infrastructure elements: ARDEA, LRU1, LRU2, lander and payload box

Heterogeneous Robotic Team: Our robotic team consists of three flying and driving autonomous robots that interact with static and mobile infrastructure elements, as shown in Figure 2. The robots have complementary capabilities: Our drone ARDEA [3] can scout far-away and hard-to-reach places such as caves or craters. Our planetary exploration rover LRU1 [4, 5] has a landing and transport platform for ARDEA. Furthermore, with its ScienceCam [6], it can take thermal and spectral images for close-up inspection of geological features. Our second rover LRU2 [4, 7] features a robotic manipulator arm with a docking interface to attach tools and to transport standardized payload boxes. These boxes can contain support infrastructure elements such as communication relays as well as scientific instruments, e.g., radio receivers to set up a low-frequency radio array (LOFAR) and a laser-induced breakdown spectroscopy (LIBS) instrument to perform elemental analysis of rocks and soil. The LIBS module prototype for planetary in-situ exploration weighs about 1kg and can scan a small surface in close distance at rates of up to 30Hz. The tools include a shovel and a robotic hand to take soil and rock samples [7]. The lander serves as a base station with payload box storage and as a global landmark for all robots. Each robot perceives its environment via stereo cameras and runs on-board localization, mapping, and task execution software in order to enable local autonomy. The robots collaborate to create a joint dense model of their environment [8, 9] for navigation and mission planning. These multi-robot 3D maps built during each exploration session are transmitted to a control center to be aligned and merged into a complete representation of the environment [10]. The high-level mission control for robot autonomy is based on hierarchical state machines modeled in RAFCON [11]. When necessary, e.g., for challenging sampling tasks, the robots can also run in shared autonomy mode with a human operator utilizing a haptic human-machine interface with six actuated degrees of freedom [12].

Scientific Sampling Scenarios: We define two scenarios for the ARCHES demonstration mission:

Low-Frequency Radio Array (LOFAR). Setting up astronomical instruments such as distributed LOFARs on the Moon allows probing the universe to unprecedented depth as the Moon lacks a dense ionosphere and its far side is the most radio-quiet area in the inner solar system [13]. In the ARCHES mission, first ARDEA and LRU1 explore and map a target area to find suitable locations for instrument placement. LRU2 then grabs sensor boxes from the lander and places them in a network formation. After placement, our novel radio communication, positioning, and time-synchronization system (Radio-CPT) is

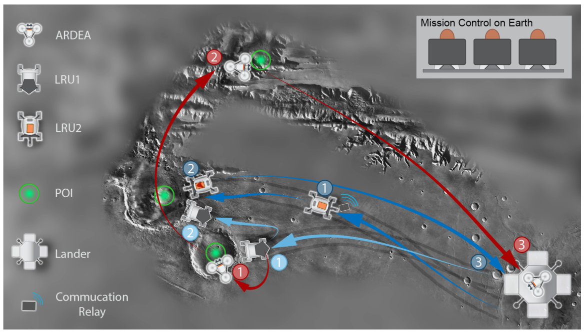

Figure 3: Geological exploration and sampling scenario with our heterogeneous robotic team [6]

used to precisely locate the boxes, and hence, the distributed antenna array elements. The LOFAR is calibrated online and the pre-processed received signals are visualized for scientists in mission control.

Geological Exploration and Sampling. Geological exploration of lunar and planetary surfaces is crucial in the search for signs of life, potentially habitable areas and exploitable resources. In the ARCHES mission, sketched out in Figure 3, a team of scientists and operators selected a landing spot based on prior satellite imagery located near three geologically interesting sites marked as points of interest (POIs). After landing, LRU1 (①) drives with autonomous obstacle avoidance to the first POI, with our drone ARDEA carried on the rover's back. As the POI is located inside a crater, ARDEA (①) is then sent to explore and map it from the close up. At the same time, LRU2 (①) places a radio relay to extend the robots' communication range towards the other two POIs. Afterwards, LRU1 (②) drives to the second POI and uses its spectral cameras to identify individual rocks for further inspection. Thus, mission control sends LRU2 (②) to deploy a LIBS instrument for laser spectroscopy. The most promising sample is then collected by LRU2 with its robotic arm and hand and returned to the lander (③). In the meantime, ARDEA (②) inspects and maps the third POI with its fisheye camera setup to estimate the scientific gain of sending the other robots there. Afterwards, it returns to the lander (③) to recharge.

Recent & Future Steps: In 2017, we successfully demonstrated an autonomous single-robot mission to deploy a network of seismic instruments at the Moon-analogue site on Mt. Etna as part of the ROBEX project [2]. In ARCHES [1], we showed an autonomous sample-return mission as well as a collaborative multi-robot mapping with ARDEA and LRU1 in more than 35 live demonstrations each at the International Astronautical Congress (IAC) in 2018 [6, 9]. In summer 2020, we will demonstrate both ARCHES mission scenarios with our three robots at the challenging Moon-analogue site on Mt. Etna. In addition, we are adapting parts of our hard- and software components for real space missions, in particular to develop a small rover to be sent to Phobos in 2024 as part of the Martian Moons eXploration mission (MMX) [14].

Acknowledgement: This work was supported by the Helmholtz Association, project alliance ROBEX (contract number HA-304) and project ARCHES (contract number ZT-0033).

References:

[1] Wedler, A. et al. (2018) From single autonomous robots toward cooperative robotic interactions for future planetary exploration missions. *IAC.*

[2] Wedler, A. et al. (2017) First Results of the ROBEX Analogue Mission Campaign: Robotic Deployment of Seismic Networks for Future Lunar Missions. *IAC.*

[3] Müller, M. G. et al. (2018) Robust Visual-Inertial State Estimation with Multiple Odometries and Efficient Mapping on an MAV with Ultra-Wide FOV Stereo Vision. *IROS.*

[4] Schuster, M. J. et al. (2017) Towards Autonomous Planetary Exploration: The Lightweight Rover Unit (LRU), its Success in the SpaceBotCamp Challenge, and Beyond. *Journal of Intelligent & Robotic Systems (JINT).*

[5] Vayugundla, M. et al. (2018) Datasets of Long Range Navigation Experiments in a Moon Analogue Environment on Mount Etna. *International Symposium on Robotics (ISR).*

[6] Schuster, M. J. et al. (2019) Towards Heterogeneous Robotic Teams for Collaborative Scientific Sampling in Lunar and Planetary Environments. *Workshop on Informed Scientific Sampling in Large-scale Outdoor Environments at IROS.*

[7] Lehner et al (2018) Mobile manipulation for planetary exploration. *IEEE Aerospace Conference.*

[8] Schuster, M. J. et al. (2018) Distributed stereo vision-based 6D localization and mapping for multi-robot teams. *Journal of Field Robotics (JFR).*

[9] Schuster, M. J. (2019) Collaborative Localization and Mapping for Autonomous Planetary Exploration: Distributed Stereo Vision-Based 6D SLAM in GNSS-Denied Environments. *University of Bremen.*

[10] Giubilato, R. et al. (2020) Relocalization With Submaps: Multi-Session Mapping for Planetary Rovers Equipped With Stereo Cameras. *RAL.*

[11] Brunner, S. G. et al. (2016) RAFCON: A graphical tool for engineering complex, robotic tasks. *IROS.*

[12] Braun, C. A. et al. (2019) A Continuous and Quantitative Metric for the Levels of Automation. *Symposium on Analysis Design and Evaluation of Human Machine Systems.*

[13] Carilli, C. L. et al. (2007) Low frequency radio astronomy from the moon: Cosmic reionization and more. *Cambridge University Press.*

[14] Bertrand, J. et al. (2019) Roving on Phobos: Challenges of the MMX Rover for Space Robotics. *Symposium on Advanced Space Technologies in Robotics and Automation.*

CONSTRAINTS ON THE BULK SILICATE MOON FEO CONTENT FROM PETROLOGICAL AND GEOPHYSICAL MODELS.

S. Schwinger[1] and D. Breuer[1], [1]German Aerospace Center (DLR), Rutherfordstr. 2, 12489 Berlin, sabrina.schwinger@dlr.de.

Introduction: Estimates of the bulk silicate Moon (BSM) composition have been proposed based on a number of different geochemical, petrological and geophysical arguments but have yet to arrive at a general consensus. Most notably the amount of FeO in the lunar interior is still poorly constrained with estimates varying between ~9-17 wt% FeO [1, 2]. In addition, seismic velocity data indicate that the lunar mantle is possibly stratified with a pyroxenitic, FeO-rich upper mantle and dunitic, FeO-poorer lower mantle [3]. However, the quality of the available seismic data is insufficient to resolve a potential gradient of the FeO content with depth [3] and distinct compositional reservoirs in the lunar mantle are hence typically not explicitly considered in seismic studies. The compositions and radial distribution of different mantle reservoirs is also relevant for other physical properties like the bulk Moon density and moment of inertia, which provides further constraints on the BSM FeO content.

Information about possible compositions and relative volumes of distinct mantle reservoirs can be obtained by modeling the formation and modification of these reservoirs by differentiation and mixing processes during early lunar evolution. The differentiation of distinct mantle reservoirs likely occurred during fractional crystallization of a global lunar magma ocean (LMO), which also produced the anorthositic lunar crust. Convection of the solid mantle during and after LMO solidification and related mixing and partial melting of the primary mantle reservoirs further modified the compositional structure of the lunar mantle.

We modeled the formation of primary mantle reservoirs during LMO solidification to investigate the effect of the BSM FeO content on the reservoir compositions and relative volumes and tested the consistency of different overturn scenarios with observed bulk moon physical properties.

Methods: *Lunar Magma Ocean Crystallization.* We modeled LMO cumulate mineralogies using a combination [4] of crystallization algorithms from the software packages alphaMELTS [5] and SPICES [6], that has been validated against recent experiments on LMO fractional crystallization [7, 8]. Thereby we assumed pure fractional crystallization of a deep LMO that extends to the core-mantle boundary so that the LMO comprises the whole BSM. The bulk LMO composition was chosen based on the estimate of [9], who assumme an FeO content of 12.4 wt%. FeO/MgO ratios of the bulk LMO composition were varied (8.0-13 wt% FeO) to investigate the effect of the FeO content on the densities and mineralogies of individual cumulate layers. All crystals forming in the LMO were assumed to sink and equilibrate with the liquid at the bottom of the magma ocean prior to fractionation, except for plagioclase, which was assumed to float to the surface to form an anorthositic crust. The average lunar crust thickness was assumed to be 40 km in accordance with recent GRAIL data [10]. Any excess plagioclase that formed after that final crust thickness was reached was assumed to remain in the mantle due to imperfect plagioclase floatation.

Mantle Mixing and Overturn. As a consequence of the higher compatibility of lighter Mg compared to denser Fe in the LMO cumulate minerals, the density of the cumulate increases with progressing LMO solidification. Since the LMO solidifies from bottom to top, this results in a gravitationally unstable cumulate stratification that facilitates convective overturn, during which dense material sinks towards the core mantle boundary while lighter material migrates toward the surface. The respective changes in pressure and temperature experienced by individual cumulate layers, as well as mixing and chemical equilibration of different layers during overturn, can affect the mineralogy and physical properties of the lunar mantle. To investigate these effects, we calculated equilibrium mineral parageneses of different cumulate layers using Perple_X [11]. For simplicity we considered five homogeneous cumulate reservoirs (olivine-dominated, pyroxene-dominated, IBC, KREEP and crust), whose compositions were derived from the results of the LMO crystallization models by averaging the compositions of adjacent cumulate layers with similar mineralogies. The mineralogies and densities of each reservoir were calculated as a function of depth along different selenotherms [12, 13]. To evaluate the effect of mixing and chemical equilibration, we also made the same calculations for a homogeneous mixture containing the olivine- and pyroxene-dominated mantle layers and a second mixture containing all three mantle layers (olivine, pyroxene and IBC). The results of these calculations were used as input in a simple density structure model in order to investigate the effect of mantle overturn on todays bulk lunar density and moment of inertia. Lunar core sizes and densities were thereby varied within the range of proposed values [14, 15].

Results: *Effects of BSM FeO content on mantle reservoir properties.* The compositions and volumes of the early formed olivine- and pyroxene dominated reservoirs remain almost unaffected by the FeO/MgO ratios assumed for the bulk LMO. Instead, higher BSM FeO contents lead to higher concentrations of FeO in the rest melt and an earlier appearance of Fe-rich minerals in the crystallization sequence. This earlier appearance and higher abundance of Fe-rich minerals leads to an increased thickness of the late formed, dense ilmenite bearing cumulate (IBC) reservoir, which we have defined not on the basis of mineralogy but due to its high density compared to underlying cumulate layers. As a consequence, IBC thickness correlates linearly with the assumed LMO FeO content, varying by a factor of about 4 (from 7-28 km) over the assumed range of FeO contents. In addition, changing LMO FeO contents affect the bulk IBC mineralogy in that the fraction of fayalitic olivine increases with increasing FeO content.

Effects of reservoir mixing. Lunar mantle models assuming only moderate mixing and chemical equilibration (i.e. assuming separate reservoirs of olivine, pyroxene and IBC cumulates in the lunar mantle) have systematically higher densities than more strongly mixed models (i.e. assuming that the olivine and pyroxene layers have mixed and chemically equilibrated). This is primarily due to differences in the distribution of Ca and Al in the cumulate. In moderately mixed models, local Ca and Al concentrations in the pyroxene-dominated reservoir are high enough to facilitate the local formation of dense garnet at larger depths, especially if plagioclase floatation is impeded, so that plagioclase is partially trapped in the cumulate. In strongly mixed models Ca and Al are sufficiently diluted to impede garnet formation, which leads to lower bulk densities.

Discussion: *Linking bulk Moon physical properties and BSM FeO content.* The modeled bulk Moon density depends on several factors, including BSM FeO content, the assumed selenotherm and the assumed core size and density. The uncertainties in present-day temperatures of the lunar interior and the properties of the lunar core make it difficult to unambiguously link bulk Moon density and BSM FeO content without additional constraints. Due to its high density the radial distribution of IBC material in the lunar interior has a significant effect on the BSM moment of inertia, even though its volume is comparatively small. The effect of the distribution of IBC on the BSM moment of inertia increases systematically with increasing IBC volume, which is in turn linked to the FeO content. Dynamical models of the sinking of IBC in a cooling Moon suggest that at present most of the IBC material is located either at the core mantle boundary or got stuck in the lithosphere right beneath the crust [16]. This distribution suggests that the low seismic velocity zone at the core mantle boundary [14, 17] might consist largely of IBC material. Hence, the thickness and density of this low seismic velocity zone [14, 17] can be used to estimate the amount of IBC that has sunken to the core mantle boundary. This establishes a relation between the total volume of IBC (and hence BSM FeO content) and the BSM moment of inertia.

Constraints on the BSM FeO content. To determine realistic ranges of BSM FeO contents and fractions of sunken IBC from our data, we systematically varied BSM FeO contents and calculated the corresponding degree of IBC overturn required to fit the observed BSM moment of inertia and bulk Moon density for each stratigraphic model and assumed selenotherm.The resulting FeO contents for all considered models range from 8.3 – 12.8 wt%. Seismic data suggest a mantle stratigraphy with a pyroxenitic upper mantle and a dunitic lower mantle, which further limits the range of plausible stratigraphic models. Considering this additional constraint, our model favor a BSM FeO content of about 8.5 – 11.5 wt% and exclude FeO contents > 12.8 wt% for the selected selenotherms. This range of FeO contents is generally consistent with petrological constrains on lunar mantle compositions and could be determined more precisely given tighter constraints on the present day selenotherm and the properties of the lunar core.

Acknowledgments: This work was funded by the Deutsche Forschungsgemeinschaft (SFB-TRR170, subproject C5).

References: [1] Jones and Delano (1989), Geochim. Cosmochim. Acta, 53 (2), 513-527. [2] Warren (1986), JGR: Solid Earth, 91 (B4), 331-343. [3] Gagnepain-Beyneix et al. (2006), Physics of the Earth and Planetary Interiors, 159 (3-4), 140-166. [4] Schwinger and Breuer (2018), AGU Fall Meeting, Washington, USA. [5] Smith and Asimow (2005), G^3, 6.2. [6] Davenport (2013), Planet. Sci Res. Disc. Report 1, 173. [7] Rapp and Draper (2018), Meteoritics & Planet. Sci. 53.7, 1432-1455. [8] Charlier et al. (2018), Geochim. Cosmochim. Acta, 234, 50–69. [9] O’Neill (1991), Geochim. Cosmochim. Acta, 55 (4), 1135-1157. [10] Wieczorek et al. (2013) Science, 339, 671. [11] Connolly (2005), EPSL, 236 (1-2), 524-541. [12] Kuskovand Kronrod (1998), Physics of the Earth and Planetary Interiors, 107.4, 285-306. [13] Laneuville et al. (2013), JGR: Planets, 118 (7), 1435-1452. [14] Weber et al. (2011), science, 331 (6015), 309-312. [15] Garcia et al. (2011), Physics of the Earth and Planetary Interiors, 188(1-2), 96-113. [16] Yu et al. (2019), JGR: Planets, 124 (2), 418-436. [17] Matsumoto et al. (2015), GRL, 42 (18), 7351-7358.

THE ESA PROSPECT PAYLOAD FOR LUNA 27: DEVELOPMENT STATUS.

E. Sefton-Nash[1], R. Fisackerly[1], R. Trautner[1], S. J. Barber[2], P. Reiss[1], D. Martin[3], C. Orgel[1], D. Heather[1,4], J. D. Carpenter[1], B. Houdou[1], the PROSPECT Science Team and Industrial Consortium. [1]ESTEC, European Space Agency, Keplerlaan 1, Noordwijk 2201AZ, Netherlands (e.sefton-nash@cosmos.esa.int), [2]The Open University, Walton Hall, Milton Keynes, UK, [3]ECSAT, European Space Agency, Harwell, Oxford, UK, [4]ESAC, European Space Agency, Madrid, Spain.

Introduction: The Package for Resource Observation and in-Situ Prospecting for Exploration, Commercial exploitation and Transportation (PROSPECT) is a payload in development by ESA for use at the lunar surface. Current development is for flight on the Russian-led Luna-Resource Lander (Luna 27) mission, which will target the south polar region of the Moon. PROSPECT will perform an assessment of volatile inventory in near surface regolith (down to ~ 1 m), and elemental and isotopic analyses to determine the abundance and origin of any volatiles discovered [1]. Lunar polar volatiles present compelling science and exploration objectives for PROSPECT, but solar wind-implanted volatiles and oxygen in lunar minerals (extracted via ISRU techniques) constitute potential science return anywhere on the Moon, independently of a polar landing site. PROSPECT is comprised of the ProSEED drill module and the ProSPA analytical laboratory plus the Solids Inlet System (SIS), a carousel of sealable ovens (for evolving volatiles from regolith) (Fig. 1).

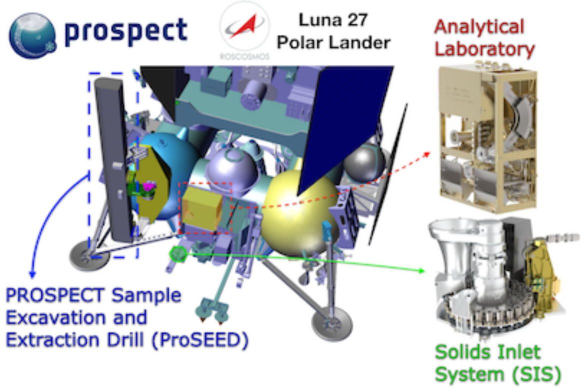

Figure 1: *Renderings of PROSPECT aboard Luna 27 polar lander, including the ProSEED drill module (left), and ProSPA (right). ProSPA comprises 1) the Solids Inlet System (lower right) to receive samples from drill sampling mechanism, with sample camera assembly (SamCam [2]) and carousel of ovens for volatile extraction from regolith samples, and 2) the analytical laboratory (upper right) containing a gas processing system, and magnetic sector plus ion-trap mass spectrometers.*

In ensemble, PROSPECT has a number of sensors and instruments (ion-trap and magnetic sector mass spectrometers, imagers, and sensors for temperature, pressure, and permittivity) that form the basis for a range of science investigations that are (almost all) led by the PROSPECT Science Team:

- Imaging, Surface Modelling and Spectral Analysis
- Drilling, Geotechnics and Sample Handling
- ProSPA ISRU Precursor Experiments
- ProSPA ISRU Prospecting
- ProSPA Light Elements & Isotopes
- ProSPA Noble Gases
- Thermal Environment and Volatile Preservation
- Permittivity (ESA-led)

Development status and current activities: PROSPECT Phase C, 'detailed definition', began in December 2019. In parallel to the industrial schedule undertaken, an associated plan of research activities has been formulated to gain from and guide ongoing development, build strategic scientific knowledge, and to prepare for operation of the payload.

Drill Testing. A plan of tests of the ProSEED Development Model was carried out in December 2019 as part of the final Phase B activities. Test procedures were formulated to demonstrate drilling and sampling functionality in ambient, cryogenic (at Leonardo laboratories) and thermal vacuum laboratory conditions (at CISAS, University of Padova). Tests included drilling into, and sampling from, well-characterized NU-LHT-2M simulant mixed with anorthosite inclusions of various sizes. Material in the test container was prepared according to a layered scheme that describe depth-density profile and distribution of inclusions. The scheme was derived by the Sample Analogue Curation Facility (SACF) at ESA ECSAT [3] to cover a plausible range of lunar regolith characteristics, and was informed by parameters measured from Apollo cores and retrieved from thermal infra-red orbital observations [e.g. [4]]. For tests in thermal vacuum, material was prepared for cases with water content representative of regolith targtetted water contents ranging from 'dry' to 'saturated' (0-~10 wt. %).

The outcome of drill tests was positive: the main functionalities of the drill system were demonstrated and required performances were achieved over the range of laboratory and representative conditions. This included: delivery from the drill sampling mechanism to ProSPA dummy ovens, delivery of a larger sample for analysis by Russian instruments, and successful drilling through/into a block of anorthosite (a single large inclusion deliberately placed in the drill path).

Simulants sampled during drill tests were collected and will be received at ECSAT [3] for curation and distribution to the Science Team, for analysis of materials to determine the extent of modification to regolith during handling.

ProSPA Bench Development Model (BDM). The BDM of the ProSPA analytical lab at the Open University has been tested to demonstrate science performance against measurement requirements. Dedicated efforts in 2019 focused on verification of evolved gas analysis (EGA) via measurement of meteorite standards, constraint of oxygen yield via demonstration of ISRU capabilities [5, 6] improving understanding of sensitivity of science requirements to regolith volatile abundance and possible contamination, and understanding the performance of oven seal materials [7].

Volatile Preservation: Particular efforts since 2018 have focused on understanding the capability of PROSPECT to sufficiently preserve volatile content in regolith throughout the sampling-analysis chain: from drilling to sealing of the ovens, and until measurement of evolved gases in ProSPA's ion-trap and magnetic sector mass spectrometers. PROSPECT's ability to meet science requirements must persist for the range of possible volatile contents expected in near-surface regolith at landing sites in the lunar south polar region, e.g. [8].

In 2020, a detailed plan of modelling and experimental work has been formulated and is being coordinated between the Science Team, industrial consortium and ESA project team to better understand water sublimation rates in realistic lunar surface operational environments, regolith structures, and geometries (such as those representative of ProSPA ovens [9]), and better constrain the potential effect on measured D/H of sublimation of lunar water ice (for example, elaborating from [10]). Results stemming from this collection of work will ensure that even in a 'hot operational case', e.g. where local illumination and thermal conditions at the landing site cause non-trivial sublimation before regolith samples can be sealed in ProSPA ovens, the original inventory and isotopics can be determined with sufficiently compact uncertainties.

Landing Sites: Locations accessible to solar-powered landers seeking a volatile-rich subsurface must meet a complex combination of low mean solar illumination (leading to metrics of volatile stability [8, 13] and abundance [14]), sufficient solar energy for the lander, safe landing site characteristics, and suitable communication geometry to support data links. Such trade-offs constitute the core of lunar polar landing site studies [e.g. 15, 16].

In the event of landing at a location that does not contain cold-trapped volatile content in the accessible subsurface, we find that roughly half of PROSPECT's science and exploration objectives would be affected only negligibly, but the remainder would suffer a reduced degree of achievement. We are assessing the spatial distribution of favourable landing sites. These are identified as locations where landing ellipses (defined by the performance of ESA's PILOT precision landing package) contain sufficiently high fractions of terrain that meet a suite of operational requirements and scientifically favourable criteria.

PROSPECT Ion-Trap Mass Spectrometer (PITMS): A variant of the ion-trap mass spectrometer in the ProSPA analytical laboratory has been selected for flight on the Astrobotic Peregrine-1 mission, which will fly to *Lacus Mortis* in mid-2021. The instrument part of PITMS is supplied by the Open University and procured by ESA. PITMS is developed through the NASA-Provided Lunar Payloads (NPLP) Program, and part of NASA's Commercial Lunar Payload Services (CLPS). PITMS will monitor the decay in the local exospheric pressure following landing, providing knowledge on lander-sourced contamination by scanning up to m/z 150 at up to 10 Hz, and time-integrating mass spectra in-situ to build S/N [11]. PITMS is the second payload confirmed in the PROSPECT series (also see [12] regarding the lunar 'i-Drill') and will add strategic value to interpreting results of future lunar volatile detection instruments/payloads.

References: [1] Trautner, R. et al., (2018) in *Proc. Int. Astronaut. Congr. IAC*, Vol. 2018-October. [2] Murray, N. J. et al. (2020) in *Lunar Planet. Sci. Conf.* [3] Martin, D. J. P. and Duvet, L., (2019) in *Lunar Planet. Sci. Conf.*, LPI, Abs #. 2663. [4] Hayne, P. O. et al., (2017) *J. Geophys. Res. Planets 122* (12), 2371–2400. [5] Sargeant, H. M. et al., (2020) *Planet. Space Sci. 180* (104751). [6] Sargeant, H. M. et al., (2020) in *Lunar Planet. Sci. Conf.* [7] Abernethy, F. A. J. et al., (2020) *Planet. Space Sci. 180* (104784). [8] King, O. et al., (2019) *Planet. Space Sci.* 104790. [9] Formisano, M. et al., (2019) *Planet. Space Sci. 169*. [10] Mortimer, J. et al., (2018) *Planet. Space Sci. 158*, 25–33. [11] Cohen, B. A. et al., (2019) in *Annu. Mtg. Lunar Explor. Anal. Group.* [12] Barber et al. (2020) in *Lunar Planet. Sci. Conf.* [13] Paige D. A. et al. [14] Sanin, A. B. et al. (2017), *Icarus* 283, 20-30 [15] Djachkova, M., et al. (2019) *Moscow Sol. Sys. Symp.,* 10MS3-MN-17. [16] Flahaut, J. et al., (2020) *Planet. Space Sci. 180* (104750).

COMPARISON OF SIMULATED LUNAR ENVIRONMENT FELSIC ROCK EMISSIVITY TO GRUITHUISEN DOMES.

K. A. Shirley[1] and T. D. Glotch[2], [1]Atmospheric, Oceanic, and Planetary Physics Department, University of Oxford, Oxford, UK (katherine.shirley@physics.ox.ac.uk), [2]Geosciences Department, Stony Brook University, Stony Brook, New York, USA.

Introduction: Several regions on the lunar surface have been identified as red spots, spectroscopically distinct areas characterized by deep ultraviolet absorptions, high albedo, and low FeO and TiO_2 concentrations [1-4]. Additionally, morphologic and mid-infrared (MIR) spectroscopic studies of some of these spots have indicated more evolved volcanism than is typical for the Moon [e.g. 5,6].

Here we use Diviner Lunar Radiometer Experiment data in the fashion of [5] to further examine the utility of the MIR in interpreting the composition of these red spots. Diviner uses its narrow bands (3, 4 & 5) centered at 7.8, 8.25, and 8.55 µm to identify the Christiansen Feature (CF), which directly indicates the silica polymerization of a material [7]. Because highly polymerized silicic material has CF positions short of the Diviner bands, concavity (*c*) and slope (*I*) indices were created to better constrain the spectral shapes. The *c* index describes the concavity between bands 3 and 5, where positive values indicate a concave up shape. The *I* index indicates the slope between bands 3 and 4. Positive *I* values are indicative of more silicic materials, and highly silicic regions display positive *c*.

In this study, we examine the Gruithuisen Domes and compare their Diviner spectra with laboratory spectra of silicic rocks. The Gruithuisen Domes have been well studied and have been identified as silicic extrusive domes [e.g. 1,5,6]. Here, we use laboratory data of terrestrial volcanic rocks to further constrain the composition. We build off of laboratory work presented in [8], in which we examine the spectra of obsidian, pumice, and rhyolite, which are several possible materials that may comprise the red spots. We compare the MIR spectra, CF values, and indices of these rocks to Diviner spectra at the Gruithuisen Domes.

Methods: Samples of rhyolite, pumice and obsidian were obtained from Wards Natural Science, ground and sieved into seven size fractions: <32 µm, 32-63 µm, 63-90 µm, 90-125 µm, 125-180 µm, 180-250 µm, and >250 µm. We measured MIR emissivity spectra using the Planetary and Asteroid Regolith Spectroscopy Environment Chamber at Stony Brook University to acquire spectra under both terrestrial ambient and simulated lunar environment (SLE) conditions following the methods of [9]. Because the thermal environment on the lunar surface is so extreme, it is important to have MIR emissivity spectra measured under similar thermal conditions to have data comparable to Diviner spectra [e.g. 8-10]. These SLE spectra were then down-sampled to Diviner resolution for direct comparison.

CF value, *c* index, and *I* index datasets were generated covering 35.2-37.5°N, 318.8-321.2°E to encompass the Gruithuisen Domes. Figure 1 shows a CF value map of the region. Subsections covering each dome (Gamma, Delta, and Northwest) were used to look at the spectral shapes in depth shown in the boxes on Figure 1.

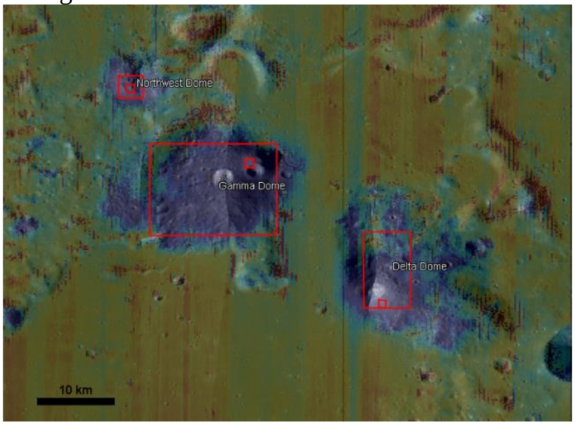

Figure 1. CF value map for the Gruithuisen Domes overlain on LRO WAC mosaic (35.2-37.5°N, 318.8-321.2°E). Dark blue indicates low CF values which correspond to more felsic composition and red higher CF values/more mafic composition. Red boxes surround portions of the domes used in this study.

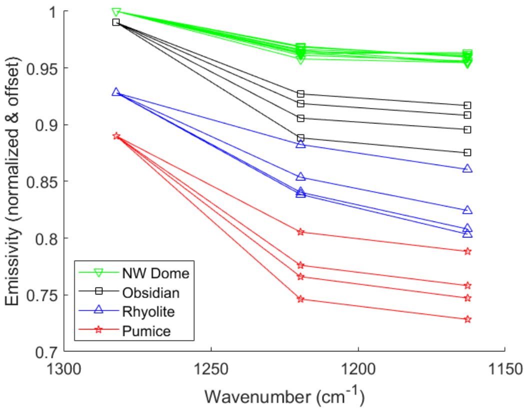

Figure 2. Spectra from the Northwest dome (green), and Diviner resolution SLE spectra of obsidian (black), rhyolite(blue), and pumice (red). Spectral groups are normalized to band 1, and offset for clarity. Shown are the 32-63 µm, 63-90 µm, 90-125 µm, and 125-180 µm size fractions.

Results/Discussion: Figure 2 shows a sampling of spectra at Diviner resolution of the terrestrial rocks and from the Northwest Dome. The overall spectral shape tends to best match the obsidian and pumice spectra better than the rhyolite, and of those, the middle range of size fractions (63-125 µm).

Because the CF values for the domes mainly fall outside of the Diviner range, we relied more heavily on the slope and concavity indices for analysis. Figure 3 shows a plot of the concavity versus slope for the domes and the laboratory data, which shows that the majority of the dome pixels (Fig.1 large red boxes) have positive slope spectra, and the 'peaks' (Fig.1 small red boxes) and laboratory data all have both positive slope and positive concavity. Having both positive indices indicates highly evolved and/or glassy material [5], however, the peak data cluster differently which could indicate slightly different compositions among the domes. There is only a small offset between the terrestrial rocks, so the higher *c* values of the NW Dome cluster could indicate that it is more obsidian rich.

The effect of particle size is obvious in the laboratory data, which have a positive trend in both indices with decreasing particle size. The most overlap of indices with the Gruithuisen data is therefore with the larger particle size materials, and the higher index values for Gamma Dome could indicate finer material there.

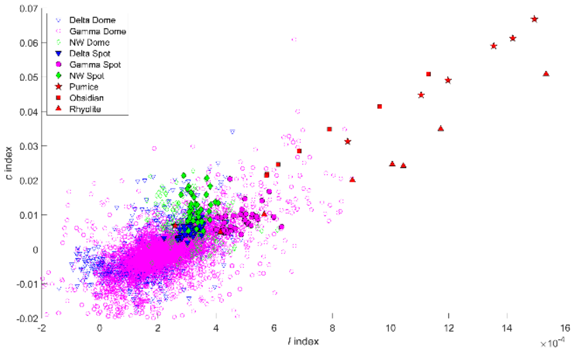

Figure 3. Comparison of the slope and concavity indices for the Gruithuisen Domes (Fig.1 large red boxes), peaks of the domes (Fig.1 small red boxes), and the laboratory felsic rocks. Positive values for both indicate highly silicic or evolved materials

There are several other variables that we will examine to better constrain the compositional differences seen here. Notably, we will look into the effects of space weathering. The domes were formed ~3.8 Ga [6], so we need to account for these effects over so long a time. One of the significant effects of space weathering on emissivity spectra is the decrease in albedo because it alters the thermal gradient in the regolith. Space weathered soils tend to have slightly shifted CF values and lower spectral contrast [e.g. 11,12], which will change the *c* and *I* indices. The rocks used in the laboratory study were pristine, therefore not exactly comparable.

To account for the decrease in spectral contrast due to space weathering, we scaled the laboratory data by 50% to better match the Gruithuisen data (Figure 4) and recalculated the indices for the scaled spectra (Figure 5). The scaled laboratory data fall to values closer to the range of Gruithuisen, which could support more fine grained material at the domes. Further investigation is needed to best approximate the effects on spectra for a more comparable dataset.

Overall, these terrestrial rocks appear to be good analogues for the Gruithuisen Domes, and will be compared to other red spots for continued analysis. Further work combining laboratory studies with lunar datasets will help us better constrain and quantify the composition of the lunar silicic volcanics.

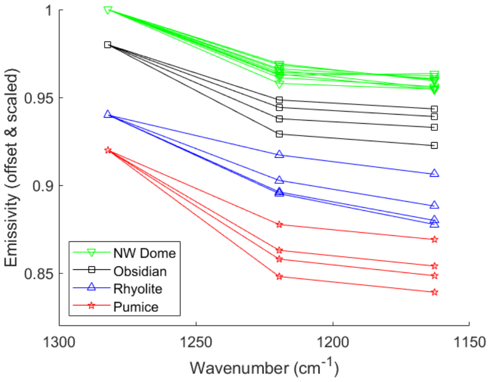

Figure 4. Diviner resolution laboratory spectra scaled by 50% to better compare spectral contrast to the Gruithuisen dataset.

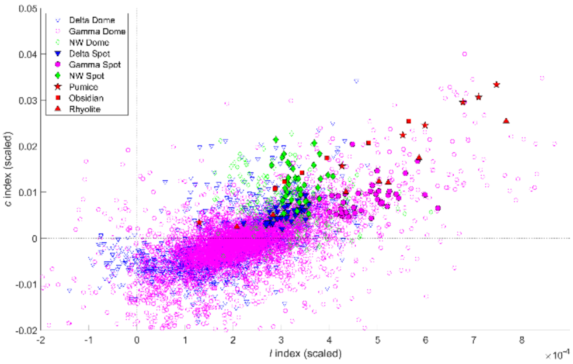

Figure 5. Comparison of the slope and concavity indices with the scaled values of the laboratory spectra.

Acknowledgements: This work is supported by the Diviner Lunar Radiometer Experiment extended science mission, and the RIS^{4}E node of NASA SSERVI.

References: [1] Whitaker, E.A. (1972) *Moon, 4*, 348. [2] Malin, M. (1974) *Earth Planet.Sci. Lett., 21*, 331. [3] Head J. W. & McCord T. B. (1978) *Science, 199*,1433. [4] Head et al. (1978) *LPSC 9*, Abst.# 488. [5] Glotch, T.D. et al. (2010) *Science, 329*, 1510. [6] Ivanov, M.A. et al., (2016) *Icarus*. 273, 262-283. [7] Conel, J.E. (1969) *JGR, 74*, 1614-1634. [8] Glotch, T.D. et al., (2017) *LPSC 48*, Abst.#1688. [9] Shirley, K.A. and Glotch, T.D. (2019) *JGR-P, 124(4)*, 970-988. [10] Donaldson Hanna, K.L. et al., (2012) *Rev. Sci. Inst., 83*, 124502. [11] Lucey, P.G. et al., (2017) *Icarus, 283*, 343-351. [12] Shirley, K.A. and Glotch, T.D. (2018) *EPSC 12*.

DATING BASALTIC IMPACT MELTS FROM APOLLO 14 AND 16.

J. F. Snape[1,2], A. A. Nemchin[3], M. J. Whitehouse[1], Q. Li[4] and Y. Liu[4], [1]Department of Geosciences, Swedish Museum of Natural Stockholm, Sweden, [2]Earth and Life Sciences, VU Amsterdam, The Netherlands, [3]Department of Applied Geology, Curtin University, Perth, Australia, [4]Institute of Geology and Geophysics, Chinese Academy of Sciences, Beijing, China.

Introduction: The Apollo 14 and 16 missions returned several ~3800-3850 Ma basaltic impact melt samples. Previous work has suggested that these rocks formed in one or more pre-Imbrium basin forming impact(s), and therefore provide an upper limit of the Imbrium event [1]. In contrast, recent ages determined for a range of breccias collected at all but the Apollo 11 landing site provide compelling evidence that the Imbrium basin was formed at ~3920 Ma [2-4]. Here, we have used an approach previously demonstrated in lunar basalts [5] to determine Pb-Pb isochron ages for two of the impact melt samples.

Samples: Both samples have crystalline textures dominated by networks of plagioclase laths (64% modal abundance in 14078 [6]; 82% in 68415 [7]) up to 3.0 mm in length. The interstices of these plagioclase networks comprise pyroxene (26% in 14078 [6]; 12% in 68415 [7]) and olivine (7% in 14078 [6]; 3% in 68415 [7]), with minor amounts of ilmenite (<1% [6,7]), mesostasis assemblages (2% [6,7]) and trace amounts of other accessory phases. The mesostasis assemblages in each sample include occurrences of K-rich glass, large enough (10-50 µm in size) to be targeted by Secondary Ion Mass Spectrometry (SIMS) analyses. In addition to this, the section of 14078 studied here included K-feldspar and sulphide grains, which were also analysed.

Results: For 14078, an isochron was defined by a combination of analyses in K-rich glass, K-feldspar, plagioclase, sulfide and fine-grained mesostasis areas, which corresponds to a date of 3853±6 Ma (95% confidence level; Fig. 1a). Furthermore, the five least radiogenic Pb isotopic compositions measured (all in plagioclase) are similar within their analytical uncertainties, and can be combined to calculate a weighted average, which is interpreted to provide a good estimate of the initial Pb isotope composition of the sample (Fig. 1a).

The isochron determined for 68415 comprises entirely K-rich glass analyses and corresponds to a date of 3835±13 Ma (95% confidence level; Fig. 1b). A single K-rich glass analysis at the unradiogenic end of the isochron represents the most primitive Pb isotopic composition analysed, but the lack of other such analyses precludes placing a confident estimate on the initial Pb composition of the sample. Nevertheless, this single K-rich glass analysis is interpreted as representing the minimum possible ^{207}Pb/^{206}Pb and ^{204}Pb/^{206}Pb ratios of the initial Pb composition.

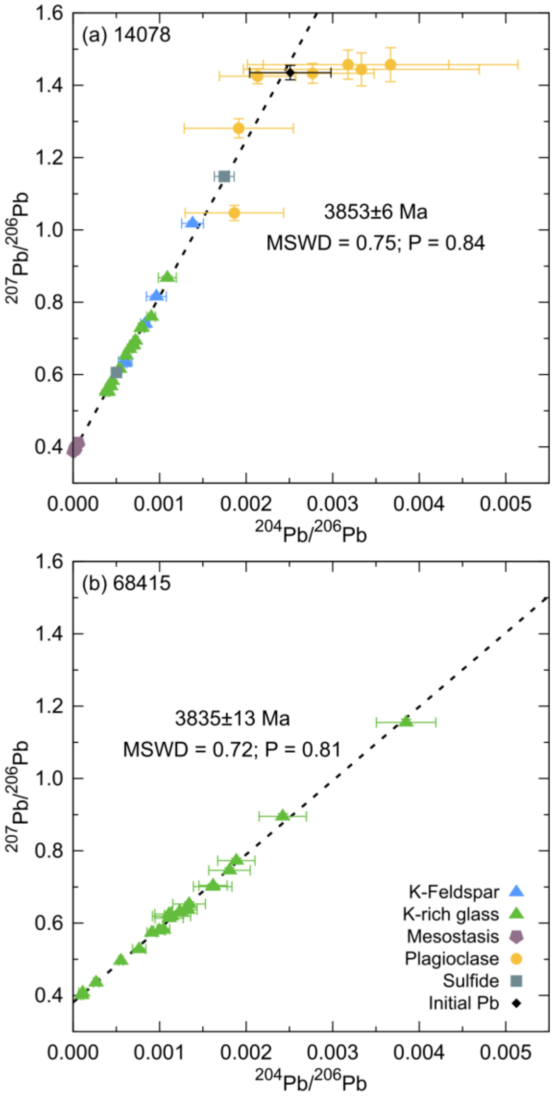

Figure 1: ^{207}Pb/^{206}Pb vs ^{204}Pb/^{206}Pb plots of the data sets for the impact melt samples 14078 (a) and 68415 (b). Isochrons are clearly defined for both samples and, in the case of 14078, the least radiogenic analyses were used to determine a likely initial Pb isotope composition. Error bars represent 2σ uncertainties.

Discussion: The ages determined for these samples clearly indicate that they crystallised after the Imbrium basin forming impact (~3920 Ma [2-4]). The two ages are only just within error of each other at the 95% confidence level. Based on these ages alone, it is not clear whether the samples could have been formed by a single large impact or not.

The initial Pb isotope composition of 14078 is similar to that presented previously for the high-Al

Apollo 14 basalt, 14072 (3904±7 Ma [5]) and a number of feldspathic clasts in Apollo 14 breccias [8]. While it was not possible to determine an equivalent value for 68415, the gradient of the isochron determined for the sample, and the composition of the least radiogenic K-rich glass analysis (i.e. the one with the highest ^{207}Pb/^{206}Pb ratio), indicate that the sample was derived from lithologies with lower ^{238}U/^{204}Pb (µ-value) sources than those of 14078, resulting in an initial Pb composition more similar to that measured in the Apollo 16 breccia 66095 [2]. Similarly, previous studies identified that, despite having some mineralogical and major element similarities to Apollo 14 basaltic impact melts, 68415 has much lower abundances of rare earth elements [7].

Given these compositional distinctions, the simplest explanation for these two samples appears to be that they formed during two separate, post-Imbrium impacts that resulted in the melting of lithologies already present at the Apollo 14 and 16 landing sites.

References: [1] Deutsch A. and Stöffler D. (1987) *GCA, 51,* 1951–1964. [2] Snape J. F. et al. (2017) *Chem. Geol., 466,* 608–616. [3] Snape J. F. et al. (2017) *GSA*, Abstract #113-6. [4] Thiessen F. et al. (2018) *GCA, 230,* 94–111. [5] Snape J. F. et al. (2016), *EPSL, 451,* 149-158. [6] McKay G. A. et al. (1978) *LPS IX*, 661–687. [7] Gancarz A. J. et al. (1972) *EPSL, 16,* 307–330. [8] Nemchin A. A. et al. (2017) *GCA, 217,* 441–461.

LASER MELTING OF LUNAR REGOLITH SIMULANT UNDER DIFFERENT GRAVITY CONDITIONS USING THE MOONRISE-PAYLOAD.

S. Stapperfend[1], N. Gerdes[2], S.Linke[1], M. Ernst[2], P. Taschner[2], J. Koch[2], P. Wessels[2], J. Neumann[2], E. Stoll[1], L. Overmeyer[2].
[1]Institute of Space Systems, Technische Universität Braunschweig, Hermann-Blenk-Straße 23, 38108 Braunschweig, Germany (s.stapperfend@tu-braunschweig.de), [2]Laser Zentrum Hannover e.V., Hollerithallee 8, 30419 Hannover, Germany (j.neumann@lzh.de).

Introduction: In-Situ Resource Utilization (ISRU) technologies pave the way for a sustainable colony on the Moon (Fig. 1). Above all, the construction of structures using only the available resources is an important factor in reducing costs and logistical effort. The MOONRISE project aims to melt lunar regolith using lasers on mobile platforms for the Additive Manufacturing of structures [1][2]. This process is called Mobile Selective Laser Melting (M-SLM) and has the advantage that only electrical energy and a moving system are required. This paper presents details about the laser system intended for melting regolith [3], the regolith simulants produced to test the manufacturing process [4], the experiments setup in the drop tower “Einstein Elevator” and finally experimental results of the laser melting.

Fig. 1: *Artistic illustration of the construction of a Moon Village. (M. Grasshoff, ITD)*

Development of the Moonrise Payload: For reasons of cost-efficiency, the hardware development approach is to profit as much as possible from components commercial off-the-shelf (COTS), i.e. commercially available components, which have no formal space qualification. These components, e.g. built for automotive or military application, often withstand harsh environments or even have space heritage without the costly and long-lasting process of formal space qualification. COTS parts – partly based on space heritage - have been screened in environmental tests and selected for Moonrise.

A detailed preliminary design of the Moonrise payload was conducted in 2019. It mainly consists of printed circuit board (PCB) for a system communication, a fiber coupled diode laser, electrical diode driver, beam focusing optics, and an LED illumination. For baseline operation, a laser power of typically 70 W will be applied for 6 s to the lunar surface at a distance of about 25 cm. The LED illumination is required for visualization of the molten regolith by external cameras. The Moonrise payload can be accommodated to a rover or a robotic arm to guaranty mobility for the melting experiments.

Following that, an Engineering Model (EM) has been assembled and tested for functionality. The dimension of the payload is 1.5 U CubeSat and it has a mass of about 2.5 kg with further reduction potential towards flight model (FM) development. In next step environmental tests, such as vibration and thermal-vacuum cycling, will be carried out with the EM.

Regolith simulants: In order to be able to test different ISRU technologies a modular regolith simulant system (Fig. 2) is currently under development at the TU Braunschweig (Germany). For that, the two regolith simulants TUBS-M and TUBS-T were developed which represent different locations on the Moon, respectively, the mare and the highland [5]. By adding agglutinates, volcanic glass and other supplements (such as olivine, ilmenite, titanium and iron), a regolith simulant can theoretically be reproduced from any known location on the Moon. Adding the necessary particle fractions with the basic simulants makes it possible to adapt the particle size distribution and particle morphology depending on the lunar location. The characteristics related to mineralogy, chemical composition and physical properties have been determined and published [4]. The simulants were also developed to support scientific and commercial institutions working on lunar science and exploration.

Fig. 2: *Components of the modular regolith simulant system for the processing of the required simulants*

Experimental Setup: In order to validate the laser melting of the regolith simulants, a vacuum chamber was designed to host powder material at pressures of around 10^{-2} mbar. Laser exposure and high speed monitoring were performed through a window. Prior to finalizing the payload design, the type of laser source, appropriate spot size, power, and duration of exposure were determined by means of experimentation. The power threshold for melting the regolith with the diode laser is 70 W for an exposure time of 3 s and a spot size of about 1 mm. More material can be fused using higher power and longer exposure.

As laser melting of regolith under vacuum conditions produced dense material, tests were continued under low gravity conditions. The large-scale research device Einstein-Elevator at the HITEC in Hannover(Germany) is a further development of a classical drop tower with which experiments are carried out under conditions of microgravity (Fig. 3) [6]. It allows experiments under zero gravity conditions for about four seconds. The flight can be repeated up to 100 times per day [7]. The Einstein-Elevator also enables adjustment of the gravity level from 0 – 5 g, a feature that was used to carry out experiments under lunar gravitation conditions.

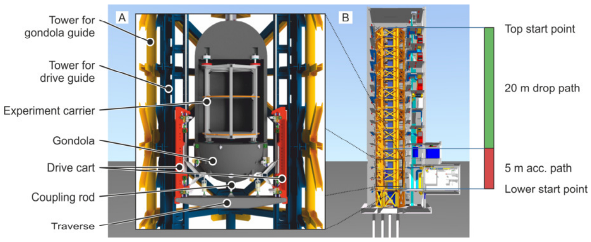

Fig. 3: *Einstein-Elevator[7]*

Experimental Results:

Regolith simulants were melted with 100 W laser exposure during the first 3 s of 0 g in the Einstein Elevator. The crucial cooling phase with a duration of 1s after exposure still took place in 0 g. This means that one melting test can be carried out during the four-second 0 g phase of the Einstein Elevator. Melted samples under 0 g are shown in Fig. 4.

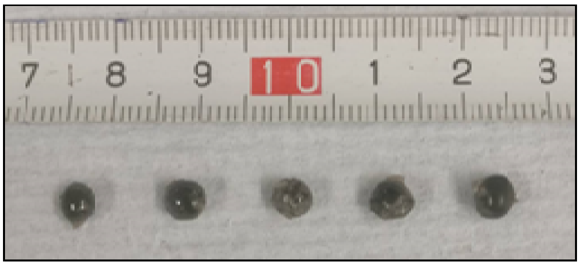

Fig. 4: *Melted globules from regolith simulant as results from laser melting experiments (70 W for 6 s at 1 g and a pressure of 1 mbar)*

TUBS-I was used for the experiments, a 50/50 mixture of two basic simulant TUBS-M and TUBS-T. This mixture is an intermediate simulant, which represents the lunar surface better than a pure mare or highland simulant regarding mineral and chemical composition. Experiments were carried out at different gravitational conditions (1 g, 0 g and moon gravity). This made it possible to verify the functionality of the MOONRISE experiment under these different gravity conditions. In addition, the examination of the samples produced, globules of melted and solidified simulant, allows a detailed investigation of processes during the melting and an assessment of the characteristics of the materials that can be produced with the M-SLM. These samples are currently being evaluated and the results will be presented at the conference.

Acknowledgements: The authors gratefully acknowledge the funding of the Volkswagen Foundation (Volkswagen-Stiftung).

References:

[1] Voß et al. (2018) *i-Sairas*. [2] Voß et al. (2018) *IAC-18-A3.2B.11, 43642*. [3] Gerdes et al. (2018) *J. Laser Appl.*, 30, 3. [4] Linke et al. (2019) *Planetary and Space Science*, 180, doi: 10.1016/j.pss.2019.104747. [5] Linke et al. (2018) *IAC-18-A3.2C.5, 43632*. [6] Lotz et al. (2018) *Advances in Space Research,* ISSN 0273-1177. [7] Lotz et al. (2017) *Gravitational and Space Research, vol. 5, no. 2, p. 11-27. ISSN 2332-7774*

THE IMPORTANCE OF MULTI-PHASE ANALYSES FOR ASCERTAINING THE HISTORY OF LUNAR VOLATILES.

A. Stephant[1], M. Anand[1,2], X. Zhao[1], and I. A. Franchi[1], [1] School of Physical Sciences, The Open University, Milton Keynes, MK7 6AA, UK., [2] Department of Earth Sciences, The Natural History Museum, London, SW7 5BD, UK. Alice.Stephant@open.ac.uk

Introduction: Since the first report of the detection of water in lunar volcanic glasses (LVG) [1], *in-situ* measurements on various lunar phases, such as LVG [1-3], apatites [4-9], olivine-hosted melt inclusions (MIs) [10-13] and plagioclases [14-15] have been carried out to ascertain the water content and hydrogen isotopic composition of the lunar interior.

While volcanic glasses are rare in the lunar sample collection, apatite was the first mineral in the limelight on account of its widespread occurrence across almost all lunar lithologies and its relatively H_2O-rich nature. Despite being present in small sizes (often < 10 μm x 5 μm), which can even be challenging for SIMS analysis, apatite has become a prime target for establishing H_2O-δD composition of lunar samples [4-9]. Such studies have revealed that apatites in mare basalts record magma degassing signatures that could account for their measured δD values of > +500 ‰ [7]. In addition, apatite in mare basalts are generally more H_2O-rich than highlands samples, which also typically display lower δD values [8]. Some workers have postulated the presence of distinct reservoirs in the lunar interior to reconcile these differences [e.g. 9]. However, apatites are late-formed minerals, and therefore, while some could still record the initial signatures of their parent magmas, others might record or be influenced by magmatic and secondary processes during crystallization of a melt. Estimating water contents of the parental magmas and their source regions using apatite data is fraught with difficulties because of the complex partitioning behavior of H_2O between the apatite and melt [16]. Therefore, other phases must be investigated in the sample in order to identify lunar samples in which apatites potentially retained initial H_2O-δD signature versus the one that recorded degassing. This will allow us to develop a robust understanding of the history of water in each case as well as to apprehend the petrogenesis of sample's parental melt and source region.

With recent improvements in the SIMS instrumentation and analytical methods it has become possible to target less-water-rich but more primitive phases in lunar samples (i.e. MIs [10-13] and nominally anhydrous minerals (NAMs) [14-15]). Melt inclusions are expected to provide more accurate information about the history of H in the lunar interior, as they are thought to be more robust for preserving pre-degassed volatiles signatures compared to later-formed phases such as apatite. Based on MIs and LVG of Apollo 17 samples, the initial δD signature of the Moon has been estimated to be +180 to +270 ‰ [2-3]. However, syn- and post-eruption processes such as post-entrapment crystallization, degassing of H as well as secondary processes such as solar wind implantation may have also altered their δD-H_2O signatures [13,17]. Among the Nominally Anhydrous Minerals (NAMs), so far only plagioclases have been studied from two Apollo samples, 15415 and 60015 [14-15], advocating H_2 degassing of the Lunar Magma Ocean.

Overall, the existence of multiple lunar reservoirs and processes have been highlighted, with δD values estimated for the lunar interior ranging between -300 and +300 ‰ [2-3; 9; 15]. Here, we demonstrate that a combined H_2O-δD analysis across multiple phases in the same sample is preferable in order to unravel the juvenile signatures of water in the lunar mantle. We present H_2O-δD data for apatites, MI and NAMs from two mare basalts, which highlight multiple processes affecting H isotopic signatures of lunar samples and potentially some degree of heterogeneity in their mantle source regions.

Samples: The samples selected are low-Ti Apollo mare basalt, 12004 and high-Al mare basalt, 14072. Both samples have a relative young cosmic ray exposure ages (60 and 21 Ma, respectively). We previously reported the H_2O-δD values for MI and apatites in these samples [17]. Here we report on our recent work focusing on NAMs.

Analytical methods: Measurements of D/H ratios and H_2O concentrations in pyroxenes and olivines were performed using the Cameca NanoSIMS 50L at The Open University. The H^-, D^-, $^{13}C^-$ and $^{18}O^-$ secondary ions were measured using a Cs^+ primary beam of ~1.4 nA. $^{13}C^-$ was used to monitor any terrestrial contamination. The primary beam was rastered over a 8×8 μm^2. Beam blanking was used and only the 4×4 μm^2 (25%) interior of the surface area was analyzed, with each measurement consisting of 2000 cycles.

Results: Apatite in 12004 has a H_2O content of 746±56 ppm with associated δD value of +961±449 ‰ while apatites from 14072 are less-water-rich, with H_2O contents ranging from 68±4 to 323± 19, and associated δD values ranging from +13±410 ‰ to +437±308 ‰. Melt inclusions in 12004 exhibit a range of water contents from 8±5 to 29±17 ppm, while pyroxenes and olivines in this sample have H_2O contents ranging from 1±0.5 to 4±1 ppm. Melt inclusions and NAMs δD lie in the same range between -478±217 ‰ and -10±318 ‰, with an outlier (pyroxene δD at +767±335 ‰). On the other hand, melt inclusions and NAMs in 14072 have H_2O contents ranging from 14±12 to 73±44 ppm and from 5±1 to 20±5 ppm, respectively. In this case as well, these two set of minerals share a similar range of δD values, from -614±218 ‰ to -108±26 ‰ (Fig. 1).

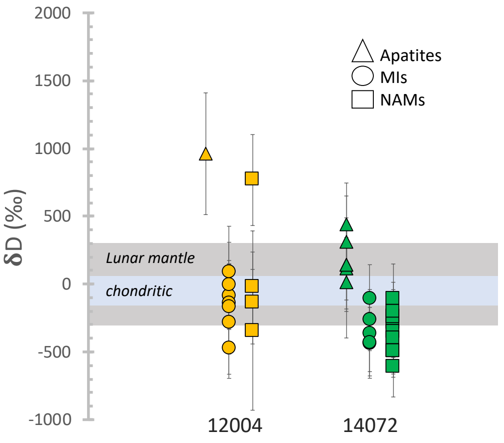

Figure 1 –δD in apatites, melt inclusions and nominally anhydrous minerals (i.e. pyroxenes and olivines) of Apollo 12004 and 14072.

Discussion: The apatite in 12004 exhibits a δD signature typical of mare basalts, which has been interpreted as reflecting fractionated D/H ratios in late-stage basaltic melts after extensive H_2 degassing from a melt containing water of carbonaceous chondrites-like H isotopic composition. Indeed, the δD values of both MIs and NAMs of 12004 suggest a chondritic δD values, with an average of -156 ‰ and -169 ‰, respectively. As such, MIs and NAMs seem largely unaffected by any H_2 degassing, with an exception of one pyroxene (i.e. +767±335 ‰). However, sample 14072 appears to have recorded a different petrogenetic history. Indeed, its apatites are less D-rich than 12004 (+192 ‰ on average); suggesting that either 14072 melt suffered a less intense H_2 degassing, or that apatites formed much earlier in the crystallization sequence, and recorded a more “pristine” signature of the parent magma. Nevertheless, both NAMs and MIs of 14072 exhibit the same range of low δD values, with average of -345 ‰ and -323 ‰ for NAMs and MIs, respectively. These values are lower than chondritic values, and cannot be explained by any H degassing starting from an initial chondritic value. Indeed, H or H_2 degassing would induce an increase of δD, as seems be the case for apatites, while H_2O degassing would induce a decrease in δD, but limited to ~100 ‰. Therefore, it seems more likely that NAMs and MIs from 14072 record a D-poor reservoir. Apollo sample 14072 is one of the most reduced lunar samples [18], for which solar wind has been hypothesized as a reducing agent. Indeed, the positive trends recorded by both NAMs and MIs in H_2O-δD space could indicate mixing with D-poor solar wind, as has been suggested for 12040 [19].

Conclusion: The combination of apatites, melt inclusions and nominally anhydrous minerals dataset allows us to establish a more robust understanding of the volatile history of the lunar samples than has been possible previously. In case of sample 12004, extensive H_2 degassing of the parent magma appeared to have taken place between the crystallization(entrapment) of NAMs(MI) and apatites. NAMs and MIs record a chondritic primitive signature for 12004 parent magma. In contrast, sample 14072 appeared to have formed from a different melt reservoir, which underwent only limited degassing but which has been reduced by solar wind hydrogen, resulting in lighter δD values as recorded in both NAMs and MIs.

References: [1] Saal A.E. et al. (2008) *Nature*, 454, 192-195. [2] Saal A.E. et al. (2013) *Science* 340, 1317–1320. [3] Fueri E. et al. (2014) *Icarus,* 229, 109-120. [4] Boyce J.W. et al. (2010) *Nature*, 466, 466-468. [5] McCubbin F.M. et al. (2010) *Am. Mineral.* 9, 1141–1150. [6] Greenwood J.P. et al. (2011) *Nature Geosci.* 4, 79–82. [7] Tartese R. et al. (2013) *GCA*, 122, 58-74. [8] Barnes J.J. et al. (2014) *EPSL*, 390, 244-252. [9] Robinson K.L. and Taylor G.J. (2016) *Nat. Geosci.* 7:401–8. [10] Hauri E.H. et al. (2011) *Science,* 333*,* 213-215. [11] Chen Y. et al. (2015) *EPSL,* 427, 37-46. [12] Ni P. et al. (2019) *GCA* 249, 17–41. [13] Singer J.A. et al. (2017) *Geochem. Jour.*, 51, 95-104. [14] Hui H. et al. (2013) *Nature Geosci.* 6, 177–180. [15] Hui H. et al. (2017) *EPSL*, 473, 14-23. [16] Boyce J.W. et al. (2014) *Science Express*. [17] Stephant et al. (2020) *LPSC 51th*, abst. 1995. [18] Taylor et al (2004) *Am. Mineral.* 89, 1617–1624. [19] Treiman A.H. et al. (2016) *Am. Mineral* 101 (7): 1596-1603.

EXPLORING THE LUNAR FAR SIDE AT TSIOLKOVSKIY CRATER.

G. Tognon[1], R. Pozzobon[2] and M. Massironi[1,2], [1]Center of Studies and Activities for Space “G. Colombo”, University of Padova, Via Venezia 15, 35131, Padova (Italy), [2]Department of Geosciences, University of Padova, Via Gradenigo 6, 35131, Padova (Italy).

Introduction: Nowadays, the ESA’s Heracles and NASA’s Artemis programs have laid the groundwork for resuming the robotic and human exploration of the Moon. Although their main target site is the lunar South Pole, other compelling sites should not be excluded a priori.

Here, we focus our attention on the less explored far side of the Moon, and in particular on the 180-km diameter Late Imbrian Tsiolkovskiy crater (20.4°S, 129.1°E).

What could make Tsiolkoskiy crater a possible future landing site for a rover-based exploration is its particularly smooth resurfaced crater floor formed by multiple eruptive events that led to the formation of one of the few mare exposures on the lunar far side [1, 2, 3]. The detection of pure anorthosite [4, 5] and olivine [6] on the central peak of the crater, moreover, could help in bringing new insights on the lunar crust origin and composition.

Data and methods: In order to perform a geological study of Tsiolkovskiy as potential landing site, the area has been geo-morphologically mapped by means of the ~100 m/pixel Lunar Reconnaissance Orbiter Wide Angle Camera [7] global mosaic together with the Lunar Orbiter Laser Altimeter and Kaguya Terrain Camera merged DEM with horizontal and vertical resolution respectively of ~59 m/pixel and 3-4 m [8]. A geo-spectral mapping, instead, has been performed on the Clementine UVVIS Warped Color Ratio mosaic with a resolution of ~200 m/pixel [9].

Results and descriptions:

Morphological mapping. In the area delimited by the rim of Tsiolkovskiy its was possible to distinguish three units ascribable to the crater floor, namely the well-preserved central peak rising ~3 km over a very smooth material characterized by a sharp boundary with respect to the adjacent hummocky material, and three units corresponding to the crater walls, namely the rough and collapsed material characterizing the crater rim in which it is possible to distinguish ponds of smooth material and steep scarps with slopes >40°. The upper panel of Fig. 1 shows the morphological mapping.

Spectral mapping. The false color band ratioed composite image allowed to distinguish several units characterized by different colors ascribable to compositional variegations which are mostly correlated to the morphological units. In particular, it is possible to discerne the yellow-orange basaltic compositions corresponding to the smooth crater floor opposed the blue hues of anorthosites, norites and troctolites correlated to the central peak and the steep scarps. The hummocky floor, the rim of Tsiolkovskiy and its smooth ponds, instead, are characterized by the red color of the mature highland soil. The spectral mapping is shown in the bottom of Fig. 1.

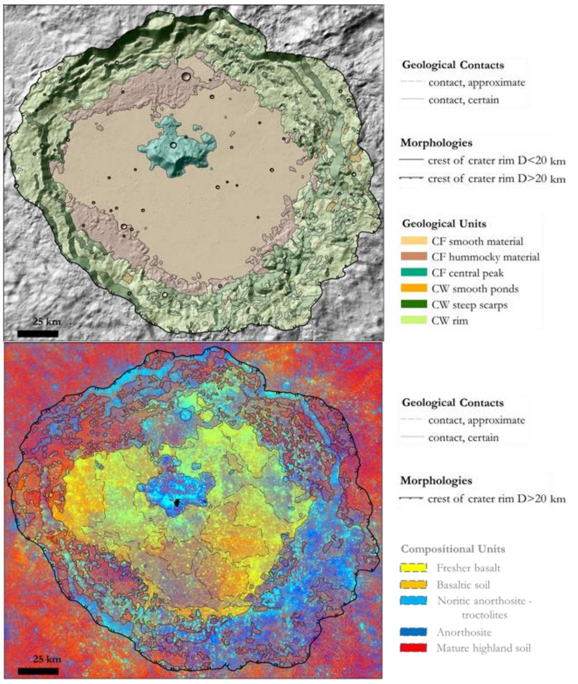

Fig. 1: Morphological mapping (upper panel) and spectral mapping (bottom panel).

Landing site analysis. A high resolution mapping performed on a Lunar Reconnaissance Orbiter Narrow Angle Camera [7] mosaic (~0.5 m/pixel but here scaled at 3 m/pixel) allows the planning of broad traverses for a rover-based exploration from potential landing ellipses. Along the traverses, the rover will have the possibility to come across different basaltic soils generated by distinct eruptions and to collect materials in proximity of sites where olivine and purest anorthosite have been detected. The location of the traverses along steep scarpes, moreover, could allow the analysis of collapsed material that otherwise would not be possible to sample. In addition, the results of the investigation of potential deep structures hidden underneath Tsiolkosvkiy performed by means of Kaguya Lunar Radar Sounder data could be integrated in the rover traverses for further in situ analysis.

Conclusions: The hereby presented data are the current results of the geo-morphological and geo-spectral mappings performed for the geologic characterization of the lunar Tsiolkosvkiy crater. Its morphology and composition provide at the same time an optimal and safe place to land and a scientifically interesting area as possible landing site for a rover-based exploration.

References: [1] Whitford-Stark J. L. and Hawke B. R. (1982) *LPSC XXXIII*, 861-862. [2] Pieters C. M. and Tompkins S. (1999) *JGR*, *104*, 21935-21949. [3] Mouginis-Mark P. J. and Boyce J. M. (2017) *LPS XLVIII,* Abstract #1206. [4] Ohtake M. et al. (2009) *Nature*, *461*, 236-241. [5] Lemelin M. et al. (2015) *JGR: Planets*, *120*, 869-8878. [6] Corley L. M. et al. (2018) *Icarus*, *300*, 287-304. [7] Robinson M. S. et al. (2010) *Space Sci. Rev.*, *150*, 81–124. [8] Barker M. K. et al. (2016) *Icarus*, *273*, 346-355. [9] Lucey P. G. et al. (2000) *JGR*, *105*, 20377-20386.

CURRENT STATUS OF LUMIO: A CUBESAT MISSION AT EARTH-MOON L2.

F. Topputo[1] and the LUMIO Team, [1]Politecnico di Milano, Department of Aerospace Science and Technology, Via La Masa 34, 20156, Milan, Italy Francesco.topputo@polimi.it

Introduction: The Lunar Meteoroid Impact Observer (LUMIO) is a CubeSat mission to observe, quantify, and characterise the meteoroid impacts by detecting their flashes on the lunar far-side. This complements the knowledge gathered by Earth-based observations of the lunar nearside, thus synthesising a global information on the lunar meteoroid environment. LUMIO envisages a 12U CubeSat form-factor placed in a halo orbit at Earth--Moon L2 to characterise the lunar meteoroid flux by detecting the impact flashes produced on the far-side of the Moon. The mission employs the LUMIO-Cam, an optical instrument capable of detecting light flashes in the visible spectrum. LUMIO is one of the two winner of ESA's LUCE (Lunar CubeSat for Exploration) SysNova competition, and as such it is being considered by ESA for implementation in the near future. An independent assessment of the mission has been performed by ESA's CDF team. In this work, the latest results on the assessment of the scientific output of LUMIO will be shown, with a focus on how they will impact the currently existing knowledge of meteoroid models. An overview of the current LUMIO CubeSat design will be also given.

LUMIO Science: Meteoroids are small Sun orbiting fragments of asteroids and comets [1]. Their formation is a consequence of asteroids colliding with each other or with other bodies, comets releasing dust particles when close to the Sun and minor bodies processing. Understanding meteoroids and associated phenomena can be valuable for the study of asteroids and comets themselves. Since the Earth and Moon are impacted by the same meteoroid streams and swarms, studying the meteoroid flux at the Moon can be useful to improve the meteoroid models of the Solar System. Understanding the meteoroid flux distribution at the Moon is also critical for future Moon surface missions, as it could help understand, for example, future lunar living areas.

In a lunar meteoroid impact, the kinetic energy of the impactor is partitioned into (i) the generation of a seismic wave, (ii) the excavation of a crater, (iii) the ejection of particles, and (iv) the emission of radiation. Any of these phenomena can be observed to detect impacts. The detection of lunar impact flashes is the most advantageous method as it yields an independent detection of meteoroid impacts, provides the most information about the impactor, and allows for the monitoring of a large Moon surface area [2-5]. Observing the lunar impacts with space-based assets, and especially on the lunar farside, yields a number of benefits over ground-based telescopes, namely: the absence of atmosphere, weather and earthshine, the increase of the observing hours, no restrictions on lunar longitudes and latitudes.

LUMIO Mission: The LUMIO mission utilises a CubeSat that carries the LUMIO-Cam, an optical instrument capable of detecting light flashes in the visible spectrum. On-board data processing is implemented to minimise data downlink. The on-board payload data processor autonomously detects flashes in the images, and only those containing events are stored.

The mission implements a sophisticated orbit: LUMIO is placed on a halo orbit about Earth-Moon L2 where permanent full-disk observation of the lunar farside is made. This prevents having background noise due to Earthshine, and thus permits obtaining high-quality scientific products. Repetitive operations are foreseen, the orbit being in near 2:1 resonance with the Moon orbit. Innovative full-disk optical autonomous navigation is proposed, and its performances are assessed and quantified.

The spacecraft is a 12U form-factor CubeSat. Novel on-board micro-propulsion system for orbital control, de-tumbling, and RW desaturation is used. Steady solar power generation is achieved with solar array drive assembly and eclipse-free orbit. Accurate pointing is performed by using reaction wheels, IMU, star trackers, and fine sun sensors.

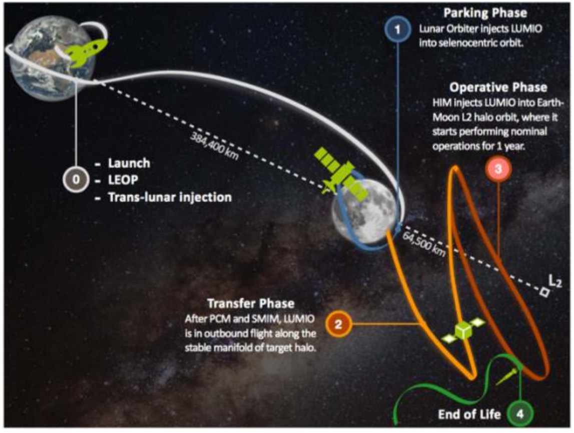

References: [1] Ceplecha, Z., et al (1998) *Space Science Review*, 84 [2] Ortiz, J. et al (1999) *A search for meteoritic flashes on the Moon*, A&A, 343. [3] Ortiz, J., et al (2000) *Optical detection of meteoroidal impacts on the Moon*, Nature, 405. [4] Suggs, R. et al (2014) *The flux of kilogram-sized meteoroids from lunar impact monitoring*, Icarus 238. [5] Bonanos, A. et al (2018) *NELIOTA: First Temperature Measurement of Lunar Impact Flashes*, A&A, 612

MELODY: Moon multisEnsor and LabOratory Data analYsis. F. Tosi[1], E. Pettinelli[2], C. Carli[1], M. Massironi[3], R. Pozzobon[3], G. Rinaldi[1], S. Fonte[1], R. Orosei[4], E. Mattei[2], B. Cosciotti[2], M. Franceschi[5], R. Avanzinelli[6], M. Casalini[6], G. Pratesi[6], L. Giacomini[1], F. Zambon[1].
[1]Istituto Nazionale di AstroFisica – Istituto di Astrofisica e Planetologia Spaziali (INAF-IAPS), Roma, Italy, federico.tosi@inaf.it. [2]Università degli Studi Roma Tre – Dipartimento di Matematica e Fisica, Roma, Italy. [3]Università di Padova – Dipartimento di Geoscienze, Padova, Italy. [4]Istituto Nazionale di AstroFisica – Istituto di RadioAstronomia (INAF-IRA), Bologna, Italy. [5]Università di Trieste – Dipartimento di Matematica e Geoscienze, Trieste, Italy. [6]Università degli Studi di Firenze – Dipartimento di Scienze della Terra, Firenze, Italy.

Introduction: The Moon is the single most important planetary body for understanding not only Earth but also all terrestrial planets in our Solar System in terms of planetary processes. The Moon preserves many of the geologic processes that occurred in the early stages of the Solar System's evolution and during the period when life formed. It preserves a record of the impact history over geologic time, which has been obliterated on planetary bodies that are active and have atmospheres. Volatile deposits at the lunar poles may contain a record of the volatiles transported to the inner Solar System.

Building on earlier telescopic observations, our knowledge about the Moon was drastically expanded by the wealth of information provided, during the Moon race, by the Apollo and Luna/Lunokhod missions. After a period of stagnation lasted about twenty years, the robotic exploration of the Moon lived a new Renaissance from 1994 onwards. Several space missions, initially led by the United States and then by other nations such as Japan, India and China, continued the Moon exploration: *Clementine*, *Lunar Prospector*, *Smart-1*, the *Selenological and Engineering Explorer* (SELENE (*Kaguya*)), *Chandrayaan 1-2*, the *Lunar Reconnaissance Orbiter* (LRO), the *Lunar Crater Observation and Sensing Satellite* (LCROSS), the *Gravity Recovery and Interior Laboratory* (GRAIL), the *Lunar Atmosphere and Dust Environment Explorer* (LADEE), and *Chang'E 1-4*. Today, the data set related to geology, geochemistry, mineralogy, petrology, chronology, and internal structure of the Moon is unequaled for any planetary body other than the Earth. These data are crucial for understanding planetary surface processes and the geologic evolution of a planet.

While 2019 celebrated the 50th anniversary of the first human landing on the Moon, robotic exploration of our natural satellite is a benchmark for future human expansion in our Solar System. Several space agencies and private companies are developing strategies to bring the man back on the Moon within this decade. This new international race will be driven by scientific, technological and economic interests, and will require an in-depth understanding of Moon surface and subsurface environment such as, for example, the landing site geochemical, mineralogical (e.g., rocks oxygen availability for propellent) and hydrological resources.

The access and utilization of lunar resources are a key component of any future space-exploration effort in cislunar space and beyond. Desirable features of systems designed for human lunar exploration include reusability as well as extended presence on the surface, and both of these characteristics will benefit immensely from the use of lunar resources from the beginning. Results from the Apollo missions, coupled with results from recent missions, indicate that the resource potential of the Moon is vast, with substantial ore deposits known to be present in lunar pyroclastic deposits and the possibility of economically viable volatile deposits at the poles. While the concepts of lunar resource utilization are fairly well-developed for lunar pyroclastic deposits and Ti-rich mare basalts, more detailed information of the resource feedstock (composition, state, physical properties, volumes and concentrations; exploitation potential) is needed to finalize the design of the processing chain for the polar volatile deposits. Additional studies and flight demonstrations of In-Situ Resource Utilization (ISRU) technologies at polar and nonpolar locations are needed to mature lunar resource utilization.

Proposed Research: The "*MELODY: Moon multisEnsor and LabOratory Data analYsis*" research project (**Fig. 1**), submitted in November 2019 in response to the PRIN INAF 2019 (RIC) call, aims to combine ambitious but realistic and achievable objectives, bringing together the necessary skills found at Italy's National Institute for Astrophysics (INAF) and other Italian academic institutions. The overarching goal of the MELODY proposal is to gather a broader understanding of our Moon by combining surface and subsurface data analysis, and the laboratory characterization of the lunar environment.

Our research project aims to perform an unprecedented analysis of an aggregated dataset (e.g. **Fig. 2**) made up of maps of geochemistry, mineralogy, and gravity anomalies, obtained from orbital missions over the last decades, which would allow us to highlight the emergence of units that are homogeneous with respect to different variables, and may not be evident from the analysis of individual datasets. In parallel, the analysis of lunar sub-surface radar data, which unlike the previous data sets have a limited coverage, (e.g. **Fig. 3**) will be performed on specific regions of interest by applying up-to-date techniques that have been recently applied to Mars orbital radar data and to lunar radar data acquired in-situ by the Chinese rovers, in addition to laboratory analysis of lunar soil analogues, important for characterizing the dielectric environment and thus the electromagnetic modeling. Finally, another novelty of our proposal is the possibility to perform laboratory measurements that are still missing on a small number of lunar meteorite samples (e.g. **Fig. 4**), to be purchased on the market.

The novel, multisensor and multidisciplinary study of lunar data we propose has scientific objectives that fall within the major lunar exploration roadmaps defined by NASA and ESA. The ability to directly compare multivariate analyses of the Moon with subsurface geophysics, even if only for a limited number of regions of interest, and with direct measurements of lunar specimens, is a plus that would hardly be achieved without bringing together experts who are already familiar with those activities or may provide a broader interpretation based on their long-term experience.

References: [1] Cooper, 2008. *Apollo 17 Lunar Sounder data provide insight into Aitken Crater's subsurface structure*. https://ntrs.nasa.gov/archive/nasa/casi.ntrs.nasa.gov/20080013155.pdf

[2] Pommerol et al., 2010. *Geophys. Res. Lett.* **37** (3), CiteID L03201.

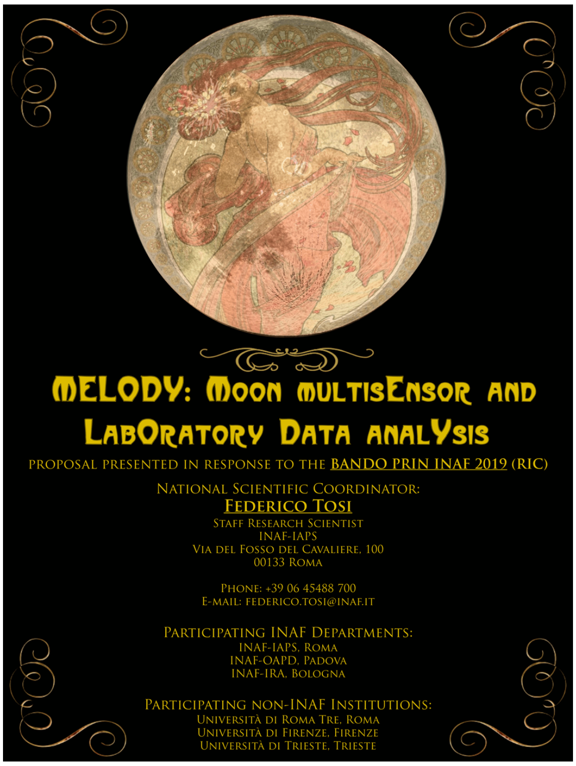

MELODY: Moon multisEnsor and LabOratory Data analYsis

Proposal presented in response to the BANDO PRIN INAF 2019 (RIC)

National Scientific Coordinator:
Federico Tosi
Staff Research Scientist
INAF-IAPS
Via del Fosso del Cavaliere, 100
00133 Roma

Phone: +39 06 45488 700
E-mail: federico.tosi@inaf.it

Participating INAF Departments:
INAF-IAPS, Roma
INAF-OAPD, Padova
INAF-IRA, Bologna

Participating non-INAF Institutions:
Università di Roma Tre, Roma
Università di Firenze, Firenze
Università di Trieste, Trieste

Fig. 1. Cover page of the MELODY research project, submitted in November 2019 in response to the PRIN INAF 2019 (RIC) call.

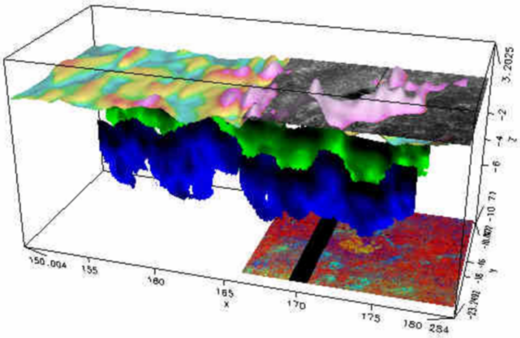

Fig. 2. Example of an aggregated dataset made from diverse lunar datasets. This graph shows magnetic data from Lunar Prospector and 750 nm grayscale imagery from Clementine combined in the upper layer. The middle layers, in blue and green, are two lines of Apollo Lunar Sounder Experiment (ALSE) radar data. The bottom layer is a Clementine multispectral ratio image. From: [1].

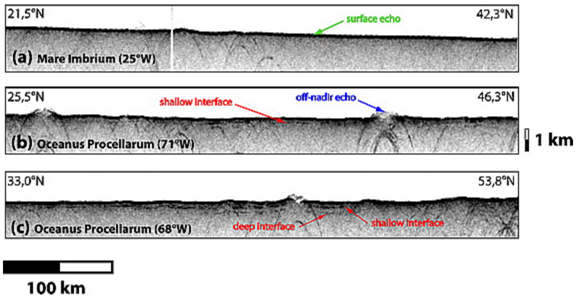

Fig. 3. Examples of SELENE/LRS sounding profiles in lunar maria with (a) no visible subsurface interface, (b) a unique shallow subsurface interface and (c) two distinct subsurface interfaces. Strong and large hyperbolic features visible on the three profiles are due to off-nadir surface echoes (*surface clutter*), generally produced by isolated craters. These three examples are representative of most profiles measured in lunar maria. From: [2].

Fig. 4. Example of a lunar meteorite sample. This is a closeup of sawn face of Dhofar 1180 (photo credit: Michael Farmer). From: http://meteorites.wustl.edu/lunar/stones/dhofar1180.htm.

INVESTIGATING SURFACE TENSION PHENOMENA OF MOLTEN LUNAR REGOLITH SIMULANT IN VACUUM.

E. Tuohy[1,2], L. Schlüter[1], A. Cowley[1], [1]European Astronaut Centre EAC, European Space Agency, 51170 Köln, Germany, [2]Irish Research Council, 3 Shelbourne Buildings, Crampton Avenue, Ballsbridge, D04 C2Y6, Ireland.

Introduction: The Marangoni effect is a mass transfer phenomena that can occur when there is a gradient in the surface tension of a fluid, where the surface tension can be driven by the concentration (the solutocapillary effect) or by temperature (the thermocapillary effect). The effect is well studied and its behaviour has many practical applications such as heat pipes in microgravity [1]. However, little research has been conducted looking at how this phenomena occurs with respect to molten lunar regolith simulant. This may be an important phenomena to understand in greater detail, as many proposed ISRU processes are carried out in a molten state [2]. The Marangoni effect in regolith was first reported by Dominguez & Whitlow as an unanticipated result when investigating the thermophysical properties of molten regolith simulant [3]. The Spaceship EAC team [4] observed a similar phenomenon while conducting molten regolith simulant experiments in vacuum. The molten simulant had migrated up the walls of the crucible it was contained in. Once cooled, the simulant had formed a permanent, relatively uniform, coating on the crucible wall. Further experimentation was conducted to investigate this effect and determine the driving factors behind it.

Experimentation: The experiments were conducted in a vacuum tube furnace (Carbolite Gero STF 15/450 + 3216 Controller). A number of experiments were conducted to determine what variables drive the Marangoni effect. These included: pressure, ambient gas, temperature, time at max temperature, type of simulant, doped simulants, quantity of simulant, and substrate type. The baseline parameters used were 1 gram of JSC-2A heated to 1300˚C for 70 minutes in an Al_2O_3 crucible at 0.02 mbar (fig. 1). These conditions repeatedly produced evidence of the Marangoni effect occurring.

Results: Immediate observation showed that the effect did not occur in atmospheric condition or in a Nitrogen atmosphere under atmospheric pressure. The effect only occurred in vacuum conditions. The temperature at which upward migration is observed varies between different simulants. With JSC-2A, the effect only occurs once the simulant is in a molten state which was achieved at 1200˚C. The effect was observed with all maria simulants tested (JSC-2A, EAC-1, LMS) but not with LHS. A LHS sample was then doped with 10% ilmenite to make its composition more similar to that of mare simulants which then showed evidence of the Marangoni effect. The effect created a strongly bonded coating to the alumina crucibles and a much weaker, brittle coating on a smooth stainless steel substrate.

Future work: Analysis is to be performed to see if the effect causes the minerals in the melt to separate. Further experimentation is to be conducted at higher temperatures (up to 1500˚C) to see if there is a change in the coating properties. In addition, the thermal properties of the different simulant coatings and possible use-cases will be analysed.

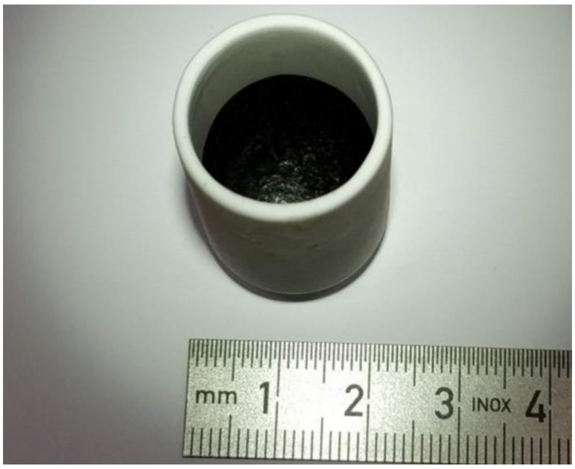

***Fig 1** - 1 gram of JSC-2A heated at 1300°C for 70 minutes*

***Fig 2** - 2 grams of JSC-2A heated at 1200°C for 70 minutes*

References:

[1] Savino R. et al. (2007) Acta Astronautica, 61, 16-26.

[2] Schlüter, L. and Cowley, A. (2019) Planetary and Space Science, 104753.

[3] Dominguez J. A. and Whitlow J. (2019) Advances in Space Research, 63, 2220-2228.
[4] Spaceship EAC:
https://www.esa.int/About_Us/EAC/Spaceship_EAC

SAMPLES NEEDED FOR IMPROVING THE LUNAR CRATERING CHRONOLOGY.

C. H. van der Bogert[1] and H. Hiesinger[1], [1]Institut für Planetologie, Westfälische Wilhelms-Universität, Wilhelm-Klemm-Str. 10, 48149 Münster, Germany (vanderbogert@uni-muenster.de).

Introduction: Recent lunar sample-return mission concepts and proposals focus on the goal of returning samples that represent either the oldest of the lunar basins (South Pole-Aitken basin, [e.g., 1,2]) or some of the youngest lunar mare basalts (P60 basalt [e.g., 3-7]; Mons Rümker [8]). Indeed, studies of in situ dating mission payloads also propose locations that would provide access to materials from ancient basins and young basalts [e.g., 9,10]. Here, we examine how each type of sample would help improve the calibration of the lunar cratering chronology (see also [11]).

Background: The lunar cratering chronology is based on (1) empirical measurement of the size-frequency distribution of craters produced on the Moon – termed the “production function” [12-14], and (2) construction of a chronology curve that relates Apollo and Luna sample ages to crater spatial densities, here N_{cum} ($D \geq 1$ km), measured at the sample sites (***Fig. 1***, [12,14-17]). The curve allows the assignment of absolute model ages (AMAs) to unsampled geological units across the Moon via crater size-frequency distribution (CSFD) measurements.

As there are no samples from other planetary bodies which have known provenance, and therefor measurable crater spatial densities for a body-specific calibration, the lunar crater chronology is modified and used for many terrestrial bodies throughout the Solar System. Consequently, the accuracy of the AMA determinations for the Moon and other planetary bodies depends on the quality of the lunar calibration, in addition to the assumptions made in translating the chronology to other bodies.

One approach for improving the lunar cratering chronology and its wider application is to test and improve the existing calibration points [e.g., 16-19], as well as to examine which samples could be collected from the Moon that would improve our understanding of the distribution of sample ages versus $N(1)$ (***Fig. 1***).

Current Status: The chronology currently depends on samples of Imbrium basin ejecta (Descartes and Fra Mauro Formations, radioisotopic ages of ~3.9 Ga), mare basalts (radioisotopic ages of ~3.2-3.7 Ga), ropey glasses from the Apollo 12 landing site that have been interpreted as Copernicus ejecta (radioisotopic age of ~850 Ma), and cosmic-ray exposure ages of ejecta and secondary crater materials of the Tycho, North Ray, and Cone craters [e.g., 20 and references therein].

Mind the Gap: The current sample set does not contain materials of indisputable provenance with ages between 3.2 Ga and the age of Copernicus crater. This means that various workers have estimated the vertical position of the chronology curve differently (blue shaded region, ***Fig. 1***)(See also [18,19]). Because the curve is flat across this time frame, small differences in measured crater spatial densities result in large differences in resultant AMAs (***Fig. 1***). For example, the $N(1)$ values for the P60 site [21], which are slightly smaller than those measured by [3], could give AMAs that could range from ~0.75 to ~1.75 Ga (pink line, ***Fig. 1***). $N(1)$ values for two basalt units in the Mons Rümker region [8] also could give largely different AMAs depending on which chronology function is used (green and orange lines, ***Fig. 1***). Thus, a sample from any of these or other young basalts are critical for pinning the position of the chronology function in this age range more accurately.

Catastrophism or Uniformitarianism: The chronology function has been extrapolated beyond ~3.9 Ga, because there are no older samples of

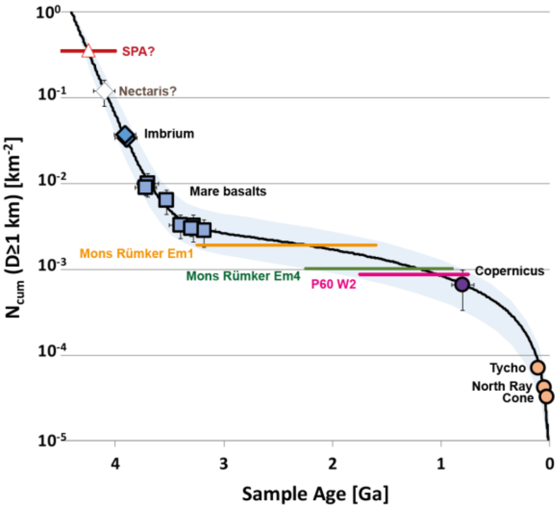

Figure 1. *The lunar cratering chronology curve (black) of Neukum et al. (2001)[15], where the shaded blue region shows the range of proposed chronology functions to illustrate the absence of a precision fitting of model ages for the 1-3 Ga time frame. There are no calibration points for ages >3.9 Ga. The colored lines mark N(1) values determined via crater size-frequency distribution measurements for proposed sample regions in Mons Rümker [8] and the P60 basalt [3,21]. Sample ages from 76535 [23] and 63503,13 [22] are proposed to either originate from the South Pole-Aitken basin or represent its minimum age, respectively. The age of Nectaris basin is not well-constrained – we use [13] as a reference.*

known provenance. Here, further calibration of the chronology is necessary to make progress on questions about the possibility and nature of a lunar cataclysm or late heavy bombardment.

A sample unambiguously from the South Pole-Aitken basin would establish the age of the oldest known basin on the Moon and set the time frame for early lunar bombardment. The similarity of lunar zircon resetting ages to the ~4.29 Ga plateau age for Apollo 16 impact melt rock 63503,13 was postulated to indicate a minimum age for the SPA basin [22]. Recently, Apollo 17 sample 76535 was theorized to be a rock excavated by SPA basin [23]. Its age of 4.25 Ga would support the absence of a spike in the early bombardment of the Moon [23], such as the accretion tail model proposed by Morbidelli et al. (2018)[24]. However, the need to interpret the meaning of resetting ages, as well as the geophysical arguments required to support 76535's provenance in SPA could eliminated if a sample were to be collected directly from SPA.

Additional samples from basins that formed between the Imbrium and SPA basins are also needed to fully investigate the uniformity or variability of the impact rate over time. Nectaris basin is proposed to have an age of ~4.1 Ga [14, 25] or to have a younger age of ~3.9 Ga [20], but it has a CSFD that places it in between the Imbrium and SPA basins [e.g., 24]. Thus, samples of the Nectaris basin, or other basins with ages of 4.1-4.2 Ga would add granularity to the calibration of the oldest lunar regions. The Crisium basin has also been examined as a sample site due to the presence of potential impact melt deposits [25-27], with CSFD measurements suggesting an age >3.9 and <4.1 Ga [26,24].

The current calibration also cannot exclude periodic excursions in recent times [e.g., 28] due to an absence of granularity. This is because the lunar cratering chronology from ~1 Ga to present is calibrated with only one radiometric age (Copernicus crater) and three exposure ages (Tycho, North Ray, and Cone craters). Additional sample ages in this time frame would allow assessment of the recent stability of the impact rate.

Lunar Chronology Site Requirements: To improve the lunar chronology, it is not enough to collect samples of well-established provenance. Indeed, it is also critical that the sample sites exhibit a surrounding region where robust CSFD measurements can be conducted. This requires a geologically homogeneous unit with little topography, minimal secondary crater contamination, and few to no other secondary features (e.g., wrinkle ridges). These requirements mean that it will be more straightforward to select appropriate calibration sites for young basalts than for ancient, heavily cratered basins. Unfortunately, the extremely young irregular mare patches [29] generally do not cover enough area to provide good counting areas, and the ejecta and impact melt deposits of young craters tend to be rugged – causing challenges in measuring their CSFDs [e.g., 30]. However, a sample return or in situ age measurement at a Copernican-aged crater could resolve questions about the self-secondary craters and strength-scaling effects on CSFDs [31-33] and allow assessment of the accuracy of the <1 Ga part of the current lunar cratering chronology.

Facet: An improved calibration of the lunar chronology will allow a clearer and more granular interpretation of the geological history of the Moon and other bodies where the lunar chronology is applied. New returned samples or in situ age determinations are thus required.

References: [1] Jolliff et al. (2012) LEAG, 3047; [2] Jolliff et al. (2017) LPSC 48, 1326; [3] Hiesinger et al. (2003) JGR 108, 10.1029/2002JE001985; [4] Eldridge et al. (2010) LPSC 41, 1486; [5] Lawrence et al. (2013) LEAG, 7048; [6] Draper et al. (2019) LPSC 50, 1110; [7] Anderson et al. (2015) Issues in Crater Studies, 9058; [8] Qian et al. (2018) JGR 123, 2018JE005595; [9] Cohen (2012) LPSC 43, 1267; [10] Cohen et al. (2018) LPSC 49, 1029; [11] van der Bogert and Hiesinger (2020) LPSC 51, 2088; [12] Neukum et al. (1975) PLSC 6, 2567; [13] Neukum (1983) NASA TM 77558; [14] Neukum and Ivanov (1994) *in* Hazards Due to Comets and Asteroids, 359; [15] Neukum et al. (2001) Space Sci Rev 96, 55; [16] Robbins (2014) EPSL 403, 188; [17] Iqbal et al. (2019) Icarus 333, 528; [18] Hiesinger et al. (2020) LPSC 51, 2045; [19] Hiesinger et al. (2020) ELS; [20] Stöffler et al. (2006) Rev Min Geochem 60, 519; [21] Stadermann et al. (2018) Icarus 309, 45; [22] Fernandes et al. (2013) MAPS 48, 241; [23] Garrick-Bethell (2020) 338, 113430; [24] Morbidelli et al. (2018) Icarus 305, 262; [25] Fischer-Gödde and Becker (2012) GCA 77, 135; [24] Orgel et al. (2018) JGR 123, 748; [25] Spudis and Sliz (2017) *GRL*, 10.1002/2016GL071429; [26] van der Bogert et al. (2018) LPSC 49, 1028; [27] Runyon et al. (2020) JGR 125, e2019JE006024; [28] Mazrouei et al. (2019) 363, 253; [29] Braden et al. (2014) Nature Geoscience, 7, 787; [30] Krüger et al. (2016) 273, 164; [31] Zanetti et al. (2017) Icarus, 298, 64; [32] van der Bogert et al. (2017) Icarus, 298, 49; [33] Plescia and Robinson (2019) Icarus, 321, 974.

SELECTING LANDING SITES FOR IN SITU RESOURCE UTILIZATION MISSIONS. C. H. van der Bogert[1], H. Hiesinger[1], A. Lewang[1], P. Gläser[2], I. Pretto[3], F. Venditti[3], and Lutz Richter[4]. [1]Institut für Planetologie, Westfälische Wilhelms-Universität, Wilhelm-Klemm-Str. 10, 48149 Münster, Germany (vanderbogert@uni-muenster.de); [2]Institut für Geodäsie und Geoinformationstechnik, Technische Universität Berlin, Germany; [3]OHB Italia S.p.A., Milan, Italy; [4]OHB System AG, Oberpfaffenhofen, Germany.

Introduction: Recent increased interest in the development of commercial space infrastructure, offers an opportunity for technology advancement parallel to progress on basic lunar science questions. In fact, planetary geologists provide critical input for the evaluation of landing sites with suitable chemical and physical characteristics for testing and implementation of in situ resource utilization (ISRU) technologies. Remote sensing datasets allow the extrapolation of knowledge from landing sites to across the Moon. However, there is a need for additional groundtruthing of materials of interest for ISRU. Moreover, basic scientific instrumentation on technology missions could also provide critical insight for scientific questions outlined in numerous reports [e.g., 1-5]. Landed studies of bulk chemistry/mineralogy, volatile contents, and geotechnical properties at previously unsampled types of resource deposits, particularly pyroclastics and unsampled mare basalts, would allow strategic knowledge gaps (SKGs) for ISRU to be addressed, as well as advance our understanding of lunar science.

ESA Strategy and Activities: Recent European Space Agency activities related to the expansion of capabilities for use of space resources [e.g., 6,7] involves a program entitled “Commercial In-Situ Resource Utilisation Demonstration Mission Preparation Phase”. The aim of the study is to assess and develop commercial capabilities for processing lunar regolith to produce oxygen and other resources. Participants are developing and testing resource extraction techniques ranging from hydrogen- and methane-reduction [e.g., 8] to application of the FFC-Cambridge electrochemical process to lunar materials [9], and designing engineering solutions for integrating these technologies onto small payloads [10]. Commercial lander providers are involved to investigate and coordinate potential ESA/industry partnerships for delivery of ISRU payloads to the Moon.

Our Study Goals: In the course of our ISRU project [10], led by OHB Italia under ESA contract, we reviewed potential ISRU resource types and evaluated potential landing regions/sites for (1) feedstock characterization mission(s) and (2) end-to-end ISRU plant demonstration(s) [see also, 11]. We focused on mid-latitude nearside regions, where commercial lander providers will most easily be able to land/operate.

The evaluation of potential sites involved analyses of high-resolution and stereo image coverage, digital terrain models, illumination conditions, spectral/compositional maps (e.g., TiO_2, FeO, indigenous water), and maps of physical properties (e.g., radar/thermal characteristics, rock abundance). Combined within GIS, along with geological maps, crater/boulder size-frequency distribution measurements, and hazard assessments (e.g., slopes, rock abundance), these datasets allow the selection of scientifically and technically relevant landing sites.

Characterization Sites: For our analysis of potential ISRU characterization sites, we combined locations discussed in Jawin et al. (2019)[4], sites relevant to ISRU oxygen extraction from those discussed and summarized in Flahaut et al. (2012)[12] and Kring and Durda (2012)[13], and regions of interest for the cancelled NASA Constellation program [14]. We then limited the selections to those which the two participating lander providers can currently reach with their technology.

The different materials of interest generally fall into four groups: (1) high TiO_2 pyroclastics with affinity to the Apollo 17 landing site, (2) high FeO, low TiO_2 pyroclastics characterized by the Aristarchus plateau deposits, (3) high TiO_2 basalts (e.g., type M2 [12]), and (4) high FeO, low TiO_2 basalts (e.g., the P60 basalt [15]). Group 1 regions include Sinus Aestuum, Rima Bode, Mare Vaporum, Sulpicius Gallus, Montes Harbinger, and Montes Carpatus. High TiO_2 pyroclastics were sampled at the Apollo 17 landing site, but it is unknown how these deposits compare to those only observed via remote sensing [e.g., 16]. Group 2 is primarily represented by the low TiO_2 and high Fe^{2+} compositions inferred from the remotely-sensed spectral properties of the most arealy extensive lunar pyroclastic deposits on the Aristarchus plateau. High TiO_2 basalts of type M2 within group 3 are not present in our sample collection [12]. Group 4 includes low TiO_2, high FeO basalts, such as the P60 basalt, which is one of the youngest basalts on the Moon [4,15], and a potential site for either sample return or in situ age-dating missions [e.g., 17 and references therein].

Locations within the first two groups exhibit potentially high concentrations of indigenous H_2O [18]. Given the need to groundtruth these values and the value of indigenous water as an ISRU resource, it may be beneficial to select a site within such deposits. These locations are, for group 1: Sulpicius Gallus, Rima Bode, or Humorum/Doppelmayer; and group 2: the Aristarchus plateau.

The selection of a site on the Aristarchus plateau would allow the characterization of previously uncharacterized materials, whereas a mission to Rima Bode or Sulpicius Gallus would allow groundtruthing of whether these materials are similar to the Apollo 17 pyroclastics. Characterization at any of these sites would allow the evaluation of the reported high concentrations of indigenous water in some pyroclastic deposits. Key measurements of bulk chemistry and mineralogy, volatile contents, and quantification of geomechanical regolith properties would address both scientific themes and SKGs for potential ISRU materials [e.g., 4].

End-to-End Demonstration Sites: For a standalone end-to-end (E2E) ISRU demonstration mission, a fuller understanding of the physical and compositional characteristics of the resource deposits is required to reduce overall risk for the demonstration. As a result, either precursor or "characterization" missions are required, or an E2E site could be selected near prior landing sites. Thus, we examined locations near Apollo and Luna landing sites, to allow extrapolation of known surface properites to nearby deposits. Because Ti-rich pyroclastic deposits appear to be most advantageous for initial E2E plant operations from both beneficiation and compositional perspectives, we selected an example landing site for an E2E demonstration to the northwest of the Taurus Littrow valley, south of Clerke crater (green unit, ***Fig. 1***). Given that some ISRU methods require the presence of ilmenite, but others do not, this location offers an opportunity to test more than one ISRU technique in a single location.

Current high resolution LROC NAC frames and stereo imaging are constrained to the eastern part of the pyroclastic deposits (green unit, ***Fig. 1***). Within this area (***Fig. 2***), we mapped landing regions that maximize both the Ti and Fe contents of the regolith, as well as offering slopes of <5° and accumulated illumination approaching 50% (~14 days)(***Fig. 2***). The next steps for selecting a landing site within this region include more detailed hazard analyses.

Summary: The selection of sites relevant for ISRU technology demonstration and development benefits from geological studies regarding the chemical and physical properties of potential feedstock.

References: [1] NRC (2007) The Scientific Context for the Exploration of the Moon, 10.17226/11954; [2] NRC (2011) Vision and Voyages for Planetary Science in the Decade 2011-2022, 10.17226/13117; [3] LEAG (2018) https://www.lpi.usra.edu/leag/reports/ASM-SAT-Report-final.pdf; [4] Jawin et al. (2019) ESS 6, 10.1029/2018EA000490; [5] ESA Strategy for Science at the Moon (2019) https://exploration.esa.int/s/WmMyaoW; [6] ESA Space Resources Strategy (2019) https://exploration.esa.int/s/WyP6RXw; [7] Meurisse et al. (2019) Dev New Space Econ, 5006; [8] Schwandt et al. (2012) PSS 74, 49-56; [9] Lomax et al. (2020) PSS 160, 104748; [10] Pretto et al. (2020) ELS. [11] van der Bogert et al. (2020) LPSC 51, 1876. [12] Flahaut et al. (2012) Adv Space Res 50, 1647-1665; [13] Kring and Durda (2012) LPI Cont 1694, https://www.lpi.usra.edu/exploration/CLSE-landing-site-study/; [14] Keller et al. (2016) Icarus 273, 2-24; [15] Hiesinger et al. (2003) JGR 108, 1-27; [16] Lawrence and Hawke (2008) LPSC 39, 1804; [17] van der Bogert and Hiesinger (2020) LPSC 51, 2088; [18] Milliken and Li (2017) 10.1038/ngeo2993; [19] Iqbal et al. (2019) LPSC 50, 1005.

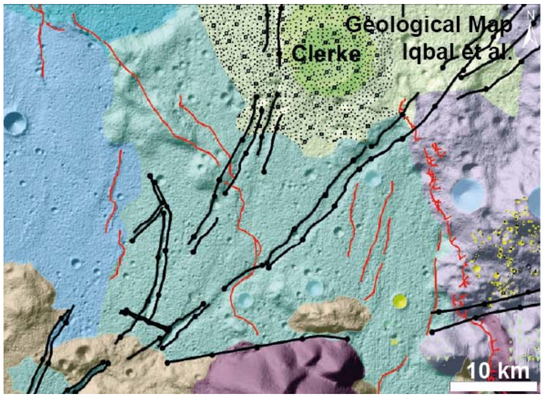

Figure 1. *Geological map of [19] showing the region around a potential end-to-end ISRU demonstration site NW of Taurus Littrow valley and south of Clerke crater.*

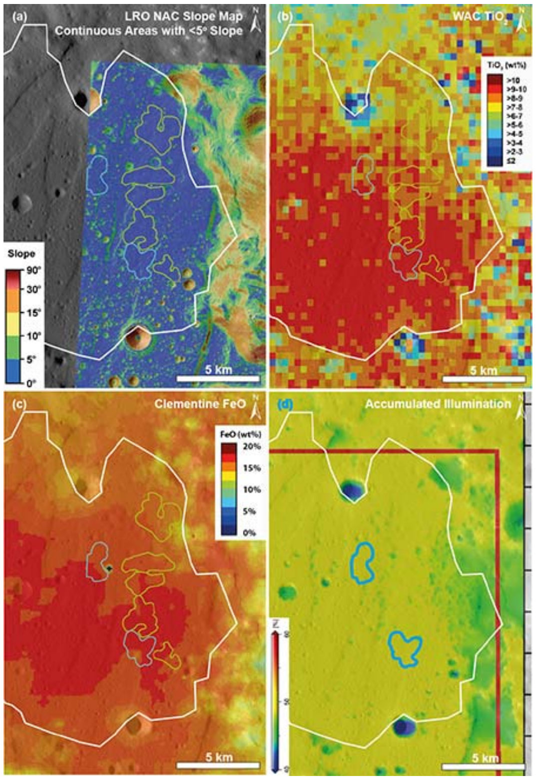

Figure 2. *Assessment of potential end-to-end ISRU demonstration sites combines analyses of (a) slopes, (b,c) Ti and Fe compositions, and (d) accumulated illumination, to select regions (e.g., cyan areas) that meet both engineering and technological constraints.*

QUANTITATIVE EVOLVED GAS ANALYSES OF APOLLO LUNAR SOILS.

A. B. Verchovsky[1], M. Anand[1,2] and S. J. Barber[1]. [1]School of Physical Sciences, The Open University, Walton Hall, Milton Keynes MK7 6AA, UK. [2]Department of Earth Sciences, The Natural History Museum, London, SW7 5BD, UK. (sasha.verchovsky@open.ac.uk).

Introduction: Recently we have developed a quantitative evolved gas analysis (QEGA) method for geological samples [1]. It is based on calibration of the registration device, a quadrupole mass spectrometer (QMS), by passing through it reference gases with known flow rates. For calibration purposes we used pure gases such as H_2, He, N_2, CO, CO_2, O_2, CH_4 and Ar as well as mixtures thereof. The method was first tested using compounds such as $CaCO_3$, $CaC_2O_4H_2O$, PdO, $NaHCO_3$ that give known amounts of simple gases upon their thermal decomposition. A precision of about 20% (1σ) was achieved for the absolute amounts of the analysed gases. The method was then applied for the analysis of meteorite reference samples, Murchison and Allende [2]. In the present study we applied the QEGA method to five Apollo lunar soil samples that have been previously analysed for C, N and noble gases using stepped combustion [3].

Samples: The samples analysed include soils collected by Apollo 12, 14, 15, 16 and 17 missions (12070, 14141, 15040, 69921 and 72501 respectively), representing a range of maturity from extremely mature, 15040 (I_s/FeO=94) to immature, 14141 (I_s/FeO=5.7) [3].

Experimental: Adapting the experimental protocol described in [1] the flow rate of reference gases was regulated with three standard (1/32 inch) capillary pipes with crimps instead of PZT valve. Each capillary is set to provide a fixed flow rate. Pneumatic valves enable the gas flow to be switched between individual or combinations of capillaries such that five different fixed gas flow rates are possible in a range over one order of magnitude. To calibrate the system for water and sulphur dioxide we used decomposition of gypsum. In all experiments the linear heating rate of 12°C/min was applied over the range from 100 to 1400 °C.

Results: Typical release patterns of the major gas species from the studied lunar soils are shown in Figures 1 and 2. Most of the released components can be clearly identified. However, the QMS has insufficient resolving power to separate N_2^+ and CO^+ hence the signal at m/z 28 can in principle be a mixture of signals from nitrogen, carbon monoxide and second order signal from carbon dioxide. Analysis of the second order signals from N_2 and CO at m/z 14 and 12 respectively can help to identify the gases contributing to the m/z 28 signal. The relationships between the main and the second order signals have been obtained from the analysis of pure gases. Similarity of signals at m/z 12 and 14 (Figs. 1 and 2) clearly indicates that at m/z 28 both N_2 and CO make a significant contribution. There are two peaks of N_2+CO release with the higher intensity observed at lower temperature (also apparent on pressure graph).

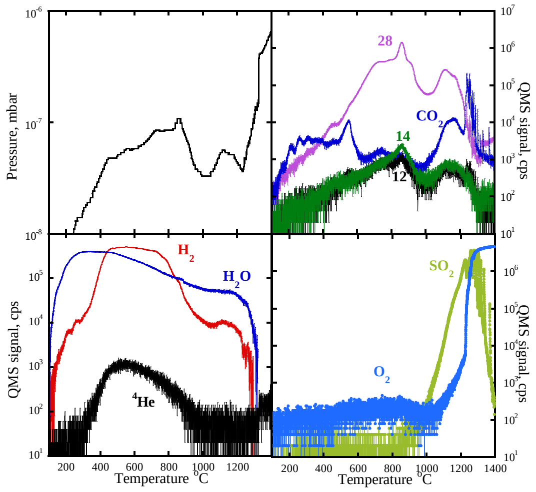

Figure 1. Release patterns of different gases during EGA of mature sample 69921. Pressure variations are also shown.

Release of H_2 basically coincides with that of ^{4}He. CO_2 appears in two temperature ranges: 200-600 °C and 1000-1300 °C. Water has a broad release pattern almost over the entire temperature range (Fig. 1). SO_2 is released at higher temperature (>1000 °C). There is also a major oxygen release at T >1200 °C associated with the highest record of pressure (Figs. 1 and 2).

Discussion: *Release patterns.* In general, the observed release pattern of different gases corresponds well with those from previously analysed lunar soils using similar (but non-quantitative) method about 50 years ago [3] in which, however, 50-100 times larger sample aliquots than in the present study were used. It includes the double peak of N_2+CO, the low temperature and simultaneous release of H_2 and ^{4}He, the high-temperature release of SO_2, the low- and high-temperature release of CO_2 and the high-temperature release of O_2. The interpretation of different gas releases associated with certain temperature intervals given in [4] seems reasonable. It concerns the release of solar H_2 and ^{4}He, the low-temperature release of CO_2 as a result of decrepitation of vesicles or voids and the chemical reactions between different minerals resulting in release of SO_2 from troilite due to its reaction with silicates, and CO due to FeO+C reaction. However, for the appearance of large amounts of O_2 at the very high temperature we suggest that

SiO_2 vapours (from the quartz extraction tube) may be decomposed by the catalytic action of Pt (used to wrap the samples). Gibson and Johnson [3] suggested that in their all-metal extraction system this O_2 was produced as a result of chemical reaction between FeO and the Pt crucible. We cannot exclude that this process is also taking place in our case but its contribution to the O_2 release budget is small since similar O_2 release is also observed in the blank experiments.

The double peak release of solar and non-solar N_2 from lunar soils is observed in experiments of stepped combustion [2, 5] that seems to be related to the lunar soil's maturity. The immature soil 14141 shows only one peak of N_2 release (Fig 2).

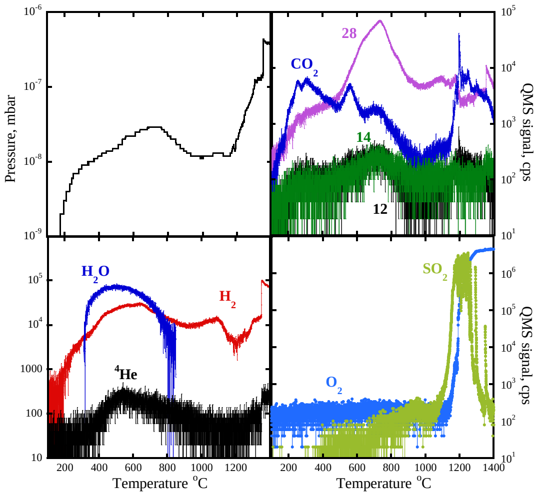

Figure 2. Release patterns of different gases during EGA of immature sample 14141. Pressure variations are also shown.

Concentrations.

1. Hydrogen. The hydrogen concentrations determined in the samples analysed are (in ppm): 14141 – 32, 15040 – 66, 69921 – 61, 12070 – 36 and 72501 – 64. These concentrations are well within the range (27-70 ppm) determined by a combination of pyrolysis with gas chromatographic methods for Apollo lunar soils [6]. Simultaneous release of ^{4}He and H_2 suggests that most of this hydrogen appears to be associated with solar wind implantation.

2. Helium. The ^{4}He concentrations calculated for the samples are (in cc/g): 14141 – 0.014 (0.019), 15040 – 0.085 (0.048), 69921 – 0.046 (0.031), 12070 – 0.072 (0.05-0.06) and 72501 - 0.22 (0.023). In parenthesis the ^{4}He concentrations measured by stepped combustion [3] are shown. In most cases the differences between the results obtained by different methods are within reasonable agreements taking into account the associated uncertainties and possible sample heterogeneity. The reason for larger discrepancy for the sample 72501 is not clear. Apart from the sample heterogeneity, formation of dimeric $[H_2]_2^+$ ions cannot be ruled out. The H/He ratio for the samples vary from 7 to 50. It suggests preferential loss of ^{4}He over H_2 in order to explain the deviations from the solar ratio (17), although a part of the H_2 may have a non-solar origin.

3. Sulphur. The total sulphur concentrations determined using the SO_2 release are (in ppm): 14141 – 970, 15040 – 880, 69921 – 730, and 12070 – 750. These concentrations are well within the range (290 -1400 ppm) determined in lunar soils by other methods [7].

4. Water. The H_2O concentrations determined in our samples by the described method are (in ppm): 14141 – 120, 15040 – 120, 69921 – 660 and 12070 – 310. These concentrations seem to be higher than actually known for lunar. In our calculations we rely on the assumption that the water transfer from the extraction furnace to the QMS through the metal pipes occurs in a similar way for the soil samples and for the reference material ($CaSO_4*2H_2O$) even when the pipes are kept at room temperature. This may not be exactly the case.

5. Nitrogen. The nitrogen concentrations in the analysed samples are (in ppm): 14141 – 82 (19), 15040 - 250 (106), 69921 – 220 (108), 12070 - 170 (50-70) and 72501 – 40 (80). In parenthesis the N concentrations determined in the samples by stepped combustion [3] are shown. In most cases the concentrations of nitrogen measured in the present study are higher than expected. There could be multiple reasons for this. Apart from using a poor second order signal at m/z 14 (instead of m/z 28) that increases uncertainty of the calculations, there might also be a contribution from CO at this mass.

6. Carbon. The total carbon concentrations calculated using both CO_2 and CO (as recorded at m/z 12) releases from the lunar soils are (in ppm): 14141 – 290 (210), 15040 – 310 (320), 69921 – 320 (740), 12070 - >70 (250) and 72501 – 160 (400). In parenthesis the C concentrations determined in the samples by stepped combustion [3] are shown. The reasons for the lower calculated than measured by stepped combustion concentrations in few cases are not yet clear and are being currently investigated.

Conclusions: The developed QEGA method has been applied successfully for the measurements of Apollo lunar samples. Future applications will likely include measurements of lunar volatiles at the lunar surface through ESA's PROSPECT payload on Luna 27.

References: [1] Verchovsky A. B. et al. (2019) *PSS* **181**, 104830. [2] Mortimer J. et al. (2017) LPSC XCVIII, abstr. #2113. [3] Mortimer J. et al. (2016) *GCA* **193**, 36-53. [4] Gibson E. K. and Johnson S. M. (1971) *Proc. 2d LSC* **2**, 1351-1366. [5] Assonov S. S. et al. (2002) *MAPS* **37**, 27-48. [6] Bustin R. et al. (1986) *LPSC XVII*, abstract, 95-96. [7] Gibson E. K. (1977) *Phys. Chem. Earth* **X**, 55-62.

VOILA: LASER-INDUCED BREAKDOWN SPECTROSCOPY (LIBS) FOR THE DETECTION OF VOLATILES IN THE LUNAR POLAR REGION.

D. S. Vogt[1], S. Schröder[1], H.-W. Hübers[1,2], L. Richter[3], M. Glier[3], G. G. Artan[3], P. Wessels[4], J. Neumann[4], [1]Deutsches Zentrum für Luft- und Raumfahrt e.V. (DLR), Berlin, Germany, david.vogt@dlr.de, [2]Humboldt-Universität zu Berlin, Berlin, Germany, [3]OHB System AG, Weßling, Germany, [4]Laser Zentrum Hannover e.V., Hannover, Germany.

Introduction: The Moon has recently come into the focus of attention of international space agencies again. Concepts for the establishment of a long-term human presence on the Moon have been proposed, such as the Moon Village concept championed by ESA and NASA's lunar outpost concepts as part of the Artemis program. One reason for this renewed interest in the Moon was the discovery of water ice in the lunar polar regions by the Chandrayaan-1 mission [1]. Water and other volatiles are important resources both for life support and for potential applications as fuels and propellants for spacecraft. In-situ resource utilization (ISRU) of volatiles could significantly reduce the costs of a sustained presence on the Moon and could be beneficial for the future human exploration of the solar system [2]. The detection of volatiles is therefore an important scientific goal for future robotic missions to the Moon.

The LUVMI-X project (Lunar Volatiles Mobile Instrumentation Extended) is developing an initial system design as well as payload and mobility breadboards for the detection of volatiles in the lunar polar region on a small, lightweight rover [3]. One proposed payload is VOILA (Volatiles Identification by Laser Analysis), a LIBS instrument developed by OHB System AG (OHB), Laser Zentrum Hannover (LZH), and the German Aerospace Center (DLR). LIBS (laser-induced breakdown spectroscopy) is a technique that requires only optical access to its target [4]. A LIBS spectrum is obtained within seconds, making it well-suited for quick analyses of multiple targets in proximity to the rover. LIBS was first used in space by the ChemCam instrument on board Curiosity of NASA's Mars Science Laboratory mission [5, 6]. The first LIBS instrument on the Moon was supposed to operate on board the Pragyan rover of India's Chandrayaan-2 mission [7], but the lander crashed onto the lunar surface during descent in September 2019.

Here, we demonstrate the potential of LIBS for the detection of volatiles on the lunar surface. We show preliminary feasibility studies as well as first results of the VOILA demonstration model.

Experimental Setups: The VOILA demonstration model will employ a pulsed laser developed by LZH with a pulse energy of at least 15 mJ at a wavelength of 1030 nm. Samples will be placed onto a nitrogen-cooled sample stage inside a simulation chamber for ambient pressures down to 0.1 Pa. This should be sufficiently low to simulate lunar near-vacuum conditions, since no changes of the LIBS signals have been observed at pressures below 1 Pa [4, 8]. LIBS spectra will be measured with several miniature spectrometers (Avantes AvaSpec-Mini) in order to achieve a broad spectral coverage.

The preliminary feasibility studies shown here were made with two LIBS setups at DLR Berlin. One uses an echelle spectrometer (LTB Aryelle Butterfly) with a spectral coverage from 270 nm to 850 nm. The second setup is used to measure spatial distributions of plasma emissions. Both use ICCDs (Andor iStar) for time gating and Q-switched Nd:YAG lasers (Continuum Inlite / Quantel Viron) at 1064 nm with pulse durations of about 6 ns. Simulation chambers were used to reduce the ambient pressure to about 0.1 Pa.

Samples: Lunar regolith simulants such as NU-LHT-2M, BP-1, and Exolith LMS-1 and LHS-1 are analyzed in this study. They were either pressed into pellets or used as loose material in order to emulate the density of the regolith dust on the lunar surface. The loose regolith was filled into a beaker up to a height of about 10 mm. Additionally, pressed pellets of varying hydrogen concentration were mixed from basalt and gypsum ($CaSO_4 \cdot 2H_2O$) in order to investigate the feasibility of hydrogen quantification.

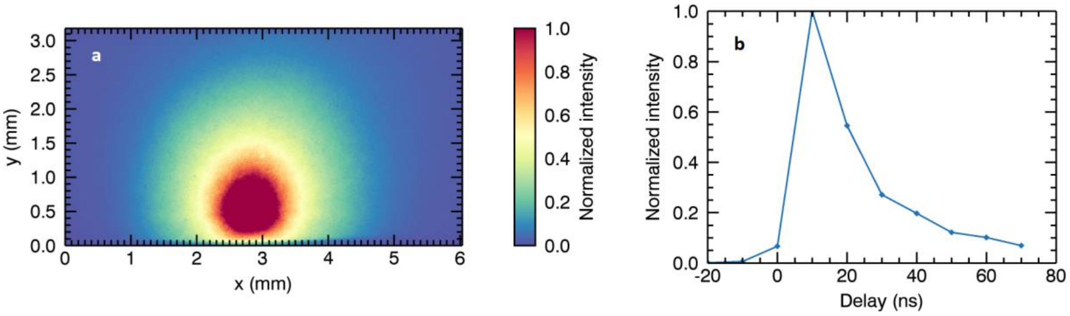

Figure 1: LIBS plasma of a pressed pellet of NU-LHT-2M at 0.1 Pa for a pulse energy of 22 mJ. a) Side view at 10 ns delay with a 10 ns gate. b) Time evolution of the total intensity. Measurements were made in steps of 10 ns with a gate of 10 ns.

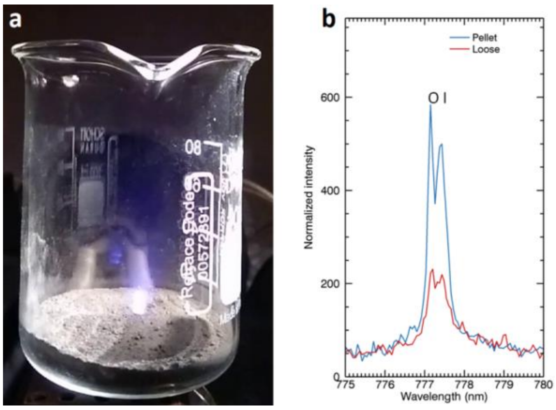

Figure 2: a) Plasma formation for loose LMS-1 regolith simulant at a pulse energy of 15 mJ. b) Spectra of O lines at 777 nm for pressed and loose LMS-1 samples (15 mJ/pulse).

Results: Plasma emissions at 0.1 Pa atmospheric pressure are still very intense (Figure 1a). The plasma plume is several millimeters large and has a circular shape. The plasma has a short lifetime of less than 100 ns (Figure 1b), so that time gating for specific spectral features is not feasible. Laser energies as low as 5 mJ/pulse produced spectra with clear lines of the major elements in the regolith in the case of pressed samples. For loose regolith measurements (Figure 2a), the ablation process is less efficient. The signal-to-noise ratio was reduced and higher laser energies of about 15 mJ/pulse were needed to produce spectra that could be analyzed (Figure 2b).

In order to analyze the low-intensity H signal in the basalt/gypsum samples, 450 individual spectra were averaged for each sample. In order to reduce the influence of atmospheric hydrogen adsorption, 5 laser shots were made at each position before measuring. In the averaged spectra, the H line at 656.3 nm can be detected clearly even for the lowest H concentration of 0.17 wt% (Figure 3a). A clear correlation of the measured H line intensities with the H concentration in the samples can be observed (Figure 3b).

Conclusion: Our initial experiments show that LIBS can be employed at low pressures and that high signal intensities can be obtained even in loose regolith. The pulse energy of about 15 mJ is achievable by the VOILA laser prototype developed by LZH. The detection and quantification of hydrogen is promising, but adsorption from the atmosphere needs to be controlled in the lab experiments. Low-temperature measurements of frozen regolith mixed with water ice should be done to investigate whether water ice can be distinguished from other hydrogen and oxygen sources. New results obtained with the VOILA demonstration setup developed by OHB, LZH and DLR will be presented at this symposium.

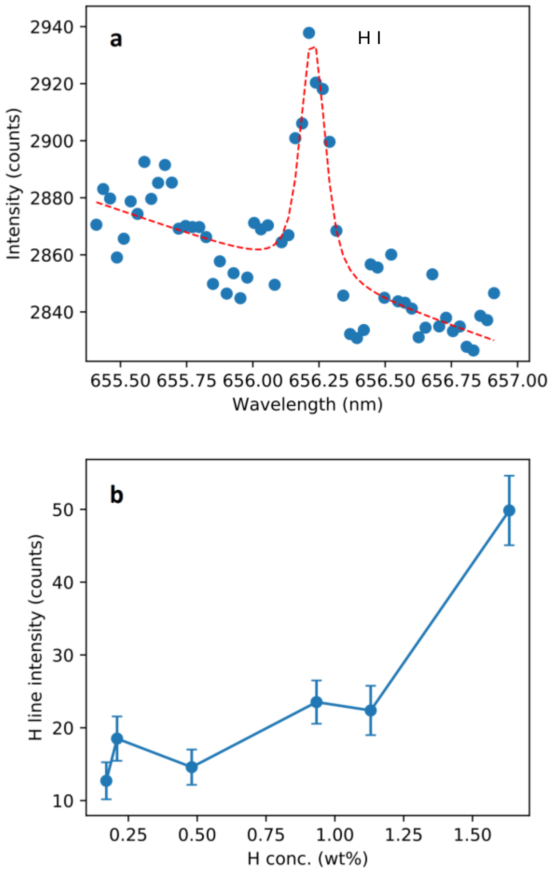

Figure 3: a) Spectrum (blue dots) and Voigt fit (red dashed line) of the H line at 656.3 nm for a 13:1 basalt/gypsum mixture (0.17 wt% H). b) Fitted intensities of the H line obtained from averaged spectra for all basalt/gypsum mixtures. All measurements were made with a laser energy of 15 mJ/pulse.

Acknowledgments: This research was funded by the European Union's Horizon 2020 research and innovation program under grant agreement No. 822018.

References: [1] Li S. et al. (2018) *PNAS, 36,* 8907–8912. [2] Anand M. et al. (2012) *Planet. Space Sci., 74,* 42–48. [3] Gancet J. et al. (2019) *ASTRA 2019*. [4] Knight A. K. et al. (2000) *Appl. Spectrosc., 54,* 331–340. [5] Maurice S. et al. (2012) *Space Sci. Rev., 170,* 95–166. [6] Wiens R. C. et al. (2012) *Space Sci. Rev., 170,* 167–227. [7] Laxmiprasad A. S. et al. (2013) *Adv. Space Res., 52,* 332–341. [8] Lasue J. et al. (2012) *J. Geophys. Res., 117,* E1.

THE OXFORD 3D THERMOPHYSICAL MODEL WITH APPLICATION TO THE LUNAR PROSEPCT MISSION.

T. Warren[1], N. Bowles[1], O. King[2], E. Sefton-Nash[3], R. Fisackerly[3], R. Trautner[3]. (1) Atmospheric, Oceanic and Planetary Physics, University of Oxford, UK, (tristram.warren@physics.ox.ac.uk neil.bowles@physics.ox.ac.uk), (2) Department of Physics & Astronomy, University of Leicester, UK (ortk1@leicester.ac.uk), (3) ESTEC, European Space Agency, Keplerlaan 1, Noordwijk 2201AZ, Netherlands (e.sefton-nash@cosmos.esa.int).

Introduction: To investigate potential in situ near surface volatiles that might be present in the lunar Polar regions, the European Space Agency (ESA) is developing the PROSPECT instrument package to fly to the South Polar region of the Moon on-board Russia's Luna-27/Luna Resurs mission, which is scheduled to launch in the next decade [1,2]. PROSPECT will consist of a drill (ProSEED) that will collect samples from the regolith at depths of up to 1 m below the lunar surface and transfer them into a miniaturised chemical laboratory (ProSPA), where samples will be heated to 1000° C in the presence of different reagent gases to extract a range of different volatile species including water.

To help investigate potential landing sites we have developed the Oxford 3D Thermophysical Model (O3DTM) [3]. Using the O3DTM, we have modelled the lunar surface and subsurface (<2.5 m) temperatures for the South Polar Region (<-76° latitude) at a resolution of ~2 km^2. As an example Figure 1 shows the maximum surface temperature map of the simulated region. The O3DTM has been written in MATLAB and all the code and data files are available on GitHub.

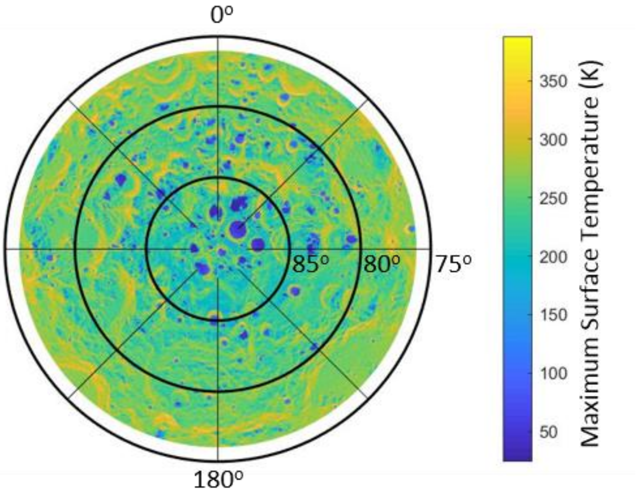

Figure 1 : Simulated maximum surface temperature map.

Oxford 3-D Thermophysical Model: One dimensional thermophysical models are poor predictors of the lunar polar surface and subsurface temperatures due to the importance of shadowing and scattering at high latitudes. To accurately model the surface and subsurface temperatures at the lunar poles requires a 3-D thermophysical model (3DTM). A new 3DTM that includes a discreet subsurface exponential density profile, surface shadowing and scattering effects has been developed at Oxford University to simulate the lunar surface and subsurface temperatures to account for these environmental effects at the poles [4,5,6]. The Oxford 3DTM combines the one-dimensional subsurface heat flow from the Hayne model [6] and the 3-D shadowing and scattering effects used in standard 3DTMs such as the Paige and Vasavada models [4,5]. To compute the shadowing and ray tracing the Oxford 3DTM uses the LOLA topography and albedo datasets. However, since the LOLA albedo measurements are performed using a 1064.4 nm laser the albedo values are scaled to represent the broadband solar albedo value using the method described in [6]. All other thermophysical modelling parameters are taken from [6].

Model Validation: There is currently no in situ data for the Polar Regions to compare to our modelled values, so the simulations have been compared to measurements from the Lunar Reconnaissance Orbiter's Diviner Lunar Radiometer instrument ("Diviner") for validation [7]. The O3DTM is in good agreement with the Diviner measurements with the absolute temperature deviation being typically less than 5 K. Where the absolute temperature deviation is defined as being the time averaged absolute difference between the modelled temperature and the Diviner measured temperature.

Ice Stability Depth: From the thermal model it was possible to define the minimum depth required to drill to reach subsurface temperatures where water ice would be expected to be stable by using the theoretical sublimation rate taken from [8] and shown in Figure 3. The O3DTM splits a single surface element into serval (>10) model layers at different depths. The O3DTM calculates how the temperatures of each layer varies throughout the lunar day night cycle which is modulated by a smaller seasonal cycle.

The temperatures for each model layer inside every surface facet was binned in 1 kelvin bins. This was then convolved with the theoretical sublimation rate given in Figure 2, to give a total sublimation rate for each layer in every facet. We assumed as in previous works [3,4] that the water delivery rate is much greater than 1 Kg/m^2/Ga and hence water ice could exist at a given depth if the total sublimation rate is less than 1 Kg/m^2/Ga. The predicted ice stability minimum depth map using this method is shown in Figure 2**.**

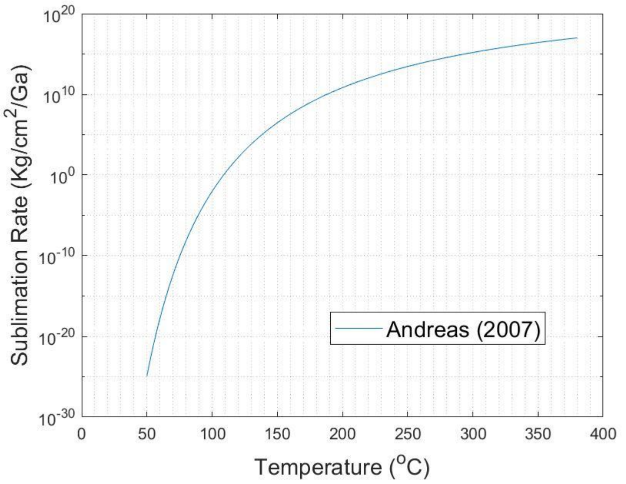

Figure 2 : Theoretical sublimation rate of water ice

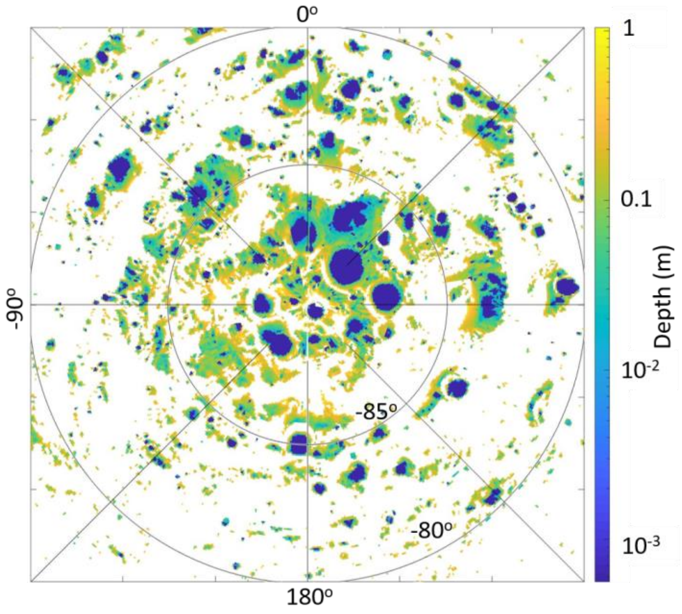

Figure 3 : O3DTM predicted ice stability map.

This method does not account for diffusion or potential pumping of water ice to greater depths [9] and is therefore just a guide to demonstrate where temperature remain cold enough for water ice to exist. We are currently working on coupling a complete diffusion model with the O3DTM to make a more physically accurate model and if completed this work will be presented.

However, at the moment the expected stable ice depth for the lunar South Pole shown in Figure 3 is our best estimate of water ice distribution. It shows there are large regions where ice is not stable at any depths and in those locations where ice is stable the minimum ice stability depth is relatively shallow (< 0.5 m). These results show that, assuming careful selection of landing site the current design depth of the PROSPECT drill (~1 m) should be sufficient to sample trapped water ice.

Comparison to Previous Models: Predicted stable water ice depths have been previously generated by other 3DTM such as Paige [4] and we will present a comparison between the two models. The models agree to within 1 mm of expected stable water ice depth in 90% of the simulated region, but in some specific locations disagree. In the regions of disagreement the O3DTM generally predicts water ice should not be present, but the Paige model predicts water ice at deep depths (> 0.2 m). Currently, the difference in the predicted water ice location is believed to be due to difference in the layering between the two models. The O3DTM use a discreet subsurface exponential density profile with multiple layers (> 10) whereas the Paige model used two discrete layers with different density's.

Conclusions: The Oxford 3DTM is available to download and new surface and subsurface temperature simulations for the lunar South Polar Region are available to download from GitHub - https://github.com/tw7044/O3DTM/

Simulations show depths at which ice would be expected to be stable are generally near the surface (< 0.5 m), so for the Luna-27 lander mission the choice of landing site location and the precision landing capability of the lander are essential given the engineering constraints on the sampling system.

There is an obvious correlation between the illumination fraction and the volatile stability conditions. Luna-27/PROSPECT will therefore have a trade-off to select a site that will satisfy both critical power/operations requirements and science objectives of the PROSPECT mission.

Acknolegents: We would like to thank the UK Science and Technology Facilities Council, the Leverhulme Trust, the UK Space Agency and the European Space Agency for supporting this work financially.

References: [1] Trautner, R. et al. (2018) IAC-18, 42773 [2] Sefton-Nash, E. et al. (2018) LPSC 2740 [3] King and Warren. et al. (2019), PSS 104790 [4] Paige, D. A. et al. (2010), Science, 330, 479. [5] Vasavada, A. et al. (1999) GJR, 193. [6] Hayne, P et al. (2017) Space Sci Rev. [7] Paige, D. A. et al. (2009), Space Sci. Rev.150, 125-160. [8] Andreas et al . (2007) Icarus 186. [9] Schorghofer and Aharonson (2014) AAS 788(2). [10] Warren et al. (2019) JGR 124(2). [11] Warren et al. (2017) Rev Sci 88(12). [12] Foote et al. (2020) Icarus 336.

Apollo Next Generation Sample Analysis: X-Ray Computed Tomography and Dissection of Sample 73002.

R. A. Zeigler[1], R. Hanna[2], D. Edey[2], S. A Eckley[2,3], C. H. Krysher[3], A. B. Mosie[3], R. A. Ketcham[2], J. Gross[1,4,5], F. M. McCubbin[1], and The ANGSA Science Team, [1]NASA, Johnson Space Center, Houston, TX,. [2]Jackson School of Geosciences, University of Texas at Austin, Austin TX. [3]Jacobs Technology, Johnson Space Center, Houston, TX. [4]Dept. of Earth & Planetary Sciences, Rutgers University, Piscataway, NJ. [5]Dept. of Earth & Planetary Sciences, American Museum of Natural History, New York, NY.

Overview: The Apollo missions collected 382 kg of rock, regolith, and core samples from six locations on the nearside of the Moon. Today, just over 84% by mass of the Apollo collection remains in pristine condition within the curation facility at Johnson Space Center. Most Apollo samples have been well characterized, however several types of samples that have remained wholly or largely unstudied since their return, and/or that have been curated under special conditions. These sample types are: (1) unopened samples sealed under vacuum on the Moon; (2) unopened (but unsealed) drive tubes; (3) Apollo 17 samples frozen shortly after their return; and (4) Apollo 15 samples opened and stored in a helium atmosphere since their return. Last summer, NASA solicited proposals for the Apollo Next Generation Sample Analysis Program (ANGSA), and 9 teams were selected to study: (1) unsealed, unopened drive tube 73002; (2) sealed, unopened drive tube 73001 (paired with 73002); and (3) a subset of frozen and He-purged samples [1].

The first sample opened as part of the ANGSA program was drive tube 73002. This is a 30 cm long, 4 cm diameter drive tube collected on a landslide deposit near Lara Crater at the Apollo 17 landing site. It was part of a 60 cm long double drive tube collected, and the bottom half of the tube (73001) was sealed under vacuum on the Moon [2]. Prior to opening sample 73002, the sample was imaged with a high resolution X-ray Computed Tomography (XCT) scan of the entire tube. Additional XCT scans have been made of "large" clasts removed from the core as part of the dissection process [3]. Here we discuss the initial dissection process, as well as present an early look at the XCT data from 73002, and talk about the utility of the scans as part of the curation process, including the potential for future science returns from the high resolutions scans.

Methodology: Sample 73002 was transported to the University of Texas High-Resolution X-ray Computed Tomography Facility (UTCT) to scan the entire length of the tube using their North Star Imaging cabinet XCT system. The tube was scanned in 6 overlapping volumes, each covering a ~4 cm length of the tube (there was only about 20 cm of regolith inside the tube). Each individual scan was corrected for uneven beam and isometric distortion in Z using a linear rescale for both CT value and geometry across Z (i.e., per-slice basis; central slice used as geometric standard). The different scans were then geometrically matched (rigid translation and rotation) and their CT values rescaled (second degree polynomial) to match the spot directly 'below' (e.g., scan 2 matched to scan 1, etc.). Seams between scans were then blended using a gradual linear combination of 9 overlapping slices centered at the matching reference slice. The voxel size for the combined scan is 25.8 µm and there are a total of 8252 "slices" along the length of the tube [Fig. 1].

In addition to the combined 25.8 µm/voxel resolution scan, each volume was also imaged at 12.9 µm/voxel resolution using sub-voxel scanning, essentially imaging each volume four times while offsetting the detector by ½ of a voxel vertically and/or horizontally, effectively doubling detector density. Due to the large data volumes, these scans are only

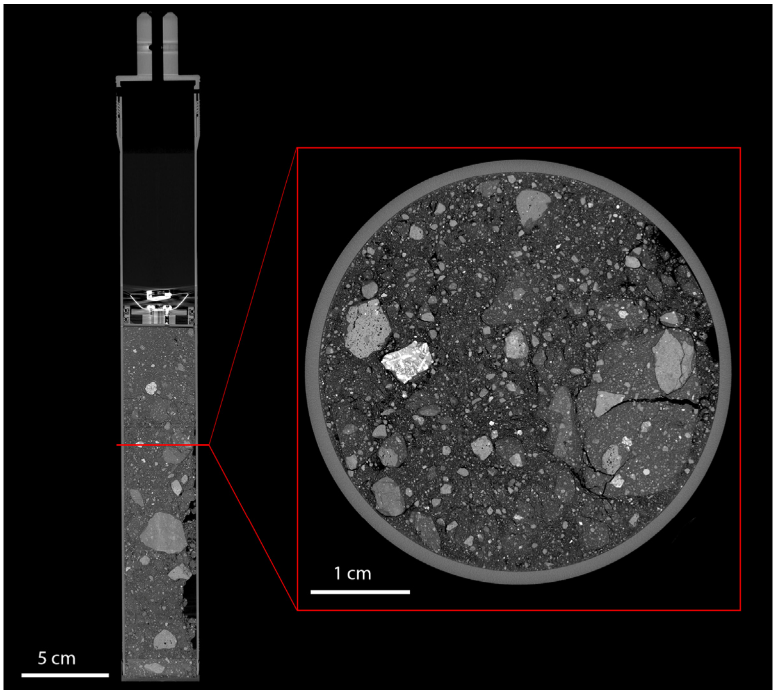

Figure 1: Vertical cross-section view of the combined XCT scan of 73002 (left side) and one of the 8252 horizontal "slices" that comprise the scan on the right.

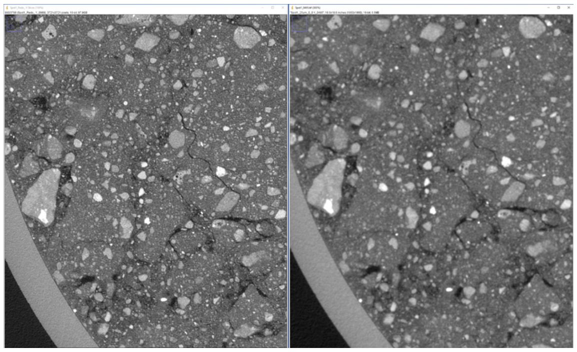

Figure 2: Comparison of the "standard" 25.8 µm/voxel scan on right, with the 12.9 µm sub-voxel scan on the left, which clearly makes lithologic identification easier.

just starting to be investigated, but the increased resolution has great potential [Fig. 2].

Individual clasts >4 mm that are separated from the core as part of the dissection process are individually bagged in Teflon under a Nitrogen atmosphere and scanned using the 180 kV nano-focus transmission source on the Nikon XTH 320 XCT system at NASA Johnson Space Center [4]. Each scan has a resolution of 3-7 µm/voxel depending on the size of the clast (Fig. 3).

Results and Discussion: The combined scan of the core tube (as well as the individual higher resolution scans of sections of the core) allows for easy detection and tentative classification of mineral and lithic clasts within the entire length of the drive tube, as well as void spaces. These scans allowed us to identify and avoid potential pitfalls that might have complicated the extrusion process of the core, such as angular clasts near the edges. It also allows for identification of "soil clods" within the core, which typically do not survive the dissection process, but could be targeted in the future. During dissection of each interval of the drive tube, the macroscopic scan is used as a guide for what to expect (voids, large clasts) and gives the processor an idea of any potential complications for each day's work. Although no large scale structural features, such as layering, have been observed, additional analysis of the data (especially the sub-voxel scan data) has the potential to make these discoveries in the future.

To date, >25 individual clasts have been scanned at high resolution; a subset of these are shown in Fig. 3. A good estimate of the lithology of each clast is readily apparent using the XCT scans. This is not possible using optical microscopy, as each clast is coated with a fine-grained dust making lithologic identification difficult. This information will be invaluable when allocating specific lithologies (e.g., basalts or impact-melt breccias) for detailed analyses and targeted investigations..

References: [1] Shearer et al. (2020) LPSC 51. [2] Shearer et al. (2018) LPSC 49, #2083. [3] Krysher et al (2020) LPSC 51. [4] Eckley et al (2020) LPSC 51, #2182.

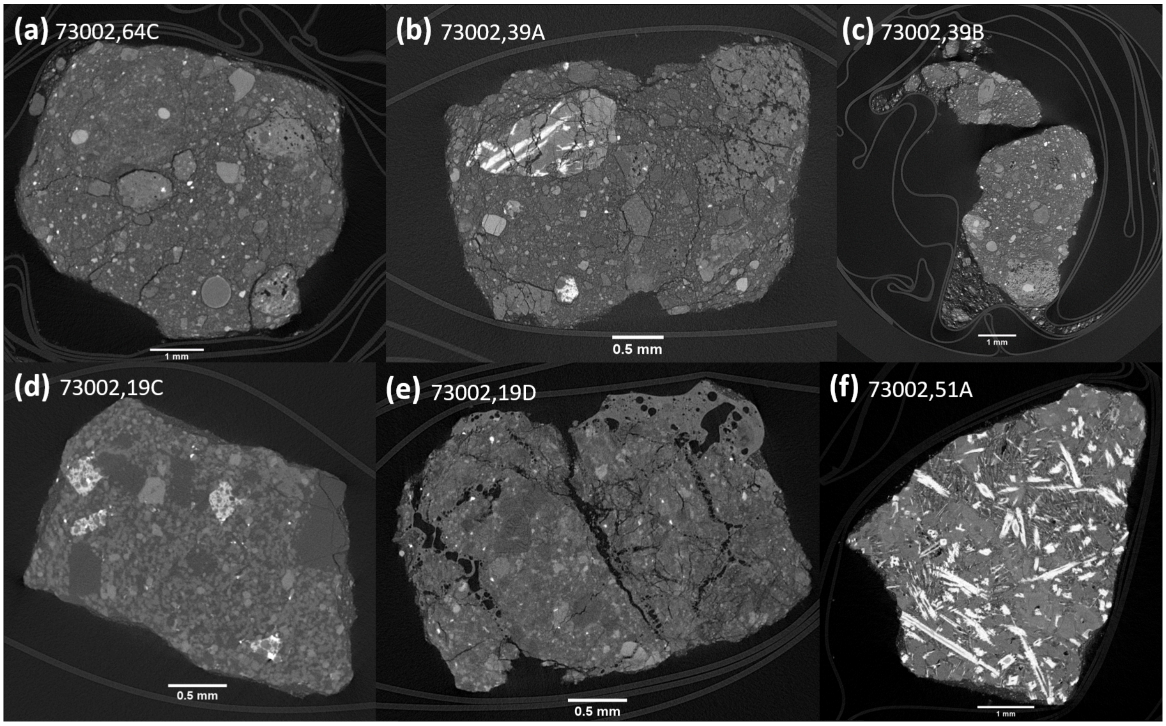

Figure 3: XCT scans of individual clasts: (a) regolith breccia (voxel = 5.9 µm); (b) regolith breccia (4.9 µm); (c) soil breccia (5.9 µm); (d) impact-melt breccia (3.5 µm); (e) Glassy regolith breccia/agglutinate (3.9 µm); (f) basalt clast (5.5 µm).